The University of Nottingham

WIND GENERATOR-ENERGY STORAGE CONTROL SCHEMES FOR AUTONOMOUS GRID

By

Meghdad Fazeli

Thesis submitted to the University of Nottingham

For the degree of Doctor of Philosophy

December 2010

ABSTRACT

Conventionally the power network operators were obliged to buy all the wind energy generated by wind farms. However, as the penetration of wind energy (or generally any other sort of renewable source) in a power system is increased, the ability of other generators to balance the demand becomes limited. This will necessitate the control of wind turbines in order to generate a given demand power rather than extracting the maximum wind power. This control approach is termed "Power Demand Control" in this thesis. In contrast to Power Demand Control, "Power Smoothing Control" utilizes energy storage systems in order to absorb high frequency wind fluctuations, hence, delivering a smoother version of wind power into the grid/load. The drawback of the Power Smoothing approach is that the average power into the grid/load is still determined by the available wind power rather than the system operator. The Power Demand Control approach, which has received little attention in literatures, is the main focus of this thesis. This research proposes control schemes with and without external energy storage for the Power Demand Control strategy.

This thesis studies different possible methods of applying Power Demand Control, in particular the droop control method. It is shown that a droop-controlled wind farm does not need a central "Supervisory wind Farm Control" unit to determine the power demanded from each DFIG. Moreover, a droop-controlled wind farm has the advantage of controlling the local grid voltage and frequency. This means that no external voltage and frequency source is required which makes a droop-controlled wind farm a more suitable option for integration of wind energy at distribution level. The classical droop control is modified in order to make the DFIGs share the demand power not only according to their ratings but also to their associated available wind power. The applications of the control paradigm are discussed, including: integration into microgrids, AC grids and HVDC connection feeders. This work mainly concentrates on microgrid applications.

An Energy Management System is proposed in order to keep the energy level of the energy storage (or the DFIG's shaft speed) within its limits using an Auxiliary Generator and a Dispatchable Load. Different possible system configurations are introduced and their advantages and drawbacks are discussed.

It is illustrated through simulation that the proposed control scheme can inherently ride-through a grid fault with no need for communication. Furthermore, it is shown that the control scheme can operate if the wind speed drops to zero.

The simulations are carried out using the PSCAD/EMTDC software.

ACKNOWLEDGEMENTS

LIST OF SYMBOLS

R_s, R_r	Stator and rotor resistance
L_s, L_r, L_o	Stator, rotor and mutual inductance
l_s, l_r	Stator and rotor leakage inductances
p	Pole pair number
J	Combined turbine and generator inertia
$\omega_e, \omega_r, \omega_s$	Supply, rotor and slip angular frequency
$i_{rd}, i_{rq}, i_{sd}, i_{sq},$	Machine rotor and stator currents in dq axis
i_{ms}	Machine magnetising current
i_{gcd}, i_{gcq}	Front-end converter current in dq axis
$v_{rd}, v_{rq}, v_{sd}, v_{sq},$	Machine rotor and stator voltages in dq axis
φ_s, φ_r	Machine stator and rotor flux
θ_s	Stator flux angle
T_e, T_m	Electrical and mechanical torque
m	Active power-frequency droop gain
n	Reactive power-voltage droop gain
N	Gear ratio
S	Machine slip
ζ	Damping factor
C	DFIG DC-link capacitance
V_{dc}	DFIG DC-link voltage
R_β	Pitch angle maximum slew rate
P_{DFIG}, P_{HVDC}	Machine and HVDC link active power
$Q_{DFIG}, Q_{HVDC}, Q_{FILTER}$	Machine, HVDC link and AC filter reactive power
α	HVDC rectifier firing angle
I_o	HVDC rectifier DC-link current
R_C	HVDC DC-link cable resistance
L_C	HVDC DC-link cable inductance
E_o	Inverter output voltage in the DC-link
ρ	Air density
β	Pitch angle

A	Rotor blade area
C_p	Power coefficient
V_w	Wind speed
λ	Tip speed ratio
αβ	αβ stationary axis
dq	*dq* rotating axis
$\_$	Vector variables
*	Reference variables
pu	Per Unit (based on the total wind farm)
pu$_{gen}$	Per Unit (based on the associated DFIG)
P_{es}	Energy storage power
E_{es}	Energy level of energy storage
$\hat{P}_{ext}$	Extractable wind power (i.e. the power transmitted to the shaft with pitch angle=0)
$\hat{P}_{ave}$	Average of the extractable wind power

Glossary of terms

DFIG: Doubly Fed Induction Generator

SCIG: Squirrel Cage Induction Generator

GB: Gearbox

DSFO: Direct Stator Flux Orientation

ISFO: Indirect Stator Flux Orientation

LCC: Line Commutated Converter

VSC: Voltage Source Converter

MPT: Maximum Power Tracking

CTM: Constant Torque Mode

CPM: Constant Power Mode

DG: Distributed Generation

T&D: Transmission and Distribution

PSC: Power Smoothing Control

PDC: Power Demand Control

AG: Auxiliary Generator

DL: Dispatchable Load

EMS: Energy Management System

PFC: Power Flow Controller

Table of contents

1. Introduction and technical background

1.1 Environmental impact to energy use

The Kyoto Protocol is an international agreement, negotiated in December 1997. The objective of the Kyoto Protocol is the "stabilization of greenhouse gas (CO_2, NO_x, SO_x, etc) in the atmosphere at a level that would prevent dangerous anthropogenic interference with the climate system" [1]. Thirty six countries are required to reduce their greenhouse gas emissions below the level specified for each of them in the treaty [2]. Some industrialized nations have committed to making substantial reductions in their greenhouse emissions by 2012. Over one hundred countries have ratified the protocol, but have no obligation beyond monitoring and reporting their greenhouse emissions. Therefore, many counties are setting targets to increase the amount of the electrical energy produced by renewable energy sources.

The United Kingdom is a signatory to the Kyoto Protocol. The energy policy of the United Kingdom fully endorses goals for carbon dioxide emissions reduction and is committed to proportionate reduction in national emissions. To achieve this, the Government has set a target that 15% of the generated electrical energy will be produced from renewable sources by 2015.

The main renewable sources of energy are wind, solar, geothermal and tidal. Amongst theses renewable sources, wind energy generation is receiving much interest all over the world. The rated capacity of installed wind power reached nearly 46000MW worldwide during 2004 and is expected to reach 175000MW by 2012 [3]. This work is concentrated on the wind energy generation.

1.2 Wind energy and energy storage

Due to the environmental and economical reasons the penetrations of wind energy in power systems is rapidly increasing worldwide. It is predicted [4] that by 2020 up to 12% of the world's electricity will be supplied from wind power. The

impacts of wind energy on power grids is better understood at present compared to a decade ago, but its integration into power grids continues to be a topic that receives a considerable amount of interest in the international community [5]. The effects of wind energy on power systems have been investigated to some extent: spinning reserve requirements, effects on power quality, reactive power demands and voltage control [6-8]. As a result of these studies, many utilities have revised their existing grid codes to include specific functionalities which must be satisfied by wind generators [9]. Technically this requires modifications to traditional wind farm designs in the form of added equipment, implementation of modern wind turbine technologies, sophisticated prediction and control strategies, or a combination of the above [7]. For example, conventionally, the power network operators were obliged to buy all the wind energy produced by wind farms. However, this is subject to change as the wind energy penetration increases and recently the Danish power operator introduced a fine for the wind farms producing energy more than the demanded value.

The primary problems associated with the wind energy are due to the nature of the source itself, which is both time varying and difficult to predict [10]. Consequently, the output power of wind farms is time varying and unpredictable as well. Since the energy to the grid must equal that of the total demand, a strict power balance must be upheld. The wind power variations in power systems with low level of wind energy penetrations are more or less tolerable. However, in cases where wind energy reaches a high level of penetration, the effect of these variations become more evident as the ability of other generators to balance the load requirements becomes limited. The situation is deteriorated in cases where the wind generators are connected to a weak system or a distributed feeder. In these cases the oscillating wind powers are reflected in voltage and frequency fluctuations at the point of connection, which can result in undesirable secondary effects. Although the majority of the wind farms are connected to the transmission systems, it is noted that in a considerable number of these cases they are connected to a weak system since wind energy sources are often far from the main grid and central generators. At the distribution level, the need to supply the local load is not

always required. However, in cases where island operation is required (i.e. microgrids); the entire local load needs to be supplied by the distributed generators including the wind turbines.

The fluctuating power results in a number of problems such as voltage flicker, balancing the demand, and instability, especially in the cases of remote or islanded power systems [10-12]. Although combining the generator with power electronic interfaces can enable the reactive power-voltage control, the real power control remains an issue which requires further attention. It is noted that spatial distribution of many turbines across the farm does in fact reduce the oscillation of the total wind farm output power as an averaging effect is produced across all the wind turbines due to the phase shift in their associated wind speeds. However, in cases where the number of wind turbines is small or when the capacity of the wind farm is significant compared with the other generators, the need for power management and improvement in power quality still exist. Furthermore, the produced wind power is still unpredictable which will require an auxiliary source and energy management scheme in order to maintain the power demanded by the load.

Energy Storage (ES) systems have emerged as a potential solution to overcome the intermittency and the short term varying nature associated with wind energy generation [13]. Integration of the ES system into wind energy generation can benefit the power system in different aspects such as [3, 14, 15]:

- Smoothing the wind power fluctuations through absorbing its higher frequencies [16].
- Controlling active power balance [5, 17].
- Providing spinning reserve in order to support the local grid frequency control [18, 19]. This uses the concept of active power-frequency control in which as power increases the frequency drops. Therefore, the ES capacity can be used to absorbs or inject energy in order to provide frequency control.

- Supporting the low voltage ride-through capability by serving as a power sink during low system voltages [14]. Recent grid codes require the wind generator to stay connected during voltage depressions. In such occasions, in which the wind power has no place to go, the ES can serve as a power sink to absorb the wind energy. This application requires ES technologies with large energy capacity especially in the case of large wind farms.

ES systems can be classified into short-term or long-term. The short-term ES systems are usually used to smooth out wind power fluctuations while the long-term ES systems are controlled to level the imbalance between the demand and available wind energy. In a short-term ES system the normal approach has been for power smoothing in which the ES absorbs the higher wind frequency fluctuations. This is called *Power Smoothing Control* (PSC) [5, 16, 17]. This thesis will address short-term (or medium-term) ES, not by PSC, but as an aid to meeting the required user power demand in conjunctions with other auxiliary energy management hardware. This will be called *Power Demand Control* (PDC). This work is mainly concentrated on the PDC strategy.

The wind turbine rotor inertia can also be used as an ES mechanism [20-22]. However, due to the obvious limitation resulting from the overspeed rating of the generator and the fact that the wind turbine exhibits unstable behaviour for low shaft speed; the use of the turbine inertia as the only ES mechanism is not very beneficial. Obviously using an external ES can enhance the benefits of the ES for the power system. This thesis will propose control structures both with and without an external ES.

1.2.1 Review of current ES technologies

A number of different ES technologies currently exist. In all of them a power electronic interface is needed in order to be properly integrated with the grid.

In selecting the type of the storage device for a given need, both the power rating and energy rating of the device must be considered. Moreover, the charging and discharging characteristics and efficiency are important factors in choosing the

type of the ES device. While the nature of the storage device will influence the power electronic interface structure, the limitation of the system and the energy capacity of the ES impose the need for a management scheme in order to coordinate the flow of energy to and from the device. The most common ES technologies can be summarized in terms of short-term, medium-term and long-term ES [14, 23] as is shown in Table 1.1:

Time scale	Short-term <10s	Medium-term 10s-60mins	Long-term 1-24hors
Storage types	Capacitors Supercapacitors Flywheel SMES	Batteries Flywheel Hydro-pumped Hydrogen generation	Hydro-pumped Hydrogen generation Regenerative fuel cell Compressed air

Table 1.1. Comparing different ES technologies in terms of short-, medium- and long-term [14]

The short-term ES systems range from 100W to 500kW, the medium-term ES systems range up to 1000kW and the long-term ES systems can be rated up to 20MW [23].

It is noted that this work concentrates mainly on short-term to medium-term ES systems. However, it will not deal with a certain type of ES technology. It is intended to study the possible control scheme for the ES systems and possible locations for them. Therefore, throughout this thesis, the ES system is simulated by an ideal DC-voltage source connected to the grid through an AC/DC converter. The different ES technologies are briefly reviewed as follows:

Batteries

Batteries come in many different types and are perhaps the most versatile than any of the storage devices as they offer desirable storage characteristics for wide ranges of applications and are generally cheaper in most cases. Rechargeable batteries such as valve-regulated Lead-acid or nickel-cadmium are the most popular due to their availability and reliability [24].

Supercapacitors

Similar to batteries, supercapacitors [5, 16] are based on an electrochemical system and are voltage based device which are usually interfaced using a DC/DC chopper. Supercapacitors are able to manage similar energy densities as the batteries but with longer lifetime and lower maintenance. However, they are only available for very low voltage (about 3V) [24].

Superconducting Magnetic Energy Storage (SMES)

In SMES [10, 12, 25], the energy is stored in form of a dc current circulating in a large inductor. The resistance of a superconductor is zero so the current can flow without reduction in its magnitude. The variable current through the superconducting coil is converted to a voltage, which can be connected to an inverter. SMESs are well-suited for fast exchange of large amount of power. However, their long-term storage capacity is limited and they are relatively expensive [24].

Flywheel

Flywheel ES [19, 26, 27] systems store energy mechanically in the form of kinetic energy by spinning a mass about an axis. The electrical energy input keeps the flywheel rotor spinning until called upon to release the stored energy through a generator [24].

Hydrogen generation

In hydrogen generation ES [11, 28-30] systems, as its name suggests, the extra wind (or sunshine) energy is used to generate hydrogen (e.g. by electrolysing water) which later can be used in *fuel cells* to generate electrical energy when there is lack of energy. The drawback of this system is their slow response to fast power transient due to the slow internal electrochemical and thermodynamic characteristic of fuel cells. This problem can be solved by using supercapacitors in order to improve the dynamic response of the system [24]. A fuel cell works like a battery but does not need recharging. It will produce electricity as long as hydrogen is supplied. A fuel cell consists of electrodes-an anode and a cathode-sandwiched around an electrolyte. Hydrogen is fed to the anode, and oxygen is fed to the cathode. Activated by a catalyst, hydrogen atoms separate into protons and

electrons, which take different paths to the cathode. The electrons go through an external circuit, creating a flow of electricity. The protons migrate through the electrolyte to the cathode, where they reunite with oxygen and the electrons to produce water. The *Regenerative (or reversible) fuel cell* produces electricity from hydrogen and oxygen, but can also be reversed and powered with electricity to produce hydrogen and oxygen.

Hydro-pumped

In Hydro-pumped storage systems the energy stored by pumping water up to a large reservoir and is released through a water turbine connected to a generator whenever required. This system is usually used in peak shaving but is well-suited for providing balance services as well. However, it usually requires suitable geological location [15].

Compressed air

Compressed air [31] energy storage system uses an intermediary mechanical-hydraulic conversion also called the liquid-piston principle. These systems are raising interest as they do not produce any waste. They also can be integrated with a cogeneration system, due to the thermal processes associated with the compression and expansion of gas. Their efficiency can be optimized by combining them with other storage system [24].

As mentioned before, this work will not concentrate on a particular ES technology and will simulate the ES by an ideal DC-voltage source interfaced through an AC/DC converter. The energy capacity and the power rating of the ES system are provided in pu. However an example of flywheel ES is considered in Appendix D in order to provide a perspective of the physical size of the required ES.

1.3 Distributed generation

The rapid growth in the electrical energy demand puts the transmission system under greater stress every year resulting in a system operation closer to its edge i.e. greater possibility for stability problems than any time in the past [32]. The basic solution to this problem is to construct more transmission lines, which is very

difficult especially with this increasingly rapid growth in demand. The other solution is to use the existing system in a more effective way. Moreover, it is well-known that the retail customers are requiring much higher power quality than ever before due to the increase of digital systems and sophisticated control [33, 34]. On the other hand, facing global environmental problems makes the increase in renewable energy penetration inevitable which in turn makes the higher power quality requirements even harder to meet [35, 36]. Therefore the three major difficulties for future Transmission and Distribution (T&D) systems can be summarized as follows:

- Providing for the rapid growth in demand and enhancing the robustness of system with minimum increase in transmission lines.
- Coping with the increase in penetration of renewable energy such as wind and photovoltaic systems.
- Improving the local reliability to ensure the power quality demanded by customers.

These difficulties necessitate the re-thinking or even re-deigning of T&D systems in order to find a more effective way to use them. Decentralisation of generation and storage systems, which is called Distributed Generation (DG), has emerged as a promising solution for the difficulties mentioned above [33, 37, 38]. DG is a variety of small power generators and storage facilities which are located as close as possible to users. The use of DG enables customers to have some degree of energy independence, increases the reliability of service, improves the efficiency of energy, and finally increases the ability of system to exploit more renewable energy. Furthermore, DG benefits the electric utility by reducing congestion on grid, decreasing the need for new generation and transmission capacity, and offering services such as local frequency and voltage control [36, 39, 40].

As the penetration of renewable energy increases, the intermittent nature of renewable energy becomes a greater problem requiring the central generation to provide the back-up energy. This increases both the stability problems (similar to

those found in intermittent load such as arc furnaces) and also grid losses [34, 36]. Distributed generation and storage can provide the required back-up energy with minimum loss and stability problem. Renewable energy generation must be supplemented with "dispatchable" resources such as storage and local generation in order to balance the generated energy with demand [33, 35].

1.3.1 Microgrids

Microgrids have received increasing attention as a means of integrating DG into the electricity network. The microgrid is an integrated energy delivery system that consists of interconnected DG units and controllable loads which may be operated autonomously and can operate in parallel with, or isolated from, the main power grid [34, 36]. Conventionally the T&D systems were not designed to accommodate generation and storage at distribution level. Therefore the main challenge is how these DG units can be integrated as a microgrid to form units that are controllable and well-behaved at grid level. If the microgrid is connected to the main grid, it will appear as a load to the main grid when the DG units cannot meet the local load. However, when the DG output exceeds the local demand, the microgrid appears as a generator to the main grid. Hence, the main challenge is when the microgrid is islanded from the main grid since the DG units must meet the local demands. Obviously, the situation deteriorates as the renewable energy penetration into the microgrid increases.

Advanced power electronics and control technologies have made it possible to integrate a range of distributed energy generation and storage with existing electrical power systems [34, 36, 41]. Figure 1.1 shows an example of microgrid consisting of a range of DG units which are integrated into a three-level hierarchy through power electronics. Using such a control structure, the microgrid can be regarded as a self-controlled entity within the power system [34, 36]. The Static Switch (SS) is used to connect the microgrid to the main grid whenever required. Microgrids are customer-friendly, as they are designed to meet their local needs for electricity and heat. They can also benefit customers through providing uninterruptible power, enhancing local reliability, reducing transmission loss and

supporting local grid voltage and frequency. In order to achieve this functionality each component of the new distribution system must react to local information such as voltage and frequency to correctly change its operation point [32, 33, 35, 42]. The other important feature is to make sure that there is no component like a master controller or a central storage unit which is critical for operation of the microgrid i.e. the microgrid can continue operation with the loss of any component.
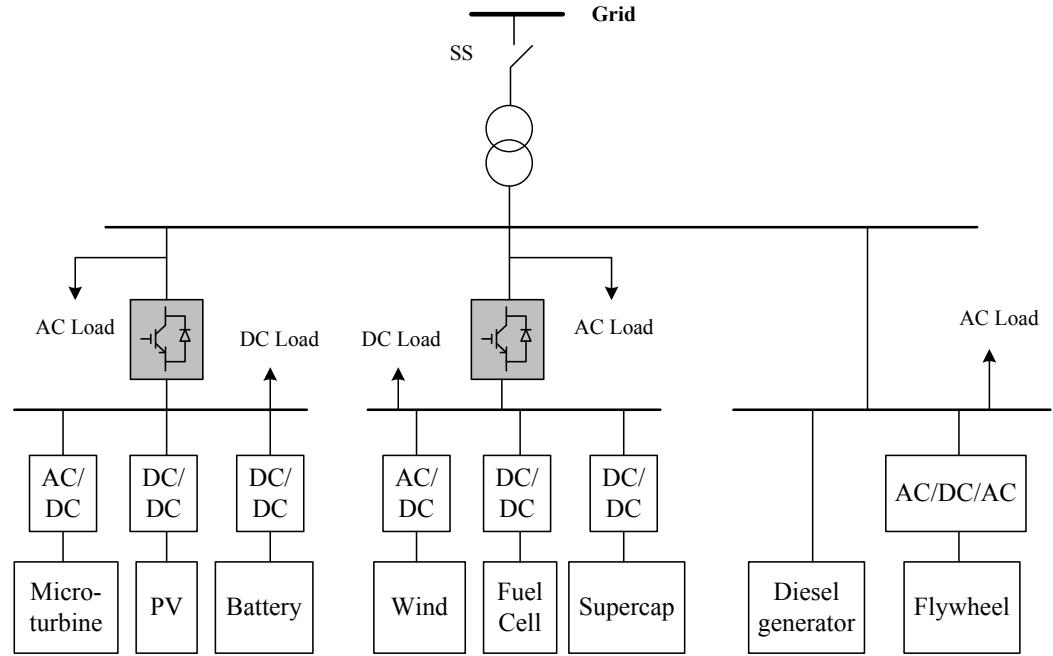
Figure 1.1. Example of hierarchical microgrid with both AC and DC links [36]

One conventional and yet robust way to achieve local control without fast-centralised communication is to control active and reactive power flow to and from each component by utilizing frequency and voltage droops [33-35]. This is pretty much similar to how current T&D systems are controlled. However the biggest obstacle is the renewable energy and the rapid increase in their penetration. Wind generators are traditionally integrated to the grid by power electronic converters that require a voltage source to provide voltage orientation for the control of the real and reactive power flow. It implies that they can neither be easily integrated within microgrids (especially in island mode) nor connected to weak grids since they cannot alone control the local grid voltage and frequency.

This becomes more crucial in cases where the wind power supplies a significant part of the load in the microgrid. This thesis is intended to address this problem.

1.4 Contribution of this thesis

This work augments an array of wind generators with frequency and voltage droop characteristics in order to share an active and reactive load. Although the proposed control structure is mainly concentrated on microgrid applications, the method is quite applicable for direct ac grid connection as well as connection via HVDC links. The active power-frequency droop will be adjusted in order to make the wind generators share the load not only according to their ratings, (which is the case for classical droop control), but also according to the available wind power. The method will be validated for both with and without auxiliary ES units. This thesis also proposes a novel ES control method in which the output power of the wind generator(s)-ES system is totally smooth and equal to the power demanded by the load. An Energy Management System (EMS) for both with and without external ES is proposed and illustrated through PSCAD simulations. This thesis will also investigate the different possible places for the ES and other components. The grid fault and zero wind power ride-through scenarios are also studied in this work.

1.4.1 Layout of the thesis

The thesis is structured as follows:

Chapter2 reviews generator drive technologies for variable speed wind turbines. The Doubly Fed Induction Generator (DFIG) will be chosen in this work. Different control methods for DFIG and wind turbine are studied. The Mathematical model of a DFIG is developed and the vector control scheme for both grid-side and rotor-side converters of the DFIG are explained. Two different control methods for DFIGs are identified: Direct Stator Flux Orientation (DSFO) and Indirect Stator Flux Orientation (ISFO). The DSFO-controlled DFIGs, which

are also called grid-connected DFIGs [43], are field orientated off the grid voltage and appear as current sources in a power system. However, the ISFO-controlled DFIGs, which are also known as standalone structure [44], operate like voltage sources in a power system and hence can be equipped with droop characteristics. Since in an ISFO-controlled DFIG the torque-component of the rotor current is determined by the load, there is lack of the direct torque control which is the main drawback of this control method. This problem will be addressed in the following chapters. The PSCAD\EMTDC wind turbine model, which is used throughout this thesis, is also briefly explained and different wind turbine control modes are discussed. Finally wind characteristics and the PSCAD wind model are explained.

Chapter 3 considers DSFO-controlled DFIGs with external ES system(s) and identifies two control strategies: Power Smoothing Control (PSC) and Power Demand Control (PDC). The application of the two strategies in a DSFO-controlled wind farm connected to both AC grid and HVDC link will be discussed. The different wind farm grid voltage and frequency control structures in each case will also be illustrated. Through PSCAD simulation it will be illustrated that in a PSC, the power into the grid is a smoothed version of the wind power, and the PSC strategy may not be appropriate for a power system with a high penetration of wind energy. It will be also shown that in the PDC structures for a DSFO-controlled DFIGs-ES system, communication between the system operator and the wind farm is necessary in order to determine the reference power and pitch angle for each wind turbine. This is in addition to the energy management communication which is usually needed to maintain the energy level of the ES within its limits. It will be discussed that the DSFO-controlled wind farms seem not to be the best choice for integrating with microgrids especially if the wind farm supplies significant part of the load.

Chapter 4 reviews the different functionalities that may be required from a wind farm including the active power-frequency and the reactive power-voltage control. The chapter also explains the existing methods for supporting the local grid

voltage and frequency and argues that an external voltage and frequency source is still required. However, an ISFO-controlled wind farm augmented with droop characteristics has the potential to fully control the local (wind farm) grid voltage and frequency. This chapter explains the different applications of a droop-controlled wind farm including AC grid connection, HVDC connection, and integration within a microgrid. This chapter will equip an array of ISFO-controlled DFIGs with the classical frequency and voltage droops and compares the active and reactive power sharing using droops with that of without droops. It will be shown through PSCAD simulation that a droop-controlled wind farm is inherently able to ride-through loss of the grid with no need for communication.

Chapter 5 considers a microgrid including a droop-controlled wind farm with no external ES. In this scenario the DFIGs control the local grid voltage and frequency and share the local load. The wind turbine moment of inertia operates as a short-term ES such that the shaft speed can be considered as an indicator for the excess or shortfall of energy. In order to keep the shaft speed within its limits, an Energy Management System (EMS) is required. The EMS consists of an Auxiliary Generator (AG) and a controllable or "Dispatchable Load" (DL). These are explained with their integrated operation with turbine pitch control. This chapter also adjusts the gains of the frequency-active power droops in order to make the DFIGs share the load according to the available wind power. This is called variable droop method. Although the proposed control scheme works with the standard droop, it will be shown that the variable droop can significantly reduce the energy needed from AGs.

Chapter 6 considers a wind generator-ES system delivering a constant power demanded by the load while no AG is available. Not having an AG is obviously impractical due to the limited capacity of ES systems. However, such a scenario is included here since it is a case study for a DFIG under a non-Maximum Power Tracking (MPT) control which is more appropriate for this scenario. The chapter consists of two main parts. The first part proposes and designs a generator

electrical torque control scheme through regulating the ES power. The same control structure will be used in the following chapters to control the torque of the generator. The second part of this chapter attempts to derive a mathematical expression for the size of the required ES for a given wind profile. The mathematical results are quite close to the simulation ones in case of a sinusoidal base wind speed profile. Although this not the case for a real wind speed profile, a similar approach might be adopted in future research to obtain satisfactory results in case of real wind speed as well. The second part covers work which was discontinued, but it is included here for completeness and it may also have archival value.

Chapter 7 considers a microgrid consisting of variable droop-controlled DFIGs, ES, AG and DL while the local grid voltage and frequency are fully controlled by the DFIGs. Two methods for controlling the ES system will be investigated. The first method exploits the turbine inertia as an ES mechanism. This method is similar to the Chapter 5 while the ES appears as a buffer between the turbine inertia and the AG and DL. In the second approach the ES power is regulated in order to control the electrical torque of the DFIG. The advantages and the disadvantages of the two approaches are discussed. A pitch angle control scheme will also be proposed which is applicable for both ES control methods. An EMS will also be explained which uses the AG and DL in order to keep the energy level of the ES within its limits. Although variable droop method is used in this chapter, the proposed control schemes are also applicable with the standard droop at the expense of more energy demanded from the AG.

Chapter 8 considers the same microgrid as Chapter 7 (i.e. an array of variable droop-controlled DFIGs, ES, AG and DL) and studies the different system configurations and fault ride-through scenarios. It will be shown that the droop-controlled wind farm is inherently able to ride-through a fault on the local grid with no need for communication. This chapter also explains the ride-through scenario in case of zero wind speed situation. In Chapter 7 the ES units are

distributed amongst individual DFIGs while the DL is aggregated on the local grid. This chapter will illustrate that it is also possible to aggregate the ES on to the local grid and/or to distribute the DL amongst the individual DFIGs.

It should be emphasized that the proposed control schemes in this thesis are quite applicable for small microgrid as well as large wind farms. Throughout this thesis, all the results will be given in pu in order to make it easier to follow. However, this PhD was initially focused upon large offshore wind farms connected to HVDC links. Therefore, the parameters are given in pu based on 1000MVA. In cases with two DFIGs, the rating of the DFIG1 is 0.66pu and that of the DFIG2 is 0.34pu. In such cases, the power and the energy level of the distributed elements (ES and/or DL) will be given based on the ratings of their associated DFIG which is denoted as pu_{gen} throughout this thesis. The DFIGs parameters, which are given in Appendix B, are originally from the previous works carried out in Nottingham University [4, 48]. It is emphasized that since all results in this thesis will be displayed in pu (or pu_{gen}), the rating of the DFIGs are not important.

Two real wind speed profiles will be used throughout this thesis. The two wind speed profiles are sampled at each second, however, the methods of their measurements are unknown.

2. Control of Doubly-Fed Induction Generator and Wind Turbine

In this chapter, generator drive technologies for variable speed wind turbines are reviewed and then different control methods for Doubly Fed Induction Generator (DFIG) and wind turbine are studied. Mathematical models of a grid-connected DFIG and a standalone DFIG are introduced. PSCAD\EMTDC wind turbine model, which is used throughout this thesis, is briefly explained and different wind turbine control modes are discussed. Finally wind characteristics and PSCAD wind model are shortly explained.

2.1 Generator drive technologies for variable speed wind turbines

There are generally two types of wind turbines: fixed-speed and variable speed. In fixed-speed wind turbine a squirrel cage induction generator (SGIG) is used to convert the mechanical energy into electrical energy. In this case almost always capacitor banks are needed to compensate the reactive power drawn by the SCIG. Due to the almost constant shaft speed (less than 1% variation), the wind power fluctuations are converted into mechanical and therefore electrical power fluctuations. This causes voltage variations especially in case of a weak grid, which is known as flicker [45, 46]. Integration of power electronics with wind turbines enabled shaft speed control [43, 44] which offers advantages such as:

- More wind energy capture by optimum shaft speed operation of wind turbine.
- Less drive train stress and less power fluctuations to grid since some wind fluctuations are stored in shaft inertia rather than directly conducted to drive train [4, 47].

- Reduction in noise at low rotational speed and improved fault ride-through ability [48].

The rotational speed of a wind turbine is very low and must be adjusted to the electrical frequency. This can be done by using either a gear box or a generator with high number of poles. There are mainly three types of variable speed wind turbine. The first one, which is known as Doubly-Fed Induction Generator (DFIG), uses a wound rotor induction generator with a partial scale power electronic converter (rated at approximately 30% of nominal generator power) connected to the rotor circuit while the stator circuit is connected to grid. In this type, which is shown in Figure 2.1.a, the speed range typically comprises synchronous speed - 40% to +30% depends on the size of the converter [45]. Similar to the fixed-speed type, it needs a gearbox (GB). Its main drawbacks are the needs of protection to meet ride-through regulations and higher maintenance due to slip rings.

New technologies enable decoupling between generator and grid using full scale converter system. This allows a wider range of generator control, the possibility of elimination of gearbox in certain cases, and better control of energy flow to the grid [15]. Figure 2.1.b shows a SCIG connected to the grid through a full scale power electronic converter. Unlike DFIG it does not need protection to meet ride-through regulation but this is achieved at the price of much bigger converter. However it still needs a gearbox. The third type of variable speed wind turbines, shown in Figure 2.1.c, is called "direct-drive wind turbine" as it does not need a gearbox. In this type a low speed multipole synchronous generator with the same rotational speed as the wind turbine is used to convert mechanical energy to electrical energy. The generator can have either a wound rotor or a rotor with permanent magnets [45]. The stator circuit is connected to the grid though a full scale converter. This type is the most expensive one since it needs a full scale converter connected to a multipole generator.
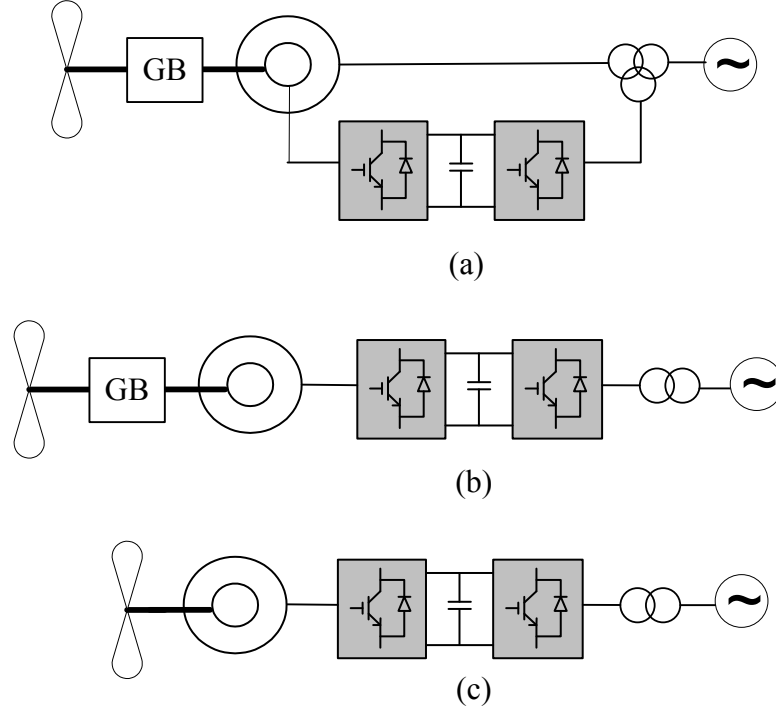
Figure 2.1 Different types of variable speed wind turbines (a) DFIG with wound rotor induction generator and gearbox (b) squirrel cage induction generator with gearbox and full scale converter (c) direct drive wind turbine with multipole synchronous generator and no gearbox

Despite the fact that DFIGs need a gearbox, they are still the most popular option in the market since they are much cheaper and yet offering great advantages such as decoupled control of active and reactive power and reasonable shaft speed variations. Therefore DFIGs are used throughout this thesis.

2.2 Control of Doubly-Fed Induction Generator

The DFIG is a wound rotor induction generator with its rotor connected to the grid through power electronic converters which in this study are two back-to-back voltage-fed PWM converters. As shown in Figure 2.1 the stator circuit is directly connected to grid (for sake of simplicity the gearbox will not be shown from now on). The ability to supply/subtract power to/from the rotor makes it possible to operate the DFIG at sub-or super-synchronous speed.
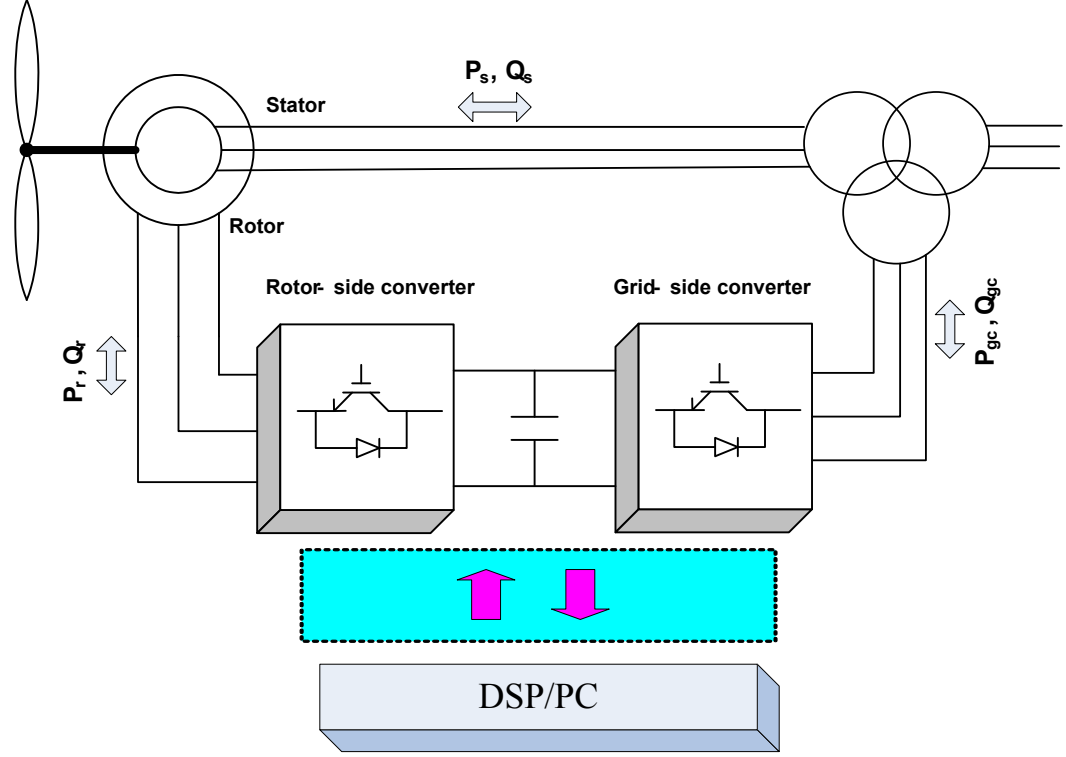
Figure 2.2. DFIG with power flow

The use of DFIG as a generator is considered in many papers and theses [43, 44, 48-51]. The DFIG is suitable for both grid connected and also standalone (or isolated load) structures. The grid connected DFIG is field orientated off the grid voltage i.e. the stator flux is determined by the grid voltage. This structure which is also known as Direct Stator Flux Orientation (DSFO) has received more attention [43, 48, 49]. In the standalone structure [44], the stator voltage is not determined by grid voltage but is set through regulating the rotor excitation current. The standalone structure uses a field orientated control known as Indirect Stator Flux Orientation (ISFO). The designs of both DSFO and ISFO have been explained in detail in literatures [43, 44, 48-50]. However the next subsections briefly review their control design.

2.2.1 Mathematical derivation of DFIG model in two-phase rotating frame

Each phase of the three-phase stator windings sets up a magnetic field rotating sinusoidally (in time domain) around the circumference of air gap. The stator field

can be visualized as a set of north and south poles rotating around the circumference of stator. The same magnetic distribution can be obtained from an equivalent two-phase system called $\alpha\beta$. The 3-phase abc and the 2-phase $\alpha\beta$ systems are transformable to one another by [43]:

$$\mathbf{F}_{\alpha\beta 0} = \begin{bmatrix} F_\alpha \\ F_\beta \\ F_0 \end{bmatrix} = \mathbf{T}_1 \cdot \mathbf{F}_{abc}$$

where $\mathbf{F}_{\alpha\beta 0}$ stands for variables in $\alpha\beta$ frame, $\mathbf{F}_{abc}$ stands for variables in abc frame while $\mathbf{F}_0 = 0$ and:

$$\mathbf{T}_1 = \frac{2}{3} \cdot \begin{bmatrix} 1 & -\frac{1}{2} & -\frac{1}{2} \\ 0 & \frac{\sqrt{3}}{2} & -\frac{\sqrt{3}}{2} \\ \frac{1}{2} & \frac{1}{2} & \frac{1}{2} \end{bmatrix}$$

Considering the equivalent 2-phase stator windings, which are fixed in space on the stator, the voltage across each winding is written down using Kirchhoff's law:

$$\underline{v}_s = \underline{i}_s R_s + \frac{d}{dt}\underline{\varphi}_s \tag{2.1}$$

Considering the equivalent 2-phase rotor windings, which are rotating at rotor speed, the voltage across each winding can be written as:

$$\underline{v}_r = \underline{i}_r R_r + \frac{d}{dt}\underline{\varphi}_r \tag{2.2}$$

where the direction of flux vector $\underline{\varphi}_s$ and $\underline{\varphi}_r$ is the direction of peak flux linkage in space.

Equations (2.1) and (2.2) are usually transformed to the stationary $\alpha\beta$ frame, which is fixed to the stator. They can also be transformed to a rotating dq frame which is fixed to the rotating magnetic field produced by the stator. In this case the dq

frame rotates at the electrical angular velocity ω_e. The advantage of the rotating dq frame is that the time varying parameters of the 3-phase system become constant when referred to the rotating dq frame. This advantage is independent of the choice of reference frame [52]. Some assumptions are needed to be made in order to develop the dq frame:

- The stator and rotor windings are symmetric and sinusoidally distributed.
- The air gap reluctance is constant.
- Saturation of magnetizing and mutual inductances are neglected.

Transformation from (2.1) and (2.2) into dq rotating frame can be done by substituting the variables in (2.1) by $x_s = e^{-j\omega_e t} x_{s\alpha\beta}$ and variables in (2.2) by $x_r = e^{-j\omega_s t} x_{r\alpha\beta}$ [43, 49] (Where x stand for $\underline{i}$, $\underline{v}$ and $\underline{\varphi}$). The electrical angular velocity of the rotating frame is ω_e and is aligned on the stator flux; ω_r is the rotor frequency and ωs is called slip frequency $\omega_s = \omega_e - \omega_r$. The equations in rotating dq frame are:

$$\underline{v}_s = \underline{i}_s R_s + \frac{d}{dt}\underline{\varphi}_s + j\omega_e \underline{\varphi}_s \tag{2.3}$$

$$\underline{v}_r = \underline{i}_r R_r + \frac{d}{dt}\underline{\varphi}_r + j\omega_s \underline{\varphi}_r \tag{2.4}$$

where

$$\underline{\varphi}_s = L_s \underline{i}_s + L_o \underline{i}_r \tag{2.5}$$

$$\underline{\varphi}_r = L_o \underline{i}_s + L_r \underline{i}_r \tag{2.6}$$

where

$$L_s = l_s + L_0 \tag{2.7}$$

$$L_r = l_r + L_0 \tag{2.8}$$

where L_s, L_r, and L_0 are stator, rotor and mutual inductances, l_s, l_r are stator and rotor leakage inductances.

Combining (2.5) and (2.6) with (2.3) and (2.4) and then separating into real and imaginary parts:

$$v_{sd} = i_{sd}R_s + \frac{d}{dt}\varphi_{sd} - \omega_e\varphi_{sq} \tag{2.9}$$

$$v_{sq} = i_{sq}R_s + \frac{d}{dt}\varphi_{sq} + \omega_e\varphi_{sd} \tag{2.10}$$

$$v_{rd} = i_{rd}R_r + \frac{d}{dt}\varphi_{rq} - \omega_s\varphi_{rq} \tag{2.11}$$

$$v_{rq} = i_{rq}R_r + \frac{d}{dt}\varphi_{rq} + \omega_s\varphi_{rd} \tag{2.12}$$

Selecting i_{rd}, i_{rq}, i_{sd} and i_{sq} as state variables, the DFIG model can be described as:

$$
\begin{aligned}
\sigma\frac{di_{sd}}{dt} &= -\frac{R_s}{L_s}i_{sd} + \omega_r i_{sq} + \frac{R_r L_o}{L_s L_r}i_{rd} + \frac{\omega_r L_o}{L_s}i_{rq} + \frac{v_{sd}}{L_s} - \frac{L_o}{L_s L_r}v_{rd} \\[2mm]
\sigma\frac{di_{sq}}{dt} &= -\frac{R_s}{L_s}i_{sq} - \omega_r i_{sd} + \frac{R_r L_o}{L_s L_r}i_{rq} - \frac{\omega_r L_o}{L_s}i_{rd} + \frac{v_{sq}}{L_s} - \frac{L_o}{L_s L_r}v_{rq} \\[2mm]
\sigma\frac{di_{rd}}{dt} &= \frac{R_s L_o}{L_s L_r}i_{sd} - \frac{\omega_r L_o}{L_r}i_{sq} - \frac{R_r}{L_r}i_{rd} - \frac{\omega_r L_o^2}{L_s L_r}i_{rq} - \frac{L_o v_{sd}}{L_s L_r} + \frac{v_{rd}}{L_r} \\[2mm]
\sigma\frac{di_{rd}}{dt} &= \frac{R_s L_o}{L_s L_r}i_{sq} + \frac{\omega_r L_o}{L_r}i_{sd} - \frac{R_r}{L_r}i_{rq} + \frac{\omega_r L_o^2}{L_s L_r}i_{rd} - \frac{L_o v_{sq}}{L_s L_r} + \frac{v_{rq}}{L_r}
\end{aligned}
\tag{2.13}
$$

where $\sigma = \dfrac{L_s L_r - L_o^2}{L_s L_r}$.

Assuming that the magnitude of the $\alpha\beta$ vector is equal to the rms phase quantity (i.e. $|x| = x_{rms}$ where x stands for $\underline{i}$, $\underline{v}$ and $\underline{\varphi}$), the electrical torque would be [44, 49]:

$$T_e = 3\frac{p}{2}\frac{L_o}{L_s}\underline{\varphi}_s \times \underline{i}_r \tag{2.14}$$

where p is the number of machine pole pair.

2.2.2 Control of DFIG using Direct Stator Flux Orientation

This section explains the vector control scheme for a grid-connected DFIG which is also known as Direct Stator Flux Orientation. In this method the stator flux is determined by grid voltage.

2.2.2.1 Vector control scheme of rotor-side PWM voltage source converter for grid-connected DFIG

The objective of the control of the rotor-side converter is to obtain a decoupled control between the stator active and reactive power. This can be achieved by choosing a synchronously rotating dq frame with the d-axis oriented along the stator flux vector position. Once the orientation is correctly done, an independent control of torque and flux is achieved i.e. the torque is controlled by torque producing current i_{rq}. The stator flux is determined by stator voltage as the stator windings are directly connected to the main voltage source [43, 49, 50]. However from (2.5) the magnetising current for $\underline{\varphi}_s$ can be supplied by either $\underline{i}_s$ or $\underline{i}_r$ i.e. form stator supply or from the rotor converter. The stator flux angle θ_s can be calculated by measuring stator current and voltage:

$$\varphi_{s\alpha} = \int \left(v_{s\alpha} - R_s i_{s\alpha}\right) dt$$
$$\varphi_{s\beta} = \int \left(v_{s\beta} - R_s i_{s\beta}\right) dt \tag{2.15}$$
$$\theta_s = \tan^{-1}\left(\frac{\varphi_{s\beta}}{\varphi_{s\alpha}}\right)$$

A Phase Lock Loop (PLL) is used to derive the position of the stator voltage. Neglecting stator resistor, the stator flux vector lags the stator voltage vector by almost 90° due to the integration effect in (2.15).

Aligning the d-axis of the reference frame along the stator flux vector position gives $\varphi_{sq} = 0$ and $\varphi_{sd} = \varphi_s = L_0 i_{ms}$, where i_{ms} is machine magnetizing current. Equations (2.5) and (2.6) can also be described in dq frame:

$$\varphi_{sd} = L_s i_{sd} + L_o i_{rd} = L_o i_{ms} \Rightarrow i_{sd} = \frac{L_o i_{ms} - L_o i_{rd}}{L_s}$$

$$\varphi_{sq} = L_s i_{sq} + L_o i_{rq} = 0 \Rightarrow i_{sq} = \frac{-L_o}{L_s} i_{rq} \tag{2.16}$$

$$\varphi_{rd} = L_o i_{sd} + L_r i_{rd} = \frac{L_o^2 i_{ms} - L_o^2 i_{rd}}{L_s} + L_r i_{rd} = \frac{L_o^2}{L_s} i_{ms} + \frac{L_s L_r - L_o^2}{L_s} i_{rd}$$

$$\varphi_{rq} = L_o i_{sq} + L_r i_{rq} = \frac{L_s L_r - L_o^2}{L_s} i_{rq} \tag{2.17}$$

Since stator windings are directly connected to main grid, the stator flux can be considered constant, thus $\frac{d}{dt}\varphi_s = 0$. Assuming negligible stator resistance:

$$v_{sd} = i_{sd} R_s + \frac{d}{dt}\varphi_{sd} - \omega_e \varphi_{sq} \approx 0 \tag{2.18}$$

$$v_{sq} = i_{sq} R_s + \frac{d}{dt}\varphi_{sq} + \omega_e \varphi_{sd} \approx \omega_e \varphi_{sd} \tag{2.19}$$

And rotor equations:

$$v_{rd} = i_{rd} R_r + \frac{d}{dt}\varphi_{rd} - \omega_s \varphi_{rq} = i_{rd} R_r + \sigma L_r \frac{di_{rd}}{dt} - \omega_s \sigma L_r i_{rq} \tag{2.20}$$

$$v_{rq} = i_{rq} R_r + \frac{d}{dt}\varphi_{rq} + \omega_s \varphi_{rd} = i_{rq} R_r + \sigma L_r \frac{di_{rq}}{dt} + \omega_s \left(L_{mm} i_{ms} + \sigma L_r i_{rd} \right) \tag{2.21}$$

where $\sigma = \frac{L_s L_r - L_o^2}{L_s L_r}$ and $L_{mm} = \frac{L_o^2}{L_s}$. From (2.20) and (2.21) one can define:

$$v'_{rd} = v_{rd} + \omega_s \sigma L_r i_{rq} \tag{2.22}$$

$$v'_{rq} = v_{rq} - \omega_s \left(L_{mm} i_{ms} + \sigma L_r i_{rd} \right) \tag{2.23}$$

Therefore the transfer functions between v'_r and rotor currents become:

$$\frac{i_{rd}(s)}{v'_{rd}(s)} = \frac{i_{rq}(s)}{v'_{rq}(s)} = \frac{1}{\sigma L_r s + R_r}$$ which means the rotor current can be regulated by v_r

using a current controller where $\omega_s \sigma L_r i_{rq}$ and $\omega_s \left(L_{mm} i_{ms} + \sigma L_r i_{rd} \right)$ are compensation terms for v_{rd} and v_{rq} respectively.

Figure 2.3 illustrates the vector control scheme of rotor-side converter for a grid connected DFIG.
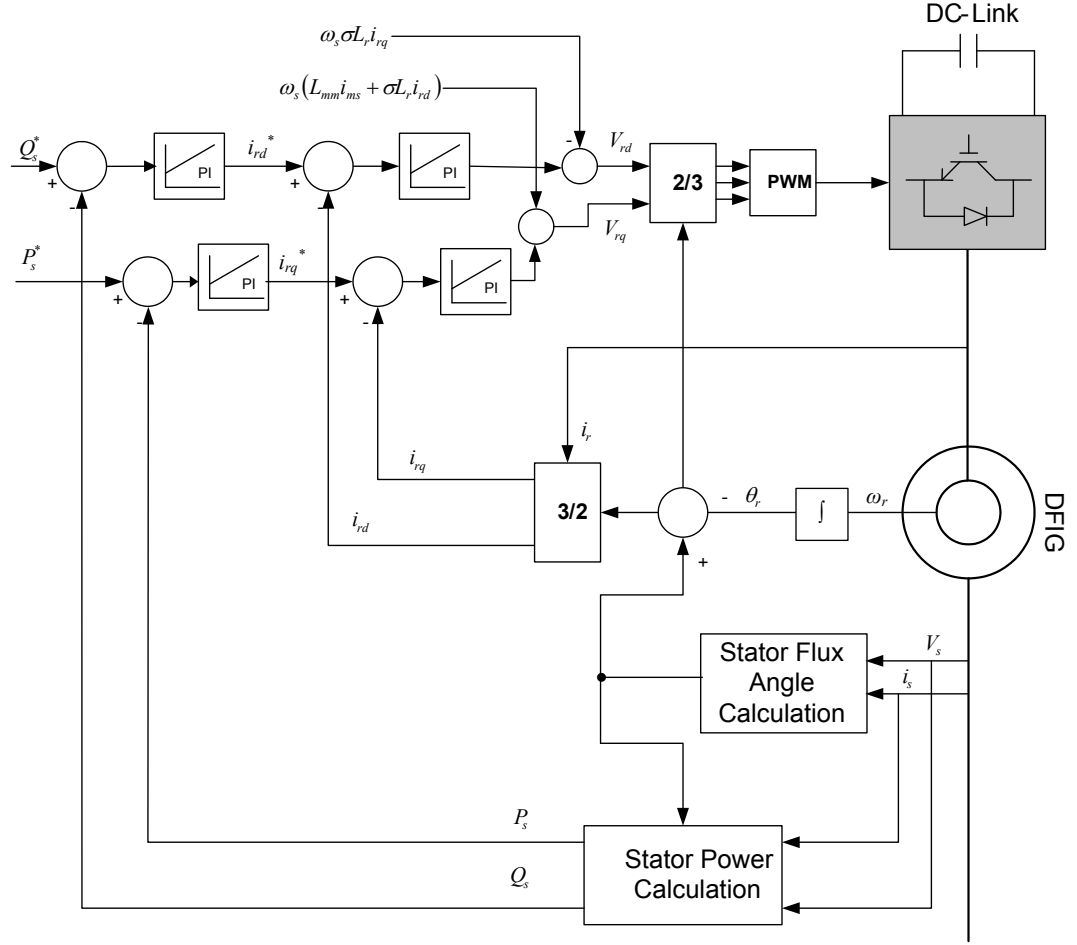
Figure 2.3. Rotor-side PWM voltage source converter for grid-connected DFIG

As can be seen from Figure 2.3, the stator active and reactive powers are controlled by regulating i_{rd} and i_{rq} respectively. Figure 2.4 shows the schematic diagram for the cascaded power and current control loops of the rotor-side converter where $\tau_r = \dfrac{\sigma L_r}{R_r}$ ($\sigma = \dfrac{L_s L_r - L_o^2}{L_s L_r}$) and $k' = -\dfrac{3L_0}{2L_s} v_s$.
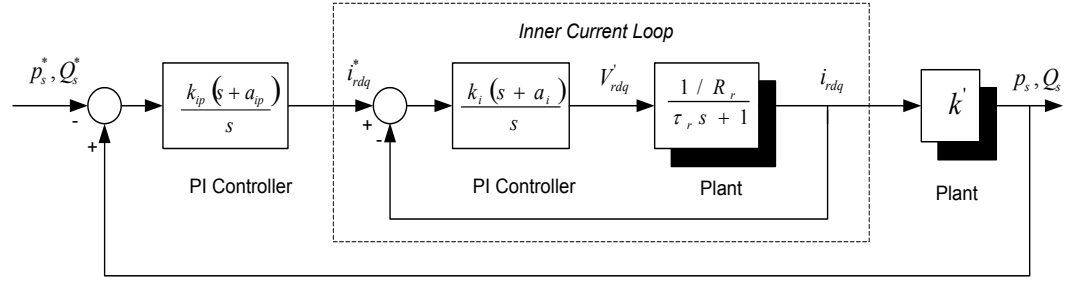
Figure 2.4. Cascaded power and current controllers for rotor-side converter

The derivation of control plants and design of PI controllers for the power and current loops are explained in the literature [43, 48, 49] using different methods. In Appendix A, Pole-placement and Characteristic Equation methods are used to design the PI controller for a 1000MVA DFIG (with parameters given in Appendix B) using Mathcad software. Appendix A can be used to get the PI controller's proportional and integral gains for a DFIG of any rating by changing the appropriate parameters. In this thesis Appendix A has been used to design the controllers for DFIGs with 1000MVA, 660MVA and 340MVA ratings. These are used throughout the thesis.

2.2.2.2 Vector control scheme of grid-side PWM voltage source converter for grid-connected DFIG

The objective of the grid-side converter is to keep the DC-link voltage constant regardless of magnitude and direction of rotor power. The reference frame used for the vector control is oriented along the stator (grid) voltage vector position. This enables the independent control of the active and reactive power flowing between grid and the grid side converter. The PWM converter is current regulated with the d-axis current used to regulate the DC-link voltage and the q-axis current used to control the reactive power [43, 49].
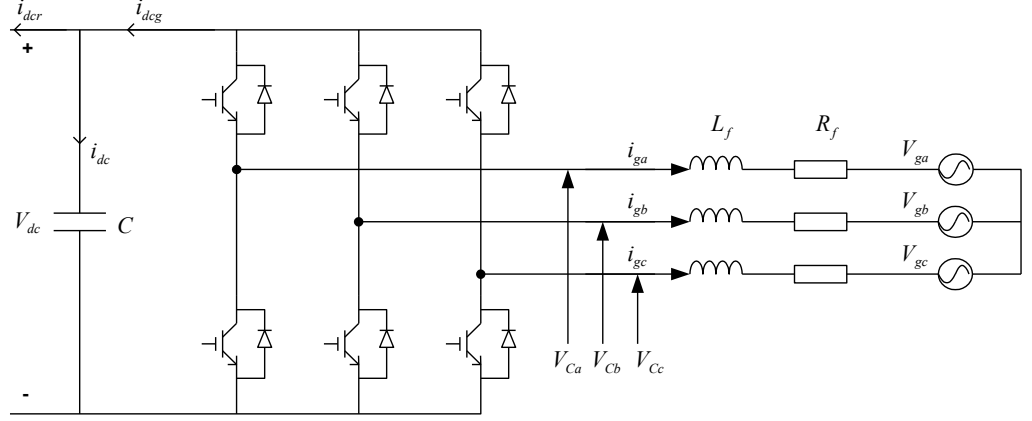
Figure 2.5. Schematic diagram of grid-side converter and line inductances and resistances

Figure 2.5 shows the schematic diagram of the grid-side PWM converter where L_f, R_f, V_g and V_c are the connecting transformer inductance, resistance, grid voltage and converter voltage respectively. The three-phase equation relating the converter voltage and grid voltage in given in (2.24) uses Kirchhoff's law:

$$V_{Cabc} - V_{gabc} = R_f i_{gabc} + L_f \frac{di_{gabc}}{dt} \tag{2.24}$$

The 3-phase equation (2.24) can be transferred into a rotating dq frame with a frequency of ω_e using the same technique explained above:

$$V_{Cd} - V_{gd} = R_f i_{gd} + L_f \frac{di_{gd}}{dt} - \omega_e L_f i_{gq} \tag{2.25}$$

$$V_{Cq} - V_{gq} = R_f i_{gq} + L_f \frac{di_{gq}}{dt} + \omega_e L_f i_{gd} \tag{2.26}$$

With the d-axis of the rotating frame orientated on the grid voltage vector, $V_{gq} = 0$ and $V_{gd} = V_g$. Using the same scaling factor explained in 2.2.1, the active and reactive power flow is:

$$P_g = \frac{3}{2}\left(V_{gd} i_{gd} + V_{gq} i_{gq}\right) = \frac{3}{2} V_{gd} i_{gd} \tag{2.27}$$

$$Q_g = \frac{3}{2}\left(V_{gq} i_{gd} - V_{gd} i_{gq}\right) = -\frac{3}{2} V_{gd} i_{gq} \tag{2.28}$$

The angular position of the grid voltage can be calculated as[43, 49]:

$$\theta_v = \int \omega_e dt = \tan^{-1} \frac{V_{g\beta}}{V_{g\alpha}} \tag{2.29}$$

Active and reactive power flow between grid-side converter and grid are controlled by regulating i_{gd} and i_{gq} respectively. It can be defined:

$$V_{gd}^{'} = V_{Cd} - V_{gd} + \omega_e L_f i_{gq} \tag{2.30}$$

$$V_{gq}^{'} = V_{Cq} - V_{gq} - \omega_e L_f i_{gd} = V_{Cq} - \omega_e L_f i_{gd} \tag{2.31}$$

Therefore the transfer function between currents and voltages is

$$\frac{i_{gd}(s)}{V_{gd}^{'}(s)} = \frac{i_{gq}(s)}{V_{gq}^{'}(s)} = \frac{1}{L_f s + R_f}$$
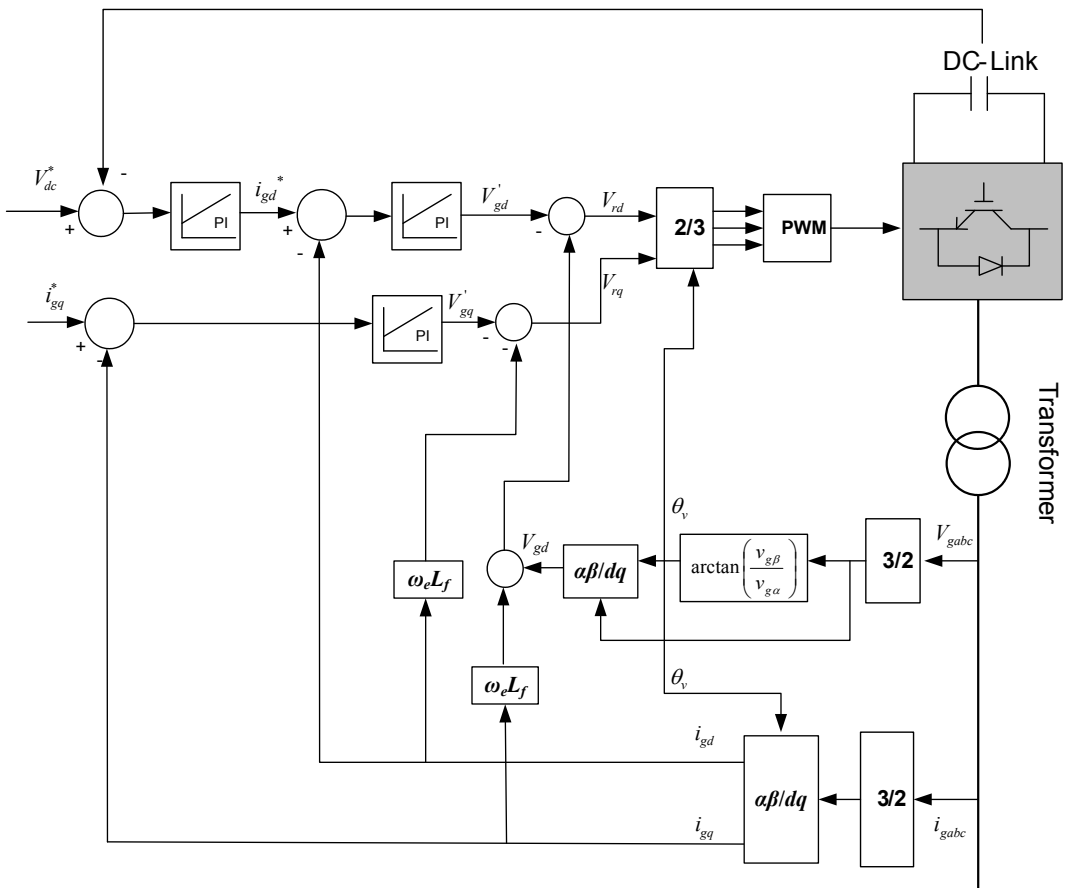
Figure 2.6. Grid-side PWM converter for grid-connected DFIG

Figure 2.6 illustrates the schematic diagram of the grid-side vector control PWM converter. The DC-link voltage is controlled by regulating d-axis current i_{gd} while the q-axis current demand i_{gq}^{*} determines the reactive power flow between the grid

and the grid-side converter. In order to ensure unity power factor, $i_{gq}{}^*$ is kept zero. Therefore the reactive power demand is supplied by DFIG magnetization. This situation is used throughout the thesis.

Figure 2.7 shows the cascade control of the grid-side converter. Where $K_{DC} = \dfrac{3m}{4C}$, m and C are PWM modulation depth of the grid-side converter and DFIG DC-link capacitance respectively.
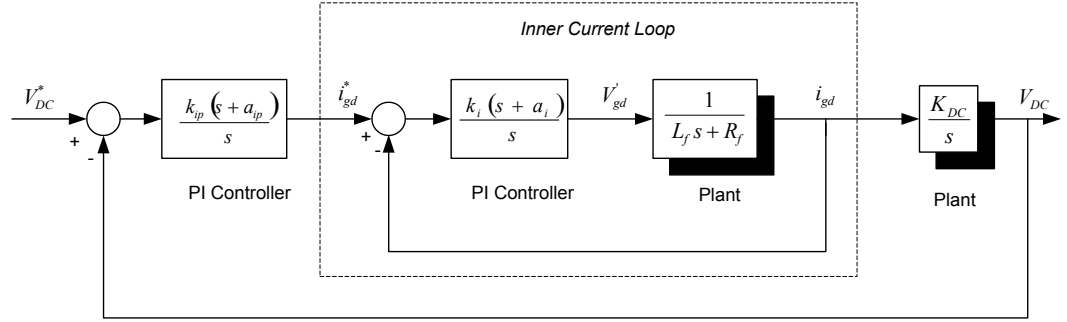
Figure 2.7. Schematic diagram of the control scheme of the grid-side converter

The derivation of control plants and design of PI controllers for the voltage and current loops are explained in the literature [43, 48, 49] using different methods. In Appendix A Pole-placement and Characteristic Equation methods are used to design the PI controller for a 1000MVA DFIG (with parameters given in Appendix B) using Mathcad software. Appendix A can be used to obtain the proportional and integral gains for the DFIG's PI controllers of any ratings by changing the appropriate parameters.

2.2.3 Control of DFIG using Indirect Stator Flux Orientation

Unlike DSFO, the stator flux is no longer determined by grid voltage and is controlled by rotor excitation current [44]. The next two subsections explain the control of the rotor- and stator-side converters.

2.2.3.1 Vector control scheme of rotor-side PWM voltage source converter

Figure 2.8 shows the control of rotor-side converter for ISFO.
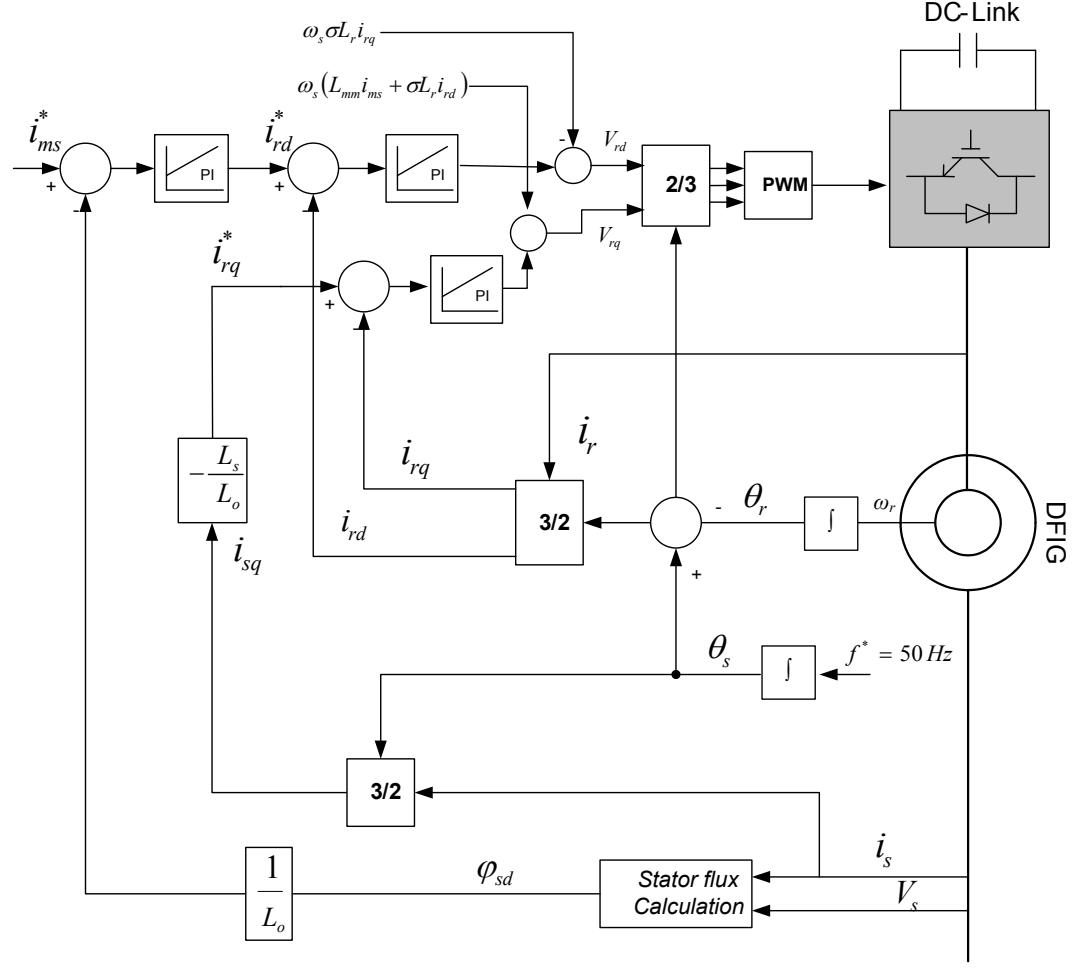
Figure 2.8. Control of rotor-side PWM converter for ISFO

As Figure 2.8 illustrates, the stator flux angle θ_s is not derived from the voltage measurement (since there is initially no voltage source) but is set through free running integration of the reference stator voltage frequency (50Hz). The stator voltage is controlled by the magnetizing current i_{ms} through regulating the rotor d-axis current i_{rd}. The magnetizing current reference value is set as $i_{ms}^* = \dfrac{V_{s-nom}}{L_0 \omega_{e-nom}}$

where V_{s-nom} is nominal stator voltage (1kV) and ω_{e-nom} is the nominal angular frequency (314.16rad/s). Aligning the d-axis of the reference frame along the stator flux vector position gives

$$\varphi_{sq} = L_s i_{sq} + L_o i_{rq} = 0 \Rightarrow i_{rq}^* = \frac{-L_s}{L_0} i_{sq} \tag{2.32}$$

$$\varphi_{sd} = \varphi_s = L_o i_{ms} \tag{2.33}$$

Equation (2.32) is the orientation condition [44] i.e. (2.32) is used to force the orientation of the reference frame along the stator flux vector position. Equation (2.32) also means that i_{rq} can not be used to control the electrical torque since it is determined by i_{sq} and this is why the ISFO is suitable for isolated load (standalone) structure. The main advantage of this structure is that the DFIG can be used to control the local grid voltage and frequency.

The design of magnetizing current PI controller is given in [44] which is also used in Appendix A.

2.2.3.2 Vector control scheme of grid-side PWM voltage source converter

The control of the grid-side converter is exactly the same as that of the grid-connected one (Figure 2.6). In a grid connected application, the grid voltage may be assumed to be free of harmonics and the θ_v is derived though voltage measurements. In the standalone case there is no low impedance voltage source and stator voltage harmonics will arise from the stator converter. Fortunately, θ_v can be derived from: $\theta_v = \theta_s + \pi/2$ [44] where θ_s is stator flux angle which is set from the integration of the frequency reference.

The ISFO has received less attention to date, and is the main focus of this thesis.

2.3 Wind turbine generator control

Figure 2.9 shows the wind turbine connected to a DFIG through a mechanical drive train. The wind turbine rotor blades convert some of the available wind power to mechanical power acting on shaft inertia. Neglecting mechanical friction and losses, the shaft speed is $\omega_r = \int \frac{T_m - T_e}{J}$ where T_m, T_e and J are the mechanical torque, electrical torque and shaft inertia.
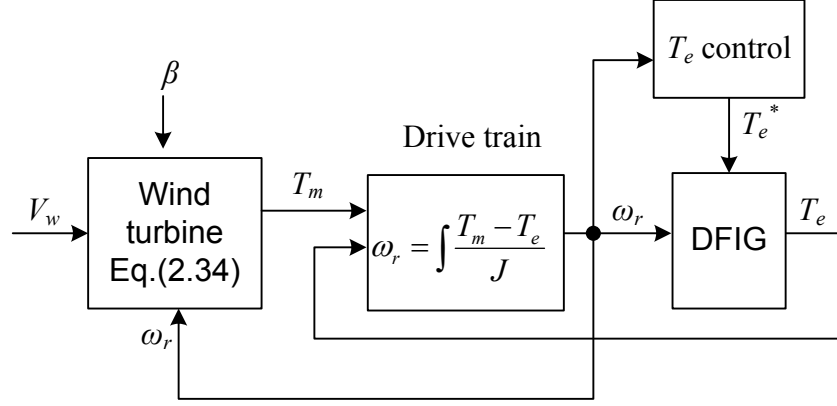
Figure 2.9. Schematic diagram of wind turbine connected to DFIG through mechanical drive train

In a DSFO-controlled DFIG, the reference electrical torque T_e^* is controlled by I_{rq} through the rotor-side converter. In an ISFO-controlled DFIG, however, an external mechanism, which will be investigated in later chapters, is needed to set the reference torque.

 In the next subsection the PSCAD wind turbine model, which is used throughout this thesis, is explained and then different wind turbine control methods are discussed.

2.3.1 Wind turbine model

The mechanical power extracted from wind speed P_t is a function of wind speed V_w, shaft speed ω_r and pitch angle β. This function is called power coefficient C_p.

$$T_m = \frac{P_t}{\omega_r}$$
$$P_t = 0.5\rho A V_w{}^3 C_p$$
(2.34)

There are a number of different equations for the power coefficient. The PSCAD one, which is used throughout this thesis, is described by [53]:

$$C_p = 0.5\left(\lambda - 0.022\beta^2 - 5.6\right)e^{-0.17\lambda}$$
$$\lambda = \frac{2.237\,N V_w}{\omega_r}$$
(2.35)

where

ρ = air density, A = rotor blade area

λ = tip speed ratio, N = gear ratio

Equation (2.34) explains that the aerodynamic power captured by wind turbine is a function of wind speed cubed, blade area and power coefficient. C_p is a function of pitch angle. The bigger the pitch angles the smaller the power coefficient and turbine power. Practically C_p is less than 0.4 which happens when β=0.

In order to extract the maximum energy from the wind, not only should the pitch angle be kept at zero, but also the generator power should be a cubic function of shaft speed. The latter is achieved by controlling the electrical torque as $T_e = K_{opt}\omega_r^2$. This method is called Maximum Power Tracking (MPT). There are however other methods that can be used to control electrical torque. Two methods have received attention in papers [54]: Constant Power Mode (CPM) and Constant Torque Mode (CTM). Other methods may also be defined as $T_e=f(\omega_r)$. The main difference of these methods is the degree to that they exploit the shaft inertia as an energy store. In principle, the more energy stored in inertia, the smoother the output power is for a given wind speed profile. As a result, a smaller external ES is needed to smooth the output power to a specific level. The three main methods are explained in following sections.

2.3.2   Control of wind turbine generator under Maximum Power Tracking

For a given wind speed, there is only one shaft speed at which the captured wind power is maximum which is called optimum shaft speed ω_{opt} [54]. Figure 2.10.a shows the MPT characteristic for different wind speeds. The control is done by controlling the electrical torque as $T_e^* = K_{opt}\omega_r^2$ (where K_{opt} is given for a wind turbine) which is shown in Figure 2.10.b. In this way the shaft speed is driven to the optimum shaft speed and thus the captured power is maximum for each wind

speed. In MPT a pitch angle control is required in order to keep generator power at 1pu whenever the wind speed is more than the rated (rated wind speed is the wind speed at which the turbine power is 1pu). In other words, when turbine power becomes more than 1pu, the pitch angle increases to reduce the energy captured and maintain power at 1pu. This pitch angle controlled is called "standard pitch control" in this thesis.

The MPT is the standard control method for wind turbines. The main advantage of the MPT method, in comparison with other torque control methods, is that it is always stable for any shaft speed [21, 54]. It also minimizes the energy required from any external generator source by maximizing the wind energy captured. On the other hand, the maximum energy captured means that a larger external Energy Storage (ES) is required to smooth the output power to a desired level.

Figure 2.10. Maximum Power Tracking is shown in (a) turbine power-shaft speed characteristic (b) mechanical torque-shaft speed characteristic

2.3.3 Control of wind turbine generator under Constant Power Mode

Figure 2.11 shows the CPM characteristic defined by $T_e^* = P^*/\omega_r$ where P^* is the demand power. In CPM, as its name suggests, the output power is constant and equal to a demand power which means that theoretically no external ES is needed. Therefore all wind power fluctuations are stored in the shaft inertia which in turn

causes the widest shaft speed variations, thus maximizing inertial ES usage. The main disadvantage of CPM is its unstable region shown in Figure 2.11. The P^*/ω_r curve is more likely to cross the T_m-ω_r curves for a given wind profile due to the wide shaft speed variation [21, 54, 55]. Figure 2.12 compares demand power with extractable wind power i.e. turbine power with $\beta=0$. When the demand power is less than the extractable power (Figure 2.12.a), CPM is possible. This case is studied in Chapter 5 where a pitch control is designed to keep the shaft speed in the stable region.
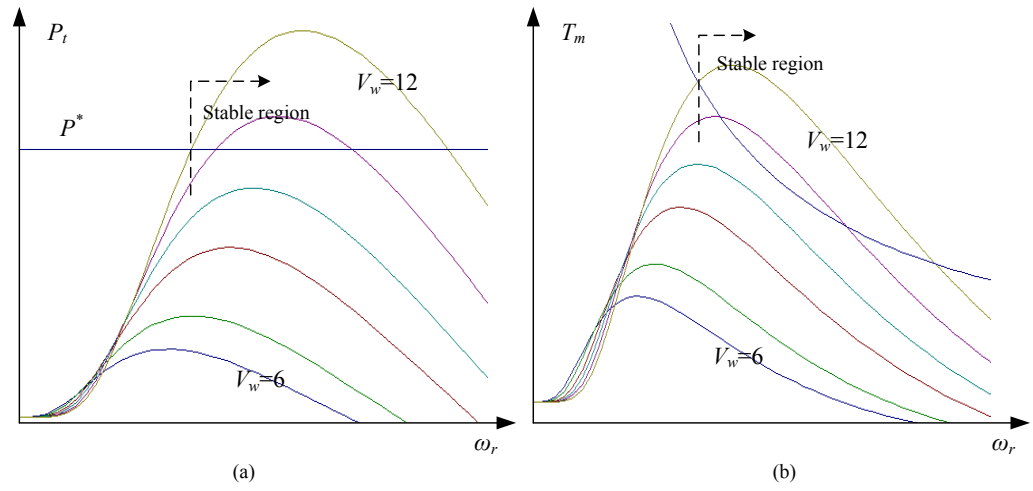
Figure 2.11. Constant Power Mode is shown in (a) turbine power-shaft speed characteristic (b) mechanical torque-shaft speed characteristic

However, when the demand power approaches the average of the extractable wind power $\hat{P}_{ave}$ (Figure 2.12.b); ES and/or an external energy source is required to compensate for the shortage of energy whenever the demand power is more than the extractable wind power. This implies that CPM is not possible in such situations.
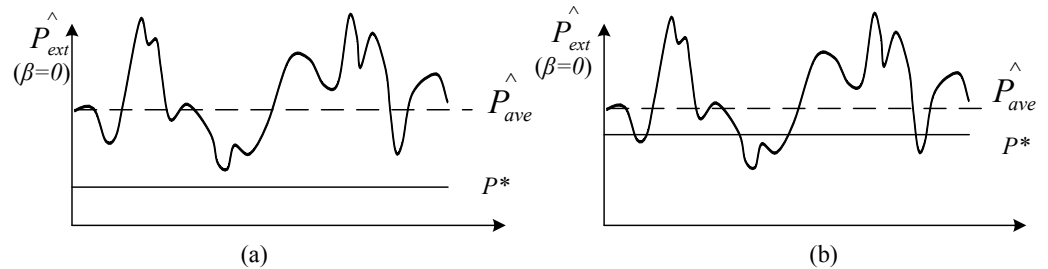
Figure 2.12. Different situations of demand power in respect to extractable wind power $\hat{P}_{ext}$

As mentioned before, an ISFO-controlled DFIG requires an external mechanism to set the reference electrical torque. Therefore, a DFIG controlled under ISFO control, which is supplying a constant power load, is inherently in CPM unless its electrical torque is controlled externally.

2.3.4 Control of wind turbine generator under Constant Torque Mode

For the Constant Torque Mode (CTM), as its name indicates, the electrical torque is constant $T_e = T_e^*$; the generator power is hence a linear function of shaft speed $P_g = T_e^* \omega_r$ (Figure 2.13). Under CTM the shaft speed variation for a given wind profile is less than that for the CPM but more than that for the MPT, so it represents a compromise in the degree to which it exploits the turbine inertia as an energy store. Instability is still possible but at much lower shaft speed which means much larger wind perturbation is required (compared to CPM) for the instability region to be approached [54, 56]. In CTM the choice of T_e^* is very important by which the instability problem can be addressed.
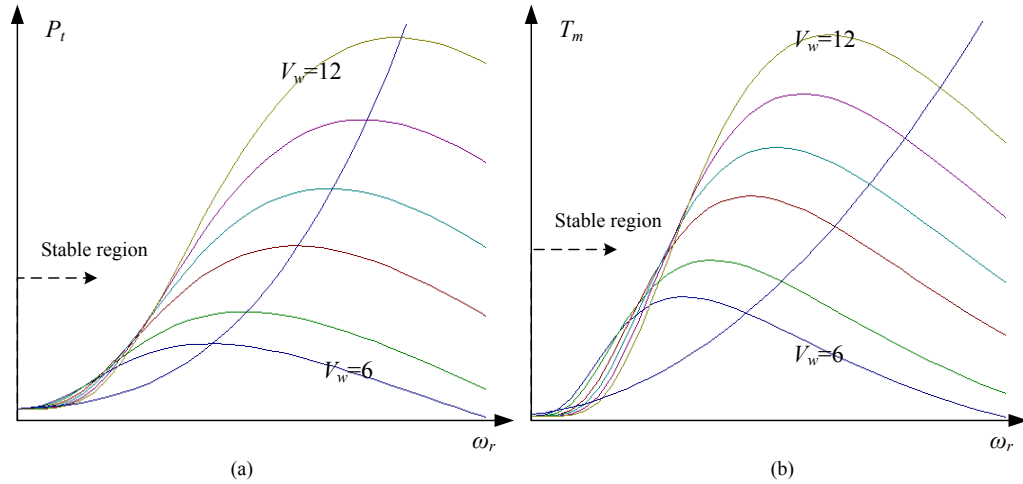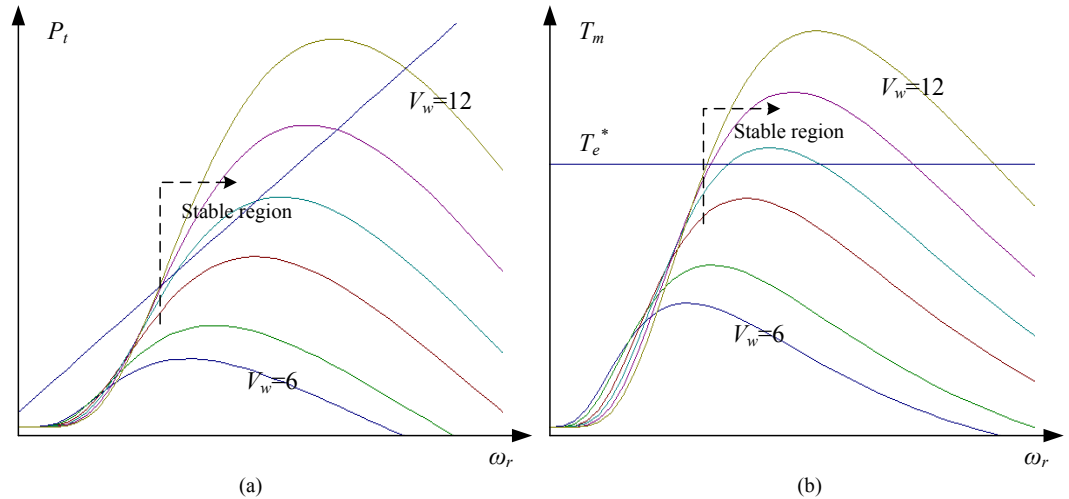

Figure 2.13. Constant Torque Mode is shown in (a) turbine power-shaft speed characteristic (b) mechanical torque-shaft speed characteristic

The control of a wind turbine-ES system under CTM in order to deliver a constant power demanded by load is the subject of Chapter 6.

2.4 Representation of wind profile in PSCAD

A wind model is required that can properly simulate the spatial effect of wind behaviour including gusting, rapid (ramp) changes, and background noise (turbulence) [45]. The PSCAD wind model is a four-component model and defined by [53]:

$$V_w = V_{wb} + V_{wg} + V_{wr} + V_{wn}$$

where V_{wb}, V_{wg}, V_{wr} and V_{wn} are base (average) wind speed, gust wind, ramp wind and noise wind components respectively. The noise component which is used to simulate the turbulence in wind is explained below.

The fluctuation in the wind speed can be represented as a mean value and a continuous spectrum or *spectral density function*. In term of power the spectral content is called *Power Spectral Density* (PSD) [45]. A number of PSD functions are used as models in wind energy engineering. The PSD used in PSCAD wind model is [53]:

$$S(\omega_i) = \frac{2KF^2\omega_i}{\pi^2 \left[1 + \left(\frac{F\omega_i}{\mu\pi}\right)^2\right]^{4/3}}$$

(2.36)

ω_i is the frequency of ith component and is defined as: $\omega_i=(i-0.5)\Delta W$.

ΔW is noise amplitude controlling parameter (0.5-2rad/s)

K is surface drag coefficient (0.0192)

F is turbulence scale (600m)

μ is mean wind speed at reference height (m/s)

The PSD is a function of frequency and the problem is to translate the PSD into a time sequence of values with the given spectral density. To solve the problem PSCAD uses a method as follows. The PSD is used to derive information about the amplitude of a signal component with a given frequency (which is defined by

ΔW and i). Then, a large number (N) of sines waves with a random initial phase angle (Φ_i) and amplitude calculated from PSD are added for each time step. Equation (2.37) describes the noise component based on the explained method [53]:

$$V_{wn} = 2\sum_{i=1}^{N}\left[S(\omega_i)\Delta W\right]^{0.5}\cos\left(\omega_i t + \phi_i\right)$$

(2.37)

In this thesis all proposed control methods are validated using real (measured) wind profile. However in some cases, for sake of explanation, constant wind speed or simulated wind speed using the model above is used.

3. Control of wind turbines-ES system with external voltage and frequency source

As discussed in Chapter 2, there are generally two methods of controlling the DFIG: Direct Stator Flux Orientation (DSFO) and Indirect Stator Flux Orientation (ISFO). The DSFO-controlled DFIG needs to be connected to an external voltage and frequency source. In other words, a DFIG controlled under DSFO is acting as a power source. This chapter deals with DSFO-controlled DFIG. In this case, the wind farm can be either directly connected to the main grid or via AC-DC-AC converters. Both scenarios are discussed in this chapter. Prior to this, two strategies regarding Energy Storage (ES) control in wind farm are explained in the next subsection.

3.1 Strategies of controlling ES

Generally two ES control strategies can be defined [56]: *Power Smoothing Control* (PSC) and *Power Demand Control* (PDC). In a PSC strategy, as its name suggests, ES is utilized to smooth a *harvested* wind power. It means that the power delivered to the grid (load) is a smoothed version of the wind power. For example in [20, 21, 55] the wind turbine shaft inertia has been exploited as an energy store to absorb wind power fluctuations. Obviously having an external ES can enhance power smoothing. This has been addressed in many papers such as [5, 16, 25-27]. Traditionally power network operators are obliged to buy all the wind energy produced by wind farms and other power generators have to balance the generation with demand by increasing or decreasing their generation. Under PSC, the best scenario is when the unwanted wind power frequencies are filtered out by ES in order to provide a smoother power to the grid to protect the network from unwanted frequencies. However, the average power delivered to the grid is still determined by the wind and this is why PSC may not be the optimum delivery for a power network with a high penetration of wind power, especially if the ability of

other generators to balance the demand is limited. As wind energy penetration increases, the capacity of other generators to balance generation and demand is reduced and this is why PDC may be viable option. Under PDC, the combination of ES and the wind turbines delivers a constant power determined by the load rather than wind. In other words, under PDC, ES is used to absorb power variations between wind power and a reference power P^* determined by the system operator. Obviously if the wind is the only source of generation, the demand power can never be more than the average of the extractable wind power $\hat{P}_{ave}$. In practice, however, a PDC will always require an auxiliary generation source. The aim of the PDC control regime is to maximise the renewable generation and minimize the auxiliary power. The PDC strategy, which has received almost no attention to date, is the main focus of this thesis.

Both PSC and PDC strategies can be applied on both DSFO- and IFSO-controlled DFIGs. However as a general rule, DSFO is more appropriate for PSC while ISFO seems to be more suitable for PDC. This will be discussed throughout the thesis. This chapter considers the DSFO-controlled DFIG using both PSC and PDC strategies. The objective of this chapter is to briefly study the PSC and PDC in a DSFO-controlled wind farm which is either directly connected to the AC grid or via a HVDC link. The simulation of all of the possible scenarios is out of the scope of this thesis. However a PSC strategy for an aggregated DSFO-controlled wind farm connected to a LCC-HVDC link will be simulated, as an example. The ISFO-controlled DFIGs are studied in the following chapters.

3.2 DSFO-controlled DFIGs-ES system with direct AC grid interface

The DSFO is the standard DFIG control in which the generator is field orientated off an external voltage and frequency source. Therefore i_{rq} and i_{rd} are used to control the stator active and reactive power respectively. This section studies ES control strategies in a wind farm based on DSFO-controlled DFIGs which are

directly connected to AC grid. This case does not seem appropriate for a weak grid. If the wind farm is integrated within a microgrid which is islanded from the main grid, it is necessary to control the *local grid*'s voltage and frequency using, for example, a STATCOM. In the next two subsections, it is assumed that the voltage and frequency control is provided by the main grid.

3.2.1 Power Smoothing Control for wind turbine-ES connected directly to the AC grid

The PSC strategy, which is shown in Figure 3.1, has been addressed in many papers [5, 16, 25-27]. In this structure DFIGs are conventionally controlled in the Maximum Power Tracking (MPT) mode. The ES can be either aggregated on to the collector bus of the wind farm or distributed and integrated with each DFIG. The total output power of the wind farm is likely to be smoother than the power generated by each wind turbine due to the possible phase displacement of individual turbine powers. Therefore in the aggregated ES, the required energy capacity of the ES in order to smooth the wind power to a certain level; tends to be smaller than that of the total distributed ES. Hence, the aggregated ES seems to be the appropriate choice in this case. However in large offshore wind farms, accommodating such a large aggregated ES can be quite an engineering challenge. In such cases, distributing ES, for example, in the space available in the turbines' tower rather than aggregating on a huge central platform; might be practically and economically beneficial.

A number of available ES technologies were explained in Chapter 1. This research concentrates on the short to medium-term ES such as: flywheel, SMES and Supercapacitors. The ES, in this thesis, is simulated by a DC voltage source which is interfaced to the AC system via an AC/DC converter. The converter is called the ESI or ES Interface. The ES power can be controlled by regulating the d- (real) component of the ESI current I_{d-es} (see Figure 3.1). The current control is the standard current control which is identical to the DFIG's current loops explained in Chapter 2.
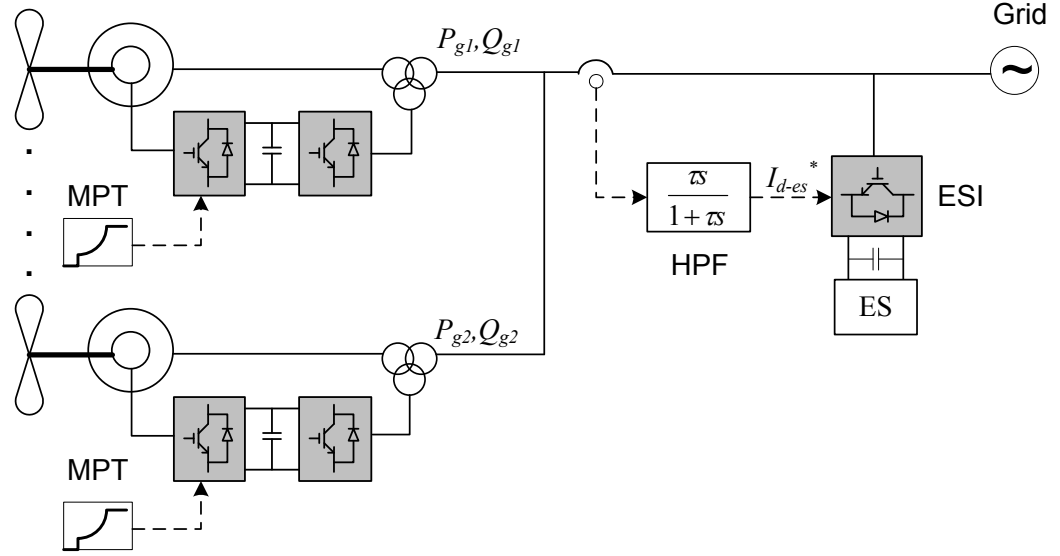
Figure 3.1. PSC in a DSFO-based wind farm with direct AC grid interface

Studies have shown that power system is more sensitive to medium frequency wind power fluctuations (0.01-1Hz) [16] since the power density of wind speed reduces as the wind frequency increases. Therefore the ES is controlled to filter out these frequencies in order to shield the power system. This can be done by subjecting the generated wind power to a High Pass Filter (HPF), the output of which sets the reference ES d-axis current $I_{d-es}{}^*$. The time constant of the HPF is used to achieve different cut-off frequencies.

3.2.2 Power Demand Control for wind turbine-ES connected directly to AC grid

In a PDC strategy, generally, the demand power P^* must be imposed on the wind farm. The easiest way to impose the demand power, in a wind farm directly connected to the AC grid, is the ES (see Figure 3.2). The ES is controlled in order to balance the power generated by the wind turbine(s) with the demand. In a DSFO-controlled wind farm, communication is required to make the wind farm generation as close as possible to P^* in order to minimize the ES.

Figure 3.2 illustrates a PDC strategy in a DSFO-controlled wind farm which is directly connected to the AC grid. In this case a Supervisory Wind Farm Control (SWFC) unit [57-59] is used to determine the reference demand power and/or

pitch angle for each wind turbine based on the total demand power P^* and wind speed associated with each wind turbine. The aim here is to minimize the ES. The total demand power is set by the system operator. It is noted that if $P_1^* + P_2^* = P^*$, no ES is needed which implies that that wind turbines are controlled under Constant Power Mode (CPM). As discussed in section 2.5.3, CPM is not possible when the demand power approaches the average of the extractable wind power. Whenever P_1^* and P_2^* are not determined by MPT, stability issues must be taken into account. The ES power is controlled using the ESI-real current in order to absorb/inject the difference between the wind farm power and P^*. If the ES is distributed within the wind turbines, the output of each individual DFIG-ES is smooth.
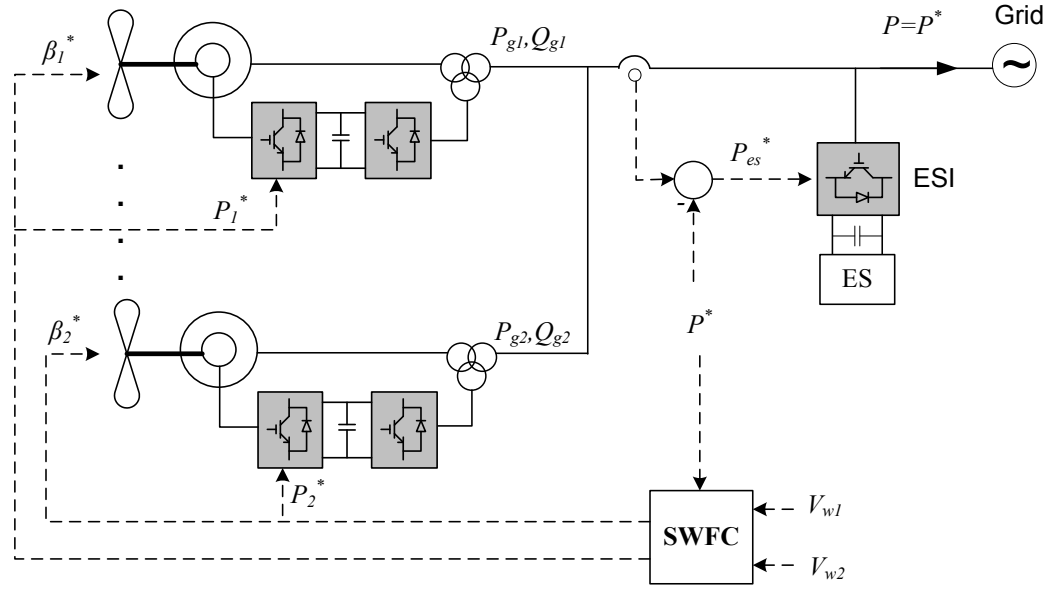
Figure 3.2. PDC in a DSFO-based wind farm with direct AC grid interface

In [60] a pitch angle control, with reference power derived from the average wind speed, is used to smooth the output power of wind turbine. A similar pitch control can be used here with the reference power given by total demand power considering the associated wind speed in order to reduce the size of ES.

3.3 DSFO-controlled DFIGs-ES system with AC/DC/AC interface

This section studies both PSC and PDC strategies for a DSFO-controlled DFIGs connected to the main grid through a High Voltage DC (HVDC)-link. Two existing HVDC technologies will be investigated. The HVDC connections are usually used to transfer large powers over large distances. They can also be used for connecting two power networks with different frequencies. One of the main applications for HVDC connections is currently for large offshore wind farms. The HVDC-link divides the power system into two parts: main grid and wind farm grid. The challenge here is to control the voltage and frequency of wind farm grid. Considering a microgrid application, the wind farm grid is connected to the *local grid* through the HVDC-link. If the local grid is islanded from the main grid, the control of the wind farm grid's voltage and frequency can be even more demanding; especially with a high wind energy penetration. The control of the wind farm grid will be studied in this section for the two HVDC technologies. The HVDC-link can also be used to impose the demand power in a PDC strategy, which is discussed in this section.

3.3.1 Introduction of HVDC technologies

This section studies the two available HVDC technologies and compares them with one another. In order to explain the HVDC technologies, an application to large offshore wind farm is considered. However, the technologies are applicable to other applications as well.

Transferring large powers (e.g. 1000MVA) produced by large wind farms, over large distance (e.g. 100km), creates an engineering challenge for system operators. Wind farms may be connected to the main grid by either High Voltage AC (HVAC) or HVDC. HVAC is an economic connection for medium range wind farms (up to a few hundreds MVA) with transmission distances less than 50-75km [61]. For distances more than 50-75km, dynamic reactive power compensation will be required in order to meet the connection agreement requirements [62]. In

such cases HVDC transmission offers advantages such as: fully defined and controlled power flow, lower cable losses than AC connection, and independent control of sending- and receiving-end frequencies [4, 61-63]. In addition the present capacity of a three-core AC submarine cable is limited to 200MVA [63] which means that for larger power multiple cable are required. Therefore the HVDC connection has technical, economical and environmental advantages for large wind farms with long distance to the main grid, which is usually the case for offshore wind farms.

Currently there are two options for HVDC connection: Voltage Source Converter (VSC) and Line Commutated Converter (LCC). LCC utilizes thyristors while VSC uses either Gate-Turn-Off thyristors (GTOs) or Insulated Gate Bipolar Transistors (IGBTs). The main difference between the LCC and VSC solutions is that the VSC is self-commutated and, unlike LCC, does not need an active voltage source for commutation. This enables a VSC converter to generate an AC three-phase voltage [62, 64], thus controlling the voltage and frequency of the wind farm grid. Therefore, independent control of active and reactive power and connection to weak grid are also possible. The VSC solution requires smaller converter platform as the required AC filters are smaller that the LCC one. The VSC connection used to be criticised for its limited rating and high switching losses compared to LCC. However both Siemens and ABB have developed a VSC connection with rating up to 1200MVA and $\pm$320kV using new switching topologies which can significantly reduce the converter losses [65]. Considering the recent improvement in VSC-HVDC topologies and their control, VSC can be an economical solution for HVDC transmission. However their reliability is yet to be fully proved in practice especially for high power rating, compared to the LCC which has been in operation for more than 30 years.

The following sections study a DSFO-controlled DFIGs-ES system connected to HVDC-link. Different topologies for both PSC and PDC strategies for both VSC and LCC solutions are briefly discussed.

3.3.2 DSFO-controlled DFIGs-ES system connected to VSC-HVDC

In a VSC-HVDC connection, conventionally the sending end converter (the one connected to wind farm) is responsible for collecting energy from the wind farm while the receiving end converter (the one connected to the grid) is responsible for maintaining the HVDC DC-link voltage constant. Constant DC-link voltage indicates the balance of active power exchanged between the two sides. The control of the receiving end converter is similar to the DFIG's grid side converter i.e. a rotating *dq* frame can be used with the d-axis fixed to the grid voltage. Therefore, the d-axis current is used to control the DC-link voltage (active power) while the q-axis current controls the reactive power and can be used to support the grid voltage. The prime objective of the sending end converter control is to collect the power produced by wind farm. The sending end converter is controlled to provide a voltage source with constant voltage magnitude and frequency. Doing so, as is the case for wind farms directly connected to AC grid, the power produced by the wind farm is absorbed by the sending end converter and transferred to the grid through the receiving end converter.

Different control methods for the sending end converter are explained in papers [62, 64, 66, 67]. In all of them the sending end converter controls the voltage and frequency of the wind farm grid.

In the following subsections the integration of the ES under both PSC and PDC with a VSC-HVDC link is studied.

3.3.2.1 Power Smoothing Control for wind turbine-ES connected to a VSC-HVDC link

Figure 3.3 illustrates a possible PSC topology for a DSFO-controlled DFIGs-ES system connected to the grid through a VSC-HVDC link. The DFIG control is identical to the one explained in section 3.2. The sending end converter controls

the voltage and frequency of the wind farm grid. The Wind power fluctuations are reflected on the DC-link voltage V_{DC}. In this scheme both receiving end converter and ES are responsible for controlling the DC-link voltage. As Figure 3.3 shows, the V_{DC} error is subject to a HPF, the output of which is used to regulate the ES current $I_{d\text{-}es}$ (which is proportional to ES power assuming a constant voltage). Therefore the high frequency fluctuations are absorbed by the ES and the low frequency fluctuations are transferred to the grid by regulating the d-axis current of the receiving end converter $I_{d\text{-}con}$. In this structure the ESI would be a DC/DC converter. However placing the ES in the HVDC DC-link may not be practical due to the high voltages involved. This may also increase the cost of insulations.
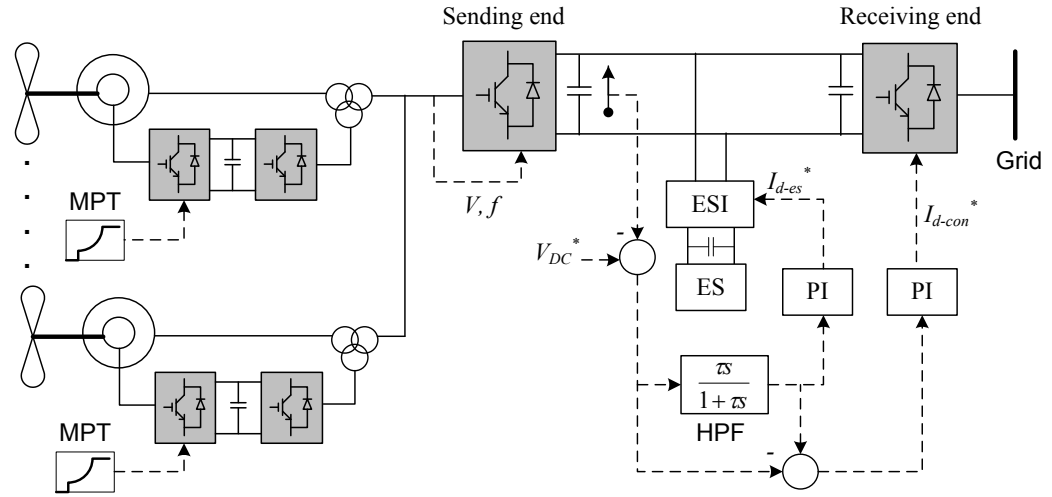
Figure 3.3. PSC in a DSFO-based wind farm connected to VSC-HVDC link

An alternative structure is to place the ES between the wind farm and the VSC-HVDC and control it in the same way as that of Figure 3.1. In this structure the power into the VSC is already smoothed by ES and the VSC is controlled conventionally. In this case the ESI is an AD/DC converter.

3.3.2.2 Power Demand Control for wind turbine-ES connected to VSC-HVDC link

A number of different structures are possible to impose the demand power in a DSFO-controlled wind farm connected to a VSC-HVDC system: One way is to place the ES between the wind farm and the VSC-HVDC link. The ES is

controlled identical to the one shown in Figure 3.2 i.e. the ESI is used to impose the demand power P^*. The wind farm grid voltage and frequency is controlled by the VSC sending end converter. Therefore, the power to the VSC is constant and equal to P^*. Again in this structure the ESI is an AC/DC converter.
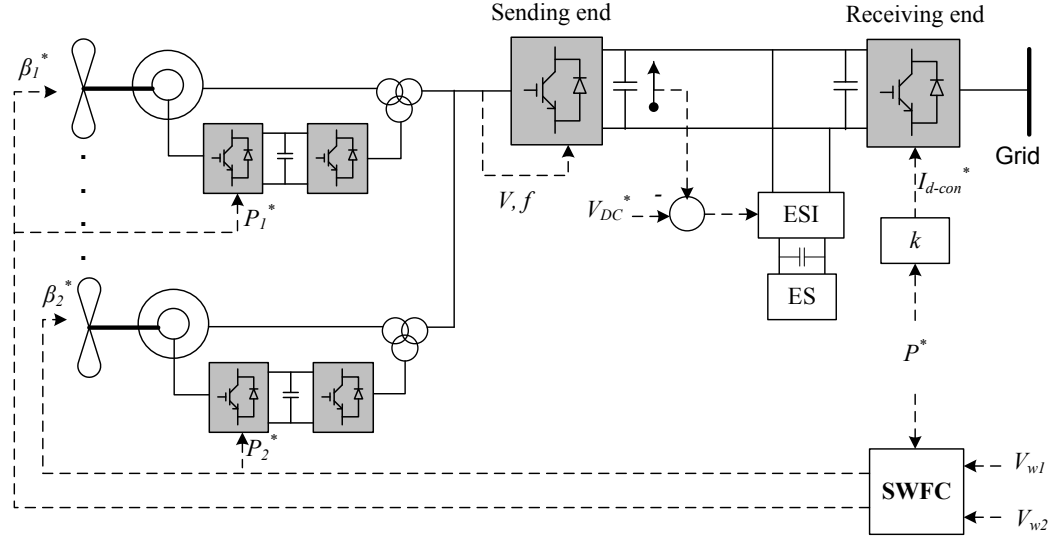
Figure 3.4. PDC in a DSFO-based wind farm connected to VSC-HVDC link

A second possible structure is shown in Figure 3.4 in which the ES is placed in the VSC DC-link and the demand power is imposed by the d-axis current of the receiving end converter I_{d-con} (where $k=1/V_{DC}$). ES controls the DC-link voltage. The ESI would be again DC/DC converter; however, this structure may not be the best one due to the high voltage of the HVDC DC-link.

A third structure is shown in Figure 3.5 in which the demand power is imposed by the d-axis current of the receiving end converter while the d-axis current of the sending end converter is used to control the HVDC DC-link voltage. The wind farm grid voltage and frequency is controlled by the ESI. Therefore the power into the VSC is constant and equal to the demand power P^*. In this structure the ESI also operates as STATCOM [12, 68]. The ESI is an AC/DC converter, controlling grid voltage and frequency by ESI. However, this structure may not make the best use of VSC-HVDC from power electronic point of view.

Figure 3.5. Alternative PDC structure for DFO-based wind farm connected to VSC-HVDC link

3.3.3 DSFO-controlled DFIGs-ES system connected to LCC-HVDC link

Unlike VSC, the LCC uses thyristors and is not self-commutated. The LCC requires an external voltage source to force commutation. The external voltage source can be either a synchronous compensator [63] or STATCOM [4, 69]. The STATCOM has faster control and lower losses than a synchronous compensator [69, 70]. The LCC converters absorb large amount of reactive power that is mainly provided by the AC filters. Therefore the LCC converters need much bigger filters than the VSC type.

The STATCOM is used to control the wind farm grid voltage and frequency, balance the active and reactive power and provide the commutation voltage needed by the LCC-HVDC link. The active power flow through the HVDC is controlled by the rectifier firing angle α [4]. The inverter is responsible for keeping the DC-link voltage constant and under normal conditions has almost no effect on the rectifier control regime [4, 48]. The control design of the STATCOM connected to the LCC-HVDC link is explained in Appendix C.

In the following subsections the integration of the ES under both PSC and PDC with a LCC-HVDC link is studied.

3.3.3.1 Power Smoothing Control for wind turbines-ES connected to LCC-HVDC link

Figure 3.6 illustrates the PSC strategy in a DSFO-based wind farm connected to "ESI-STATCOM" [12, 68] and a LCC-HVDC link. The ESI, which also operates as a STATCOM, controls the wind farm grid voltage and frequency using the control scheme explained in Appendix C and [4]. Constant voltage and frequency implies that any unbalance in power is reflected on the DC-link voltage of the ESI-STATCOM. In [4] the STATCOM DC-link voltage variations is used to regulated the rectifier firing angle α, hence transferring the power generated by wind farm through the HVDC link. Here, the ESI-STATCOM DC-link voltage is kept constant by the ES. The power generated by wind farm is measured and filtered by a Low Pass Filter (LPF). The output of the LPF is used to set the reference current of HVDC link I_0^* where $k=1/E_0$. Therefore the smoothed version of the wind farm power is transferred to the main grid through the HVDC link while the high power frequencies are absorbed by ES.

Figure 3.6. PSC for DSFO-controlled DFIGs connected to ESI-STATCOM and LCC HVDC link
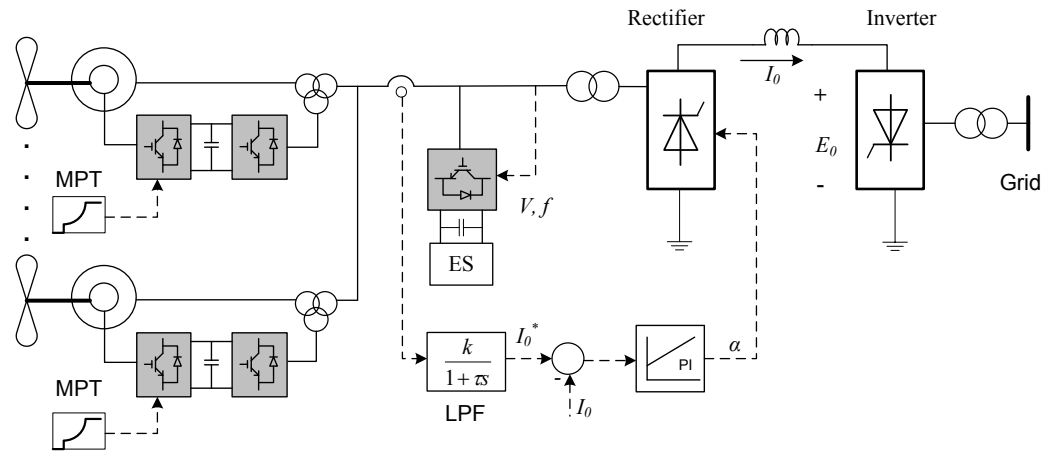
Power grids are more sensitive to the medium frequencies of wind power fluctuations (0.01-1Hz) [16]. Therefore the ES is usually designed to absorb these

frequencies. This can be achieved by adjusting the time constant τ of the LPF. The HVDC current loop control design is out of the focus of this thesis and is explained in [4].

Simulation results

This section simulates an aggregated DSFO-controlled DFIG connected to a LCC-HVDC link and ESI-STATCOM, as shown in Figure 3.6. The control of the ESI-STATCOM is given in Appendix C. This case is simulated as an example of standard PSC strategy which has more or less similarly been used in many papers such as [5, 16, 25]. The results will also be used as benchmark to be compared with the later results from a proposed PDC strategy.

Figure 3.7shows the PSCAD simulation results of a 1000MVA DSFO-controlled DFIG connected to the STATCOM-ES and LCC-HVDC link shown in Figure 3.6. The DFIG's parameters are given in Appendix B. The rated wind speed for all wind turbines used in this thesis is kept almost around 12.5m/s. Therefore, the rating of DFIG does not make any difference in the results (in pu), since the parameters of all DFIGs are the same in pu. The DFIG is controlled under conventional MPT. The time constant of the LPF is set at 16sec in order to filter out the frequencies more than 0.01Hz [16]. The ES, for the sake of simplicity, is simulated by a 35kV DC voltage source. AC-filters (not shown in the Figure) are tuned for the rated HVDC power (1000MVA), the fine reactive power balance is clearly provided by the ESI-STATCOM. The HVDC inverter, for the sake of simplicity, is replaced by a DC voltage source (E_0=490kV). The pitch angle control (not shown in the Figure) is the standard MPT pitch control which controls the output power at 1pu for wind speeds above the rated wind speed. The wind profile, shown in Figure 3.7.a, is a real (measured) wind speed with average and standard deviation of approximately 11.5m/s and 1.39, respectively. The perturbation of the wind is relatively large. Figure 3.7.b1 shows the DFIG output power under MPT control while Figure 3.7.b2 is the power into HVDC. The time constant of the LPF (τ=16sec) determines the smoothness of the HVDC power. The larger the time constant, the smoother the HVDC power; and thus the larger

ES would be. Figure 3.7.c is the power absorbed from/injected into the wind farm grid by the ES which is the difference between the wind farm output power and the HVDC power. Figure 3.7.d shows the energy of the ES which is derived by integrating the ES power. Figure 3.7.e depicts the wind farm grid voltage (132kV) and frequency (50Hz) which are controlled by the ESI-STATCOM.
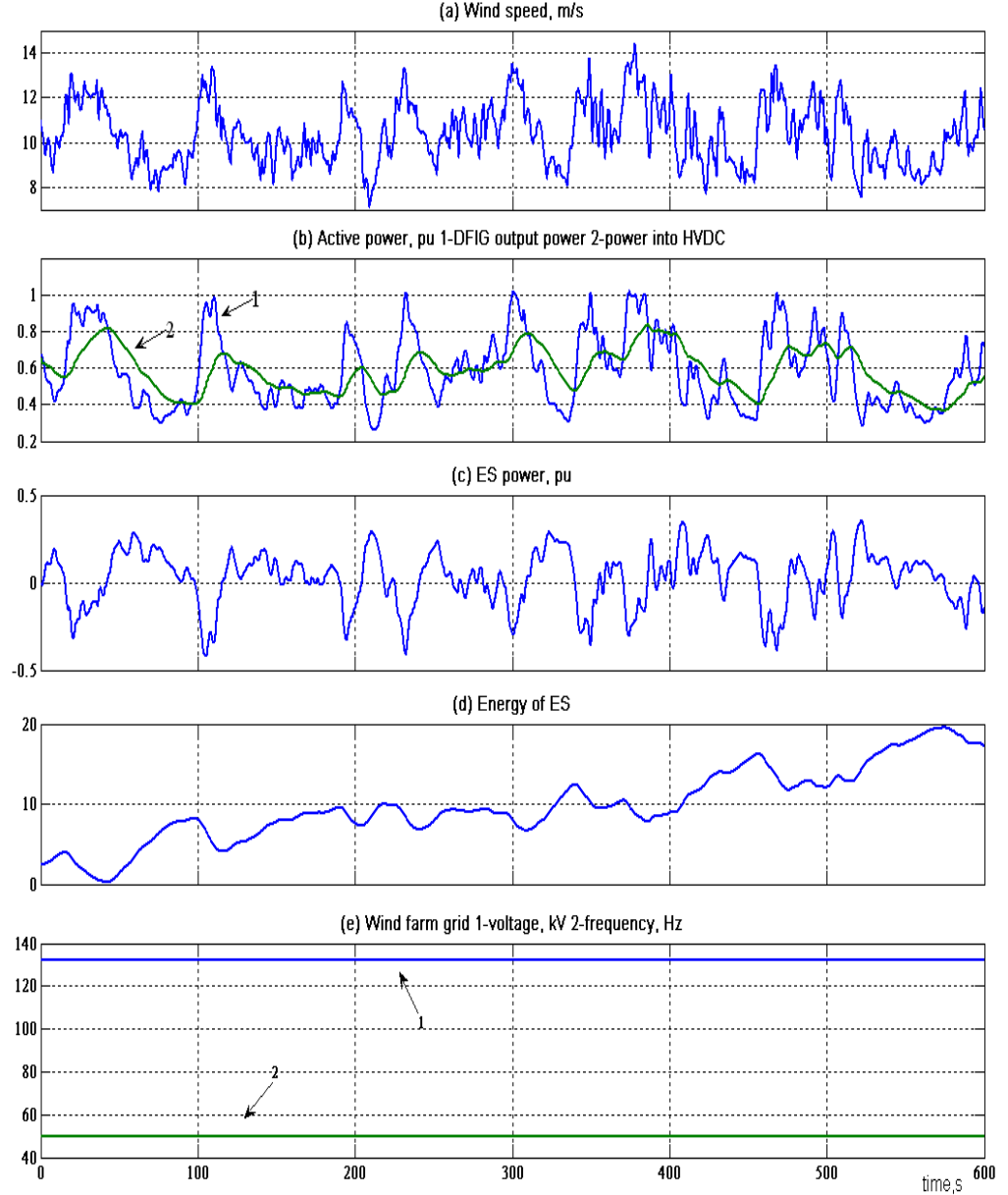
Figure 3.7.Results of a PSC strategy for a 1000MVA DSFO-controlled DFIG connected to ESI-STATCOM and LCC HVDC link

The size of ES is characterized by its power rating and its energy capacity. Here it was assumed that the size of ES is infinite. However, in practice it will have a finite value and a pitch angle control can be used to prevent ES from hitting its maximum limit. A slow pitch control can be also applied to make the average of ES power zero; this will reduce the power rating of ES. These results demonstrate that in order to filter out the power frequencies more than 0.01Hz, the required ES capacity is about 20pu while the power rating of ES is just less than 0.5pu. The required ES capacity and power rating are a function of the wind speed perturbation, shaft inertia and the LPF time constant. Appendix D gives a perspective of the size of the required ES. In order to maintain the energy of ES within its limits, Energy Management System (EMS) is usually required. These methods will be discussed in later chapters. The next section considers Power Demand Control (PDC) for LCC-HVDC connection.

3.3.3.2 Power Demand Control for wind turbines-ES connected to LCC-HVDC link

One structure for implementing a PDC for a DSFO controlled wind farm connected to the ESI-STATCOM and LCC HVDC link is shown in Figure 3.8.
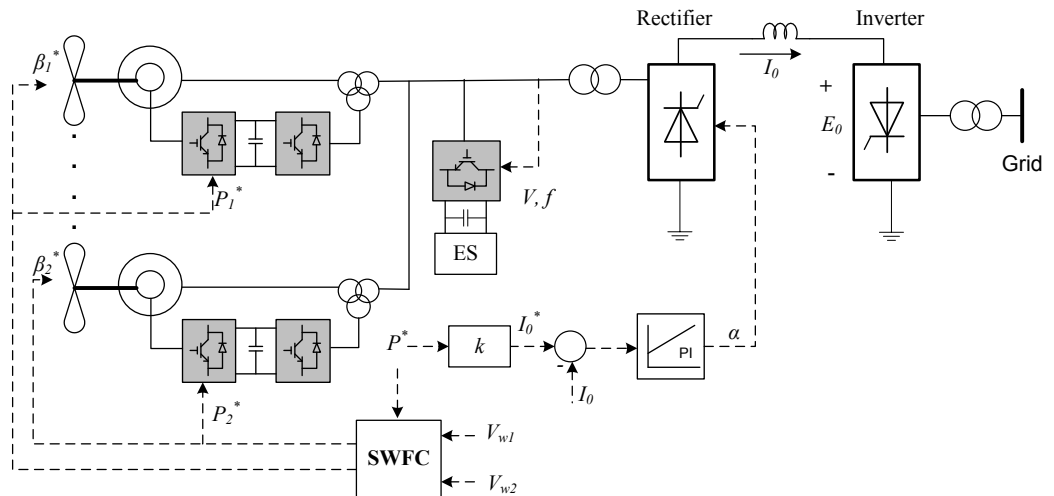
Figure 3.8. PDC for DSFO-controlled DFIGs connected to STATCOM-ES and LCC HVDC link

The demand power P^* is imposed by the HVDC rectifier firing angle α (where $k=1/E_0$). The Supervisory Wind Farm Control (SWFC) unit [57, 58] adjusts the pitch angle and the reference power of each wind turbine in order to minimize the external ES. If the reference powers of the DFIGs are not determined by the MPT, stability issues must be taken into account. If the demand power is less than the extractable wind power, CPM is possible which means that no external ES is needed. This is the subject of Chapter 5.

3.4 Discussions and conclusions

This chapter introduced two strategies of controlling a wind generators-ES system: Power Smoothing Control (PSC) and Power Demand Control (PDC). The application of the two strategies in a DSFO-controlled wind farm connected to both AC grid and HVDC link has been discussed. The different wind farm grid voltage and frequency control structures in each case was illustrated. Through PSCAD simulation it was illustrated that in a PSC, the power into the grid is a smoothed version of the wind power. Therefore the PSC strategy may not be appropriate for a power system with a high penetration of wind energy. This is because the system operator cannot determine the wind power generation, and the ability of other generators to balance the power may be limited. In the PDC structures for a DSFO-controlled DFIGs-ES system, communication between the system operator and the wind farm is necessary in order to determine the reference power and pitch angle for each wind turbine. Moreover the wind turbine cannot control the wind farm grid voltage and frequency.

In future, an increase in both electrical energy and power quality demanded, beside the rapid rise in renewable energy penetration may necessitate the re-designing of T&D systems. Small-scale distributed power generation combined with power electronic systems lead to the concept of future network technologies such as the microgrid which seems to be a promising solution for such problems. The microgrid is an intentionally islanded power system including Distributed Energy Resources (DER), controllable loads and ES which can operate in parallel with, or isolated from the main grid [33, 35]. Microgrids are designed to provide the local

costumer with uninterruptible power, enhance local grid reliability and improve power quality by supporting the local grid voltage and frequency. To achieve this functionality each active component must be able to change its operating point based on local voltage and frequency variations. The most robust way to do so is the use of classical frequency and voltage droops.

This chapter has proposed some structures for a PDC in a DSFO-controlled wind generator. In all of them, fast communication between the system operator and each wind generator unit is necessary in order to share the demand power (i.e. Power Management Communication). The existence of the central communication unit may reduce the system reliability. Furthermore, a DSFO-controlled DFIG cannot contribute to local grid control since they are field orientated off the grid voltage. Therefore a method involving droop characteristics cannot be applied to DSFO-controlled DFIGs. This means that they may not be so suitable for integration into a microgrid. However DFIGs controlled under Indirect Stator Flux Orientation (ISFO) are able to control the local grid voltage and frequency and can be augmented with droop characteristics. These properties make the ISFO-controlled DFIGs a more proper and flexible choice for microgrids.

In the next chapter an array of ISFO-controlled DFIGs are augmented with classical frequency and voltage droops in order to share, respectively, the active and reactive power demanded by the load. The droop characteristics are initially a function of the DFIGs' ratings. The droop characteristics are adjusted in Chapter 5 in order to share the load according not only to the ratings of the DFIGs but also the available wind power.

4. Local grid voltage and frequency control using ISFO-controlled DFIGs

4.1 Introduction

The Indirect Stator Flux Orientation (ISFO) control of DFIG is explained in [44] and has received little attention. The structure is suitable for isolated load since the q-axis of the stator current i_{sq} is imposed by the load rather than the wind. Therefore the q-axis of the rotor current i_{rq} has to be kept proportional to i_{sq} in order to maintain the field orientation of the DFIG. This structure does not require an external voltage source. The voltage magnitude is controlled by the magnetising current i_{ms} through regulating the d-component of the rotor current i_{rd} while the voltage frequency is imposed by the stator flux angle through free running integration of the reference stator voltage frequency. The control structure is given in section 2.2.3. Therefore, a DFIG under ISFO control operates as a voltage and frequency source rather than a power source (which is the case in the DSFO-controlled DFIG). As a result, the ISFO structure can be augmented by voltage and frequency droop characteristics which is explained in this chapter. Moreover, the ISFO seems to be a suitable option for integration within a microgrid as they can support local grid voltage and frequency control and hence enhance the power quality. The main drawback of the ISFO structure is that i_{rq} cannot be used to control electrical torque T_e, since i_{rq} has to be kept proportional to i_{sq}. In this structure the electrical torque is imposed by the load, hence, an external mechanism is needed to control T_e. In [44] an auxiliary load is used to control T_e in the Maximum Power Tracking (MPT) mode. In this thesis, the current component corresponding to the ES power will be used to control the electrical torque whenever required. Without an external torque control mechanism, the electrical torque is directly determined by the load power. This implies that the DFIG is under Constant Power Mode (CPM), assuming a constant load. Figure 4.1 compares the implementation of the CPM in an ISFO-controlled DFIG with that in

a DSFO-controlled DFIG. Figure 4.1b illustrates that in an ISFO-controlled DFIG the local grid voltage is regulated by the DFIG and the DFIG output power is equal to the power demanded by the load.
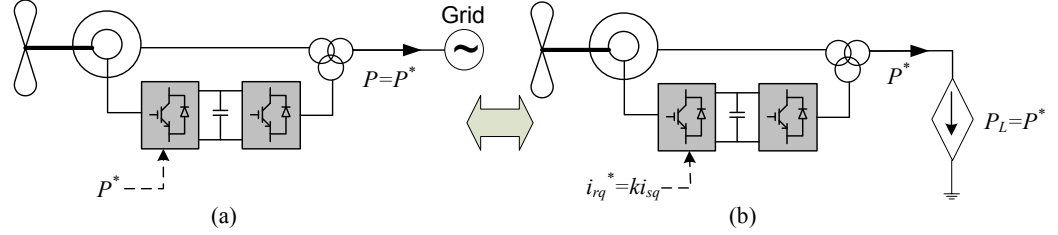
Figure 4.1. Constant Power Mode in (a) DSFO- (b) ISFO-controlled DFIG

However in a DSFO-controlled DFIG the voltage is set by an external voltage source (e.g. grid) and, in order to get a smooth output power equal to P^*, the power loop reference must be set at P^*.Hence communication is needed.

4.1.1 Introduction to technical requirements for wind farms

With increasing wind energy penetration, the impacts of variable wind energy on the T&D system become more significant, necessitating stricter requirements from the wind generators [3, 5, 14]. Currently, the requirements are intended to limit the disturbances of wind energy generation on grid, for example, fault ride through capability. With increasing penetration of wind energy, especially at distribution level, wind farms may be required to provide grid control functions normally associated with conventional power generation units [16, 25, 57]. This problem becomes more severe in an isolated power system like that of a small island which has poor capability of power regulation. Therefore, a modern wind farm may in future be requested to provide advanced grid support such as control functions for both active power-frequency and reactive power-voltage control. These functionalities required from a wind farm can be summarised as follow [22, 58]:

- **Balance control** means that the wind farm can increase or decrease its active power generation in order to balance the demand.

- *Delta control* means that the wind farm is required to generate less than the maximum power such that a reserved available power can be used for a limited frequency control action.

- *Frequency control* means that the wind farm increases or decreases its active power generation in order to compensate for frequency fluctuations.

- *Reactive power control* means that the wind farm is required to absorb or inject a certain amount of reactive power.

- *Voltage control* means that the wind farm controls the voltage of the point of common coupling by absorbing or injecting reactive power.

The next section reviews different conventional methods for supporting wind farm grid voltage and frequency control. In a DSFO-controlled DFIG, unlike the ISFO one, an external voltage and frequency source is always needed as the DFIGs are seen as power source by the power system. The ISFO-controlled DFIGs, however, appear as voltage and frequency sources and it will be shown in later chapters that they can maintain grid voltage and frequency when even there is no wind.

This chapter considers ISFO-controlled DFIGs and augments them with classical frequency and voltage droop characteristics in order to share active and reactive power demanded by the load according to their ratings. The philosophy is to make the wind farms operate as a conventional power plant, for example, like a synchronous generator. In Chapter 5, the droops will be adjusted to share the power according to both the available wind power and the rating of DFIGs.

4.2 Conventional methods for supporting grid voltage and frequency

In a DFIG based wind farm, the reactive power-voltage support can be achieved by supplying reactive power from the DFIG stator [56, 71-73] and/or by regulating the q-axis current of the grid-side converter. The *balance control* can be done by regulating the pitch angle and/or using ES. In order to support the grid frequency control in a DSFO-controlled DFIG, it is required to have enough reserve active

power (*delta control*). In other words, it is generally necessary to force the wind turbine to operate in a non-maximum power point which is commonly referred to as "de-loading" [18]. Regarding participation in frequency control for a DSFO-controlled DFIG, two different types of operation can be defined [22]:

- Participation at full load, when wind speed is higher than rated wind speed: in this case a pitch control reduces the active power to a value less than the wind turbine rated value. Therefore the active power reserved can be delivered to the grid in order to control the frequency when required [18].
- Participation at partial load: Again pitch angle can be utilized to de-load the generator to a value less that the maximum available wind power and use the reserve power to regulate frequency. An alternative way is to set the shaft speed at a non-optimum speed resulting in a power generation less than the maximum one. Therefore, the grid frequency can be regulated through the use of the power reserved [22].

It is also possible to support the grid frequency through using the energy stored in an external ES [19, 59]. In all of these methods, however, an external voltage and frequency source is still required.

The previous chapter considers a STATCOM (which also operates as ES interface) control for a DSFO-controlled wind farm connected to a LCC-HVDC link. In the literature, however, some STATCOM-less solutions have been suggested which are briefly reviewed below.

4.2.1 STATCOM-less solutions for LCC-HVDC connected wind farms to control wind farm grid

In [48, 72, 74] a wind farm connected to a LCC HVDC link is considered. The active power flow through the HVDC link is controlled by regulating the rectifier firing angle. As discussed in the previous chapter, for a DSFO-based wind farm

connected to a LCC HVDC link, an external voltage and frequency source such as a STATCOM is usually needed. However, [48] proposed three STATCOM-less solutions which are summarized as follows.

The *grid frequency control* method [72] in which the wind farm grid frequency is controlled by regulating the rectifier firing angle. The frequency fluctuation is used to regulate the rectifier firing angle in order to transfer the power generated by the wind farm to the main grid through the HVDC link. With a controlled grid frequency, the DFIGs are controlled to set the magnitude of grid voltage by controlling the stator flux through regulating magnetizing current i_{ms}. The DFIGs are controlled such that the rotor d-axis current demand i_{rd}^{*} is set by the magnetizing current while i_{rq} is set by a MPT scheme. However, this control scheme is not valid for system start-up due to the absence of the stator voltage frequency for the field orientation. Therefore, the wind farm has to be initiated under the ISFO control scheme in which a frequency demand is imposed on the system and i_{rq} is kept proportional to i_{sq}. After the start-up, i_{rq} is switched over to a MPT scheme while the wind farm grid frequency is controlled by regulating the rectifier firing angle. In this case the wind farm is not contributing to the main grid frequency control since all the wind power generated is transferred to the main grid. Therefore, large wind power fluctuations may result in large frequency fluctuations in the main grid especially in case of a weak grid. In [74] it was shown that if the main grid frequency is too high or too low, active power flow through the HVDC link can be decreased or increased by introducing a droop at the rectifier control loop. At the same time the pitch angle will increase or decrease to reduce or increase the power generated by the wind farm.

The *grid control via classical droop* method which is intended to make wind turbines operate like a conventional synchronous generator. This approach allows the DFIGs to contribute to a shared control of the grid voltage and frequency. In order to achieve this, each rotor side converter imposes a stator voltage frequency and stator flux level on each of the DFIG stators. The author, as a member of the research team, utilized the droop method in [48] in order to provide ride-through in case of loss of the main grid. However the present thesis is intended to apply the

droop characteristics in both normal and fault ride-through operations. This is the subject of this chapter.

The *master-slave* approach in which one DFIG controls the wind farm grid voltage and frequency (the master) and the others (slaves) operate under standard DSFO control. The master one is controlled under ISFO method in order to set the wind farm grid voltage and frequency while the slaves are field orientated off the grid voltage (DSFO-controlled). In this structure the HVDC rectifier firing angle is regulated to control the electrical torque of the master DFIG. Therefore, communication between the HVDC link and the master DFIG is required. In the master-slave method, similar to the grid frequency control approach, the wind power fluctuations are transferred to the main grid via the HVDC link and may cause large frequency variations particularly in the case of a weak grid. Moreover, the power into the grid is determined by the wind rather than the system operator. Therefore these approaches may not be appropriate for a power system with a large penetration of wind energy, nor for integration into a microgrid. In the methods mentioned above, some level of active power reserve is needed to contribute to frequency control. This implies that the frequency control is not possible under MPT mode. Furthermore, the degree to which the frequency control can be done is limited to the level of the active power reserved. As a result the wind farm cannot be the only voltage and frequency source of the system. However, ISFO-controlled DFIGs enable full control of the local grid voltage and frequency regardless of the wind speed and the demand power. This can be achieved by applying the droop characteristics on the wind generators. As a result, the wind farm can be the only voltage and frequency source in the system and can be well-integrated into a microgrid. This is the subject of this chapter.

4.3 Wind farms and microgrids

Microgrids are supposed to operate in both grid connected and islanded modes. In the grid connected mode, most of the system dynamics are imposed by the main grid due to the relatively small size of the microgrid. However the challenge is in the islanded mode [42, 75] since the microgrid has to meet the local energy

demand and provide the power quality required by the local loads. These requirements can be achieved only if all active units support the local grid voltage and frequency and be able to adjust their operating points very fast according to the demand. These functionalities are normal for the conventional power plants equipped with droops characteristics. The requirements become harder to meet as the wind energy penetration increases since the ability of other power generators may become limited. Moreover, the DSFO-controlled wind turbines have limited capacity to support the local grid.

Two different strategies for controlling a wind farm-ES system were identified in the previous chapter [56]: Power Demand Control (PDC) and Power Smoothing Control (PSC). The latter is the conventional one under which the ES filters out high wind power frequencies in order to provide the main grid with a smoothed power. The power into the grid is still a measure of the wind power. This may cause difficulties for other power generation units to meet the demand especially in a power system with a high wind energy penetration. In the PDC strategy, the combination of wind turbine(s)-ES is controlled in order to deliver a constant demand power to the grid. This strategy seems to be more suitable for a microgrid with a high wind energy penetration. In the previous chapter some control structures for the PDC strategy using the DSFO-controlled DFIGs have been discussed. In those structures a central Supervisory Wind Farm Control (SWFC) unit is required which determines the reference power and pitch angle for each wind turbine. This is called Power Management System in this thesis. Beside the fact that the DSFO-controlled DFIG has limited capacity for the local grid support, the need for a central control unit to determine the power reference for each individual DFIG may undermine the system reliability. It is noted that in the PDC strategy using the DSFO-controlled DFIGs, an Energy Management System (EMS) is also necessary in order to prevent the ES from hitting its energy limits in addition to the Power Management System. However, the ISFO-controlled DFIGs equipped with the droop characteristics enable the full control of the local grid voltage and frequency and increase the system reliability by eliminating the need

for a SWFC unit. The EMS, however, is still required which is quite acceptable for microgrids [42].

4.3.1 ISFO-controlled wind farm and microgrids

In an ISFO-controlled DFIG the electrical torque cannot be controlled by i_{rq}, and is imposed by the load. In the case of an ISFO-controlled wind farm integrated into a microgrid, two scenarios can be considered: with or without an external torque control mechanism.

ISFO-controlled wind farm without external torque control mechanism
Figure 4.2 illustrates an example of an ISFO-controlled wind farm integrated into a microgrid without an external torque controller.

Figure 4.2. ISFO-controlled wind farm integrated within microgrid without external torque control mechanism

The microgrid is assumed to contain the ISFO-controlled wind farm, an Auxiliary Generator (AG e.g. diesel generator), Dispatchable Loads (DL) and other power generators (such as PV, micro-turbines, combined heat and power, etc). The AG and the DL are used in the EMS which will be explained later. It is assumed in this

thesis that the local grid voltage and frequency is fully controlled by the ISFO-controlled wind farm, however in practice, other generators can also contribute to control the voltage and frequency. There is no external mechanism to control the electrical torque and assuming a constant local load means that the DFIGs are under Constant Power Mode (CPM). This implies that the wind power variations are reflected on the shaft speed of the DFIGs which increases the risk of instability. In the next chapter a pitch control is designed to keep the shaft speed within the stable region when the demand power is less than the extractable wind power. If the demand power approaches the average of the extractable wind power, the shortage of energy is compensated by the energy stored in the shaft inertia causing a reduction in shaft speed. In this case the EMS is responsible for keeping the shaft speed within the stable region. If the shaft speed decreases more than a certain threshold, the AG injects energy in order to maintain the demand power. If the demand power is too low, the shaft speed may increases more than a certain level which is used to regulate the DL in order to absorb the excess of energy.
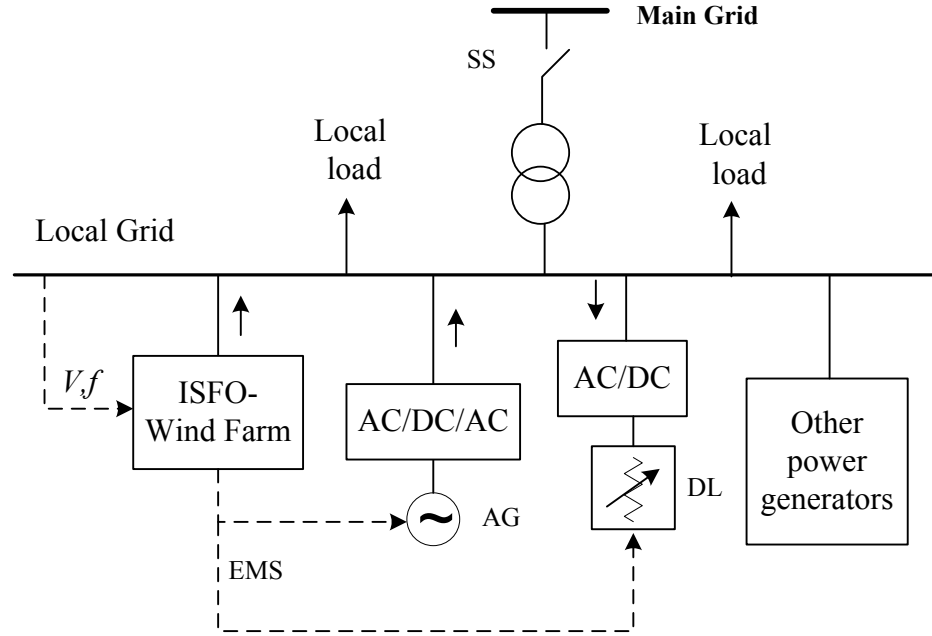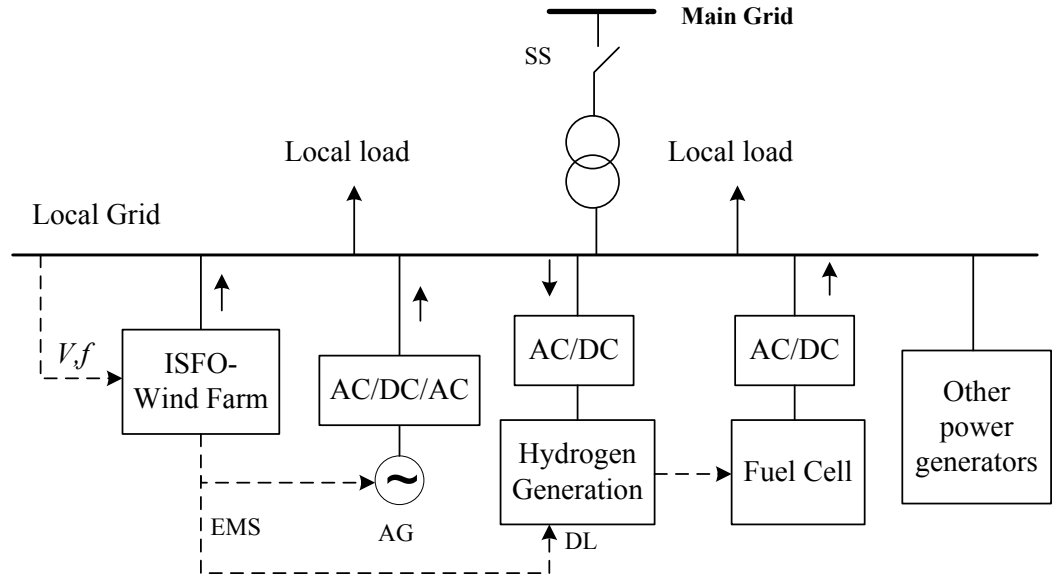

Figure 4.3. ISFO-controlled wind farm integrated within microgrid without external torque control mechanism with the DL as a hydrogen generation station

The DL can be anything from resistor sets to hydrogen generation station or an irrigation system. Figure 4.3 shows the DL as a hydrogen generation unit. In such a case the DL can also operate as a long-term ES. For instance, whenever the local load is low (compared to the extractable wind power); the DL can generate hydrogen which later can be used in fuel cells (i.e. as an auxiliary generator) in order to minimize the fuel consumption of the AG when the demand is raised.

The extra energy can also be shed by the pitch control. There is a trade-off between the power rating of the DL and the maximum slew rate of the pitch control. It will be shown in later chapters that a slow pitch control may result in a relatively large DL whilst a normal pitch control can eliminate the need for a DL. It is noted that even in a standard DSFO-controlled DFIG under MPT mode, the pitch angle is used to maintain the power at the rated value and prevent the shaft speed from exceeding the maximum limit for wind speeds above rated.
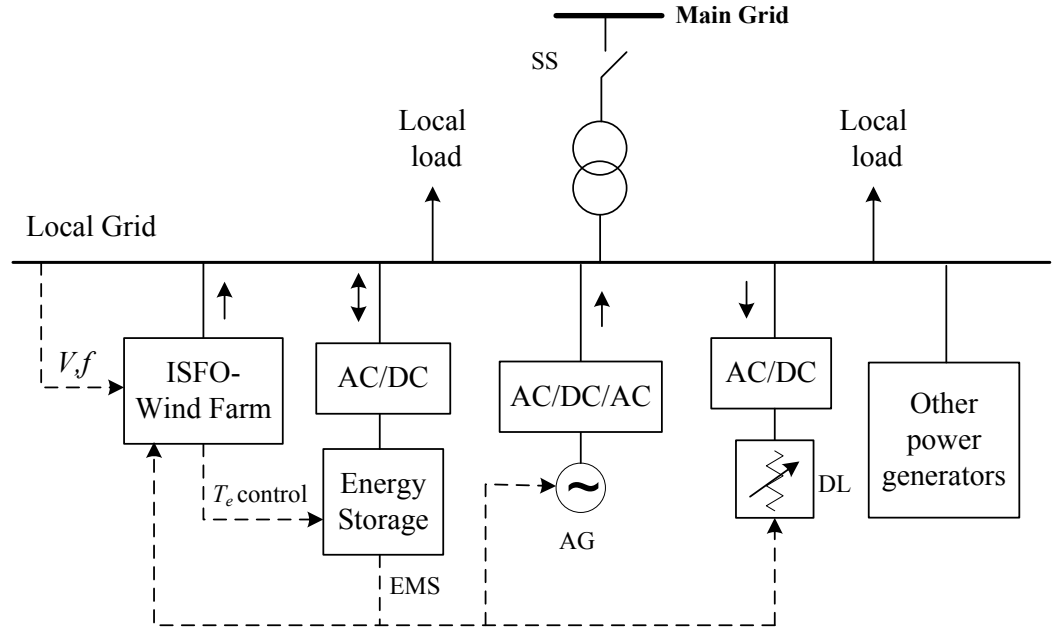

Figure 4.4. ISFO-controlled wind farm integrated within microgrid with external torque control mechanism (i.e. ES)

ISFO-controlled wind farm with external torque control mechanism

The second scenario is shown in Figure 4.4 where an ISFO-controlled wind farm is integrated into a microgrid with an external ES. The ES is used to control the DFIGs electrical torques. This can be either aggregated on the local grid or distributed within individual wind turbines. The EMS, which is used to prevent the ES from hitting its energy limits, is based on the same logic as the first scenario. This structure enables the control of DFIGs under the standard MPT mode which is investigated in Chapter 7. In Chapter 6, which can be considered as a transition step from Chapter 5 (CPM) to Chapter 7 (MPT), the microgrid is the same as that of Figure 4.4 but without any external energy source (i.e. AG). Although this may sounds impractical, it is a suitable case study for DFIGs under a non-maximum power tracking control such as Constant Torque Mode (CTM).

In the next section the ISFO-controlled DFIGs will be augmented by the classical frequency and voltage droops in order to share a demand active and reactive power according to their ratings.

4.4 Voltage and frequency control using classical droop characteristics

4.4.1 Introduction and applications

The droop method, which has been used for many years, is based on a well known concept in power networks that consists of reducing the frequency of the synchronous generator when its output power increases [32]. The concept is also adopted in the control of parallel inverters such as Uninterruptable Power Supplies (UPS) [76-79]. The advantages of such a power configuration include "high reliability and no restriction on the physical location of the UPS units" [80] since there is no communication and units use only local variables. Similarly, the droop characteristics can be applied on Distributed Energy Resources, including wind turbines, in order to increase the system reliability and obtain autonomous operation. This section discusses some different applications involving a droop-

controlled wind farm. In section 4.4.2, an array of wind generators are augmented with droop characteristics in order to share a variable active and reactive load. The ISFO-controlled DFIGs augmented with droops do not require a SWFC unit to set the reference power for each DFIG; unlike the DSFO-controlled ones (section 3.3.2.2). In other words, there is no need for power management system; however, EMS is still required which will be investigated in the following chapters.

Figure 4.5 shows an array of ISFO-controlled DFIGs integrated into a microgrid. It is assumed, in this thesis, that the wind farm is the main power supply of the system and is responsible for controlling the local grid voltage and frequency. However, other generators can also contribute to the local grid control (using the droop characteristics), if requested. As Figure 4.5 illustrates, the reactive power-voltage droop determines the stator voltage magnitudes which in turn sets the reference magnetising currents i_{ms}^*. The magnetising current is controlled by regulating i_{rd} (not shown in the figure). The active power-frequency droop determines the stator voltage frequency reference f_s^* which sets the stator flux angles θ_s.
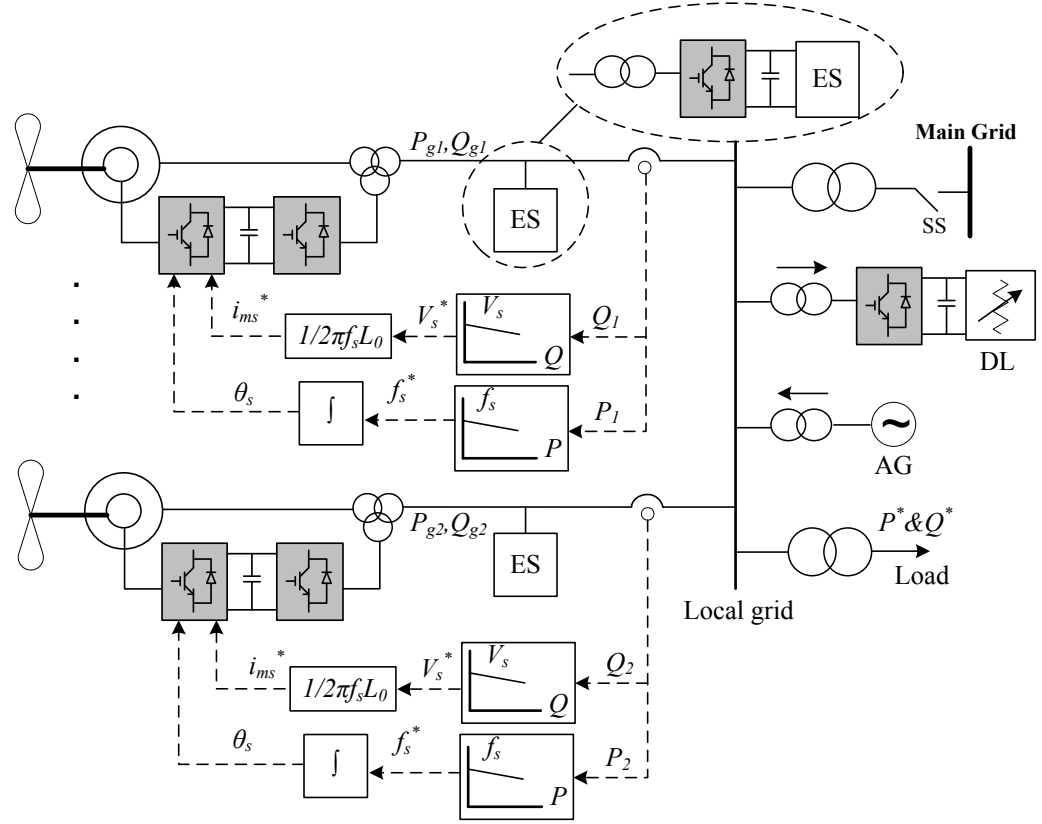
Figure 4.5. Local grid control by an array of ISFO-controlled DFIGs integrated within a microgrid

The ES can be aggregated on to the local grid or distributed and integrated with the generators, either as shown in Figure 4.5 or affixed to the DC-link of each DFIG. The DL and AG are controlled in order to keep the energy level of the ES within its limits. This chapter is intended to study an array of ISFO-controlled DFIGs augmented with classical droops and assumes that the DFIGs are driven at a constant shaft speed. This implies that the load power is always less than the hypothetical available wind power. Therefore at this stage, the control of the ES, DL and AG are not considered.

Figure 4.6 shows another application in which an ISFO-controlled wind farm is buffered from the main grid by a set of power electronic converters. These are effectively Power Flow Controllers (PFC). The PFCs can control the active power flow to/from the main grid in order to prevent the energy level of the ES from hitting its upper/lower limits. In this case, there is theoretically no need for the DL

and AG. However, the AG could be required if the aim was to minimize the power from the main grid due to a higher price of the main grid energy.
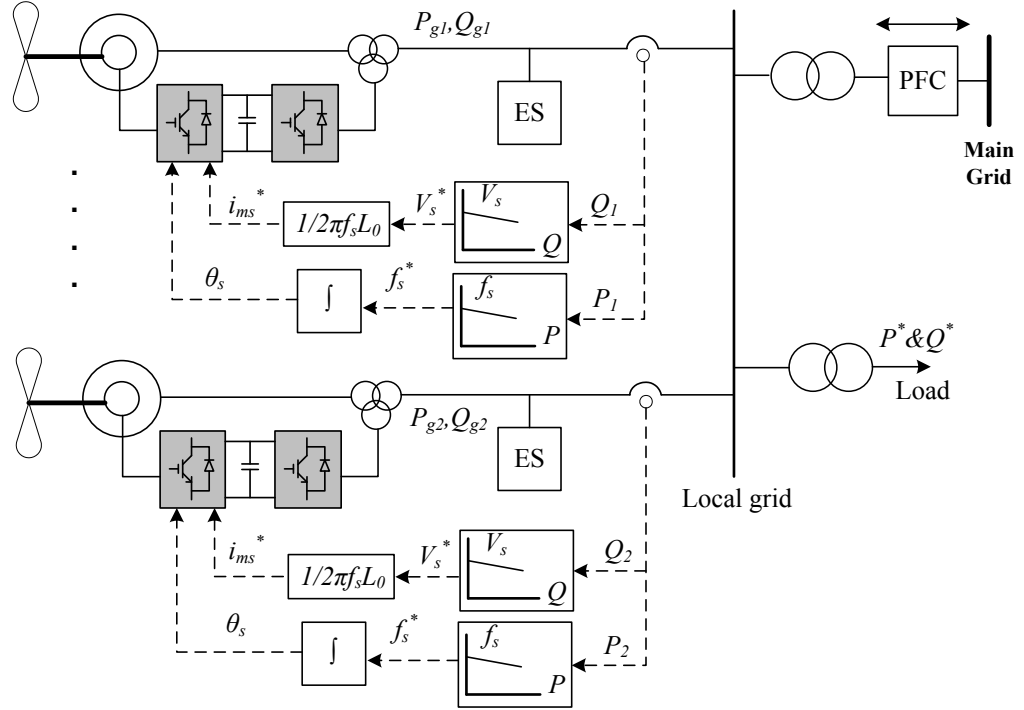
Figure 4.6. A droop-controlled wind farm buffered from the main grid by Power Flow Controller (PFC)

The method is also applicable to an ISFO-controlled wind farm connected to the grid through a HVDC-link. Both VSC- and LCC-HVDC connections are possible. Figure 4.7 shows an array of ISFO-controlled DFIGs connected to a VSC-HVDC link. In this scenario the wind farm grid is controlled by the DFIGs rather than the sending end converter of the VSC-HVDC link. The demand power is imposed by the d-axis current of the receiving end converter as $I^*_{d-con} = P^*/V_{DC}$, where V_{DC} is the voltage of the HVDC DC-link. The HVDC DC-link voltage is controlled by the d-axis current of the sending end converter which is the reverse of the standard control of VSC.

Figure 4.7. An ISFO-controlled wind farm equipped with classical droop characteristics and connected to the main grid though a VSC-HVDC link

Figure 4.8 illustrates an ISFO-controlled wind farm connected to the grid through a LCC-HVDC link. The local (wind farm) grid is controlled by the DFIGs utilising droop characteristics. Therefore, neither an external voltage source, such as a STATCOM, nor a SWFC unit (compared to the DSFO-controlled wind farm explained in section 3.3.3.2) is required. The EMS, however, is still needed to control the energy level of ES within its limits using the DL and AG. The demand power sets the reference current of the HVDC DC-link as $I_0^* = P^*/E_0$, where E_0 is the voltage of the HVDC link. The HVDC current is controlled by regulating the rectifier firing angle α. The HVDC DC-link voltage is controlled by the HVDC inverter. This case will be simulated later in this chapter to illustrate the droop control.
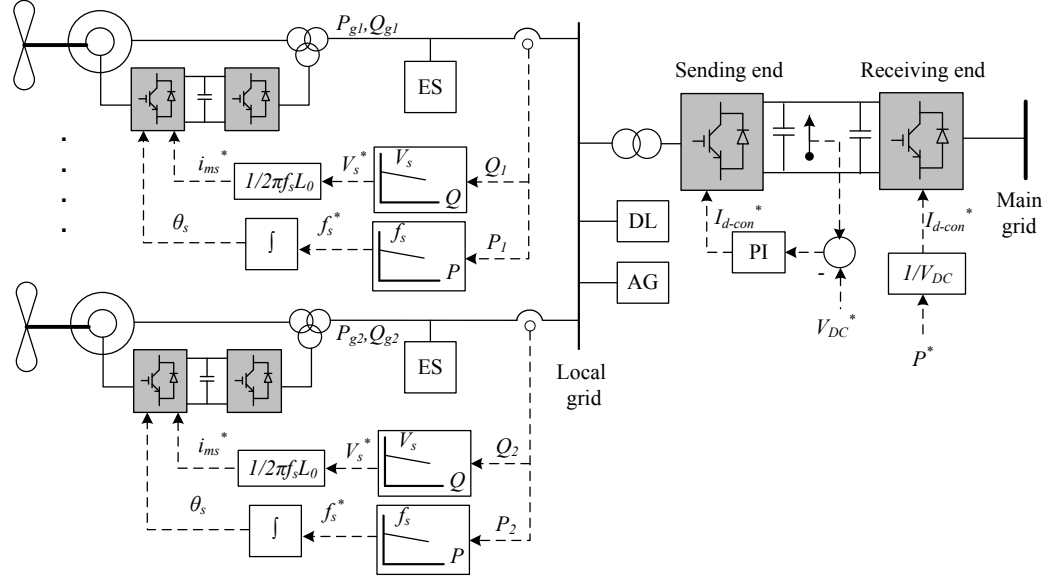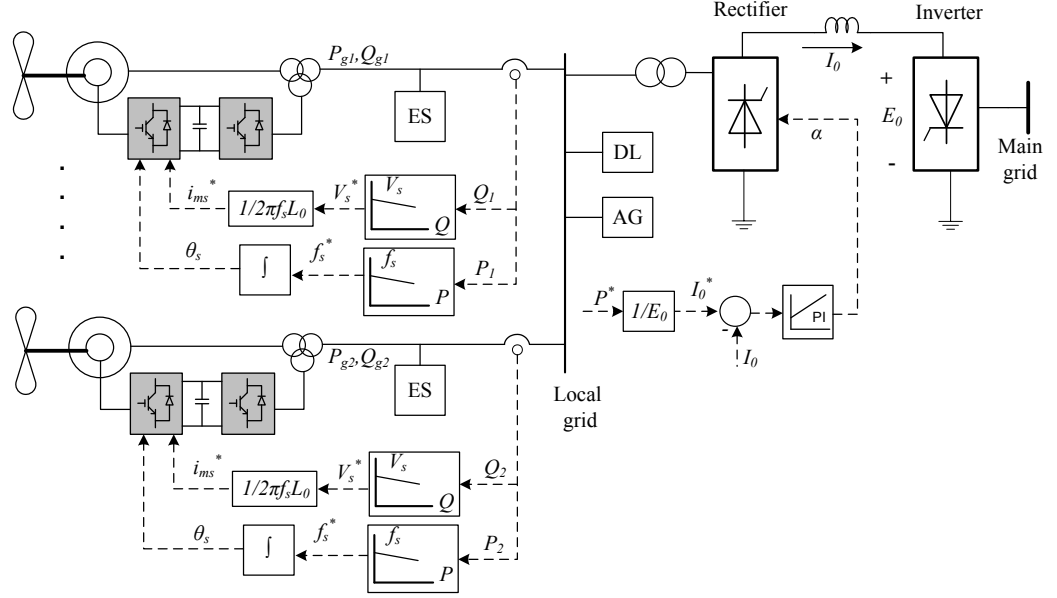
Figure 4.8. An ISFO-controlled wind farm equipped with classical droop characteristics and connected to the main grid though a LCC-HVDC link

Prior to applying the droop method on an array of ISFO-controlled DFIGs, the following subsection reviews the theory behind the droop characteristics in brief.

4.4.2 Voltage and frequency droops

Each generator (in this case DFIG), can be represented as a voltage source connected to a common bus (the local grid) through a decoupling impedance Z as shown in Figure 4.9 [32, 79].
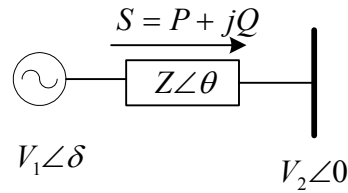
Figure 4.9. Generator connected to the local grid through an impedance

The complex power flowing from the generator to the common bus can be written as [77]:

$$S = P + jQ = V_2 \left(\frac{V_1 e^{-j\delta} - V_2}{Ze^{-j\theta}} \right) = \frac{V_1 V_2}{Z} e^{j(\theta-\delta)} - \frac{V_2^2}{Z} e^{j\theta} \tag{4.1}$$

where V_1 and V_2 are the amplitude of the generator voltage and the common bus voltage, δ is the power angle, and Z and θ are the magnitude and the phase of the generator output impedance. Using (4.1), one can write:

$$P = \frac{V_1 V_2}{Z} \cos(\theta - \delta) - \frac{V_2^2}{Z} \cos\theta$$
$$Q = \frac{V_1 V_2}{Z} \sin(\theta - \delta) - \frac{V_2^2}{Z} \sin\theta \tag{4.2}$$

Equation (4.2) shows that the output impedance affects the relation between the voltage amplitude or phase difference and the active and reactive power components circulating between the generators [81]. Assuming a mainly inductive output impedance (i.e. $Z=jX$, $\theta=90°$), the following well-known expressions of active and reactive power can be derived from (4.2) [77, 78]:

$$P = \frac{V_1 V_2}{X} \sin\delta$$
$$Q = \frac{V_1 V_2 \cos\delta - V_2^2}{X} \tag{4.3}$$

From (4.3), and assuming small power angles ($\cos\delta \approx 1$ and $\sin\delta \approx \delta$), it can be seen that the active power is strongly dependent on the power angle δ, and the reactive power is mainly dependent on the difference between the voltage magnitudes [79]. Obviously the control of the frequency dynamically controls the power angle. Therefore, the frequency can be controlled by active power while the generator voltage amplitude can be controlled by reactive power. This concept leads to the well-known frequency and voltage droop equations:

$$f = f_0 - mP$$
$$V = V_0 - nQ \tag{4.4}$$

where f_0 and V_0 are the output voltage amplitude and frequency at no load (set point), and m and n are the frequency and voltage droop coefficients respectively. As a general rule, the larger the droop coefficients, the better the power sharing would be at the expense of degrading the voltage and frequency regulation. Usually, the maximum acceptable deviation of voltage and frequency are $\Delta V=5\%$ and $\Delta f=2\%$ respectively [79]. If the voltage or frequency drops more than this level, their set point values can be increased (using communication or a very slow bandwidth control) in order to compensate for the reduction.
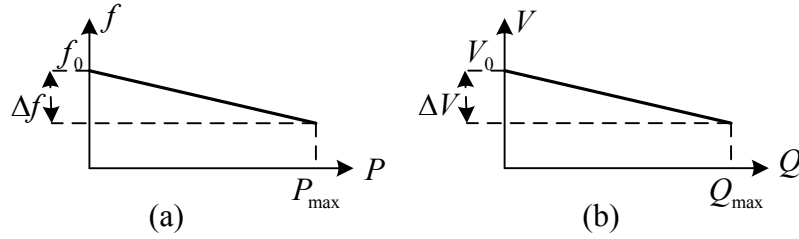
Figure 4.10. Droop characteristics (a) frequency-active power (b) voltage-reactive power

Figure 4.10 illustrates the droop characteristics basing on (4.4). The droop coefficients can be calculated as:

$$m = \frac{\Delta f}{P_{\max}}$$
$$n = \frac{\Delta V}{Q_{\max}}$$

(4.5)

where P_{max} and Q_{max} are the maximum active and reactive power (usually the generator rated value), and Δf and ΔV are the maximum acceptable frequency and voltage deviations. Usually, Δf and ΔV are chosen to be equal for all the units:

$$m_1 P_{\max 1} = m_2 P_{\max 2} = ... = \Delta f$$
$$n_1 Q_{\max 1} = n_2 Q_{\max 2} = ... = \Delta V$$

(4.6)

Choosing the droop coefficients according to (4.6) ensures that the active and reactive powers drawn from each generator are shared by them according to their ratings [76]. It should be noted that (4.4) is only truly valid for mainly inductive output impedance, which is usually the case. This is because of the large filter-inductance and small resistance of overhead lines [32, 81]. However, in the case of resistive or capacitive output impedance, it can be shown that the active power becomes mainly dependent on voltage while reactive power can be regulated by frequency [80] i.e. the reverse of the inductive impedance case. In this thesis the output impedance is assumed to be inductive, however, the resistive or capacitive ones seem applicable as well.

Active power-frequency droop:

The stator voltage frequency is controlled by the stator flux angle θ_s through the free running integration of the frequency reference value f_s^*. Substituting the reference frequency with the *f-P* droop equation given in (4.4), yields:

$$\theta_s = 2\pi \int f_s^* dt = 2\pi \int (f_0 - mP) dt \tag{4.7}$$

Using (4.7), the active power-frequency droop control scheme is shown in Figure 4.11.
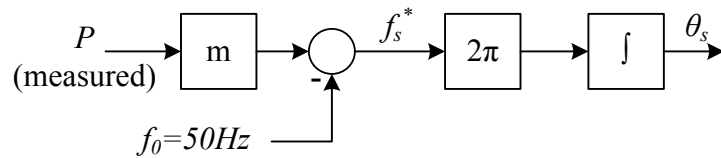
Figure 4.11. Active power-frequency droop control scheme

In this thesis the frequency set point will be always set at 50Hz, however, in practice the set point can increase in order to compensate for the frequency drop.

Reactive power-voltage droop:

The stator voltage magnitude is controlled by regulating the magnetising current i_{ms} which in turn is controlled by i_{rd}. Neglecting the stator resistance, the stator

voltage can be written as $V_s = \omega_e \varphi_s$ where ω_e and φ_s are the electrical angular frequency and the stator flux. Since $\varphi_s = L_0 i_{ms}$, one can write $V_s = \omega_e L_0 i_{ms}$. Using the Q-V droop equation given in (4.4), one can derive:

$$i_{ms}^* = i_{ms0} - \frac{n}{\omega_e L_0} Q \qquad (4.8)$$

Figure 4.12 illustrates the reactive power-voltage droop control scheme basing on (4.8).
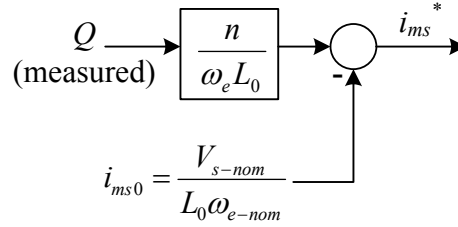
Figure 4.12. Reactive power-voltage droop control scheme

where i_{ms0} is the magnetising current at no load which is usually set as $i_{ms0} = \frac{V_{s-nom}}{L_0 \omega_{e-nom}}$ where V_{s-nom} and ω_{e-nom} are the nominal values of the stator voltage magnitude and the electrical angular frequency respectively. However if necessary, i_{ms} can become more than the nominal value in order to compensate for the voltage reduction. Although i_{ms0} for DFIGs with different rating is different, choosing droop coefficients using (4.6) leads to the same stator voltage for any given reactive power.

In the next section the droop characteristics will be applied on two ISFO-controlled DFIGs connected to a LCC-HVDC link.

4.4.3 Simulation of a droop-controlled wind farm connected to a LCC-HVDC link

This section simulates two ISFO-controlled DFIGs equipped with the droop characteristics as shown in Figure 4.13.
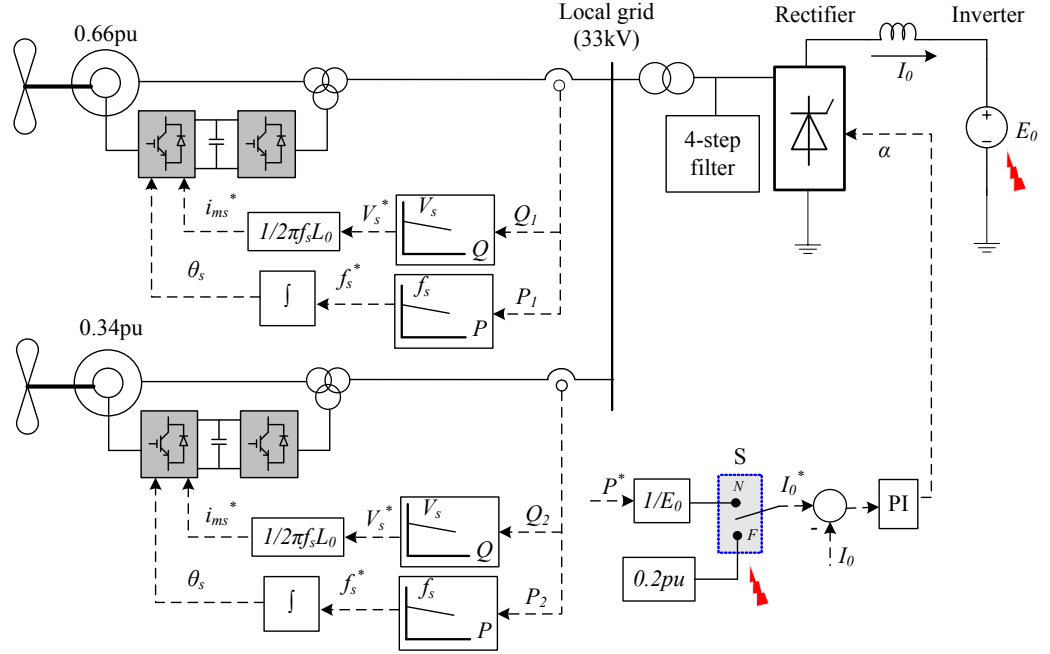
Figure 4.13. A ISFO-controlled wind farm augmented with droop characteristics and connected to the grid through a LCC-HVDC link

The wind farm is connected to the grid through a LCC-HVDC link. The first DFIG is 0.66pu and the second one is 0.34pu with parameters given in Appendix B. It should be noted that "pu" represent the per unit value based on the total wind farm rating. From now on in the thesis, "pu_{gen}" will stand for the per unit value based on the rating of the associated DFIG in multi DFIGs systems. The demand power is imposed by regulating the HVDC DC-link current I_0 which in turn is controlled by α. In the normal operation $I_0 = P^*/E_0$. The parameters of the HVDC DC-link cable are given in Appendix B. The control of the HVDC current loop is explained in [4] and is beyond the scope of this thesis. The rated value of the HVDC DC-link current is 2kA with the rated voltage of 500kV. The inverter controls the HVDC DC-link voltage and is replaced by a DC-voltage source [4, 48] E_0=490kV. A 4-step (0.25, 0.5, 0.75, 1pu) switchable AC-filter is designed, with parameters given

in Appendix B, in order to absorb the 11th and 13th harmonic currents and also compensate for the rectifier reactive power demand. In this simulation, in order to investigate the effect of the droop characteristics, the DFIGs are driven in a constant shaft speed. This implies that the demand power is always less than the hypothetical wind power. However, real wind speed profiles will be applied throughout the following chapters. Both normal and fault ride-through operations are simulated. In the normal operation the switch S, shown in Figure 4.13, is in position N while in the fault operation the switch is in position F. This will be explained below.

Simulation results of normal operation

This section compares the active and reactive power sharing with and without the droop characteristics explained above.

Figure 4.14. Comparison between active and reactive power sharing with and without droop characteristics for an ISFO-controlled wind farm connected to a LCC-HVDC link

77
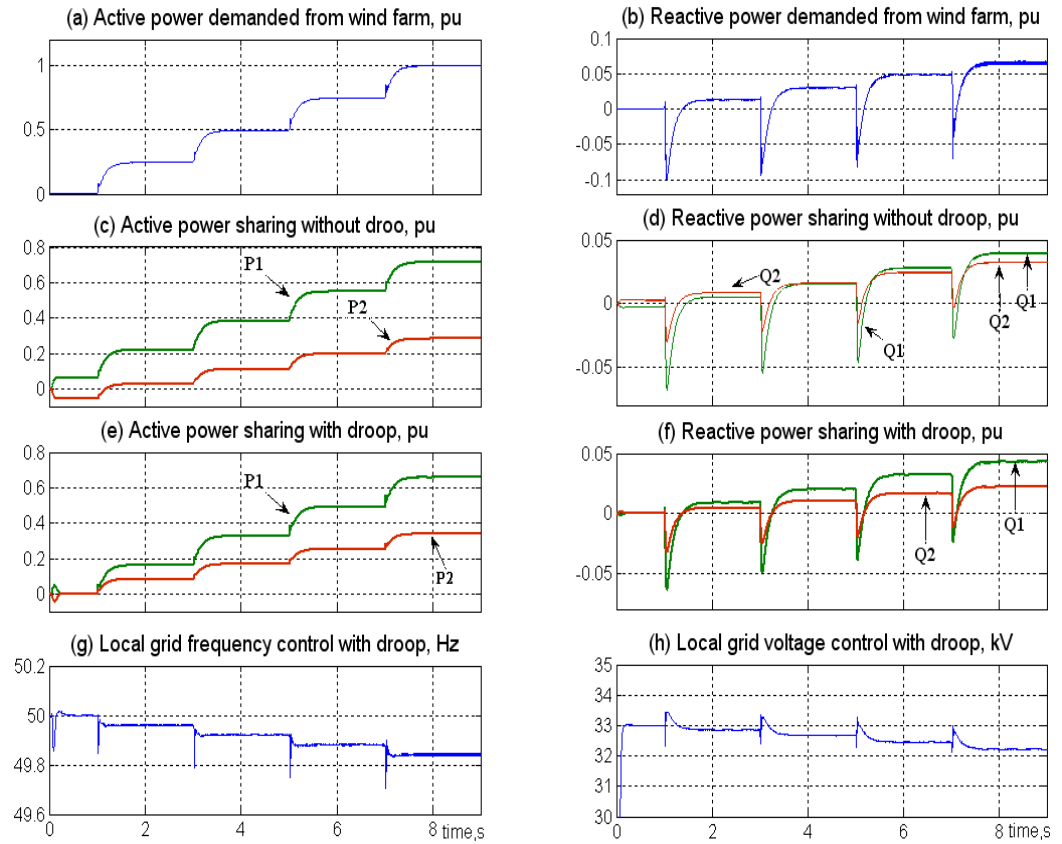
In both cases the active power demand is increased from 0 to 1pu in four steps, as shown in Figure 4.14a. The reactive power demand by the rectifier is $Q^*=P^*\tan(\alpha)$ which is mainly supplied by the AC-filters. The reactive power demanded from the wind farm (Figure 4.14b) mainly covers the reactive power absorptions in the transformers which increase as the demand active power rises. Figure 4.14c and Figure 4.14d illustrate the active and reactive power sharing without droop. As it can be seen, before 1sec, during which no power is demanded, the output power of the DFIGs are non-zero. This implies that there is circulating active and reactive power between DFIGs. Moreover, Figure 4.14c shows that the first DFIG is overloaded, when the demand power is 1pu, while the second DFIG generates far less than its rated value. The situation for reactive power sharing without droop is even worse and the second generator generates more than the first one until 3sec. Figure 4.14e and Figure 4.14f show the active and reactive power sharing using the proposed droop characteristics with the droop coefficients given inTable 4.1.

	Rating, pu	m, Hz/pu	n, kV/pu
DFIG 1	0.66	0.151	0.0757
DFIG 2	0.34	0.294	0.147

Table 4.1. Droop characteristics coefficient of DFIGs

It can be seen that there is no circulating active and reactive current. Furthermore, applying the droops, the active and reactive power are shared in proportion to their ratings: $P_1/P_2 = Q_1/Q_2 = 0.66/0.34$. These improvements have been achieved at the expense of a very small frequency and voltage deviations as is shown in Figure 4.14g and Figure 4.14h, respectively. The transient voltage and frequency fluctuations are due to the switching effects of the AC-filters.

In this simulation, the reactive power from the DFIGs covers only the losses in the transformers' reactance. However in practice, the DFIGs may need to cover the excess/shortage of reactive power between each filter level and its upper/lower level. Assuming the 4-level filter of Figure 4.13, the reactive power unbalance will be always less than 0.15pu. Therefore in the simulations carried out in the following chapters the reactive power demanded by the load is set at 0.15pu.

Fault ride-through operation

This section considers an ISFO-controlled wind farm connected to a LCC-HVDC link as shown in Figure 4.13. The ride-through of loss of the AC-main grid, in which the power has no where to go, is simulated. The fault, as illustrated in Figure 4.13, is simulated by a short circuit on the HVDC at the inverter end i.e. the voltage of the DC-voltage source representing the inverter drops to 0kV. The fault lasts for 150msec. The objective of this simulation is to demonstrate that the ISFO-controlled wind farm equipped with the droops have the ability to ride-through without any communication.

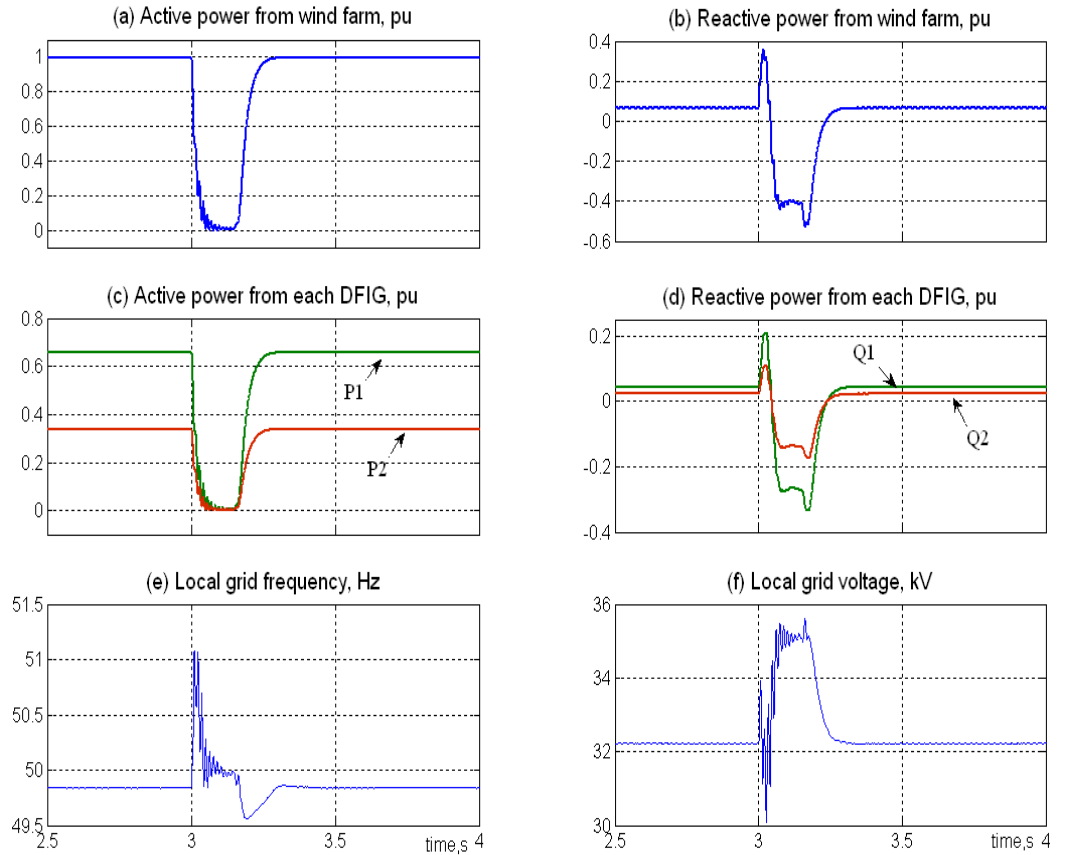Figure 4.15. Fault ride-through for an ISFO-controlled wind farm augmented with droops

Since the AC-filters (see Figure 4.13) cannot be switched fast enough following the fault, maintaining some DC current demand is useful in order to keep the reactive power demand of the rectifier. Therefore, following the fault, the switch S in Figure 4.13 is switched to position F which imposes a DC-current reference of

0.2pu. However, this is not a mandatory requirement and will only affect the dynamic of the ride-through response and not the nature of it. It is noted that operation with constant shaft speed may affect the dynamics of the ride-through responses as the power unbalance is only reflected on the voltage and frequency. The simulation results are given in Figure 4.15. Before the fault occurs (at 3sec), the demand power is 1pu. It can be seen that after the fault is cleared the active (Figure 4.15a) and the reactive (Figure 4.15b) power recover to their pre-fault values with no communication. The active and reactive power sharing using droops also returns to normal after fault clearance. Figure 4.15e and Figure 4.15f show that the frequency and voltage controls are restored while their variations during the fault are about 2% and 6% respectively, which are acceptable. In the later chapters a similar fault ride-through scenario will be simulated (without the HVDC-link) while a real wind speed profile is applied.

4.5 Discussions and conclusions

This chapter reviewed the different functionalities that may be required from a wind farm including the active power-frequency and the reactive power-voltage control. Current methods for supporting the local grid voltage and frequency have been discussed. In all of these methods, an external voltage and frequency source is still required. It was emphasised that a conventional DSFO-controlled wind farm has limited capacity for supporting the local grid frequency according to the level of the active power reserved. However, an ISFO-controlled wind farm augmented with droop characteristics has the potential to fully control the local (wind farm) grid voltage and frequency. The different applications of a droop-controlled wind farm including AC grid connection, HVDC connection, and integration within a microgrid has been discussed.

This chapter has addressed the control of an array of ISFO-controlled DFIGs with classical droop characteristics. The active and reactive power sharing using droops has been compared with that of without droops. It was demonstrated, using PSCAD simulations, that the droops eliminate the active and reactive power circulations and force the DFIGs to share the load in proportion to their ratings. It

was shown through PSCAD simulation that a droop-controlled wind farm is inherently able to ride-through loss of the grid with no need for communication. It is proposed that an array of ISFO-controlled DFIGs augmented with droops is a more suitable option for integration into a microgrid than that controlled under DSFO. This is due to their ability to control the local grid voltage and frequency and adjust their operating point using only local measurements, with no central power control communication. However, energy control communication is still needed in order to control the DFIGs' shaft speed and/or to keep the energy level of the ES within its limits. This is the subject of the following chapters.

This chapter assumed that the demand power is always less than the extractable $\hat{P}_{ext}$ wind power. In practice the demand power may be more than $\hat{P}_{ext}$. In that case an ES and/or external energy source is needed to compensate for the energy shortfall. The next chapter proposes an energy management system using an external energy source while the control of ES will be introduced in Chapter 6. An energy management system consisting of both ES and an external energy source is considered in Chapter 7.

The DFIGs equipped with the droop control in this chapter share the demand power in proportion to their ratings, regardless of the available wind power. The next chapter adjusts the droops in order to take the available wind power into account. It will be shown that the improved droop can significantly reduce the energy required from an external source since it enables the DFIGs with sufficient extractable wind energy to compensate for those with insufficient extractable wind energy.

5. Droop-controlled wind farm delivering a constant demand power without an external ES

5.1 Introduction

This chapter studies an array of ISFO-controlled DFIGs equipped with droop characteristics. The different applications of such a control method, including AC grid connection, HVDC connection, and integration into a microgrid, were investigated in the previous chapter. This chapter considers the microgrid application without a direct torque control mechanism, as discussed in section 4.3.1 and shown in Figure 5.1.

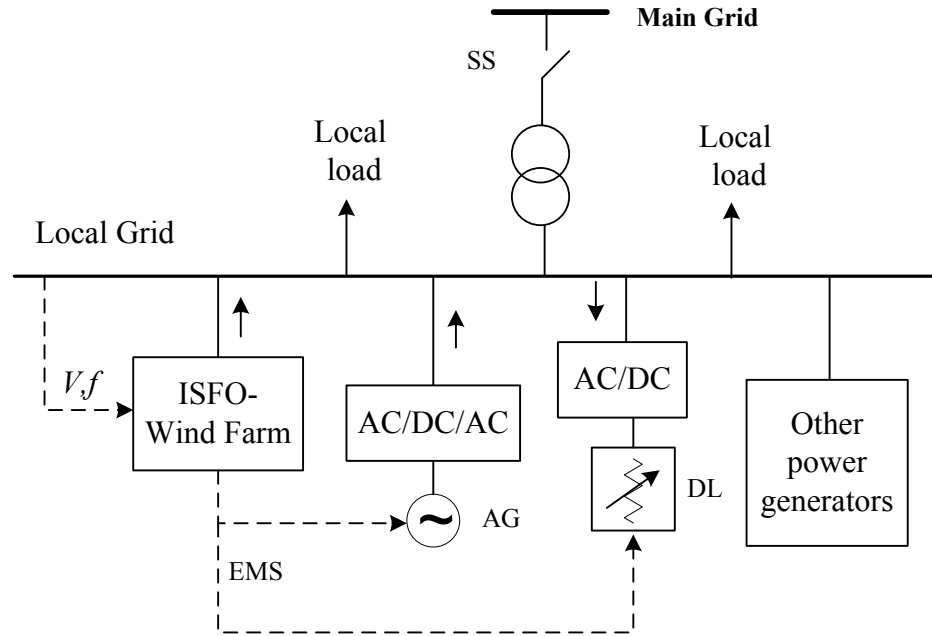Figure 5.1. Integration of a droop-controlled wind farm into a microgrid without external torque control mechanism

In this scenario the DFIGs control the local grid voltage and frequency and share the local load through the droop method. The wind turbine inertia operates as a short-term ES and there is no external ES. Therefore, the shaft speed varies according to the demand load and the available wind power. This means that the

shaft speed can be considered as an indicator for the excess or shortfall of energy. In order to keep the shaft speed within its limits, an Energy Management System (EMS) is required which will be explained in this chapter. It is noted that the EMS is not an extra requirement for this system and is also needed for the standard DSFO-controlled wind farm with ES. The EMS consists of an Auxiliary Generator (AG) and a controllable or "Dispatchable Load" (DL). The AG is used to compensate for the lack of the energy when the shaft speed decreases too much. On the other hand, if the shaft speed increases too much, the DL is utilized to absorb the extra energy. The DL can be sets of resistors, an irrigation system, a hydrogen generation station, etc. It will be shown in Chapter 7 that using a pitch angle control with slew rate up to 3-5º/sec can eliminate the need for a DL. However, the DL as hydrogen generator combined with fuel cells, for example, can be used as a long-term ES to reduce the fuel consumption of the AG (Figure 5.1). This last scenario is out of the scope of this thesis. It will be shown in Chapter 8, that the DL can also be distributed among the DFIGs which might be a better place for resistive DLs.

5.1.1 Constant Power Mode (CPM) control

It was discussed in Chapter 2 that ISFO-controlled DFIGs usually require an external mechanism to control their electrical torque T_e. In [44] an auxiliary load is used to control T_e and the next chapter will control the electrical torque by regulating the ES interface (ESI) real current. This chapter deals with the case that there is no external torque control mechanism; hence the electrical torque is imposed directly by the load. Such a case is depicted in Figure 5.2. Assuming that no energy is injected/absorbed by the AG/DL shown in Figure 5.2, the DFIGs are under CPM for a constant load demand. As argued in section 2.3.3, the CPM has the widest shaft speed variation but the system may be exposed to instability. A pitch angle control will be designed in this chapter to control the shaft speed within the stable region for demand powers which are always less than the extractable wind power $\hat{P}_{ext}$ (Figure 5.1a).
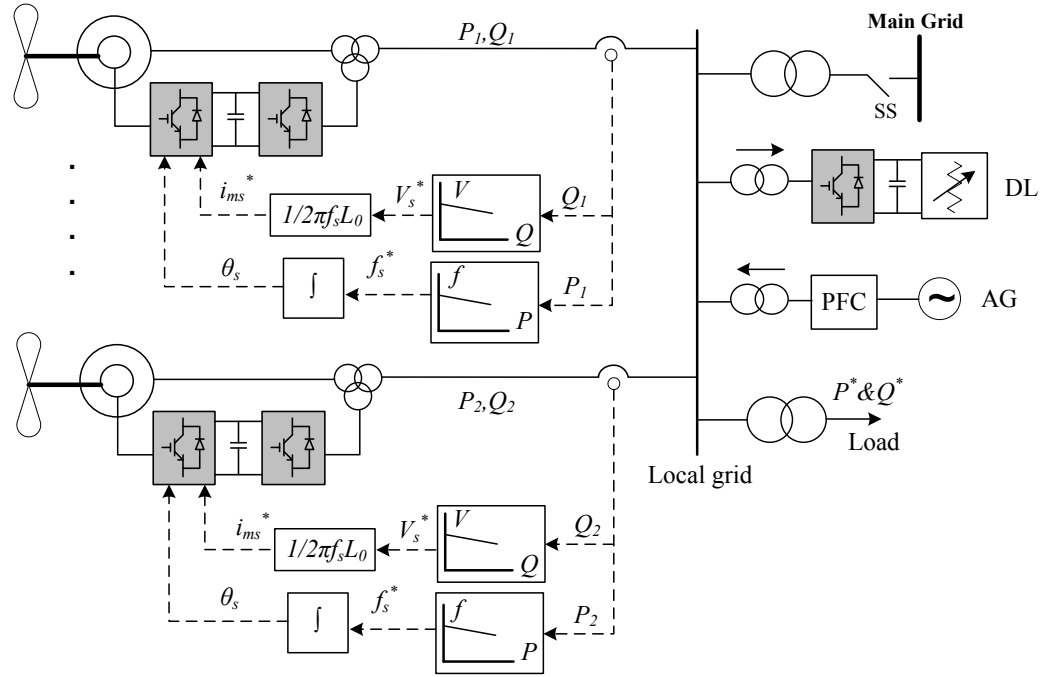
Figure 5.2. ISFO-controlled DFIGs controlling local grid using droop characteristics

If the demand power approaches the average of the extractable wind power $\hat{P}_{ave}$ (Figure 5.3b), ES and/or an AG is required to inject the energy shortfall whenever the demand power is more than $\hat{P}_{ext}$.
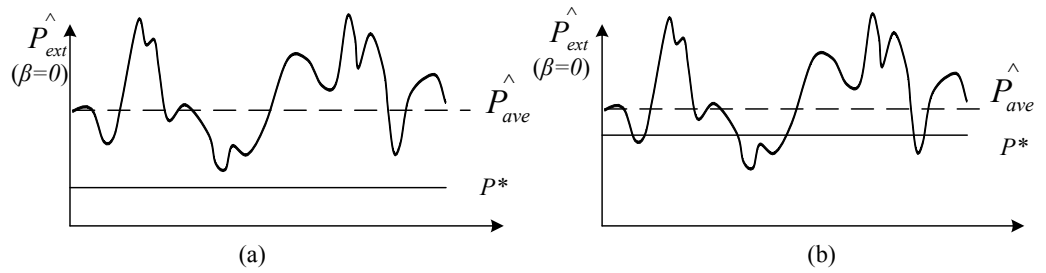
Figure 5.3. Different situations of demand power in respect to extractable wind power $\hat{P}_{ext}$

This chapter considers a system that uses an AG to address the shortfall. The integration of the ES will be introduced in Chapter 6.

5.2 Constant demand power delivery using pitch control

This chapter designs a pitch controller in order to deliver a constant power demanded by load as shown in Figure 5.4. It will be designed for one DFIG and validated with two DFIGs equipped with droop.
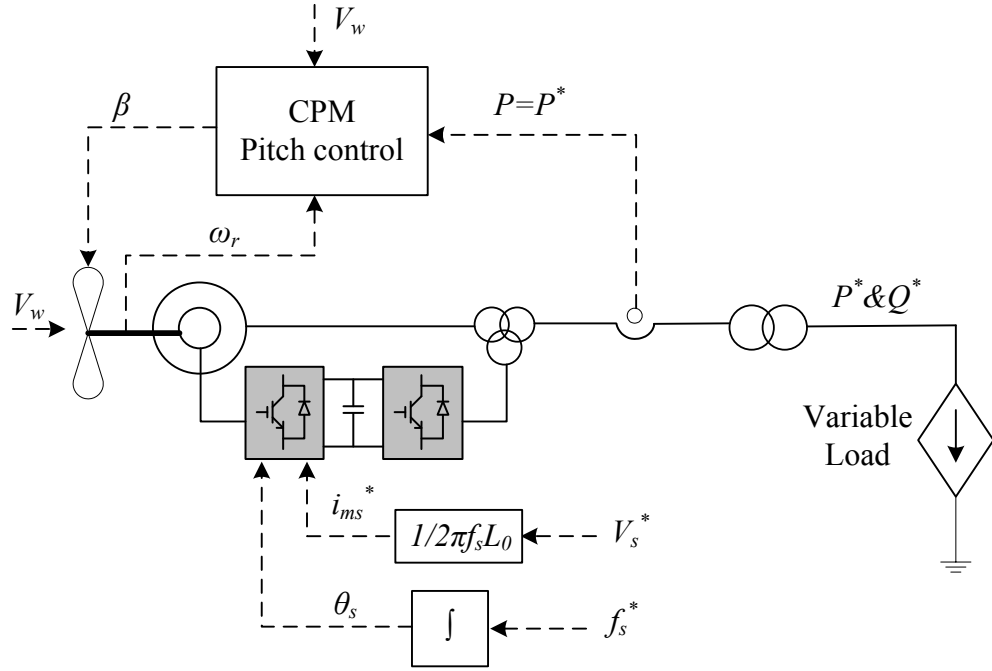
Figure 5.4. Pitch angle control for delivering a constant demand power

It is emphasized again that the method of pitch control alone is only applicable if P^* is less than $\hat{P}_{ext}$ (Figure 5.3a). In [82] a pitch control was designed in order to smooth the output power. The reference power for the pitch controller is derived from the average wind speed calculation. However in this thesis the reference power is imposed by the load.
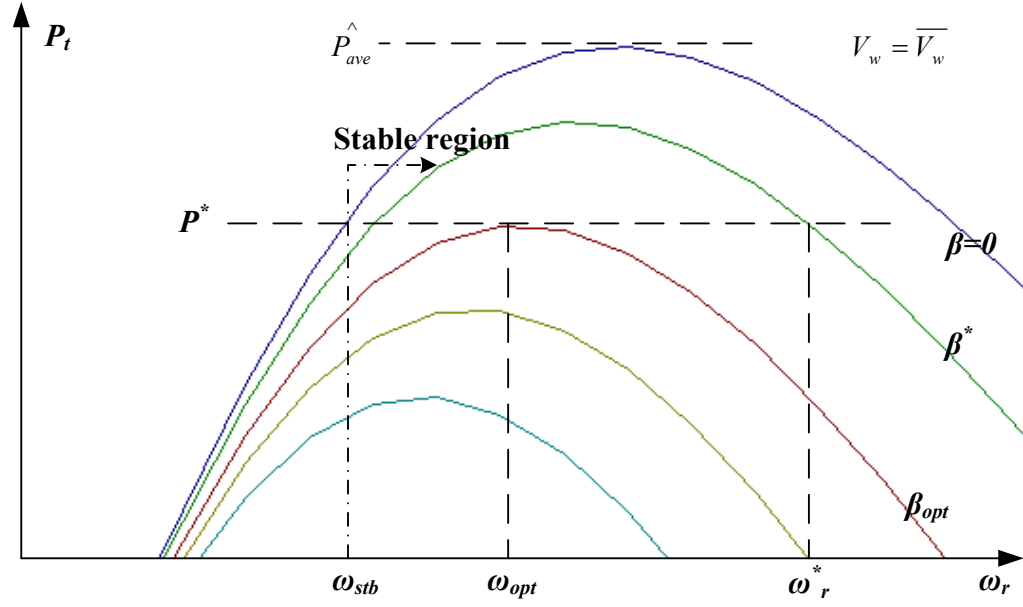
Figure 5.5. P_t-ω_r characteristics for a constant wind speed and different pitch angle

Assuming a constant wind speed, Figure 5.5 illustrates the turbine power vs shaft speed characteristics for different pitch angles. For a given demand power there is only one pitch angle β_{opt} which is tangential with P^*. The shaft speed associated with β_{opt} and P^* is called the optimum shaft speed ω_{opt}. If $P^* = \hat{P}_{ave}$, there is only one option for the reference shaft speed ω_r^* which is its corresponding ω_{opt}. However in practice (i.e. real wind speed) the demand power cannot approach $\hat{P}_{ave}$ unless an ES and/or an AG is used. The control structure using an AG is covered in section 5.3. As Figure 5.5 illustrates, the intersection point of the demand power and the reference shaft speed lines determines the reference pitch angle β^*. The calculation of β^* for a given P^* and ω_r^* is explained later in this section. The choice of the reference shaft speed will be discussed later in this chapter. The minimum stable shaft speed for a given demand power and wind speed is denoted by ω_{stb}.

Since there is no direct torque control mechanism, the electrical torque is imposed by the load, hence the electrical torque effectively is $T_e = P^*/\omega_r$. Therefore the system can be simplified as depicted in Figure 5.6.

86
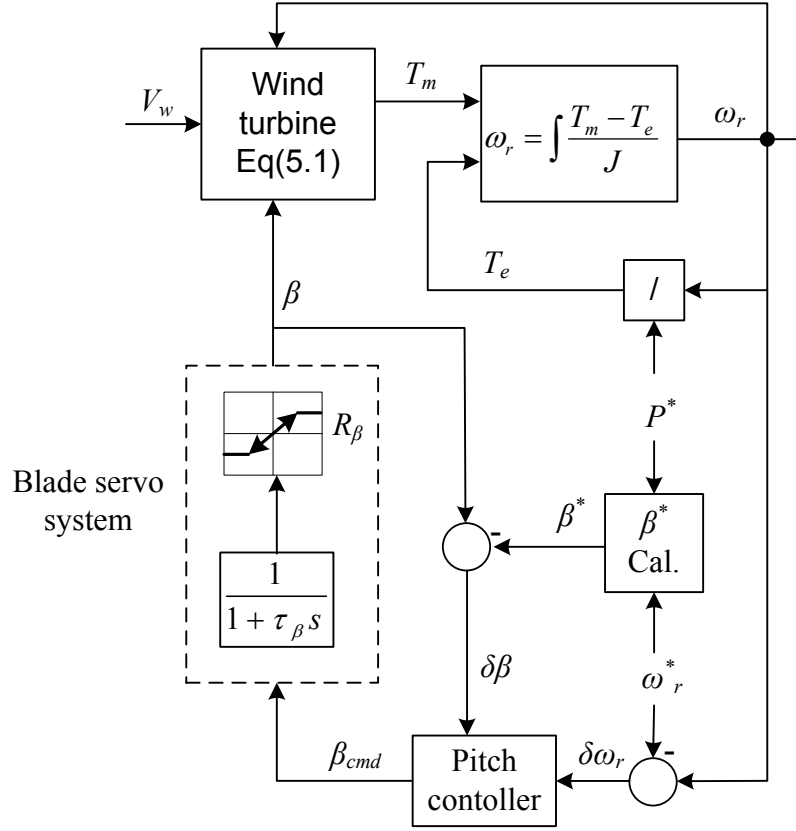
Figure 5.6. Simplified block diagram of system for control purpose

As shown in Figure 5.6, the pitch angle control system consists of three main parts: β^* *calculation*, *pitch controller*, and *servo system*. The β^* calculation unit, as its name suggests, is responsible for calculating the reference pitch angle for a given demand power and reference shaft speed. The Pitch controller is based on the wind turbine linearized model and controls the states of the system to their desired values. The servo system follows the pitch angle command β_{cmd} provided by the pitch controller. The servo system is modelled by a first order lag [82, 83] and a rate limiter in order to make sure that the pitch angle cannot vary faster than the allowed rate R_β. The next two subsections explain the β^* calculation and pitch controller units.

5.2.1 Calculation of the reference pitch angle

In order to calculate the reference pitch angle, a wind turbine model is needed. In this thesis the PSCAD wind turbine model, which was explained in section 2.3.1, is used. The model is described by (5.1):

$$C_p = 0.5\left(\lambda - 0.022\beta^2 - 5.6\right)e^{-0.17\lambda}$$
$$\lambda = \frac{2.237\,NV_w}{\omega_r}$$

(5.1)

where C_p and λ are the power coefficient and tip speed ratio respectively. As Figure 5.5 shows, for $\beta = \beta^*$ and $\omega_r = \omega_r^*$, the turbine power is equal to the demand power:

$$P^* = P_t = 0.5\rho A V_w^3 C_p^* \rightarrow C_p^* = \frac{P^*}{0.5\rho A V_w^3}$$

(5.2)

The C_p^* is called reference power coefficient. Similarly the tip speed ratio corresponding to the reference shaft speed can be called reference tip speed ratio λ^*:

$$\lambda^* = \frac{2.237\,NV_w}{\omega_r^*}$$

(5.3)

Substituting (5.2) and (5.3) into the power coefficient equation given in (5.1) and then simplifying it for β, yields:

$$\beta^* = \sqrt{45.454\left(\lambda^* - 5.6 - \frac{2C_p^*}{e^{-0.17\lambda^*}}\right)}$$

(5.4)

5.2.2 Pitch angle controller

The wind turbine characteristic is nonlinear. In order to design a controller the wind turbine model needs to be linearized. This approach is based on the assumption that small signal stability across the operational envelope results in global stability. Although this is not necessarily true for all nonlinear system, it is normally the case for nonlinear systems without discontinuities. One can linearize (5.1) as:

$$\delta\lambda = \left(\frac{2.237N}{\omega_{r0}}\right)\delta V_w + \left(\frac{-2.237NV_{w0}}{\omega_{r0}^2}\right)\delta\omega_r$$
$$\delta C_p = \left[0.5e^{-0.17\lambda_0}(1.952 - 0.17\lambda_0 + 0.0037\beta_0^2)\right]\delta\lambda + \left(-0.022\beta_0 e^{-.17\lambda_0}\right)\delta\beta$$

(5.5)

where variables with suffix "0" represent the linearization point. The turbine power and turbine torque equations can also be linearized as follows:

$$P_t = 0.5\rho A C_p V_w^3 \rightarrow \delta P_t = \left(1.5\rho A C_{p0}V_{w0}^2\right)\delta V_w + \left(0.5\rho A V_{w0}^3\right)\delta C_p$$
$$T_m = \frac{P_t}{\omega_r} \rightarrow \delta T_m = \left(\frac{1}{\omega_{r0}}\right)\delta P_t + \left(\frac{-P_{t0}}{\omega_{r0}^2}\right)\delta\omega_r$$

(5.6)

Equations (5.5) and (5.6) can be simplified as:

$$\delta\lambda = K_1\delta V_w + K_2\delta\omega_r$$
$$\delta C_p = K_3\delta\lambda + K_4\delta\beta$$
$$\delta P_t = K_5\delta V_w + K_6\delta C_p$$
$$\delta T_m = K_7\delta P_t + K_8\delta\omega_r$$

(5.7)

Equations (5.7) can be further simplified as:

$$\delta T_m = M_1\delta V_w + M_2\delta\omega_r + M_3\delta\beta$$

(5.8)

where $M_1 = (K_7K_5 + K_7K_6K_3K_1)$, $M_2 = (K_7K_6K_3K_2 + K_8)$ and $M_3 = K_7K_6K_4$

Equation (5.8) is the wind turbine linearized model.

As Figure 5.6 shows, the system is second order. There are two states variables which are the pitch angle and the shaft speed. Assuming that around the operating point the change of the pitch angle is less than R_β, the rate limiter can be neglected. Therefore the blade differential equation would be:

$$\frac{\beta}{\beta_{cmd}} = \frac{1}{\tau_\beta s + 1} \rightarrow \dot{\beta} = \frac{\beta_{cmd}}{\tau_\beta} - \frac{\beta}{\tau_\beta} \tag{5.9}$$

The second differential equation is:

$$\dot{\omega}_r = \frac{1}{J}(T_m - T_e) \xrightarrow{T_e = P^*/\omega} \dot{\omega}_r = \frac{1}{J}\left(T_m - \frac{P^*}{\omega_r}\right) \tag{5.10}$$

Equation (5.10) can be linearized as:

$$\delta\dot{\omega}_r = \frac{1}{J}\delta T_m - \frac{1}{J}\left(\frac{1}{\omega_{r0}}\delta P^* - \frac{P^*}{\omega_{r0}^2}\delta\omega_r\right) \tag{5.11}$$

Substituting (5.8) into (5.11) and simplifying that, gives:

$$\delta\dot{\omega}_r = \frac{M_1}{J}\delta V_w + \left(\frac{M_2}{J} + \frac{P^*}{J\omega_{r0}^2}\right)\delta\omega_r + M_3\delta\beta - \frac{1}{J\omega_{r0}}\delta P^* \tag{5.12}$$

Using (5.9) and (5.12), one can write the space state equations as:

$$\delta\dot{\mathbf{x}} = \mathbf{A}_0\delta\mathbf{x} + \mathbf{B}_0\delta\mathbf{u}$$
$$\delta\mathbf{y} = \mathbf{C}_0\delta\mathbf{x} + \mathbf{D}_0\delta\mathbf{u} \tag{5.13}$$

Where the state variables and input variables are respectively:

$$\delta\mathbf{x} = \begin{bmatrix} \delta\beta \\ \delta\omega_r \end{bmatrix}, \delta\mathbf{u} = \begin{bmatrix} \delta\beta_{cmd} \\ \delta P^* \\ \delta V_w \\ \delta\omega_r^* \end{bmatrix} \tag{5.14}$$

The state matrix $\mathbf{A}_0$ and the input matrix $\mathbf{B}_0$ are respectively:

$$\mathbf{A_0} = \begin{bmatrix} \dfrac{-1}{\tau_\beta} & 0 \\[2ex] \dfrac{M_3}{J} & \left(\dfrac{M_2}{J} + \dfrac{P^*}{J\omega_0^2} \right) \end{bmatrix}$$

$$\mathbf{B_0} = \begin{bmatrix} \dfrac{1}{\tau_\beta} & 0 & 0 & 0 \\[2ex] 0 & \dfrac{-1}{J\omega_0} & \dfrac{M_1}{J} & 0 \end{bmatrix}$$

(5.15)

By choosing shaft speed as output, the output matrix $\mathbf{C_0}$ and the direct transmission matrix $\mathbf{D_0}$ would be:

$$\mathbf{C_0} = \begin{bmatrix} 0 & 1 \end{bmatrix}, \ \mathbf{D_0} = \begin{bmatrix} 0 & 0 & 0 & 0 \end{bmatrix}$$

(5.16)

The control and reference inputs are $\delta\beta_{cmd}$ and $\delta\omega^*$, respectively. The demand power δP^* and wind speed δV_w are disturbances and therefore are not included in the control law given by:

$$\mu = -\mathbf{K_f} \begin{bmatrix} \delta\beta \\ \delta\omega_r \end{bmatrix}$$

(5.17)

The state feedback matrix is $\mathbf{K_f} = \begin{bmatrix} K_{f1} & K_{f2} \end{bmatrix}$ and is designed to place the system closed loop poles at their desired place. Figure 5.7 shows the *pitch angle controller* (of Figure 5.6) using the control law given in (5.17).
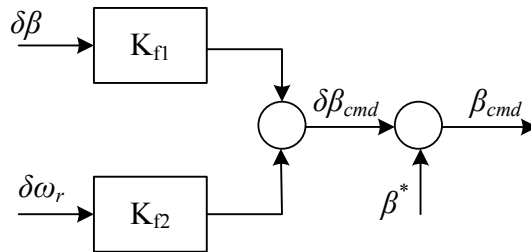

Figure 5.7. Pitch angle controller

In Figure 5.7, K_{f1} and K_{f2} are the sate feedback gains which are determined in order to place the system closed loop poles at their desired locations. Since all the states variables are measurable, there is no need for an observer. The necessary and sufficient condition that the closed loop poles can be placed at any arbitrary locations in the s plane is that the system be completely state controllable [84]. Generally a system described by $\dot{\mathbf{x}} = \mathbf{Ax} + \mathbf{Bu}$ where $\mathbf{A}$ is an $n \times n$ matrix and $\mathbf{u}$ is an r-vector, is completely state controllable if the $n \times nr$ controllability matrix $\left[\mathbf{B} \vdots \mathbf{AB} \vdots ... \vdots \mathbf{A}^{n-1}\mathbf{B} \right]$ is of rank n, (i.e. contain n linearly independent column vectors) [84]. In this case the 2×8 controllability matrix is of rank 2 which means that it is state controllable.

The system open loop poles, which are the eigenvalues of the matrix $\mathbf{A_0}$, may change for different linearization points. For this study it is felt sufficient to derive a single control law that will give acceptable performance for all the linearization points (the alternative approach would be to have a gain-scheduling procedure). Prior to choosing the desired closed loop pole, the worst-case linearization point is determined. Therefore, first the variations of the system eigenvalues for the different linearization points are studied in order to find the worst case for linearization.

There are two open loop poles: one is associated with the pitch angle and is always at $-1/\tau_\beta$ and the other is associated with the shaft speed and varies with the linearization points. So the first eigenvalue is always stable. The linearization point is defined by P_0, V_{w0}, and ω_{r0}. Figure 5.8 shows the movement of the open loop poles when P_0 increases from 0.2 to 1pu (in four steps), V_{w0}=13m/sec, ω_{r0}=1.1pu, and τ_β=1. It can be seen that as power increases the system tends towards instability and the system is unstable for power more than approximately 0.75pu. It is noted that even for P_0=1pu, the pitch angle $\beta_0 \approx 4°$ (using (5.4)) which implies that the closed loop system can be stable using a proper control design. In other words, all these linearization points are within the stable region shown in Figure 5.5. For unstable region ($\omega_r < \omega_{stb}$), pitch angle control cannot be used to stabilize the system since that region corresponds to Figure 5.3b i.e. when the extractable wind power is less than the demand power.
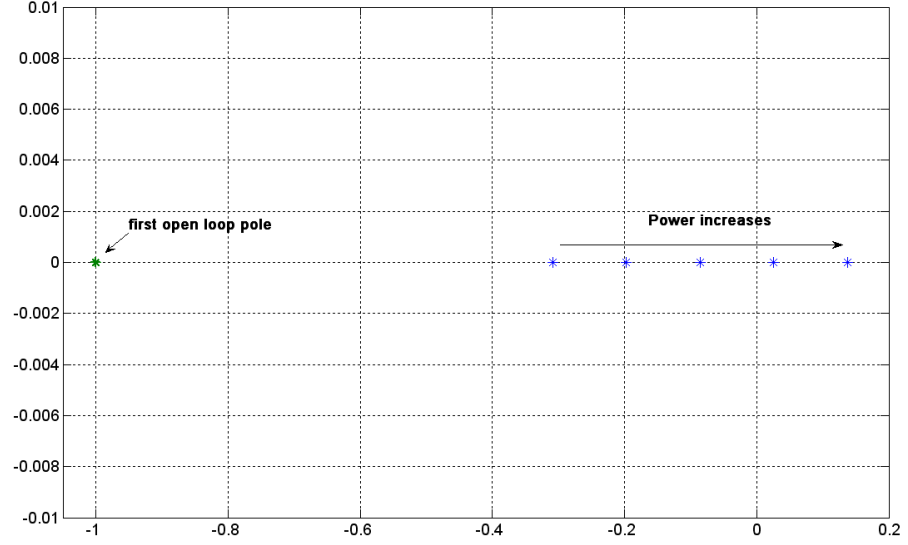
Figure 5.8. Movement of system open loop poles for variation of P_0 from 0.2 to 1pu while V_{w0}=13m/s, ω_{r0}=1.1pu and τ_β=1

Figure 5.9 shows the open loop poles movements when V_{w0} varies from 10 to 16m/sec, P_0=0.5pu, ω_{r0}=1pu, and τ_β=1.
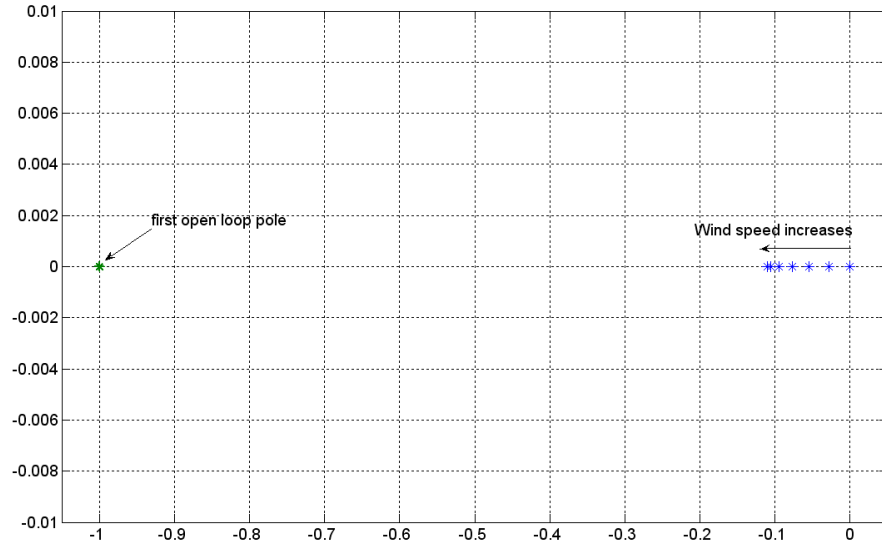
Figure 5.9. Movement of system open loop poles for variation of V_{w0} from 10 to 16m/sec while P_0=0.5pu, ω_{r0}=1pu and τ_β=1

Figure 5.9 illustrates that as the wind speed decreases the second eigenvalue moves toward instability. Again, closed loop control can address this provided that the extractable wind power is not less than the demand power.
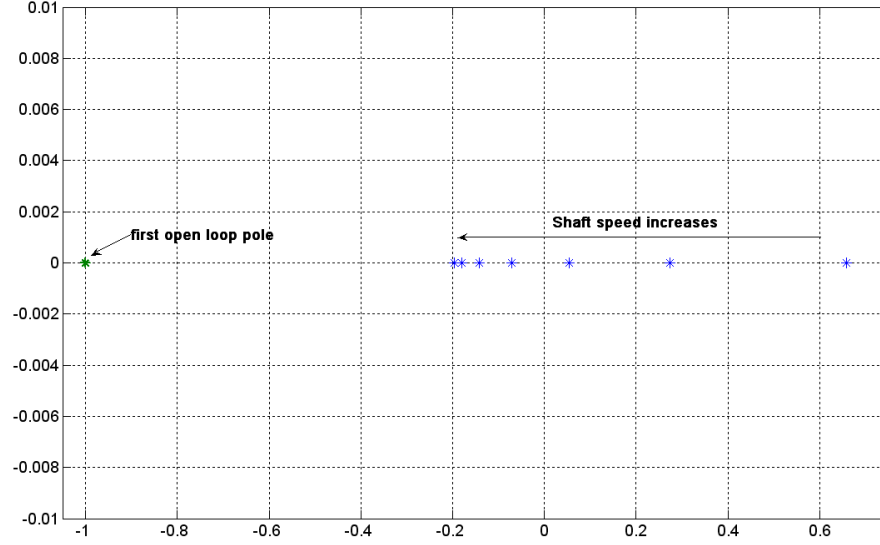
Figure 5.10. Movement of system open loop poles for variation of ω_{r0} from 0.7 to 1.3pu while P_0=0.5pu, V_{w0}=12.5m/sec and τ_β=1

Finally the movements of the open loop eigenvalues when ω_{r0} changes from 0.7 to 1.3pu (in 6 steps), P_0=0.5pu, V_{w0}=12.5m/sec and τ_β=1 is shown in Figure 5.10. As can be seen, the second open loop pole is unstable for shaft speed less than approximately 0.95pu.

Figures 5.8, 5.9 and 5.10 demonstrate that as P_0 increases and V_{w0} and ω_{r0} decrease, the system tends toward instability. Therefore one can set the linearization point as: P_0=1pu, ω_{r0}=1.2pu, V_{w0}=12.5m/sec and hence β_0=1.6°. At this point since $P_0 \approx \hat{P}_{ave}$, $\omega_{r0} \approx \omega_{opt}$ and the pitch angle is small. Therefore this point can be considered as the worst case. It is emphasized again that all the linearization points considered above are within the stable region of Figure 5.5. Therefore the closed loop pitch angle control can make them stable. The points outside the stable region (shown in Figure 5.5) correspond to the case when the demand power is more than $\hat{P}_{ext}$ which will be addressed in Section 5.3 using an AG. Knowing the linearization point, the desired closed loop pole can be determined and hence the proper state feedback gains can be found. The state feedback gains, of course, vary for DFIGs with different ratings. In the next subsection two DFIGs with different ratings are considered.

The state feedback gains are determined according to the desired closed loop poles. As a general rule, the system response becomes faster as the dominant closed loop poles are placed further from the $j\omega$ axis. It is noted that a high-speed response requires large amount of control energy which means that heavier actuator is needed. There are a number of methods for finding proper K_{f1} and K_{f2} including, the pole-placement and the quadratic optimal regulator methods. The latter has the advantage of determining the desired closed loop poles such that it balance the acceptable response and the amount of the control energy required [84]. However, in this case the pitch angle variation is rate limited. It will be shown that it never varies faster than 5°/sec, which is a decent maximum rate of change for the blades. This implies that the required control energy is acceptable. Therefore in this research the pole-placement method is used.

The next subsection demonstrates the control structure using PSCAD simulations.

5.2.3 Simulation results of constant demand power delivery using pitch angle control

This section consists of three parts. The first part validates the proposed pitch angle controller using one ISFO- controlled DFIG and constant wind speed. The second simulation considers another ISFO-controlled DFIG with a different rating, but this time with real wind speed profile. The third part simulates the two DFIGs (of the two previous simulations) equipped with droops and the pitch control scheme explained above while real wind speed profiles are applied.

Simulation 1:

This section considers one ISFO-controlled DFIG connected to a variable load as shown in Figure 5.4. The voltage and frequency is controlled by the DFIG. The DFIG1 with parameters provided in Appendix B is simulated in this section. The objective of this simulation is to validate the proposed control structure. Therefore constant wind speeds are used in order to be able to cover a wider range of cases.

t	0-5s	5-12s	12-20s	20-28s	28-36s	36-46s	46-57s	57-75s
V_w, m/s	10	**12**	12	12	**14**	14	14	**12.5**
P^*, pu	0.4	0.4	0.4	**0.6**	0.6	0.6	**1**	1
ω_{ref}, pu	0.8	0.8	**1**	1	1	**1.2**	1.2	1.2

Table 5.1. Sequence of events of the simulation shown in Figure 5.11

Using the linearization point explained above (i.e. P_0=1pu, ω_{r0}=1.2pu, V_{w0}=12.5m/sec) and setting τ_β=1 [82, 83], the open loop poles are -1 and 0.047. The desired closed loop poles should be determined such that they assure a well-damped response without hitting the maximum slew rate which is R_β=3°/sec. Trial and error shows that setting the closed loop poles at -0.15 and -1.5 gives a reasonably fast and well-damped response. Therefore state feedback gains K_{f1} and K_{f2} are set respectively at 0.65 and -0.88 using MATLAB pole-placement command. Table 5.1 explains the sequence of events of the simulation results shown in Figure 5.11. In each column, the bolded number represents the parameter which has been changed compared to the previous period. It can be seen that a very wide range of different possible situations has been simulated. In each situation the pitch angle (Figure 5.11c) is adjusted in order to control the shaft speed (Figure 5.11.d), hence maintaining the demand power (Figure 5.11b). The transient fluctuations in the pitch angle, which is still less than 3°/sec, are due to the step changes in the wind speed and reference shaft speed. In the case of the demand power (Figure 5.11b) changes (at 20s and 46s), a first order filter with time constant of τ=0.5 is introduced to reduce the rate of the change in power demand. This results in smoother pitch angle variations. Obviously in practice, step changes in wind speed and shaft speed are not possible. The last part of the simulation (57-75s) corresponds to the linearization point (i.e. P^*=1pu, V_w=12.5m/sec and ω_r=1.2pu). It can be seen that the pitch angle is < 2° which means that the demand power is almost equal to the extractable wind power.
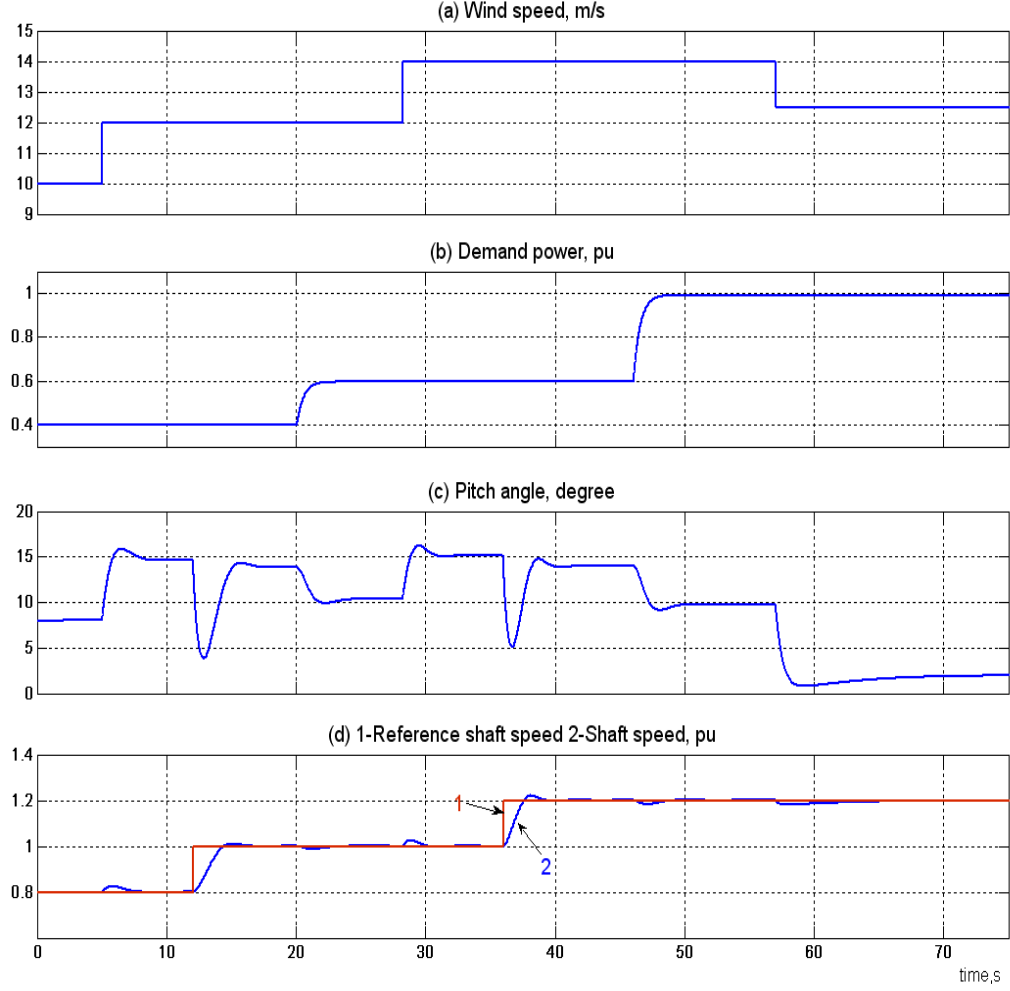
Figure 5.11. Validation of the pitch control for constant power delivery

In a case with real wind profile, however, it is not possible to approach this close to $\hat{P}_{ave}$ unless using ES and/or an external energy source. This is shown in the next simulation results.

Simulation 2

The model simulated in this section is shown in Figure 5.4 but this time a real wind profile is considered. In this part the DFIG2 with parameters given in Appendix B is used. The different rating (compared to the previous simulation) results in different state feedback gains for the same linearization point. The linearization point is again $P_0=1$pu, $\omega_{r0}=1.2$pu, and $V_{w0}=12.5$m/sec. Setting the

desired closed loop poles at -1.5 and -0.15 leads to the state feedback gains K_{f1} and K_{f2} equal to 0.65 and -0.59, respectively. The reference shaft speed is 1.1pu (the choice of which will be discussed later in this chapter). The maximum pitch angle slew rate is R_β=3º/sec. The PSCAD simulation results are given in Figure 5.12.
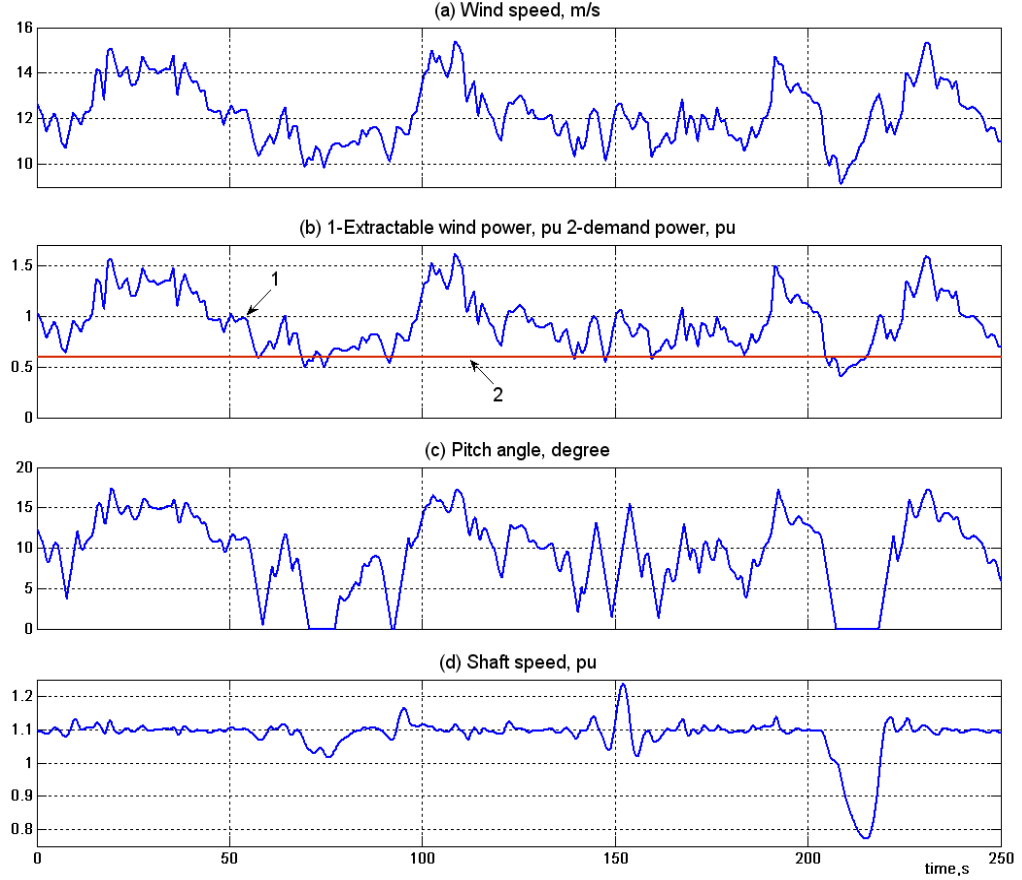
Figure 5.12. One ISFO-controlled DFIG delivering a constant demand power while real wind speed is applied and the demand power approaching the average of the extractable wind power

The wind speed profile (Figure 5.12a) is a real (measured) wind speed with average of approximately 12.5m/s ($\hat{P}_{ave} \approx$ 1pu) and standard deviation of 1.39 (which is relatively large perturbation). The extractable wind power $\hat{P}_{ext}$ (i.e. with β=0) is shown in Figure 5.12b1. The demand power (Figure 5.12b2) is 0.6pu and it can be seen that $\hat{P}_{ext}$ is occasionally less than the demand power. Whenever the demand power is more than $\hat{P}_{ext}$, the pitch angle (Figure 5.12c) becomes zero;

hence the shaft speed control is lost. Therefore, the shaft speed (Figure 5.12d) reduces in order to compensate for the energy shortage. Although in this simulation the shaft speed recovers as the wind speed increases, this is not a secure operation since failure will occur if the shaft speed keeps dropping. This case will be addressed in section 5.3. It can be seen that in normal operation (demand power less than $\hat{P}_{ext}$), the pitch angle variation barely hits the 3°/sec while the shaft speed is very well controlled.

Simulation 3

This part simulates the two ISFO-controlled DFIGs of the two previous simulations as shown in Figure 5.13. The wind farm supplies a variable load and controls the voltage and frequency of the local grid using the droop characteristics explained in the previous chapter.
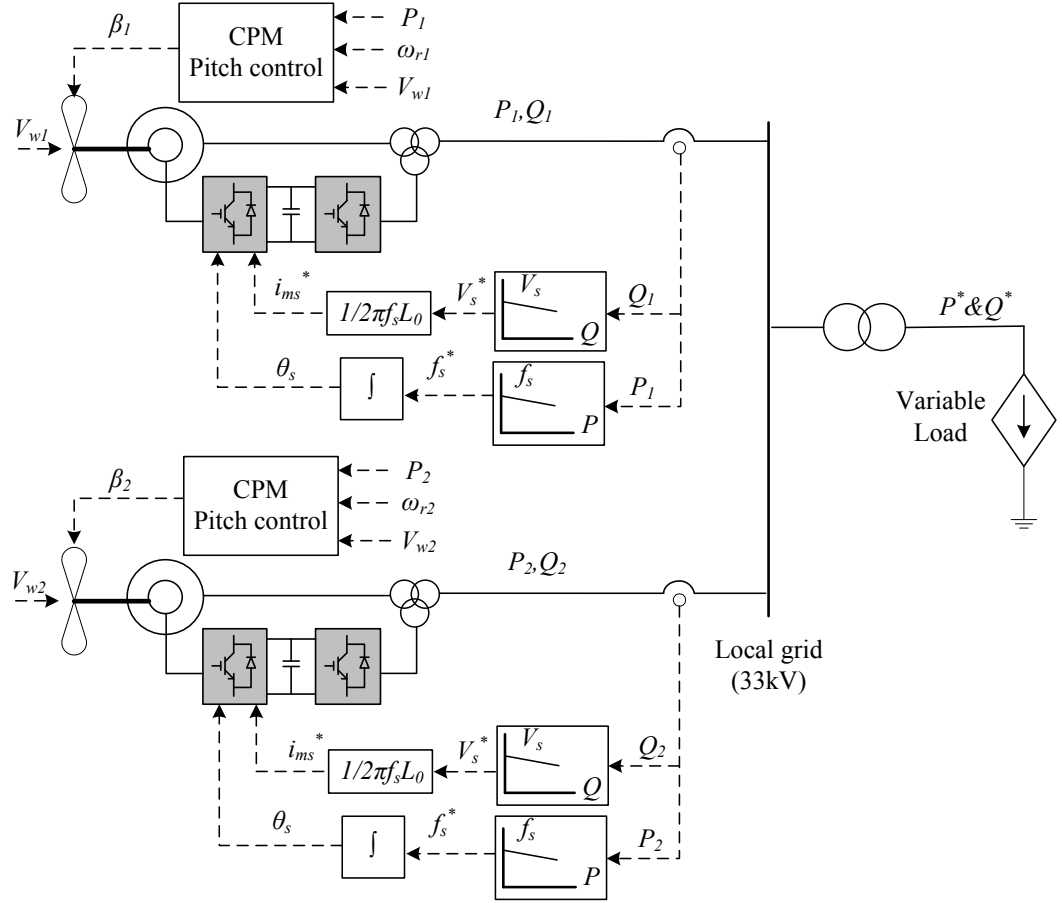
Figure 5.13. Droop-controlled DFIGs operating in CPM

The objective the simulation is to validate the proposed pitch control while the DFIGs are under droop control and real wind speed profiles are applied. The droop coefficients are given in Table 5.2:

	Rating, pu	m, Hz/pu	n, kV/pu
DFIG 1	0.66	0.151	0.0757
DFIG 2	0.34	0.294	0.147

Table 5.2 Droop characteristics coefficient of DFIGs

The DFIGs share a variable load which is simulated by a variable current source. The rating of the first DFIG is 0.66pu and that of the second one is 0.34pu. The pitch controllers of the DFIGs were explained in the two previous simulations. The simulation results are given in Figure 5.14. The average of the two real wind speed

profiles (Figure 5.14a) is approximately 12.5m/s which correspond to $\hat{P}_{ave} \approx 1\text{pu}_{gen}$. The standard deviations of the first and the second wind profiles are, respectively, 1.28 and 1.39 which are relatively large perturbations. Appendix E explains how the characteristics of the wind speed profiles can vary. Figure 5.14b shows the active power sharing when the demand power is P^*=0.1, 0.3, and 0.5pu (total wind farm pu). It can be seen that the power demanded by the load is shared proportional to the rating of DFIGs while the local grid frequency (Figure 5.14f2) is very well regulated at approximately 50Hz. The first DFIG pitch angle (Figure 5.14e1) never hits the maximum slew rate of 3°/sec and this is why its shaft speed (Figure 5.14d1) is very well controlled. When the demand power is 0.5pu, however, the pitch angle of the second DFIG (Figure 5.14e2) becomes occasionally almost zero. This implies that the power generated from the second DFIG becomes very close to (or even slightly more than) its associated $\hat{P}_{ext}$. This causes the pitch angle to hit the 3°/sec limit which in turns causes the large shaft speed variation. Although the shaft speed is still within the acceptable boundary for DFIGs, it suggests that the demand power cannot increase anymore unless an external ES and/or energy source is introduced. This is the subject of the next section. Figure 5.14c shows that the reactive power demanded by the load (Q^*=0.15pu) is shared by the DFIGs in proportion to their ratings while the local grid voltage is very well controlled around 33kV.
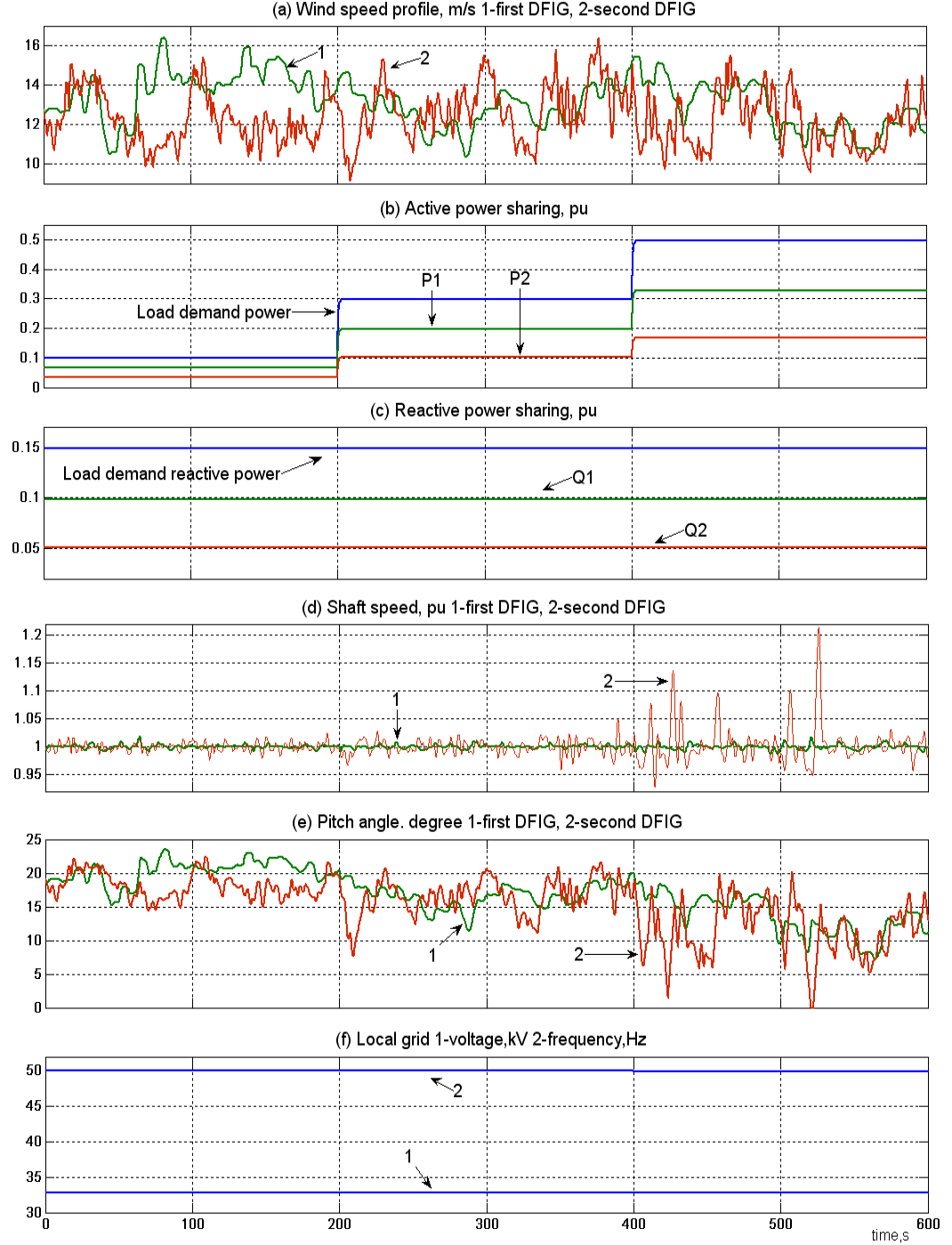
Figure 5.14. Results of two droop-controlled DFIG operating in CPM and supplying a variable load

The next section proposes an Energy Management System (EMS) in order to control the shaft speed of the DFIGs. In section 5.3.2, the droop method will be adjusted in order to take the available wind power into account, in addition to the rating of the DFIGs.

5.3 Constant demand power delivery using external energy source

5.3.1 Energy Management System (EMS)

It was shown in the previous section (Figure 5.12) that when the demand power becomes more than $\hat{P}_{ext}$, the kinetic energy stored in the shaft inertia compensates for the lack of the energy which obviously causes reduction in the shaft speed. If the shaft speed decreases below ω_{stb} (Figure 5.5), the system will become unstable. Therefore this situation must be avoided. Figure 5.15 proposes an EMS in order to maintain the shaft speed within the stable region.
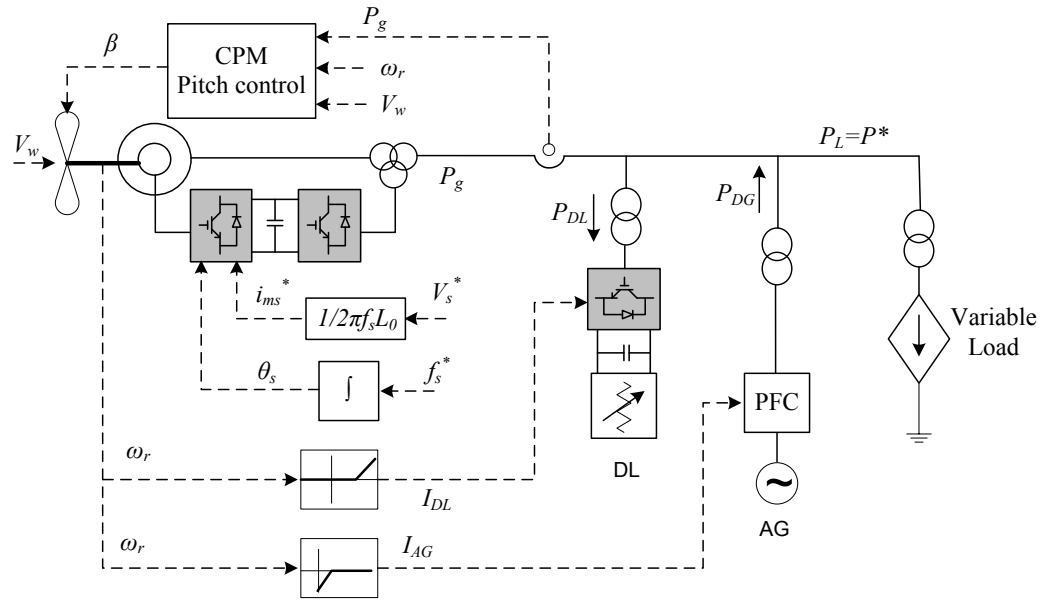
Figure 5.15. EMS for an ISFO-controlled DFIG operating under CPM

As Figure 5.15 illustrates, if the shaft speed drops below a "low-threshold", a current demand I_{AG} is sent to the Power Flow Controller (PFC) of the AG. The PFC is a converter which controls the power demanded from the AG. Hence I_{AG} can be considered to be the real or d-axis component of the converter current in phase with the local grid voltage. Assuming that the voltage is well-regulated by the DFIG, I_{AG} is equivalent to the instantaneous AG power P_{AG}. Therefore, the AG supplies the energy shortfall between the wind generated power P_g and the demand

power P^*. Hence the shaft speed will recover. In another situation the demand power might be low while the wind power is high. This may cause the shaft speed to increase more than the DFIG maximum limit (i.e. 1.3pu which was discussed in Chapter 2), thus the wind power needs to be shed. The wind power can be shed either by the pitch control or a "Dispatchable Load" (DL). A trade-off mechanism is possible in which a slow pitch control (or none) results in a higher DL rating, whilst a normal pitch control slew rate (3-5º/sec) may results in the DL being unnecessary. Assuming that the pitch control is not fast enough to prevent the shaft speed from exceeding its maximum limit, a DL would be required. If the shaft speed hits a "high-threshold", the DL is turned on via a converter (real) current demand I_{DL} which absorbs the excess wind generation. This chapter deals with the cases in which the pitch angle is fast enough to prevent the shaft speed from exceeding 1.3pu. It is noted that in the standard DFIG control, also, the pitch angle is used to control the shaft speed for the wind speeds above rated.

Now the shaft speed high- and low-thresholds must be chosen. The high-threshold must be chosen as (1.3-ε)pu, for example 1.25pu. The closeness of the high-threshold value to 1.3pu depends on the dynamics of the DL and the pitch control. For choosing the low-threshold, two scenarios can be considered based on whether the ω_{stb} is less than the DFIG minimum shaft speed limit (i.e. 0.7pu) or not. If $\omega_{stb}<0.7$, the low-threshold must be chosen at (0.7+ε)pu. The second case is when $0.7< \omega_{threshold} < \omega_{stb}$. In such a case, when the shaft speed becomes less than ω_{stb}, the system becomes unstable which causes further reduction in shaft speed. As a result, the shaft speed drops below $\omega_{threshold}$, hence, the AG is turned on and injects the shortage of energy in order to recover the shaft speed. This will be shown in the simulation carried out in the next subsection. This control structure is, therefore, a "self-recovery" system and the low-threshold value can be even less than ω_{stb} (this will be shown by simulation). Thus, the low-threshold value can always be chosen at (0.7+ε)pu. The closeness of the low-threshold to 0.7 depends on the dynamics of the AG. The study of the dynamic of the AG is beyond the scope of this thesis. In this chapter the low-threshold is set at 0.85pu, however, closer values are also possible which require larger gains, hence faster response

from the AG. This thesis is only intended to validate the proposed control scheme and a detailed engineering design is beyond the scope of the research.

5.3.1.1 Simulation results of EMS for constant demand power delivery

This section undertakes two simulations: the first validates the proposed EMS for one DFIG while the second one simulates two DFIGs with the EMS. In this research the shaft speed low threshold is set at 0.85pu. In the both simulations for $\omega_r<0.85$pu, $I_{AG}{}^*=$-Kω_r (K=-150). The communication delay between the EMS and the AG is neglected. It is noted that if there is a delay in the power transfer of the AG, it may be necessary to increase the low-threshold value of the shaft speed or increase the gain K to compensate for the delay.

Simulation 1:

The model simulated in this part is shown in Figure 5.15. The DFIG1 with parameter given in Appendix B is simulated in this chapter. The pitch controller is the same as before with the maximum slew rate of 3°/sec. The AG is simulated by a DC-voltage source connected to a converter (PFC) which controls the power demanded form the DC-voltage source. The objective of this simulation is to validate the proposed EMS. The simulation results are shown in Figure 5.16. The average and the standard deviation of the real wind speed (Figure 5.16a) are 12.5m/s and 1.28, respectively. The results can be divided into four parts which are specified by capital letters A, B, C and D on Figure 5.16b. Over part A the demand power (Figure 5.16b1) is 1pu while the wind speed is above the rated (12.5m/sec). Therefore the pitch angle (Figure 5.16e) controller is able to control the shaft speed (Figure 5.16d) and no power from the AG (Figure 5.16c) is needed.
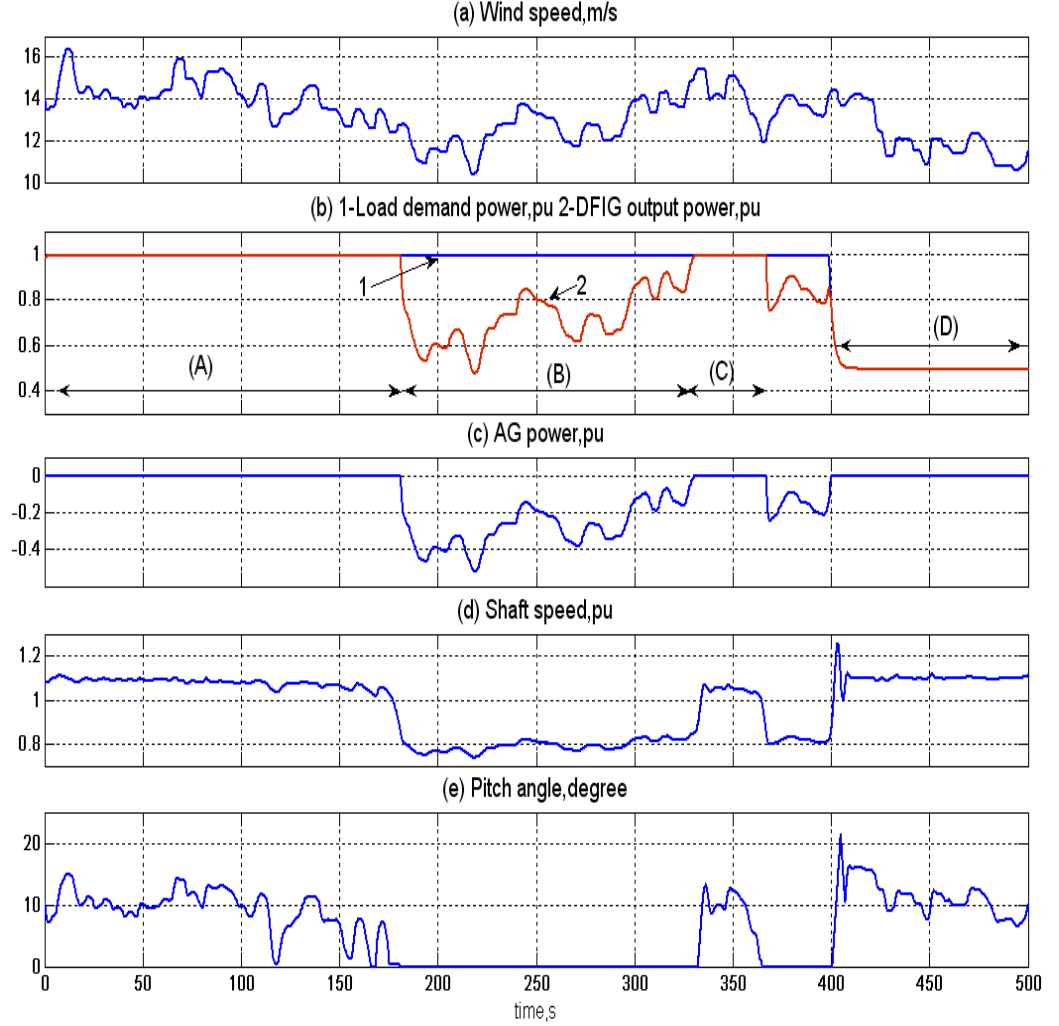
Figure 5.16. Results of the EMS for a hybrid wind generator and AG system

Then over part B the wind speed drops below rated while the load demand power is still 1pu. The pitch angle becomes zero in order to extract the maximum wind power which is still less than the 1pu demand. Thus the shaft speed reduces to compensate for the lack of the energy. It can be seen that just after part B starts the wind speed varies from approximately 10.5-13.5m/s. Figure 5.17 shows the mechanical torque vs shaft speed characteristic of the wind turbine for wind variation from 10.5-13.5m/s. Figure 5.17 also depicts the electrical torque of the DFIG over parts A and B. It can be seen that over part A the electrical torque is under CPM and since the wind speed is always more than the rated wind speed (12.5m/s), the system is stable. The wind speed reduction during part B causes the

shaft speed to decrease. Even assuming that the wind speed is 13.5m/s, ω_{stb} is around 0.95pu which is more than the low-threshold of shaft speed (0.85pu).
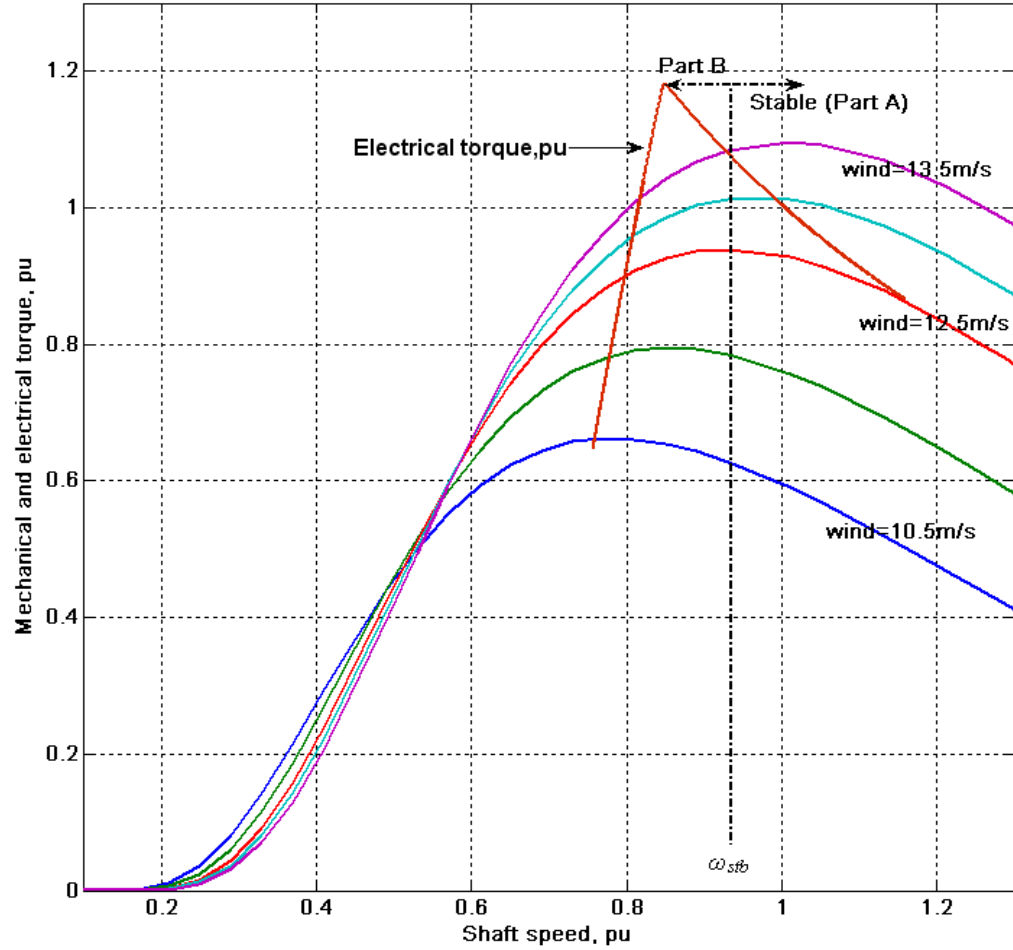
Figure 5.17. The electrical torque associated with parts A and B of the simulation results shown in Figure 5.16 on the T_m vs ω_r characteristics of the wind turbine for different wind speed

However as the shaft speed drops below 0.85pu, the AG is turned on and injects the energy shortfall in order to prevent the shaft speed from further reduction and maintain the demand power. Since the DFIG output power (Figure 5.16b2) is no longer 1pu, and varying according to the available wind power, the stability issue is no longer a concern. Figure 5.17 demonstrates that the system becomes temporary unstable but will recover automatically. Over part C the wind speed increases above the rated wind speed. As a result, the shaft speed becomes more than 0.85 and the AG is switched off. Thus, the DFIG supplies once again the total 1pu power demanded by the load. In part D the demand power drops down to

0.5pu. It can be seen that the shaft speed increases, the AG is turned off and the total demand is supplied by the DFIG. The pitch angle transiently hits the 3°/sec slew rate limit which in turn causes the shaft speed spike. However this is due to the fact that the demand power reduces by 0.5pu in one step which is impractical. Parts C and D demonstrate the ability of the proposed control scheme to enable the DFIG to take over the total supply of the demand power due to an increase in the wind power or a reduction in the demand. The reference shaft speed in this simulation is 1.1pu.

If the wind speed was constant (like Figure 5.11) the choice of the reference shaft speed would be very important. However in practice, the wind speed is fluctuating. Therefore two scenarios can be defined. First scenario is when $\hat{P}_{ext}$ is more than P^* (parts A, C and D). Such cases imply that the 0.7-1.3pu is partially or fully within the stable region. Obviously, the larger the shaft speed reference, the larger the energy stored in rotor inertia which can be used later if either wind speed reduces or the demand increases. However, too large shaft speed reference required relatively faster pitch angle to keep the shaft speed away from the maximum limit. Thus, choosing the reference shaft speed from 1.0-1.1pu is the best as a compromise between stored inertial energy and pitch control. When the P^* is more than $\hat{P}_{ext}$ (part B), the shaft speed drops; regardless of the reference shaft speed. The simulation results demonstrate that the system is automatically able to recover from possible instability. So the choice of the reference shaft speed is not important and in this chapter is always set at 1.1pu.

Simulation 2

The objective of this simulation is to demonstrate the proposed EMS for a multi-DFIG system. The model simulated in this section, which is shown in Figure 5.18, consists of two droop-controlled DFIGs equipped with the EMS and the CPM pitch controller explained above. Again the ratings of the DFIGs are 0.66pu and 0.34pu with the droop coefficients given in Table 5.2. As can be seen from Figure 5.18, the AG and the DL are aggregated on the local grid, the voltage and

frequency of which are controlled by the DFIGs. Each DFIG has its own EMS which produces I_{AG} and I_{DL}. Therefore the summations $\sum I_{DL}$ and $\sum I_{AG}$ are formed and communicated over communication links to the AG and the DL. In this section only two DFIGs are simulated, however, the concept is applicable to more DFIGs. (Section 5.4 simulates four DFIGs using a "reduced model"). The DL and the AG are simulated by DC-voltage sources buffered from the local grid by a VSC converter. The converters control the current from/to AG/DL. It will be shown in later chapters that the DL can also be distributed within individual wind generators, if required. In such case, obviously, no communication is needed for the DL.
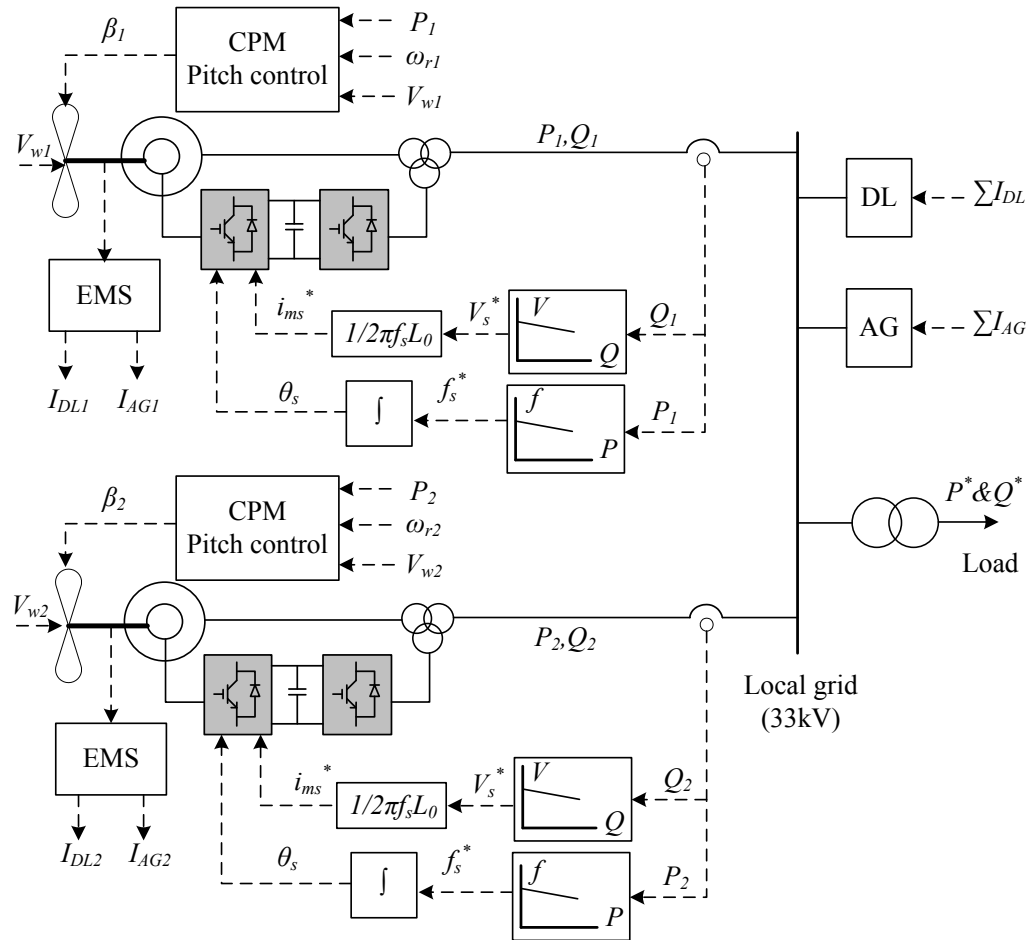
Figure 5.18. EMS for droop-controlled DFIGs

The results are shown in Figure 5.19. The average of the two real wind speed profiles (Figure 5.19a) are about 12.5m/sec which corresponds to $1pu_{gen}$. The

standard deviations of the first and the second wind profiles are, respectively, 1.28 and 1.39 which are relatively large perturbations. Figure 5.19b shows the active power sharing when the demand power is 0.5, 0.75 and 1pu. For the first 200sec, the demand power is 0.5pu which is less than $\hat{P}_{ext}$, hence the pitch angles (Figure 5.19e) control the shaft speeds (Figure 5.19d) and no power is demanded from the AG (Figure 5.19c). The output power of each DFIG is constant and proportional to its rating. During 200-400sec, the demand power is 0.75pu and it can be seen that the shaft speeds occasionally drop below 0.85pu$_{gen}$ as the power demanded from either of the DFIG becomes more than the associated extractable wind power. When either of the shaft speed drops below 0.85pu the AG is turned on and injects the energy shortfall in order to maintain the demand power and prevent the shaft speed from further reduction. As Figure 5.19b shows whenever the demand power is available, the AG is switched off and the demand is shared by the DFIGs in proportion to their ratings. Over the last 200sec, the demand power is increased to 1pu. As it can be seen P^* is more than $\hat{P}_{ext}$ for almost the entire period. Therefore the AG compensates for the shortage of energy. Figure 5.19h shows that the local grid frequency is very well regulated by the DFIGs using droop characteristics. Figure 5.19f shows that the reactive power demanded by the load (0.15pu) is shared by the DFIGs according to their ratings while the local grid voltage (Figure 5.19g) is very well controlled through the droops. Figure 5.19d shows that the pitch angle control with slew rate of 3°/sec is able to prevent the shaft speed from exceeding 1.3pu, hence no DL is needed.

Next section adjusts the droop characteristics in order to share the demand power according not only to the ratings of the DFIGs but also the available wind power.
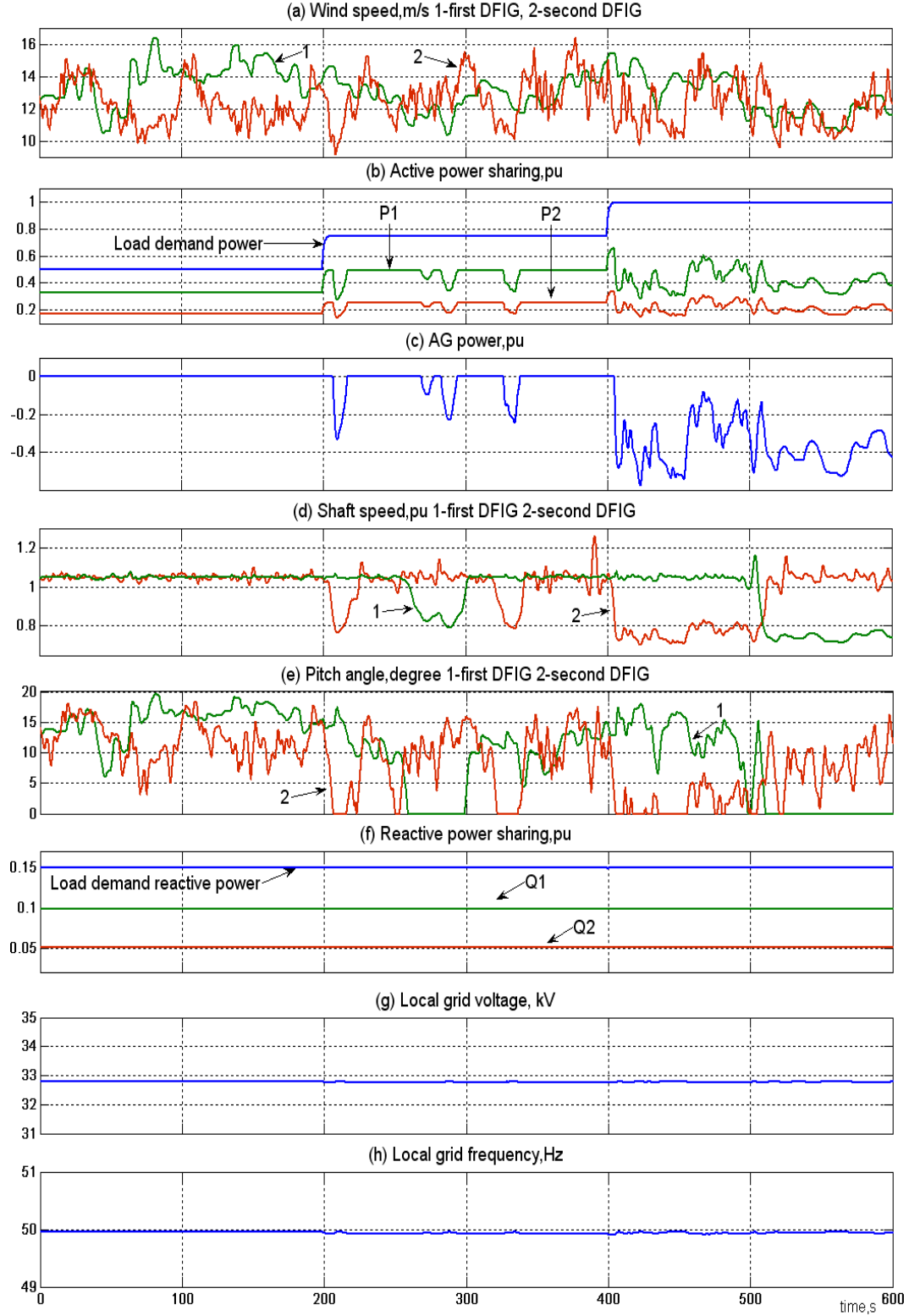
Figure 5.19. EMS for two droop-controlled DFIGs

5.3.2 Variable droop gain control

Using the standard droop characteristics, the demand power is shared by the generators proportional to their ratings. This is because the frequency-power droop coefficient is set as $m = \Delta f / P_{max}$, where P_{max} is the rating of the associated generator and Δf is the maximum allowed frequency deviation which is kept the same for all generators. This is an acceptable sharing approach in case of synchronous generators fed by a prime mover in which the input power can be represented by, for example, natural gas. However in an intermittent generation, like wind energy, this is not necessarily the best sharing method. To explain this, consider two DFIGs sharing a load in proportion to their ratings using the standard droop method (Figure 5.18). If the extractable wind power in one of the DFIG drops below the contribution required from the DFIG, the output power of the DFIG will reduce accordingly. This reduction is acceptable and of course inevitable. However, the standard droop will force the other DFIG to decrease its output power too. The reason of this behaviour is illustrated in Figure 5.20.
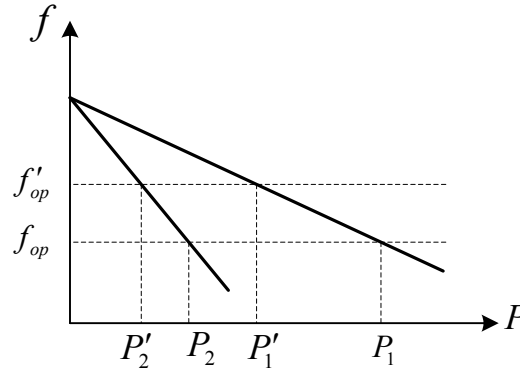
Figure 5.20. *f-P* droops when wind speed of one f the DFIG drops

Let us assume that the operational frequency prior to the wind speed reduction is f_{op}. Hence, the output powers of the first and the second DFIGs are P_1 and P_2, respectively. Following the wind speed reduction in either of the DFIGs, the operational frequency increases to f'_{op} due to the DFIG output power reduction. As a result, the other DFIG has to reduce its output power in order to comply with the new operational frequency. This is because of the fixed droop coefficients. If

the droop coefficients could vary according to the available wind power, the output power of the second DFIG could stay the same or even increase (subject to the wind power availability) following the wind power reduction in the first one. This can be achieved through making the droop coefficients vary as a cubic function of the shaft speed i.e. $m = \Delta f / k_{opt} \omega_r^3$, where k_{opt} is a given constant for maximum power tracking of wind power. This is due to the fact that the maximum power of wind is a cubic function of shaft speed. The main advantage of the variable droop gain is that the power required from the AG significantly decreases since the DFIGs equipped with the variable droop can compensate for one another. This will be shown through the following PSCAD simulations. However the variable droop gain method can affect the system stability which will be discussed later in this section.

5.3.2.1 Simulation results of the variable droop gain method

This section includes two simulations. The model simulated in the both cases is shown in Figure 5.18. The model consists of two ISFO-controlled DFIGs augmented with the variable droop control explained above with Δf=0.1Hz and k_{opt}=0.5pu. The voltage-reactive power droop and the pitch control are the same as before. The ratings of the DFIGs are 0.66pu and 0.34pu with parameters given in Appendix B. The first simulation uses constant wind speed while in the second one real wind speed profiles are applied.

Simulation 1

The objective of this simulation is to illustrate the proposed variable gain droop and to compare that with the standard droop. For the sake of explanation, constant wind speeds are used. The simulation results, which are shown in Figure 5.21, consist of parts A and B. The part A illustrates the results with the standard droop while the part B shows those with the variable droop. In the both cases the demand power is 0.78pu. The wind speed of the both DFIGs is 12.5m/sec until 20sec when the wind speed of the second DFIG drops to 10m/sec (corresponding to extractable wind power of approximately 0.5pu$_{gen}$).
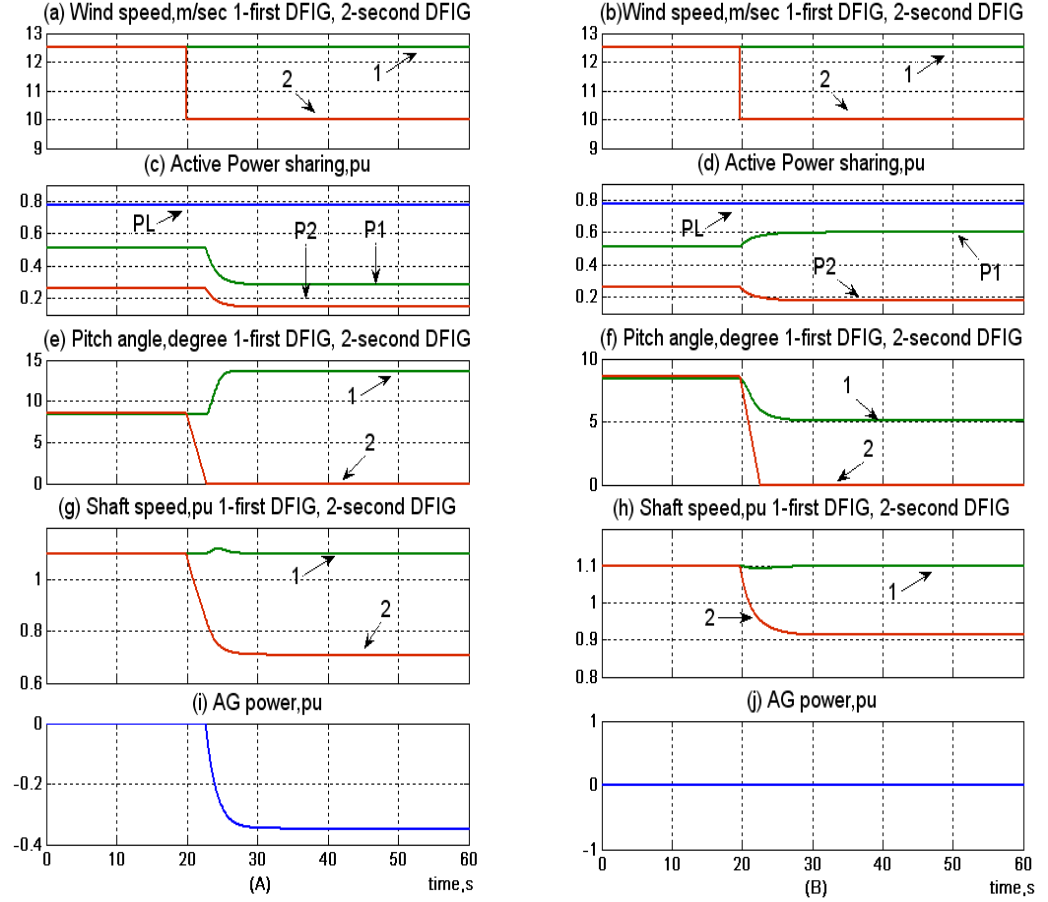
Figure 5.21. Comparing the behavior of two droop-controlled DFIGs when the wind speed of the second one drops from 12.5 to 10m/s (A) standard droop (B) variable gain droop

The wind speed reduction causes the output power of the second DFIG to reduce (Figure 5.21c). As explained, the standard droop forces the first DFIG to reduce its output power too. With the reference shaft speed set at 1.1pu, the first DFIG pitch angle (Figure 5.21e) increases to control its shaft speed (Figure 5.21g). Since the contribution demanded from the second DFIG is more than its $\hat{P}_{ext}$, the pitch angle of the second DFIG becomes zero. This causes the shaft speed to drop below 0.85pu which turns on the AG. The AG injects power (Figure 5.21i) in order to compensate for the shortfall and prevent the shaft speed from further reduction. It is noted that the pitch angle of the first DFIG is about 13º which means that the DFIG is generating far less than its available wind power. However using the variable droop gain method, the output power of the first DFIG increases (Figure

114

5.21d), causing a decrease in its pitch angle (Figure 5.21f). In other words, the first DFIG compensates for the output power reduction of the second one. This leads to no power demanded from the AG (Figure 5.21j). It can be seen from Figure 5.21d that until 20sec, during which the demand power is less than the extractable wind power, the demand power is shared by the DFIGs according to their ratings, even though the variable droop gain is used.

Simulation 2

The model simulated in this section is the same as before (Figure 5.18). The objective of this simulation is to validate the variable droop gain method with real wind profiles and compare its results (Figure 5.22) with those of the standard droop shown in Figure 5.19. Therefore the same procedures as Figure 5.19 are simulated here. The averages of the real wind speed profiles (Figure 5.22a) are approximately 12.5m/sec with the standard deviations of 1.28 and 1.39 respectively. Over the first 200sec, the demand power (Figure 5.22b) is 0.5pu which is less than $\hat{P}_{ext}$ of the both DFIGs. Because of this the demand power is shared in proportion to the DFIG ratings and the output power of each DFIG is almost smooth. The pitch angles (Figure 5.22e) control their associated shaft speeds (Figure 5.22d) and no power from the AG is needed. It can be seen that in this part the situation is very similar to the Figure 5.19. For the second 200sec, the demand power increases to 0.75pu which is occasionally more than $\hat{P}_{ext}$. It is shown in Figure 5.22b that the output powers of the DFIGs are not smoothed anymore and in fact are varying according to the wind speeds. This helps the DFIGs to compensate for the energy shortage of each other when the demand power is more than $\hat{P}_{ext}$. As a result, unlike the one with the standard droop (Figure 5.19c), no power is demanded from the AG (Figure 5.22c). It is noted that the power generated from the total wind farm is smoothed and of course equal to the demand, in spite of the varying output power of each DFIG. During the last 200sec, the demand power is 1pu which is almost always more than $\hat{P}_{ext}$.

Therefore, both shaft speeds reduce and the AG is switched on to compensate for the shortfall. Since the demand power is almost always more than $\hat{P}_{ext}$, the amount of the energy saved using the variable droop gain method is not significant. However it can be seen from Figure 5.22c that the power from the AG becomes temporarily zero during the last 200sec which does not happen using the standard droop (Figure 5.19c). Although the variation of the local grid frequency (Figure 5.22h) is slightly more than that of the standard droop (Figure 5.19h), it is still less than 0.3Hz. The reactive power demanded from the wind farm is 0.15pu which is shared in proportion to the rating of the DFIGs during the first 200sec. From 200sec onwards, as the frequency variation increases due to the variable droop, the output reactive power of each DFIG varies accordingly. However, the total reactive power from the wind farm is still smooth and equal to the demand reactive power. Figure 5.22g shows that the local grid voltage is still very well regulated.

The simulations above demonstrate the ability of the variable droop gain method to force the DFIGs to compensate for one another and significantly reduce the energy required from the AG while both voltage and frequency are controlled.
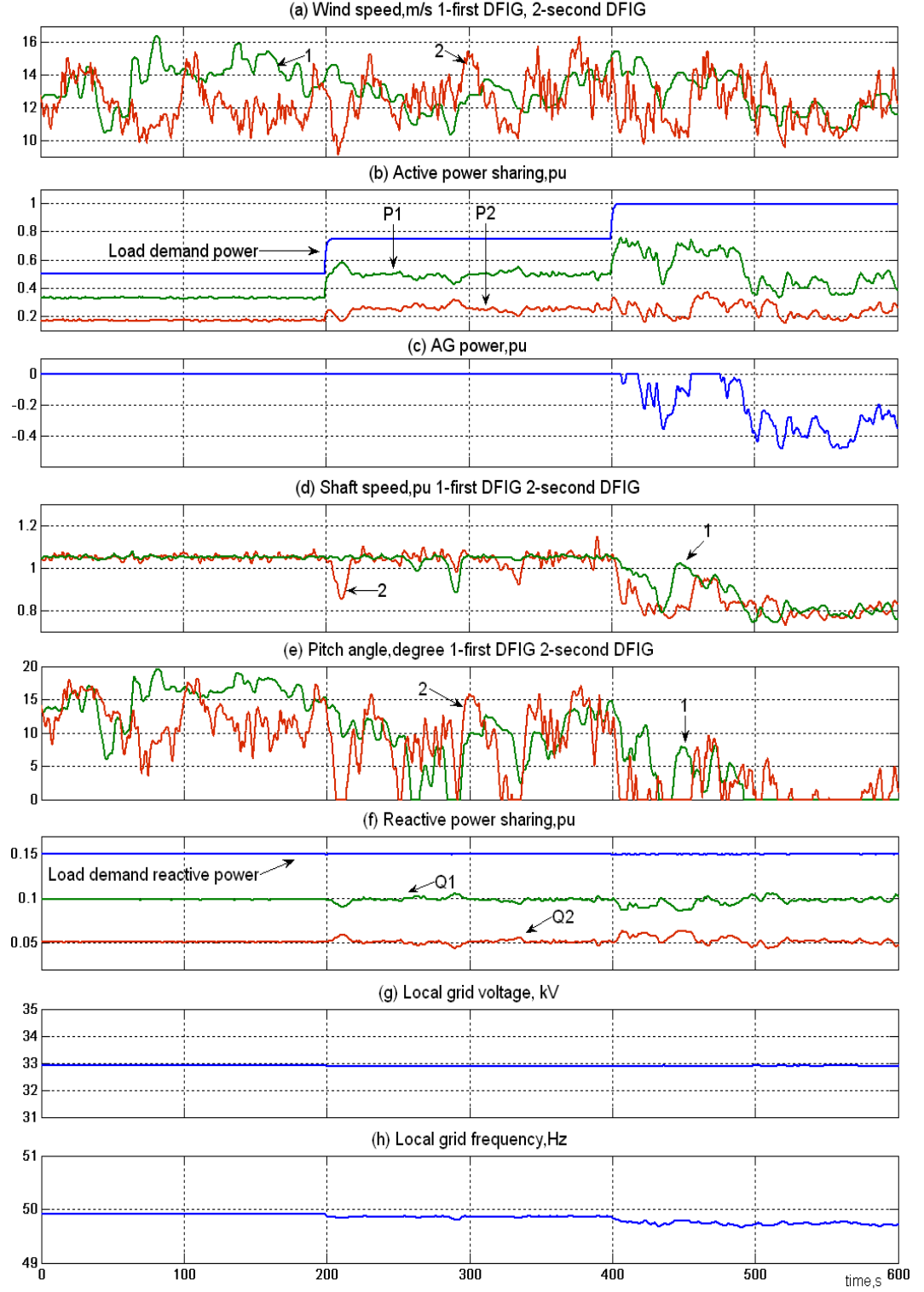
Figure 5.22. Sharing with the variable droop gain method

117

The main drawback of the variable droop method is that the system stability may be affected. A similar scenario was consider in [42] in which three 10kW inverters feed an islanded microgrid. The droops in [42] were a function of the dispatched power being fed through each inverter. It was shown in [42] that in the worst case scenario the largest possible *f-P* droop gain is 3.1×10^{-5} Hz/W (or 0.31Hz/pu). This is due to the fact that the system eigenvalues varies with the *f-P* droop gain and in fact the eigenvalues move toward instability as the *f-P* droop gain increases[42, 75]. Translating their findings to the present study means that there is a minimum shaft speed for the variable droop gain method which is around 0.32pu. This means that the system will become unstable for wind speeds less than the cut-in wind speed. This will be illustrated in Chapter 8. Therefore, it seems that the system is stable within the allowed shaft speed region for DFIGs (i.e. 0.7-1.3pu). Having said that, the author admits that a full system stability study is required that is beyond the scope of this thesis. It is noted that the proposed EMS works with the standard droop and the variable droop gain method is suggested in order to improve the system efficiency through reducing the energy required from the AG.

The next section proposes a simplified model for ISFO-controlled DFIG in order to be able to simulate more numbers of DFIGs.

5.4 Simplified ISFO-controlled DFIG model

PSCAD simulation of a multi-DFIG system including the wind turbine, pitch angle controller and real wind profile connected to the AG and DL for a long time (600sec) takes several hours. This causes difficulties for simulating different scenarios especially for models with more than two DFIGs. Therefore, this section proposes a simplified model which will be used to simulate a system consisting of a larger number of DFIGs in order to validate the EMS. Both standard and variable gain droops are simulated.

5.4.1 Explaining the simplified model

It was discussed that an ISFO-controlled DFIG appears like a voltage source in the system. Therefore the DFIG can be represented by an AC voltage source while its voltage and frequency are set through droop characteristics. Figure 5.23 shows the simplified model of two DFIGs controlling the local grid voltage and frequency using droop characteristics. The electrical torque of each DFIG is derived through dividing its measured output power by the shaft speed. It can be seen that the full model of the wind turbine is considered. It was shown in [54] that the stable region of the DFIG (the generator itself) is much wider that that of the wind turbine. Therefore the stability characteristic of this simplified model is the same as that of the one with the full DFIG model since the full wind turbine model is considered in the simplified model. The pitch angle control and the EMS are the same as before.
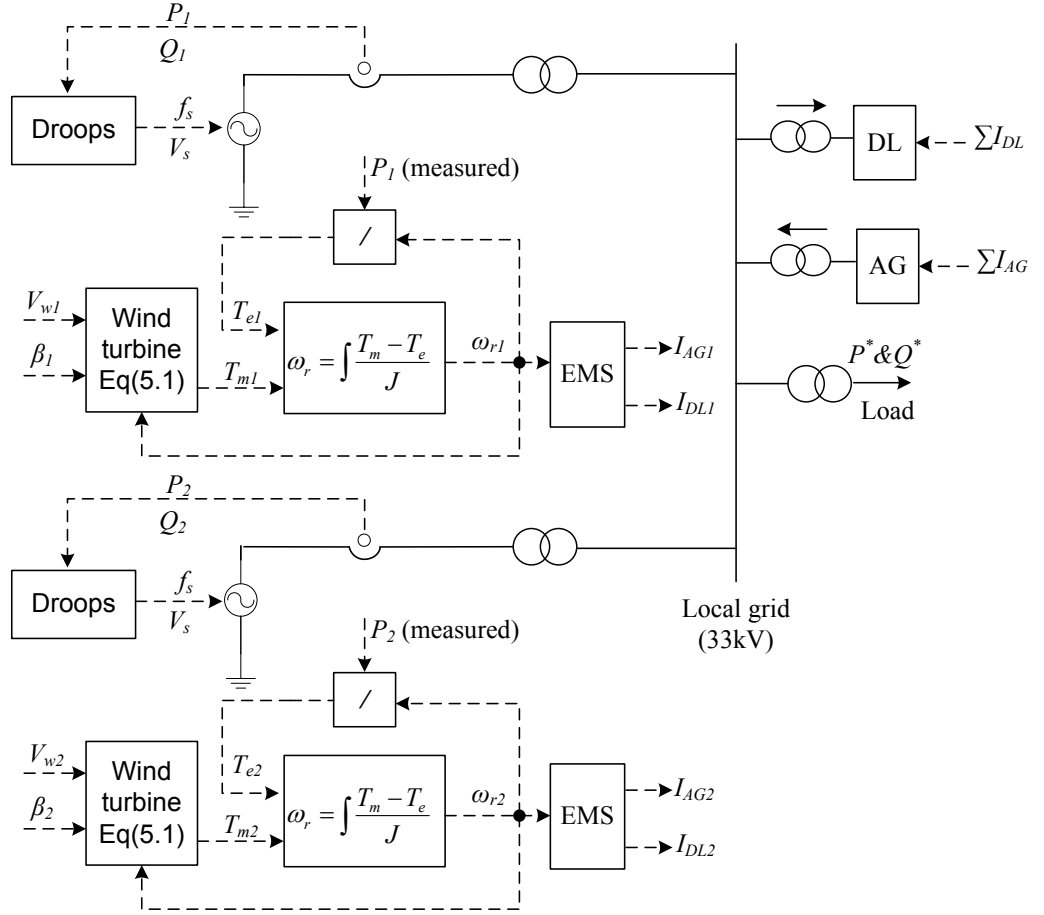
Figure 5.23. Simplified model of two DFIGs controlling the local gird voltage and frequency

Now the simplified model will be use to simulate four droop-controlled DFIGs using PSCAD.

5.4.1.1 Simulation results of four droop-controlled DFIGs using the simplified model

The model simulated in this section consists of four simplified ISFO-controlled DFIGs supplying a local load, as is shown in Figure 5.23. In Figure 5.23, for the sake of simplicity, only two DFIGs are depicted. However in the model simulated, four DFIGs are used. The pitch angle control (not shown in the figure), EMS and AG are exactly the same as before. Two simulations are undertaken. The objective of the simulations is to validate the EMS for four DFIGs using both the standard droop and the variable droop gain methods. The ratings of the first and the third

DFIGs are 0.33pu while those of the second and the fourth DFIGs are 0.17pu. There are two real wind speed profiles with the average of approximately 12.5m/sec and the standard deviations of 1.28 and 1.39. The first wind speed profile is applied to the first and the fourth DFIGs while the second wind speed profile is applied to the second and the third DFIGs. As a result, the DFIGs with the same rating are applied different wind speed profiles. Figure 5.24 shows the results with the standard droop characteristics. The droop gains are those used in section 4.4.3. Figure 5.24b shows the active power sharing. The demand power, for the first 200sec, is 1pu which is equal to the average of the extractable wind power. Therefore, when the demand is more than $\hat{P}_{ext}$ of any of the DFIGs, its shaft speed (Figure 5.24f&g) reduces and turns on the AG (Figure 5.24c). Since the output power of each DFIG cannot be more than 1pu$_{gen}$, the pitch angles (Figure 5.24d&e) are not always at zero. In other words, the pitch angles increases to shed power more than 1pu$_{gen}$. Over the second 200sec, the demand power reduces to 0.75pu which is less than the average of the extractable wind power. As a result, the AG is turned on in only three occasions. During the last 200sec, in which the demand is 0.5pu, no power is needed from the AG. The reactive power demand (not shown in the results) is 0.15pu which is shared proportional to the ratings of the DFIGs. It is noted that the output power of the first and the third DFIGs, which have the same rating, are identical. This is also the case for the second and the fourth DFIGs. This is due to the standard droop which shares the power according to the ratings of the DFIGs regardless of the wind speed. Figure 5.24h shows that the local grid voltage and frequency are well-regulated.

Figure 5.25 shows the results using the proposed variable droop gain method while the same procedures as the one with standard droop are simulated. For the first 200sec the demand power is 1pu. As Figure 5.25b shows the output powers of the DFIGs with the same ratings are not identical anymore. This is because of the variable droop gain method which makes the DFIGs share the demand according to both their ratings and the available wind power. As a result, less active power is needed from the AG (Figure 5.25c) than that of with the standard droop (Figure 5.24c). During the second 200sec, the demand power drops to 0.75pu. In this case

the power from the AG is zero, unlike the case using the standard droop. Finally for the last 200sec the demand power is 0.5 which is less than $\hat{P}_{ext}$. Therefore, the demand power is shared almost proportionally to the ratings of the DFIGs, similar to the case with the standard droop. Figure 5.25h shows that the local grid voltage and frequency are still very well-controlled.

These results demonstrate that the proposed EMS and the pitch controllers are able to maintain the shaft speeds within its acceptable region in a multi-DFIG system. The results in Figure 5.24 show the functionality of the standard droop control in a multi-DFIG system. Figure 5.25 shows that the proposed variable droop gain control method is able to operate is a multi-DFIG system without violating the system stability.
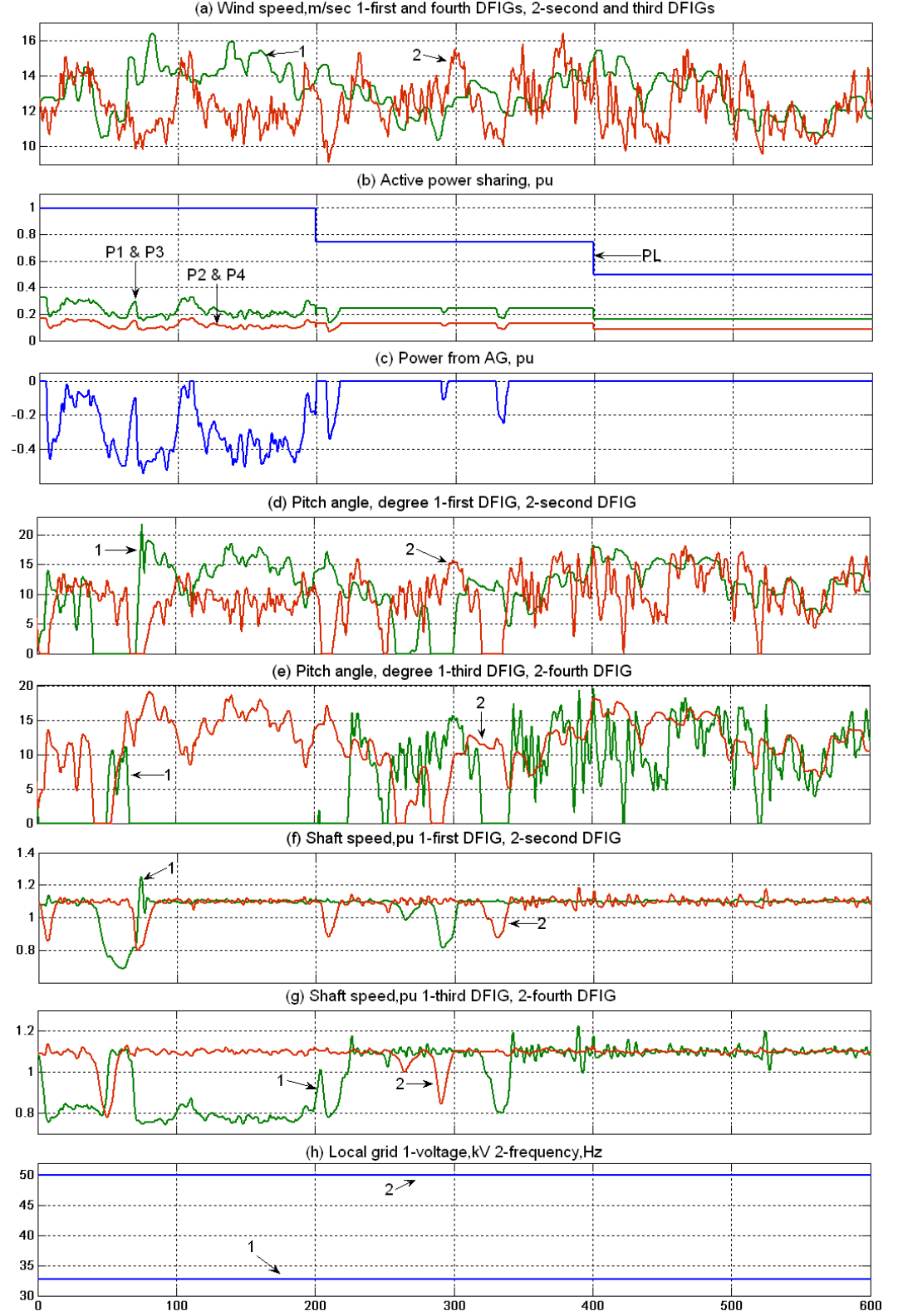
Figure 5.24. Power sharing of four simplified ISFO-controlled DIFGs using standard droop
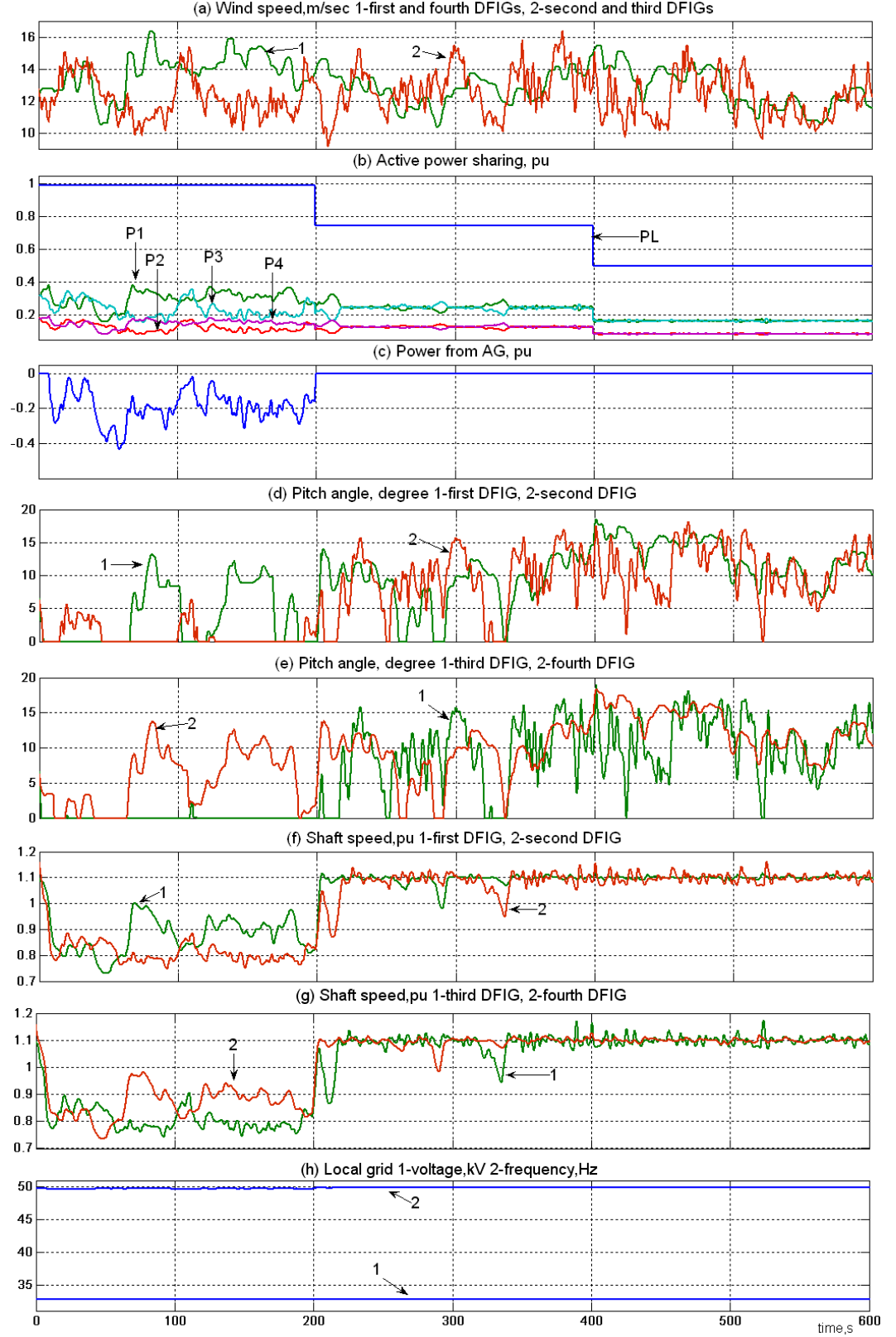
Figure 5.25. Power sharing of four simplified ISFO-controlled DIFGs the variable droop gain

5.5 Discussions and Conclusions

This chapter dealt with an ISFO-controlled wind farm without an external torque controller for the DFIGs. An application of such a structure involving a microgrid has been taken into consideration. A pitch angle control has been designed and validated to maintain the shaft speed within its limits when the demand power is less than $\hat{P}_{ext}$. The pitch angle maximum slew rate is always kept at 3°/sec. The pitch angle control is also illustrated for a two-DFIG system while the demand power is shared by the DFIGs using droop characteristics. When the demand power approaches the average of the extractable wind power, the energy stored in the shaft inertia compensates for the shortage of the energy whenever the demand becomes more than $\hat{P}_{ext}$. This causes shaft speed reduction. If the shaft speed reduces to less than a certain threshold, an EMS is used to switch on an AG in order to compensate for the energy shortage and prevent the shaft speed from the further reduction. The EMS using standard droop characteristics has been validated in a system with two DFIGs while real wind speed profiles are used. It has been shown that using the standard droop, if $\hat{P}_{ext}$ of one DFIG drops below its contribution to the demand power, the output power of the other DFIGs will drop accordingly in order to operate at the new frequency forced by the first DFIG. A variable droop gain control paradigm has been proposed to overcome this problem with the standard droop. It was shown that using the proposed variable droop gain control method, the power demanded from the AG can be significantly reduced. This is because that the DFIGs equipped with variable droop gain control are able to compensate for one another. The drawback of the variable droop gain is the fact that the large droop gains can affect the system stability [42, 75]. This can occur when the shaft speed is too low which happens when the demand power is more than $\hat{P}_{ext}$. However, it was shown in [42] that instability occurs only for very large droop gains. The very large droop gains seem to correspond to wind speed less than the cut-in wind speed in case of the multi-DFIG system equipped with the

variable droop. In other words, the DFIGs augmented with the variable droop control seem to be stable within the operating shaft speed region. The stability study of the variable droop gain control is out of the scope of this thesis. It is noted that the proposed EMS works with the standard droop control. In order to validate the proposed EMS in a system with more than two DFIGs, a simplified DFIG model has been proposed. The simplified model still considers the full model of the wind turbine. Therefore the stable region of the simplified model is identical to the system with the full DFIG model. This is due to the fact that the stable region of a DFIG is much wider than that of a wind turbine [54]. A model consisting of four simplified DFIGs has been simulated using both standard droop and the variable droop gain methods.

This chapter focused on constant demand power delivery methods without an external ES. This reduces the cost of the system significantly. However, since the DFIGs are not under MPT control, the power from the AG is not necessarily minimized. This is definitely the case when the standard droop is used. Moreover, using an external ES may increases the efficiency of the AG through decreasing the incident of power demanding from the AG. Constant demand power delivery methods using an external ES are the subjects of the next chapters.

The following chapters deal with an ISFO-controlled wind farm using the ES as an external generator torque controller. The next chapter considers CTM control. The MPT mode is studied in Chapter 7.

6. Wind turbine-ES system delivering a constant demand power without an auxiliary generator

6.1 Introduction

The previous chapter investigated the control strategies involving an ISFO-controlled wind farm and an Auxiliary Generator (AG) in order to deliver a constant power demanded by the load. It was shown that if the demand power is less than the extractable wind power, the proposed pitch angle control with a slew rate of 3-5º/sec can control the shaft speed within its stable region. If the demand power becomes more than the extractable wind power, the shaft speed reduces in order to compensate for the energy shortfall. This may expose the system to instability. In order to avoid such situations, for shaft speeds less than a certain threshold (0.85-0.8pu), the AG is turned on and injects the energy needed in order to prevent shaft speed from further reduction and maintain the demand power. No external ES was considered in the previous chapter.

In Chapter 7 a full model consisting of both an AG and an external ES will be studied. Chapter 6, however, studies the control of an ISFO-controlled DFIG with an external ES while no AG is considered. The ES power will be regulated to control the electrical torque of the DFIG. Not having an AG is obviously impractical due to the limited capacity of ES systems especially when the demand power approaches the average of the extractable wind power $\hat{P}_{ave}$. However this chapter is included, in order to explain and design the generator torque control loop and to study the Constant Torque Control (CTM) mode. In Chapter 7, the DFIGs are controlled under standard Maximum Power Tracking (MPT) mode in order to minimize the energy from the AG when the demand power is more than the extractable wind power. This chapter, since no AG is considered, is a proper case study for DFIGs under a non-MPT control such as CTM. Considering an isolated load fed by wind turbines with no AG, CTM (or in fact any non-MPT

control) has the advantage of reducing the required external ES compared to the MPT mode. This is because of the fact that the shaft speed variation of CTM is more than that of MPT for a given wind speed and demand power [54]. In papers such as [54], the CTM is named as a possible method of controlling a DFIG. However, as far as the author is aware, no publication has considered the stability issue of CTM control. One of the objectives of this chapter is to study the instability problem of the CTM control and attempt to address the issue without using an AG. The MPT seems to be the best choice, at least when the demand power is more than the extractable wind power to minimize the power from the AG.

This chapter consists of two main parts. The first part proposes a generator electrical torque control scheme through regulating the ES power. The proposed control scheme will be validated for both CTM and MPT controls. The same control structure will be used in the following chapters to control the torque of the generator. The second part of this chapter attempts to derive a mathematical expression for the size of the required ES for a given wind profile. The second part covers work which was discontinued, but it is included here for completeness and it may also have archival value.

6.2 Electrical torque control by regulating ES power

In an ISFO-controlled DFIG, i_{rq} is kept proportional to i_{sq} in order to maintain the field orientation of the DFIG [44]. Therefore the electrical torque must be controlled externally. In [44] an auxiliary load is used to control the DFIG under MPT mode. This section proposes a torque control scheme using the ES power. The control structure will be validated using PSCAD simulations for both CTM and MPT controls. Figure 6.2 illustrates the proposed electrical torque control scheme for the ISFO-controlled DFIG.
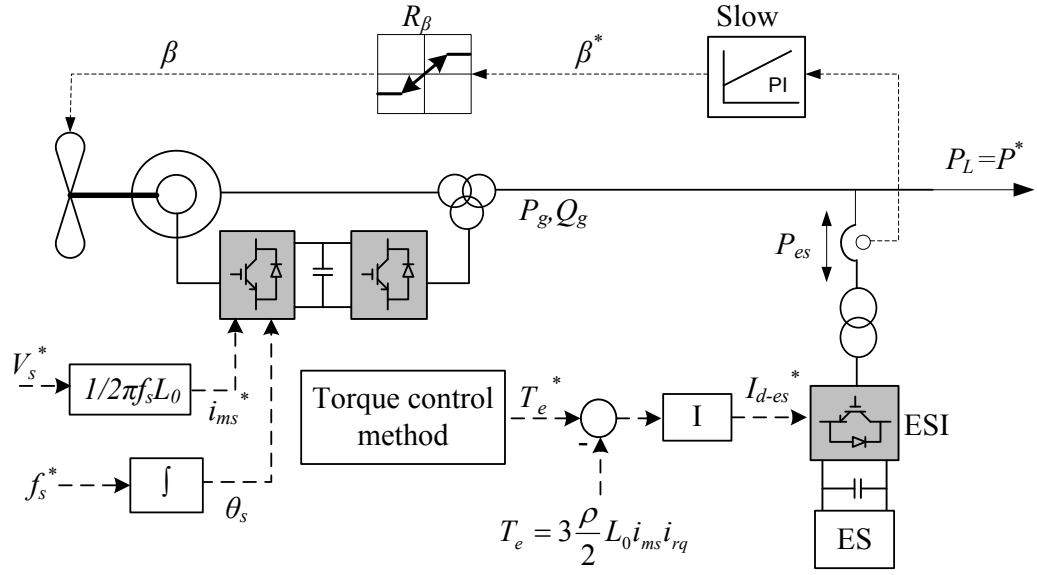
Figure 6.1. Proposed electrical torque control structure for an ISFO-controlled DFIG

The load power P_L is equal to the demand power P^* which is determined by the system operator. In a multi-DFIG system, the demand power is shared by the DFIGs using droop characteristics, as explained in the previous chapters. It will be shown in Chapter 8 that the ES can also be aggregated on to the wind farm collector bus which necessitates communication between wind farm and the ES. The generator power is $P_g=P_{es}+P_L$, where P_{es} is the ES power. The electrical torque of the DFIG effectively is $T_e=P_g/\omega_r$. Therefore, the electrical torque can be controlled by regulating P_g through P_{es}. Since the local grid voltage is controlled by the DFIG, the ES real component current I_{d-es} is equivalent to the instantaneous ES power P_{es}. As a result, the electrical torque can be controlled through regulating I_{d-es}^*. The ES interface (ESI) is an AD/DC PWM converter. The q-component of the ES current I_{q-es}^* is set at zero but it can also be used to support the local grid voltage V_g if the demand reactive power is too large for the DFIG. The ESI currents loops (not shown in the figure) are the standard current controllers identical to those of the DFIG's grid side converter explained in Chapter 2 and [48, 49]. An integral controller is shown to be sufficient to control the electrical torque. The reference electrical torque T_e^* is determined according to the required torque control method (i.e. MPT, CTM, etc). The fed-back electrical

torque is calculated from $T_e = 3\dfrac{\rho}{2}L_0 i_{ms} i_{rq}$ [44], where ρ and L_0 are the number of the pole pairs and mutual inductance respectively.

A pitch angle control can be utilized to reduce the average of the ES power towards zero through using a slow PI controller, as shown in Figure 6.1. The output of the pitch angle PI controller will drive any DC or low frequency components (within the controller bandwidth) of the ES power towards zero. Since the controller averages the ES power toward zero, this has the effect of reducing the power rating of the ES. The next subsection derives the control plant and designs the integral controller of the proposed torque control scheme.

6.2.1 Torque control loop design

This section considers the electrical torque loop design which is also used in Chapters 7 and 8.

According to Figure 6.1, one can write:

$$P_g = P_{es} + P_L \tag{6.1}$$

Assuming a rotating *dq* frame with the d-axis fixed to the grid voltage, P_{es} can be written as:

$$P_{es} = \frac{3}{2}\left(V_{gd}I_{d-es} + V_{gq}I_{q-es}\right) = \frac{3}{2}V_{gd}I_{d-es} \tag{6.2}$$

Substituting (6.2) and $P_g = T_e\omega_r$ into (6.1) and simplifying it, yields:

$$T_e = \left(\frac{3}{2}I_{d-es} + \frac{P_L}{V_{gd}}\right)\frac{V_{gd}}{\omega_r} \tag{6.3}$$

The grid voltage V_{gd} can be considered constant and well regulated by the DFIG. The load demand power P_L is an external disturbance. According to (6.3), the control structure is given in Figure 6.2:
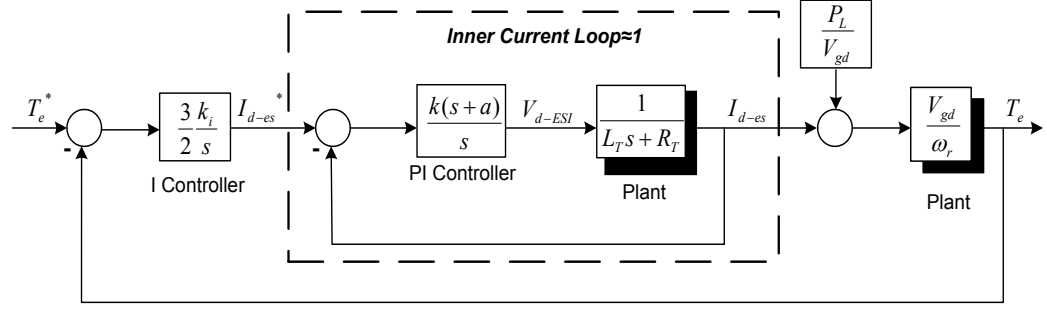
Figure 6.2. Electrical torque controller structure

The inner current loop controls the current flowing through the ES transformer with inductance L_T and resistance R_T given in Appendix B.

The load power P_L is an external disturbance and can be neglected in the control design. The grid voltage is constant and well-controlled by the DFIG. Therefore, the control plant is a variable gain that varies with only ω_r. Due to the rotor inertia, ω_r varies smoothly. Hence, it is expected that T_e also varies quite smoothly. As a result, the outer torque loop bandwidth can be 15-30Hz (this is similar to the power loop of a standard DSFO-controlled DFIG). Since the bandwidth of the inner current loop is 250Hz which is much faster than the outer torque control loop, the closed loop transfer function of the inner loop can be assumed to be 1. This means that the inner current loop can be neglected for designing the outer torque control loop. As mentioned, the control plant is a gain varying with ω_r. However, since the operating region for a DFIG shaft speed is limited to only 0.7-1.3pu, the control plant is assumed a constant gain with ω_r=1pu. Because the plant can be represented as a gain for the frequencies of interest, an integral controller is sufficient. Therefore the characteristic equation of the outer torque loop is:

$$1 + \frac{3}{2}\frac{k_i}{s}\frac{V_{gd}}{\omega_r} = 0 \rightarrow s + \frac{3}{2}k_i\frac{V_{gd}}{\omega_r} = 0 \tag{6.4}$$

Thus

$$\frac{3}{2}k_i\frac{V_{gd}}{\omega_r} \approx \omega_{T_e} \rightarrow k_i = \frac{2\omega_r\omega_{T_e}}{3V_{gd}} \tag{6.5}$$

where ω_{T_e} is the bandwidth of the outer torque control loop. If ω_{T_e}, ω_r and V_{gd} are 15Hz, 1pu and 33kV (line-line rms), k_i is 240.

6.2.1.1 Performance of the electrical torque control loop

This section validates the torque control loop using PSCAD simulations. In the first part the electrical torque is controlled under CTM while in the second part MPT mode is considered.

CTM control

Under CTM the reference electrical torque is constant for a given demand power. The reference electrical torque can be defined as:

$$T_e^* = \frac{P_L}{\overline{\omega_r}} \tag{6.6}$$

where $\overline{\omega_r}$ is called the average shaft speed. The choice of the average shaft speed will be discussed later in this chapter. In a multi-DFIG system, P_L is the power determined by the droop characteristics. Assuming a constant average shaft speed, T_e^* will change as the demand power changes.

Simulation results

The objective of this simulation is to validate the proposed torque control scheme for CTM control. The model simulated in PSCAD is shown in Figure 6.1. The DFIG1 with parameters given in Appendix B is used for this simulation. Figure 6.3 shows the simulation results. The average of the real wind speed profile (Figure 6.3a) is approximately 12.5m/s ($\hat{P}_{ave} \approx 1\text{pu}$) with the standard deviation of

1.28. The degree to which P^* can approach $\hat{P}_{ave}$ without violating the system stability will be discussed later.
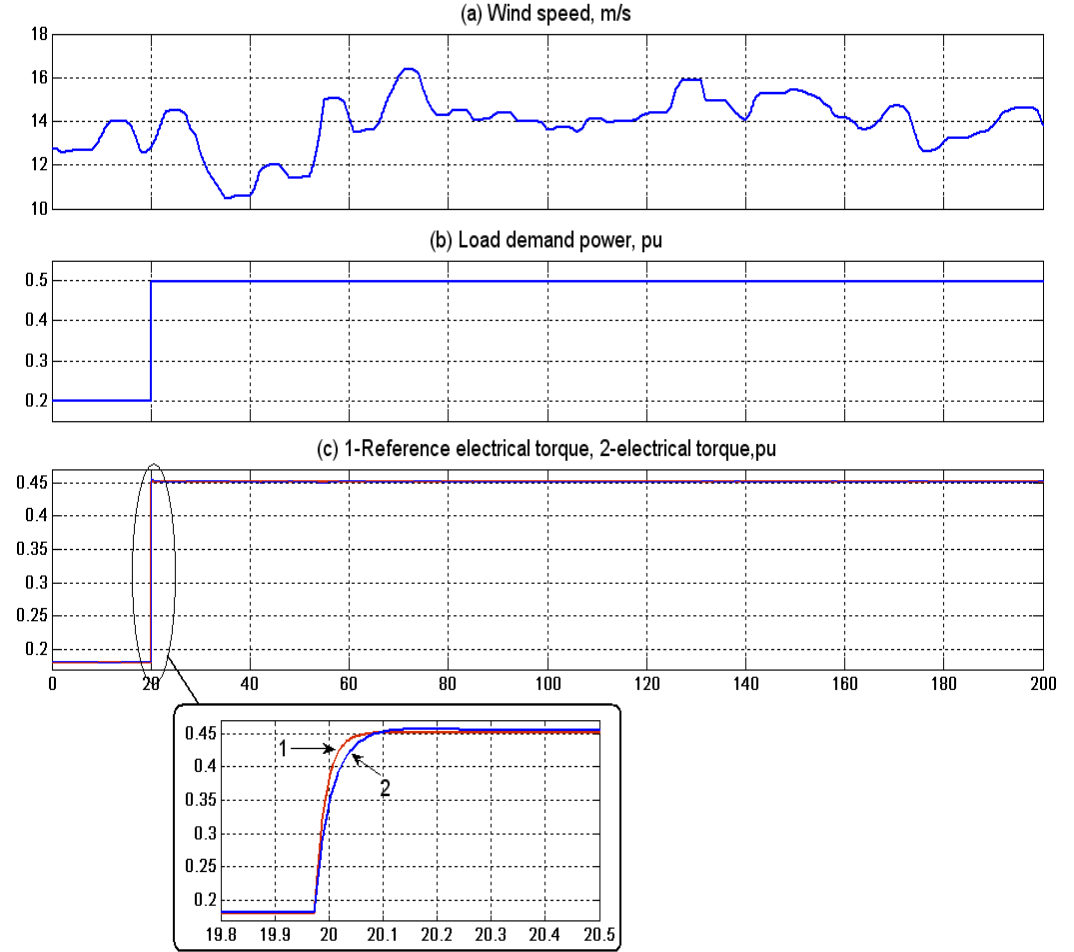
Figure 6.3. CTM control using the proposed control structure

The reference electrical torque is given in (6.6) with the average shaft speed of 1.1pu which is kept constant during the simulation. The demand power (Figure 6.3b) is increased from 0.2pu to 0.5pu in a step change. As a result, the electrical torque reference (Figure 6.3c1) increased from 0.2/1.1=0.18pu to 0.5/1.1=0.45pu. Figure 6.3c2 shows the electrical torque following its constant reference. Figure 6.3 demonstrates the ability of the proposed electrical torque control scheme via ES power regulation to control a DFIG under CTM.

MPT control

Under MPT mode, the DFIG output power P_g is a cubic function of the shaft speed. Therefore, the reference electrical torque must vary as a quadratic function of the shaft speed:

$$T_e^* = k_{opt} \omega_r^2 \tag{6.7}$$

where k_{opt} is a constant coefficient given for each wind turbine.

Simulation results

The model simulated is shown in Figure 6.1 with the same DFIG rating as the previous simulation. This time, the reference electrical torque is given in (6.7) with k_{opt}=0.52pu. The simulation results are illustrated in Figure 6.4. The average of the real wind speed profile (Figure 6.4a) is about 10.5m/sec with the standard deviation of 1.28. The demand power (Figure 6.4b) increased from 0.5pu to 0.8pu at 50sec. Figure 6.4c shows that the electrical torque follows its reference with a small transient error. However Figure 6.4c shows only that T_e follows its reference and does not prove that the DFIG is under MPT control. In order to show that the DFIG is under MPT control, Figure 6.5 depicts the DFIG output power P_g vs the shaft speed on the turbine power vs shaft speed characteristic for different wind speeds. Figure 6.5 clearly shows that the DFIG output power is following the maximum extractable wind powers. These results demonstrate the ability of the proposed torque control scheme to control a DFIG under MPT mode via regulating the ES power.
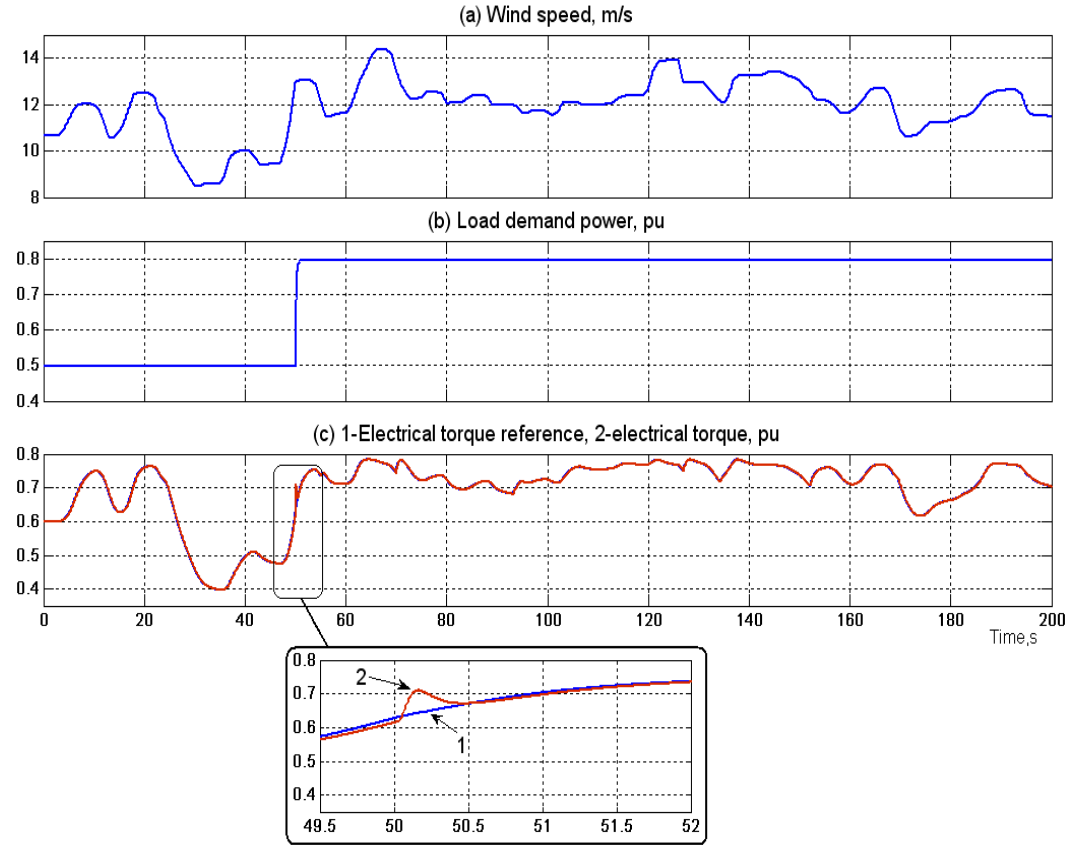
Figure 6.4. MPT control using the proposed control structure
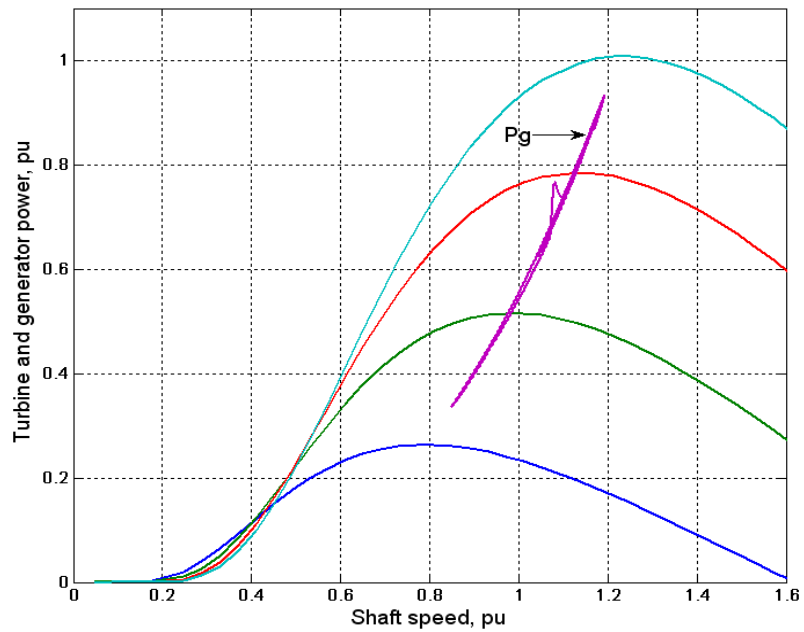
Figure 6.5. MPT control using the proposed control structure on P_t-ω_r characteristic

6.3 Mathematical derivation of the size of ES for a given wind profile

6.3.1 Introduction

This section attempts to derive a mathematical expression for the power rating and the energy capacity of the required ES. Obviously, this can be done for a known wind speed profile. The following assumptions are made:

- The DFIG is controlled under CTM (however, the method can be adopted for MPT in future).
- The wind speed profile is known and has the average of $\overline{V_w}$, the wind speed variation of δV_w and an arbitrary frequency of f_w.

The idea behind choosing a frequency f_w was that it was assumed that the pitch control could be used to smooth power frequencies less than f_w. Hence the ES could be used to absorb frequencies more than f_w. Considering such a assumption, the ES energy capacity rating would be determined by the (lowest) frequency f_w. However the approach was not found to be effective and (as stated) was discontinued. However the work is included as it derives the relationship between ES capacity and wind power frequency which may have archival value and find application in future. The derived mathematical expression will be validated using PSCAD simulations considering the above assumptions into account.

6.3.2 Mathematical derivation of ES rating

It was discussed in Chapter 2 that the main drawback of the CTM is its instability as shown in Figure 6.6a. However, the stable region of the CTM is wider than that of the CPM [54]. Therefore, the method explained in the previous chapter for CPM, in which an AG is used to drive the DFIG to its stable region, is quite applicable for CTM as well. However, this chapter concentrates on constant demand power delivery without an AG. In fact the assumption that there is no AG

justifies the control of the DFIG under CTM. Otherwise the MPT control is the proper choice in order to minimize the energy demanded from the AG. As mentioned before, under CTM, the electrical torque is $T_e = \dfrac{P_L}{\overline{\omega}_r}$. The choice of the

$\overline{\omega}_r$ is very important and can help the system to keep away from instability. This will be discussed later. In order to predict instability the shaft speed variation $\delta\omega_r$ (see Figure 6.6a and equation (6.11)) must itself be predicted. The calculation of the shaft speed variation leads to the energy and power rating of the ES.
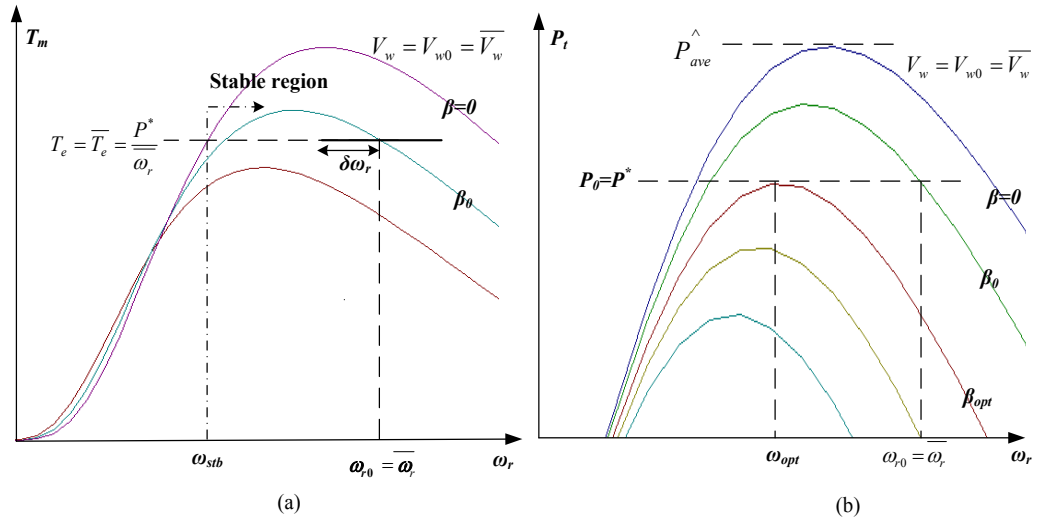
Figure 6.6. Wind turbine characteristics (a) T_m-ω_r characteristic showing CTM stable region (b) P_t-ω_r characteristic defining the average shaft speed and linearization point

In order to calculate $\delta\omega_r$, the wind turbine model needs to be linearized. This was carried out in Chapter 5 and the linearized model can be expressed as:

$$\delta T_m = M_1 \delta V_w + M_2 \delta\omega_r + M_3 \delta\beta \qquad (6.8)$$

where M_1, M_2 and M_3 are functions of the linearization point which is $P_0 = P^*$, $V_{w0} = \overline{V}_w$ and $\omega_{r0} = \overline{\omega}_r$ (see Figure 6.6).

Assuming a wind variation at the sinusoidal frequency f_w:

$$V_w = \overline{V}_w + \delta V_w \cos(2\pi f_w t) \qquad (6.9)$$

the turbine mechanical torque can be approximated by:

$$T_m = \overline{T_e} + \delta T_m \cos(2\pi f_w t)$$ (6.10)

Therefore, the shaft speed is:

$$\omega_r = \overline{\omega_r} + \delta \omega_r \sin(2\pi f_w t)$$ (6.11)

There is a small phase shift between the mechanical torque and the shaft speed due to the mechanical loss which is neglected in (6.11).

In CTM, $T_e = \overline{T_e}$, so one can write:

$$T_m - \overline{T_e} = J \frac{d\omega_r}{dt}$$ (6.12)

where J is the combined generator and turbine inertia as seen from the generator. Substituting (6.10) and (6.11) into (6.12) and simplifying, yields:

$$\delta T_m \cos(2\pi f_w t) = 2\pi f_w J \delta \omega_r \cos(2\pi f_w t) \rightarrow \delta T_m = 2\pi f_w J \delta \omega_r$$ (6.13)

Equating (6.8) with (6.13) and assuming that at steady state $\delta\beta \approx 0$, the shaft speed variation can be derived as:

$$\delta \omega_r = \frac{M_1 \delta V_w}{2\pi f_w J - M_2}$$ (6.14)

Assuming that at steady state the average of the generator power is P^*, the amplitude of the ES power P_{es} is the shaft speed variation multiplied by the electrical torque:

$$P_{es} = \delta \omega_r T_e = \delta \omega_r \left(\frac{P^*}{\overline{\omega_r}} \right)$$ (6.15)

Given the time period of the selected wind frequency $T_w=1/f_w$, each half period of ES power can be approximated by a triangle with a base of $T_w/2$ and height of P_{es}

given in (6.15). The area of this triangle represents the required energy from the ES (E_{es}) to be exchanged with the grid:

$$E_{es} = \frac{P_{es}T_w}{4}$$

(6.16)

Equations (6.14), (6.15) and (6.16) derive respectively shaft speed variation, ES power and ES energy for a given J, P^*, f_w, δV_w, $\overline{V_w}$ and $\overline{\omega_r}$. This will be validated using PSCAD simulations later in this chapter.

6.3.2.1 Stability study

Figure 6.6a shows the stable region for a given P^*, $\overline{V_w}$ and $\overline{\omega_r}$. As Figure 6.6a illustrates, the choice of $\overline{\omega_r}$ assists the system to retain stability. If an AG is available, an Energy Management System (EMS) identical to the one explained in Chapter 5 can be used in order to recover the system from possible instability. In such a scheme the AG is turned on when the shaft speed drops below a certain threshold and injects the energy shortage to prevent the shaft speed from further reduction. It was shown in Chapter 5 that the shaft speed threshold can be less than ω_{stb}. In such a scenario, the choice of $\overline{\omega_r}$ is not important and can always be set at 1-1.1pu. However, assuming a system in which no AG is available, the choice of $\overline{\omega_r}$ becomes very important. Figure 6.6a illustrates that as $\overline{\omega_r}$ increases, the system is further from the instability shaft speed ω_{stb}. However Figure 6.6b shows that as P^* approaches $\hat{P}_{ave}$, the choice of $\overline{\omega_r}$ is limited. If $P^* = \hat{P}_{ave}$, the only choice for $\overline{\omega_r}$ is the associated optimum shaft speed ω_{opt}. In order to predict instability, first a value of ω_{stb} needs to be derived. According to Figure 6.6a, at $\omega_r = \omega_{stb}$ the following holds:

$$T_m = \frac{P_t}{\omega_r} = \frac{0.5\rho A C_p \overline{V_w}^3}{\omega_r} = \overline{T_e}$$

(6.17)

In the PSCAD wind turbine model, the power coefficient C_p is defined as:

$$C_p = 0.5\left(\lambda - 0.022\beta^2 - 5.6\right)e^{-0.17\lambda} \tag{6.18}$$

The shaft speed as a function of Tip Speed Ratio (λ) is:

$$\lambda = \frac{2.237\,N\overline{V_w}}{\omega_r} \rightarrow \omega_r = \frac{2.237\,N\overline{V_w}}{\lambda} \tag{6.19}$$

Substituting C_p from (6.18) and ω_r from (6.19) into (6.17) and simplifying it, gives:

$$Ke^{-0.17\lambda}\left[\lambda^2 - \left(0.022\beta_0^2 + 5.6\right)\lambda\right] = \overline{T_e} \tag{6.20}$$

where $K = \dfrac{0.1176\,\rho A\overline{V_w}^2}{N}$. As Figure 6.6a shows, two λ values satisfy (6.20). One corresponds to $\overline{\omega_r}$ and the desired one to ω_{stb}. Equation (6.20) is not easily solved although a search solution is quite feasible. Since the work was discontinued the search algorithm will not be reported here.

Once ω_{stb} and $\delta\omega_r$ are calculated, the instability can be predicted. In order to enhance the safety margin of the calculations, $\delta\omega_r$ can be increased by 10-30%. Therefore, if $\overline{\omega_r} - 1.3\delta\omega_r \leq \omega_{stb}$, the system is considered too close to the instability region for the given P^* and $\overline{\omega_r}$. The algorithm of choosing $\overline{\omega_r}$ can be summarized as follows:

- If $P^* = \hat{P}_{ave} \rightarrow \overline{\omega_r} = \omega_{opt}$, and in this case if $\overline{\omega_r} - 1.3\delta\omega_r \leq \omega_{stb}$, the demand power reduces to prevent instability.

- If $P^* < \hat{P}_{ave}$, a search solution for $\overline{\omega_r}$ is required where for each operational shaft speed (i.e. 0.7-1.3pu), ω_{stb} and $\delta\omega_r$ are calculated. The search loop should continue until the stability criteria is achieved (i.e. $\overline{\omega_r} - 1.3\delta\omega_r >$

ω_{stb}). If no operating shaft speed satisfies the stability criteria, the demand power needs to be reduced.

It means that the degree to which P^* can approach $\hat{P}_{ave}$ (without violating the stability criteria) depends on $\delta\omega_r$. As $\delta\omega_r$ increases, the degree to which P^* can approach $\hat{P}_{ave}$ decreases. According to (6.14), for a given P^* and $\overline{\omega_r}$, $\delta\omega_r$ mainly depends on δV_w and f_w. As δV_w increases and/or f_w decreases, $\delta\omega_r$ increases. This is because more energy is stored in the rotor inertia. Therefore, the maximum degree to which P^* can approach to $\hat{P}_{ave}$, reduces.

This thesis is not intended to design the search loop for choosing $\overline{\omega_r}$. The next section carried out some simulations, in order to illustrate the calculated ES power rating and energy capacity.

6.3.3 Simulation results for ES energy and power rating

The objective of these simulations is to validate the mathematical expressions for the required ES power rating and energy capacity given by (6.15) and (6.16) respectively. The model simulated is shown in Figure 6.1. The DFIG 1 with parameters provided in Appendix B is used for simulations. Since the results are given in pu, the rating of the DFIG is not important and for DFIGs with different ratings but with the same parameters in pu (i.e. rating wind speed, inertia, etc), the results will be the same. The parameters of the pitch angle PI controller are: k_p=0.01 and k_i=0.005. The ES is again simulated by a DC-voltage source connected to the local grid through an AC/DC converter. The wind speed profiles used in these simulations are made by PSCAD standard wind model explained in Chapter 2. The wind profile consists of a mean value added to 14 sinusoidal components determined with the equation (2.37). The total wind speed variation is δV_w=2.86m/sec (which is a normal wind perturbation) and f_w=0.0833Hz. These values of δV_w and f_w are chosen in order to be able to increase the demand power

P^* up to $\hat{P}_{ave}$ and hence consider a wider range of cases. Figure 6.7 compares the simulation (solid lines) and calculation (dashed lines) values of P_{es} (bottom) and E_{es} (top) for different demand powers and average wind speeds. The average wind speeds are 12.5, 11.5, 10 and 8m/sec and for each of them the demand power is increased up to its associated $\hat{P}_{ave}$ while δV_w and f_w are kept the same.
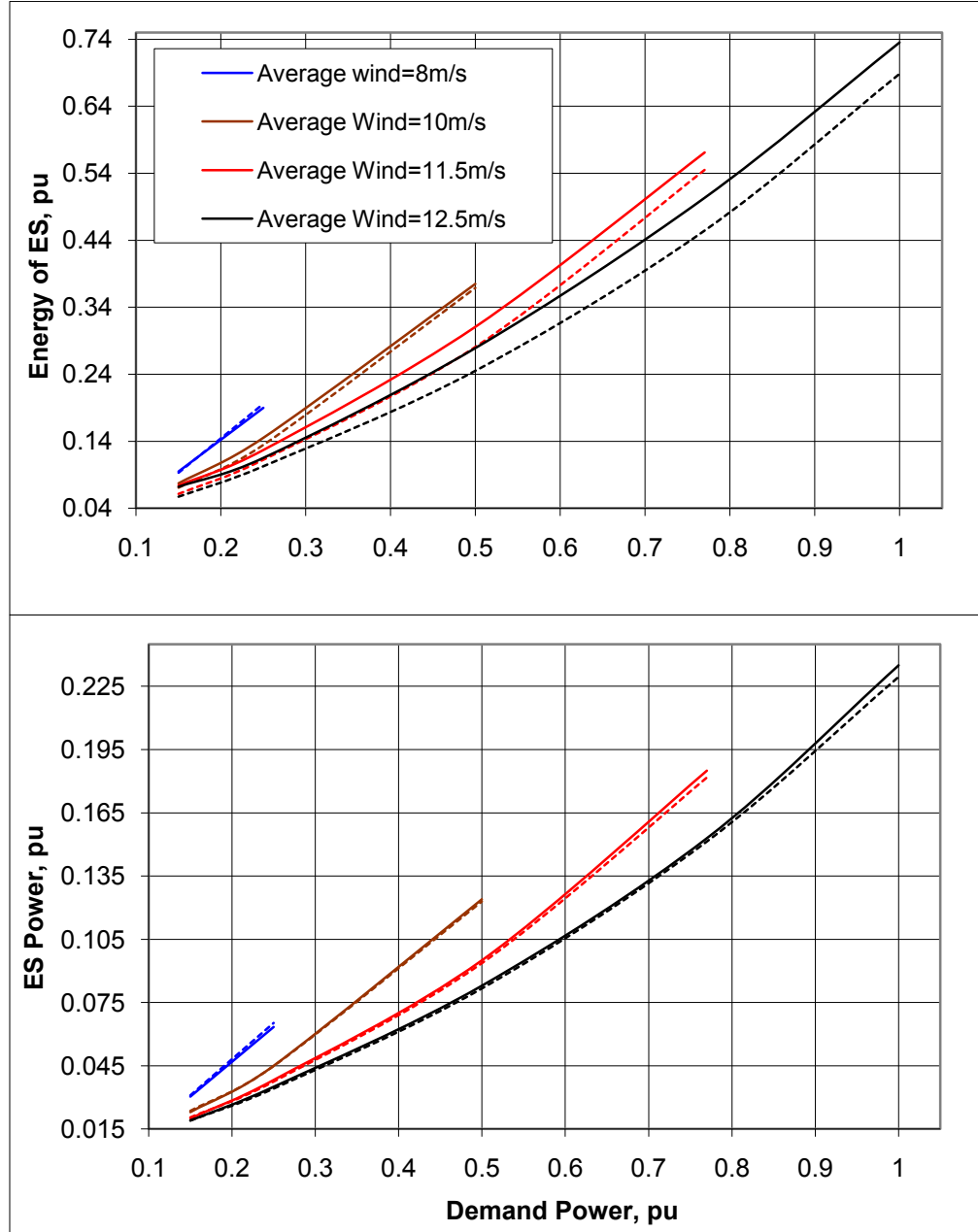

Figure 6.7. Comparison of simulation (solid lines) and calculation (dashed lines) values of P_{es} (bottom) and E_{es} (top) for different demand powers and average wind speeds

For each average wind speed, $\overline{\omega_r}$ is kept at its ω_{opt} for $P^* = \hat{P}_{ave}$. The calculation of ω_{opt} for a given demand power and wind speed is given in Appendix F.

Figure 6.7 shows that the calculation values for P_{es} and E_{es} (given by (6.15) and (6.16)) are acceptably close to their simulation values. The error between the calculation and simulation values for E_{es} is, generally, more than that of the P_{es}. This is simply because of the fact than in calculating E_{es} more simplifications are made. It can be seen that as P^* increases the error increases and the worst case is when $P^* = \hat{P}_{ave} = 1$pu. Since depicting all of the simulation cases shown in Figure 6.7 are not possible, Figure 6.8 shows four cases with different values of P^* and $\overline{V_w}$. The wind speed profile (Figure 6.8a), as explained, is simulated by the PSCAD standard wind model with δV_w and f_w given above. Table 6.1 illustrates the sequence of the events simulated in Figure 6.8. The bold numbers represent the parameter changed compared to the previous event.

Time	0-100sec	100-200sec	200-300sec	300-450sec
$\overline{V_w}$, m/sec	**12.5**	12.5	12.5	**10**
P^*, pu	**0.77**	**1**	**0.5**	0.5

Table 6.1. Sequence of events of the simulation results shown in Figure 6.8

It can be seen that the ES power (Figure 6.8c) and the ES energy (Figure 6.8d) are the same as those given in Figure 6.7. Figure 6.8c shows that the pitch angle (Figure 6.8e) control makes the average of the ES power zero.
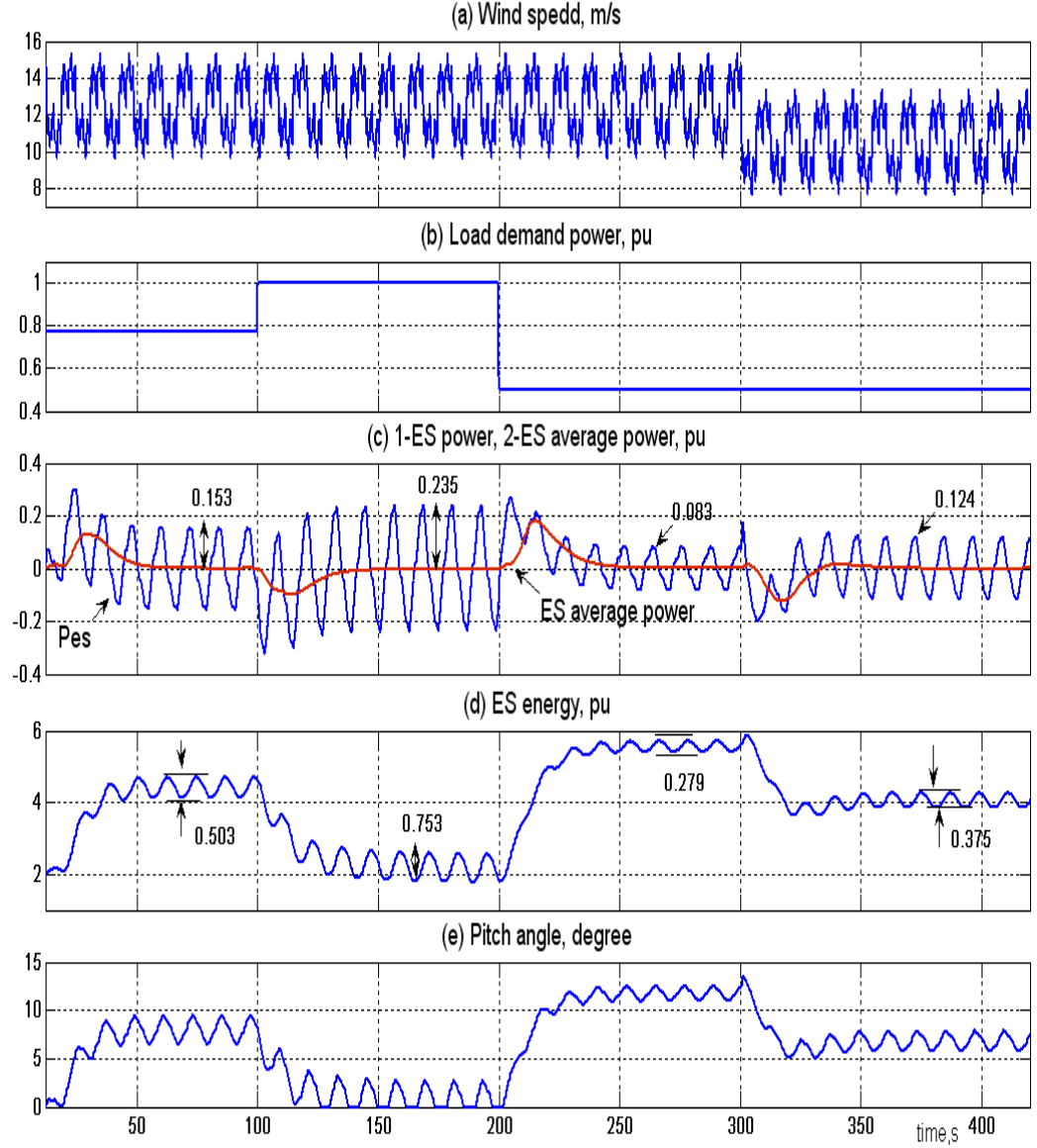
Figure 6.8. Simulation results for validating P_{es} and E_{es} given by (6.15) and (6.16)

The results shown in Figures 6.7 and 6.8 validate the mathematical expressions of P_{es} and E_{es} for a wind speed profile consisting of several sinusoidal components. However, the derived equations do not predict P_{es} and E_{es} satisfactorily in the case of a real wind speed profile. This is because of the fact that in a real wind profile f_w, δV_w and $\overline{V}_w$ are continuously varying. This causes transient variations in P_{es} and E_{es} which are not predictable. It is noted that even in Figure 6.8 the transient values, caused by changing $\overline{V}_w$ or P^*, are not predicted in the mathematical equations. However, it might be possible to find out an experimental coefficient to

adjust the results given by the equations in order to make them more appropriate for cases with real wind speed profiles. This is out of the scope of this research.

6.4 Discussions and conclusions

This chapter considers a wind generator-ES system delivering a constant power demanded by the load while no AG is available. Such a scenario is a case study for a DFIG under CTM control. This is because any non-MPT control (like CTM) stores more wind energy in the rotor inertia and hence reduces the required external ES. When an AG is present, there is no advantage to non-MPT methods since in practice the demand power will exceed the momentary extractable wind power which requires the MPT control in order to minimize the energy demanded from the AG. This chapter describes an electrical torque control scheme by regulating the ES real current. The torque control scheme has been illustrated for CTM and MPT control using PSCAD simulations. However, the control structure can be used to control the electrical torque in any other control method as well. The MPT control will be used in the following chapters.

This chapter attempts to derive mathematically the power rating and energy capacity of the required ES for a given wind profile and demand power. The mathematical results are quite close to the simulation ones in case of a sinusoidal base wind speed profile. Although this not the case for a real wind speed profile, a similar approach might be adopted in future research to obtain satisfactory results in case of real wind speed as well.

As mentioned before the ES rating did not work for real wind profiles. This was because the pitch control did not work to effect a minimum power frequency seen by the ES. The values for f_w tend to be very low for real winds which results in larger ES capacity required. Due to the technological constraints, the capacity of the ES systems is limited. Therefore, in the next two chapters the capacity of the ES system is assumed to be a given parameter. Appendix D calculates the physical size of a hypothetical flywheel ES system for the energy capacity of 1, 5, and 20pu for a 3MVA DFIG. It shows that a 5pu ES system represents a very reasonable

size of the rotating mass. Thus, the capacities of the ES systems in the next two chapters are set at 5pu.

Chapter 7 will consider a full system consisting of droop-controlled DFIGs, external ES, AG and Dispatchable Load (DL). Two different control approaches will be discussed. Chapter 8 will study different structures and scenarios involved such as fault ride-through, no wind scenario, etc.

7. Droop-controlled wind farm delivering a constant demand power with external ES and auxiliary generator

7.1 Introduction

In Chapter 5 a microgrid consisting of a droop-controlled wind farm, an Auxiliary Generator (AG) and a controllable or "Dispatchable Load" (DL) was studied while no external ES is considered. It was shown that in such a scenario the shaft speeds of DFIGs indicate the shortage or excess of the wind energy for a given demand power. If the shaft speed exceeds a high-threshold, the DL is turned on in order to shed the excess energy. Similarly, if the shaft speed drops below a low-threshold, the AG is switched on to inject the energy shortfall and maintain the demand power. It was shown that the low-threshold can be even less than the shaft speed at which the instability occurs ω_{stb} (Figure 5.5) since the proposed control structure prevents the shaft speed from further reduction and inherently recovers the system into the stable region (Figure 5.17). Therefore, the high- and low-thresholds are chosen to keep the shaft speed within the operating region (i.e. 0.7-1.3pu).

Chapter 6 considers a wind generator-ES system when no AG is available. A torque control scheme using the ES real current was proposed and validated using PSCAD simulations. It was seen that such a scenario (i.e. no AG) is a proper case study for a non-Maximum Power Tracking (MPT) control. Therefore, Constant Torque Mode (CTM) control was studied. It was explained that as wind perturbation increases, the shaft speed variation for a given turbine inertia increases which in turn reduces the extent to which P^* can approach $\hat{P}_{ave}$ (the average of the extractable wind power $\hat{P}_{ext}$) without violating the system stability.

This chapter studies a full model consisting of droop-controlled wind farm, external ES, AG and DL, as shown in Figure 7.1. This work assumes that the local

grid voltage and frequency are controlled only by the wind farm using droop characteristics. However in practice, other generating units can also participate in the voltage and frequency control.
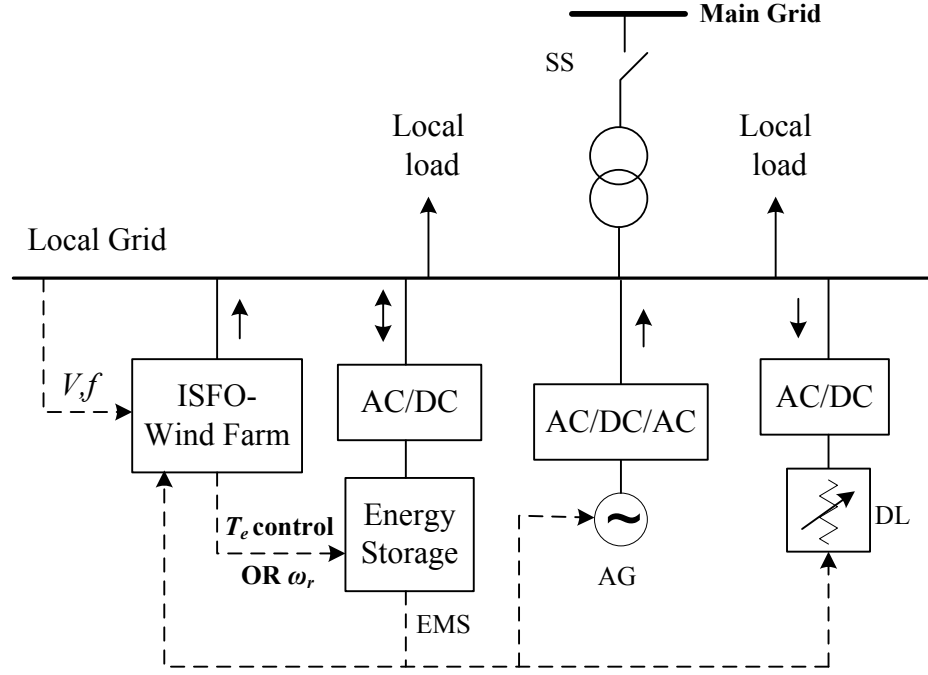
Figure 7.1. Microgrid consisting of droop-controlled wind farm, external ES, AG and DL

Two approaches for controlling the ES are identified in this chapter: The first is similar to the control scheme explained in Chapter 5 in which the shaft inertia is considered only as an ES mechanism. In Chapter 5 the shaft speed of the DFIG is used to actuate the AG and the DL. In the current chapter, however, the ES is actuated by the shaft speed. In other words, if the shaft speed increases/decreases too much, the ES is used to absorb/inject the excess/shortage of energy in order to keep the shaft speed within its operating region. This method will be discussed in section 7.3. An alternative approach, which was explained in Chapter 6, is to use the ES power to control the electrical torque of the DFIGs. This approach, which is the main focus of this chapter, is considered in section 7.4. Chapter 8 will also use the torque control approach and will investigate different possible structures and scenarios.

Each ES system has an energy capacity limit which is imposed by the ES technology and the physical constraints. Therefore, it is necessary to ensure that the energy level of the ES does not exceed the maximum limit, nor becomes less than zero (since negative energy has no physical meaning). As a result, in any ES control method, including the two control approaches considered in this chapter, an Energy Management System (EMS) is required to prevent the ES from saturation. This is explained in the next section.

This chapter utilizes the variable droop control method explained in Chapter 5, however, the proposed control schemes in this chapter are also applicable with the standard droop as well.

7.2 Energy Management System for ES

The EMS and the pitch angle control are illustrated in Figure 7.2. First the maximum limit of the ES must be determined. As discussed in the previous chapter, sizing of the required ES is not easily possible due to the random nature of real wind speed profiles. Appendix D shows that a 5pu ES for a 3MVA DFIG represents a very modest rotating mass, assuming a flywheel ES. Therefore, in this chapter the maximum energy capacity of the ES is chosen to be $5pu_{gen}$. However, the proposed control structure, shown in Figure 7.2, is quite applicable for ES systems with other energy ratings.

When the demand power P^* is more than the extractable wind power (i.e. power transmitted to the shaft with $\beta=0$) $\hat{P}_{ext}$, the energy stored in the ES reduces to compensate for the energy shortage. If the energy level of the ES drops below a certain low-threshold E_{es-low} (e.g. 0.5-1pu), the AG is turned on via a real current demand I_{d-AG}^* in order to supply the shortfall between P^* and $\hat{P}_{ext}$ and prevent the energy of the ES from further reduction. It is noted that since the local grid voltage is regulated by the DFIG, the AG power P_{AG} is proportional to I_{AG} controlled by the Power Flow Controller (PFC).
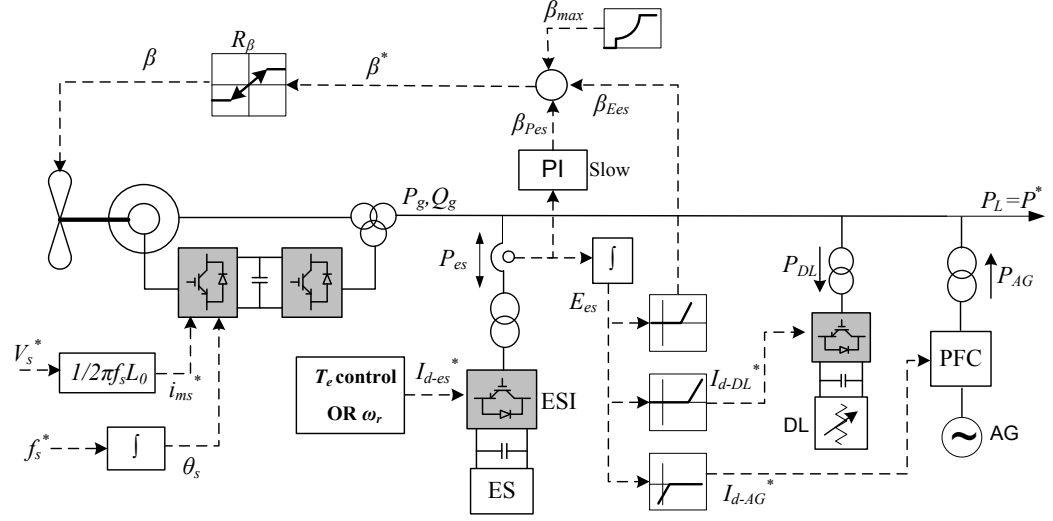
Figure 7.2. Energy Management System and pitch angle control schemes

In another situation the demand power can be too low compared to the available wind power. Therefore, the extra energy is absorbed by the ES and causes E_{es} to increase. If E_{es} exceeds a high-threshold ($E_{es-high1}$), the pitch angle is increased through the signal β_{Ees} in order to reduce the wind energy captured. If the maximum slew rate of the pitch angle R_{β} is not fast enough, E_{es} keeps rising until it exceeds a higher-threshold $E_{es-high2}>E_{es-high1}$. The DL is then switched on via a converter real current demand I_{d-DL}^{*} and absorbs the extra wind energy to prevent the ES from saturation. In such a case a trade-off mechanism is possible in which a slow pitch angle may result in a large DL. It will be shown in this chapter that a pitch control with a slew rate of maximum 5°/sec, (which is a normal rate), results in elimination of the need for a DL. It is emphasized that the concept of using pitch angle in order to shed the output power is quite acceptable and is applied on current wind generators.

7.2.1 Pitch angle control

The pitch angle control, which is shown in Figure 7.2, consists of three parts: $\beta^{*} = \beta_{Pes} + \beta_{Ees} + \beta_{\max}$. The β_{Pes}, which was introduced in Chapter 6, is used to reduce the power rating of the ES through controlling the average of P_{es} toward zero using a very slow PI controller. The bandwidth of the PI controller is not

critical as system can operate without this part. The β_{Ees} is part of the EMS explained above and can be used to reduce the rating of the DL. Finally, the β_{max} is the standard pitch angle control for wind generators and is used to keep the output power around 1pu and to prevent the shaft speed from exceeding its maximum limit (i.e. 1.3pu) for wind speeds above rated. The summation of the three parts is rate-limited to make sure that the pitch angle cannot vary too fast.

The next two sections studies the two ES control approaches mentioned above.

7.3 ES actuated by shaft speed

The idea behind this control approach is similar to the one used in Chapter 5 in which the shaft speed is controlled within its operating region (i.e. 0.7-1.3pu) using the AG and the DL. In a similar way, the ES can be used to control the shaft speed within its operating region, as is shown in Figure 7.3.
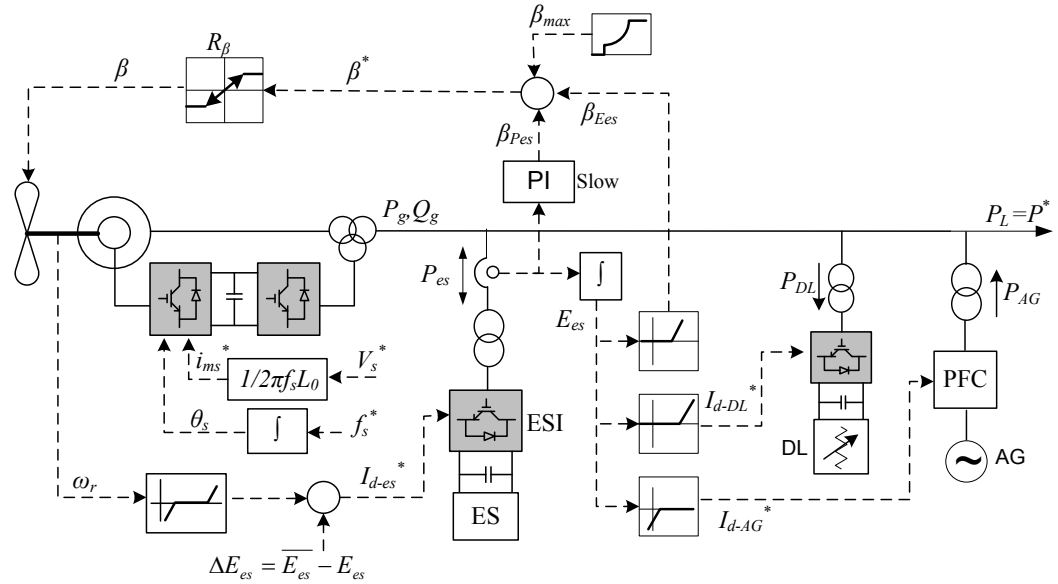

Figure 7.3. ISFO-controlled DFIG with external ES while ES is actuated by the shaft speed

When P^* is less than $\hat{P}_{ext}$, the shaft speed increases. If ω_r exceeds a high-threshold value, the ES absorbs the extra energy through a real current demand I_{d-es}^* which is controlled by the ES interface (ESI). Therefore, ω_r stops rising. Since the local

grid voltage is controlled by the DFIG, the ES power P_{es} is proportional to $I_{d\text{-}es}$.

For P^* more than $\hat{P}_{ext}$, the shaft speed reduces. If ω_r drops below a low-threshold value, the ES injects the energy shortfall to prevent the shaft speed from further reduction. Comparing this structure with the one proposed in Chapter 5 (i.e. without ES), the ES operates as a buffer between the wind farm, on one side, and the AG and DL, on the other. This may help to reduce the frequency of events in which the AG and the DL are turned on. Reducing the turn on and off events is an advantage if for example the AG is a diesel generator. As shown in Chapter 5, the low-threshold value can be less than ω_{stb} (see Figure 5.17).

As discussed in Chapter 2, the operating region of DFIGs shaft speed is 0.7-1.3pu. Considering at least 0.1pu for a safety margin (0.05pu for each side), the maximum inertial energy can be stored is $E_J=0.5J(1.25^2\text{-}0.75^2)=1.75$pu for $J=3.5$pu, which is not a very large amount of energy. Therefore, it is expected that, as wind speed varies, the shaft speed varies from the low-threshold to the high-threshold frequently which in turn causes the ES to switch on and off quite frequently (this will be shown through simulation). It is noted that in Chapter 5 the pitch angle controls the shaft speed. However, since there is no direct shaft speed control in this structure (i.e. a specific shaft speed reference), ω_r varies as wind speed changes. The frequent turning on and off of the ES may not be desirable for certain ES technologies. Therefore, the best control scenario is to make the shaft speed stay around the high-threshold value for $P^*<\hat{P}_{ext}$, and stay around the low-threshold value for $P^*>\hat{P}_{ext}$. This makes the best use of the shaft inertia as an ES mechanism, because the energy level of the turbine inertia (which is a function of ω_r) is around the maximum limit (high-threshold value) when there is excess of energy, while when there is lack of energy, ω_r is around the minimum (low-threshold) value. In order to achieve this, the term $\Delta E_{es} = \overline{E_{es}} - E_{es}$ is added to the output of the shaft speed limit controller (Figure 7.3). The $\overline{E_{es}}$ value is half of the ES capacity and E_{es} is the instantaneous energy of ES. Therefore, the term ΔE_{es} is

always positive for $P^* > \hat{P}_{ext}$, and is always negative for $P^* < \hat{P}_{ext}$. Using this method the ω_r and E_{es} are synchronized in the sense that, for $P^* > \hat{P}_{ext}$, both ω_r and E_{es} approach their maximum limits together and for $P^* < \hat{P}_{ext}$, they both stay around their minimum limits. In other words, the shaft inertia appears solely as an ES mechanism for the system. Although this control structure makes the best use of the shaft inertia as an ES mechanism, it will be shown in section 7.4 that this is not necessarily the best wind generator control method. The next section validates the proposed control structure using PSCAD simulations.

7.3.1 Simulation results for ES actuated by shaft speed

This section consists of two simulations. The term ΔE_{es} is considered in the first simulation results while it is not considered in the second simulation. The objective of the simulation is to validate the proposed control structure. The simulated model, which is shown in Figure 7.4, consists of two variable droop-controlled DFIGs with the ES system distributed within individual DFIGs.
In Figure 7.4 the AG and the DL are aggregated on to the local grid while the ES is distributed amongst the turbines. However, the DL can also be distributed within individual DFIGs while the ES can be also aggregated on to the local grid. These structures will be investigated in Chapter 8.
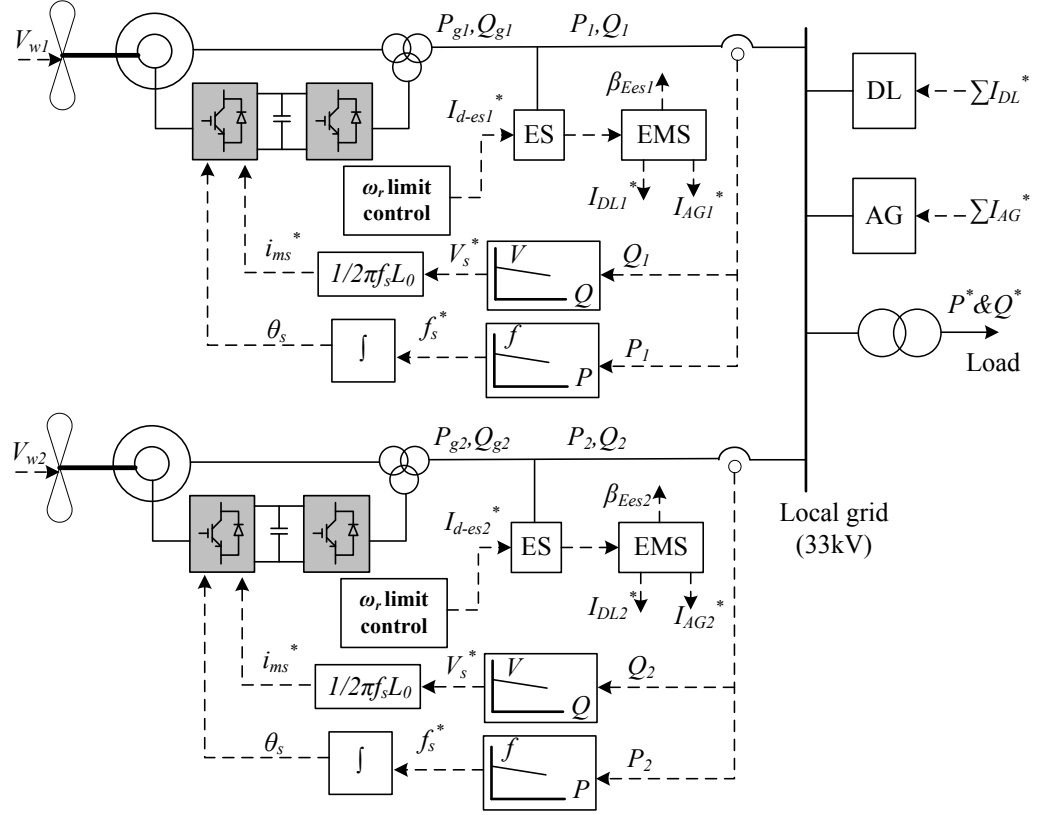
Figure 7.4. Droop-controlled wind farm with distributed ES within individual wind generators while the ES is actuated by the shaft speed

As it can be seen from Figure 7.4, each ES system is equipped with the ω_r limit control and the EMS explained above. The pitch angle control (not shown in the Figure) is the same as the one depicted in Figure 7.3 with maximum slew rate of $3°/\text{sec}$. The parameters of the pitch angles PI controllers are: $k_p=0.01$ and $k_i=0.005$. Each EMS produces the current references for the DL and the AG. The summations $\sum I_{DL}{}^*$ and $\sum I_{AG}{}^*$ are formed and transferred over a communication link since these are aggregated. Obviously, the communication is local for the distributed elements. The ratings of the first and the second DFIGs are 0.66pu and 0.34pu with the parameters given in Appendix B. Although the variable droop method is considered here, the standard droop is applicable too. The ES, AG and DL are simulated by DC-voltage sources connected to the local grid through an AC/DC converter. The energy capacity of each ES is 5pu$_{\text{gen}}$. For $\omega_r > 1.2\text{pu}$, $I_{d-es}{}^* =130\omega_r$ and for $\omega_r<0.8\text{pu}$, $I_{d-es}{}^*=-150\omega_r$. For $E_{es}>3.3\text{pu}$, $\beta_{Ees}=20E_{es}$, for $E_{es}>4.3\text{pu}$, $I_{DL}{}^*=50E_{es}$ and for $E_{es}<0.7\text{pu}$, $I_{AG}{}^*=-80E_{es}$. These gains are determined

by trial and error, however, in practice they must be designed taking the dynamics of the ES, AG and the DL into account. The slower the dynamic, gains with larger absolute values are needed. Moreover, if there is a delay in turning on the ES, AG and DL, the high/low-threshold values may need to be decreased/increased in order to compensate for the delay. This thesis is only intended to illustrate the proposed control structure and a full-detailed engineering design is beyond the scope of the research. The ES, AG and DL current control loops are identical to the DFIG grid side converter explained in Chapter 2. The load is simulated by a variable current source demanding active and reactive power determined by the system operator.

Simulation results1: ΔE_{es} *is considered*

This part simulates the model illustrated in Figure 7.4 while the term ΔE_{es} is included in the ω_r limit controllers of Figure 7.4. Since the ES capacity is 5pu$_{gen}$, $\overline{E_{es}} = 2.5$. The simulation results are illustrated in Figure 7.5.

The average of the real wind speed profiles (Figure 7.5a) is approximately 12.5m/sec which corresponds to $\hat{P}_{ave} = 1$pu$_{gen}$. The standard deviations of the first and the second wind profile are 1.28 and 1.39 respectively which are relatively large perturbations. Over the first 200sec, the demand power (Figure 7.5b) is 0.5pu which is less that $\hat{P}_{ext}$. Therefore, the extra wind energy increases the shaft speeds (Figure 7.5c). However, since the inertial ES of the turbine is not sufficient, for $\omega_r>1.2$pu, the ES systems absorb the excess of the wind energy, hence the E_{es} value (Figure 7.5d) is increased. As a result, the shaft speeds stop increasing. For $E_{es}>3.3$pu$_{gen}$, the pitch angles (Figure 7.5i) increase in order to reduce the wind energy captured. It can be seen that with the pitch angle control with a maximum slew rate of 3°/sec the DL (Figure 7.5h) is not activated. Slower pitch angle slew rate will be considered for the torque-control ES in the section 7.4.
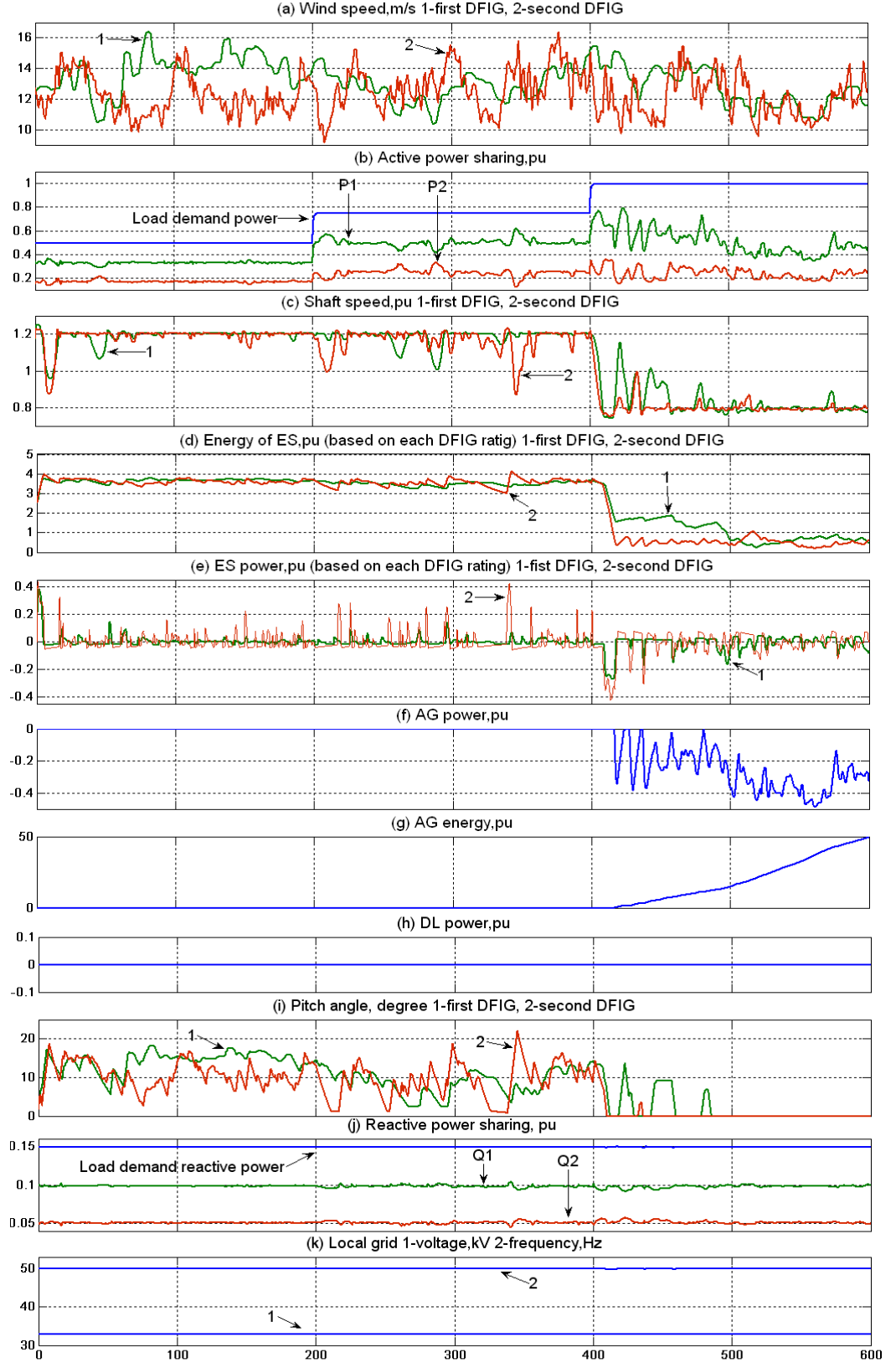
Figure 7.5. Simulation results of model shown in Figure 7.4 with $\overline{E_{es}} - E_{es}$ included

During the second 200sec the demand power is increased to 0.75pu which is occasionally more than $\hat{P}_{ext}$. This causes the shaft speeds to reduce occasionally. However, since the shaft speeds never drop to less than 0.8pu, the energy levels of the ES (Figure 7.5d) do not decrease. Over the last 200sec the demand power is raised to 1pu which is more than $\hat{P}_{ext}$ for almost the entire period. Therefore, the both shaft speeds drop below 0.8pu which cause the energy level of the ES to reduce. Since the energy stored in the ES systems is not enough, the energy level of the ES systems becomes less than 0.7pu which in turn switches the AG on. The total energy demanded from the AG (Figure 7.5g), which is derived by integrating P_{AG} (Figure 7.5f), is 50pu. Provided that the wind energy is enough to fill the ES, increasing the capacity of the ES can reduce the total energy demanded from the AG. The ES powers (Figure 7.5e) are always less than ±0.6pu$_{gen}$. This means that the ES systems can be connected to the DFIG DC-link, hence reducing the required power electronic devices. Figure 7.5j shows the reactive power sharing for Q^*=0.15pu. It can be seen from Figure 7.5k that the local grid voltage and frequency are well-regulated by the wind generator through droop controls.

Simulation results1: ΔE_{es} not considered

This part also simulates the model shown in Figure 7.4. But this time the term ΔE_{es} is not included in the ω_r limit controllers. The main objective of this simulation is to compare these results with those with the term ΔE_{es} (Figure 7.5). The results are shown in Figure 7.6. The same wind profiles and simulation scenario as Figure 7.5 is considered here. As expected, unlike Figure 7.5, the shaft speeds (Figure 7.6c) varies from the low-threshold to the high-threshold quite frequently. This is because in this case the shaft speed is not "synchronized" with E_{es} (Figure 7.6d) i.e. does not increase or decrease with an increase or decrease of E_{es}, unlike the one with ΔE_{es} (Figure 7.5c &d). The method without ΔE_{es} requires the ES systems to turn on and off very frequently (as can be seen from Figure 7.6e) which may not be desired for some ES technologies. However, increasing

the turbine inertia can result in a smoother shaft speed variation which in turn can reduce the ES turn on and off incidents. The reactive power sharing, pitch angle control and the local grid voltage and frequency are identical to those of Figure 7.5 and not shown here. The results of Figure 7.6 show that the system can still operate without the term ΔE_{es} .
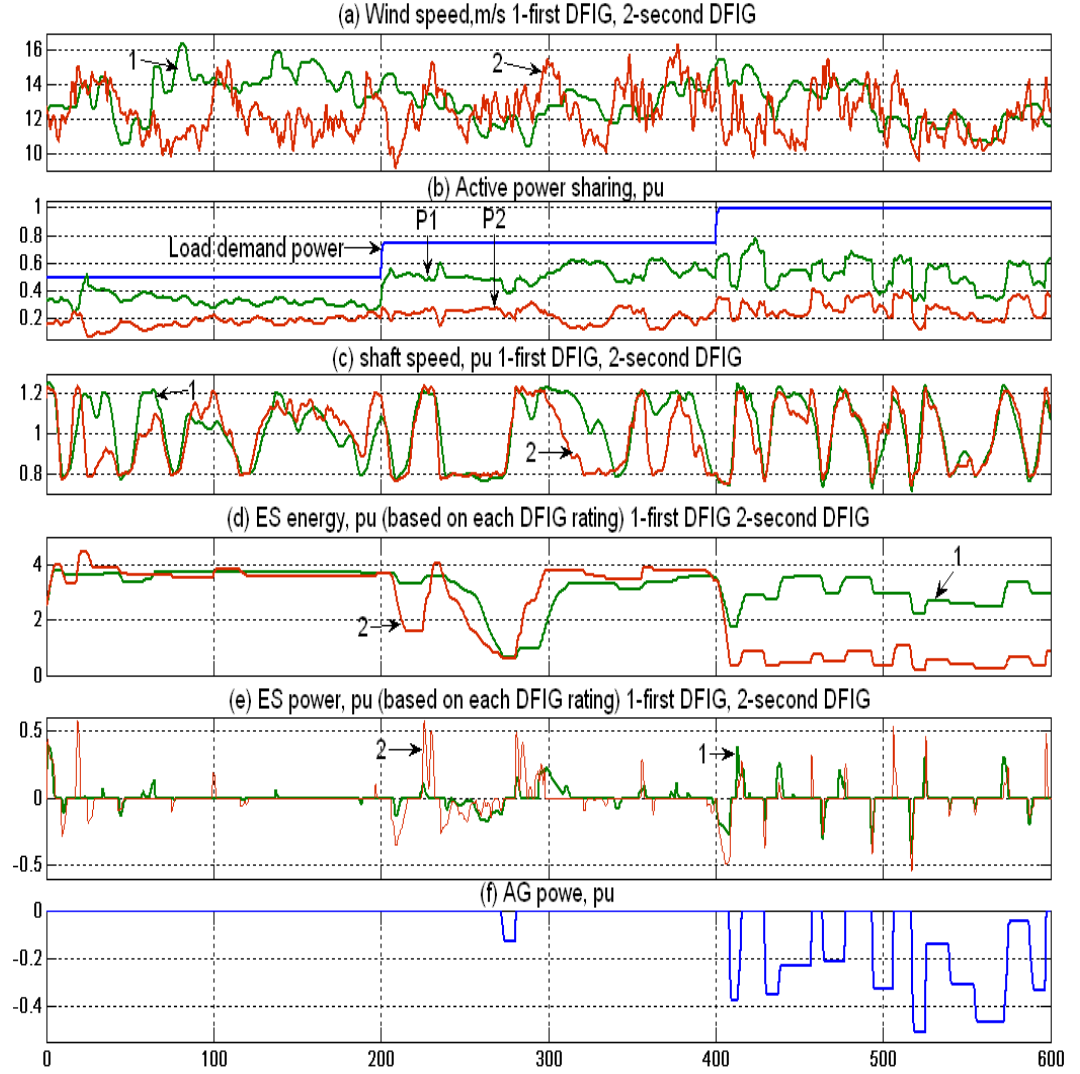
Figure 7.6. Simulation results of model shown in Figure 7.4 while $\overline{E_{es}} - E_{es}$ is not included

In the proposed control structure in this section, in which the ES is actuated by the shaft speed, the turbine inertia is being exploited as an ES mechanism which can have the advantage of reducing the external ES required. The main drawback of this approach is more evident for $P^* < \hat{P}_{ext}$. In such cases, the wind generator is

expected to generate the maximum wind power in order to minimize the energy demanded from the AG. It implies that the DFIG must be controlled under the Maximum Power Tracking (MPT) mode, which is not the case in the proposed control structure. In the control scheme proposed in Chapter 5, it is not possible to control the electrical torque T_e directly, as there is no external ES. However in this chapter, the ES real current can be used to control T_e under MPT, as shown in Chapter 6. This is the subject of the next section.

7.4 ES power regulating the DFIG electrical torque

Chapter 6 proposes a T_e control scheme through regulating ES real current. The control scheme was validated using PSCAD simulation for controlling the DFIG under MPT mode. The same control structure, as shown in Figure 7.7, is used in this section.

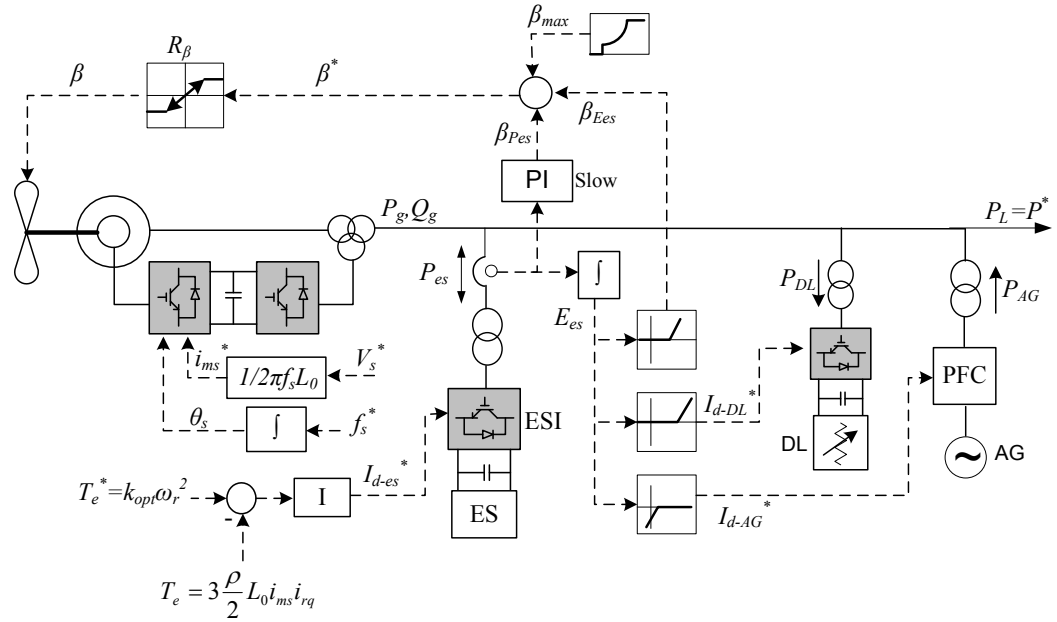Figure 7.7. Proposed scheme to control an ISFO-controlled DFIG under MPT mode

The pitch control and the EMS are identical to those explained in section 7.2. The torque control loop design was explained and validated in Chapter 6. In Chapter 6 no AG and DL were considered. However, it was shown that the load demand power appears as a disturbance and can be ignored in the control design. Similarly,

the AG and DL powers can be neglected for designing the torque control loop. The effectiveness of the proposed control loop in a multi-DFIG system including the AG and the DL will be validated in this section through PSCAD simulations.

7.4.1 Simulation results for ES controlling the DFIG electrical torque

This section is intended to validate the proposed torque control scheme, the EMS and the pitch control in a multi-DFIG system. Two simulations are undertaken in this section. The first simulation considers a pitch angle control with normal slew rate while the second one considers a slow pitch control. The objective here is to show the trade-off between the pitch angle slew rate and the size of the required DL. The model simulated in this section is depicted in Figure 7.8. Although the ES systems are distributed within individual DFIGs, it will be shown in Chapter 8 that the ES can be aggregated on to the local grid which necessitates communications. The ratings of the first and the second DFIGs are 0.66pu and 0.34pu with parameters given in Appendix B. The pitch angle controls (not shown in the figure) and the EMSs are identical to the one shown in Figure 7.7. The threshold values for the EMSs are those explained in section 7.3.1. It was explained in Chapter 6 that an integral control is sufficient for the torque control loop since the controlled plant is modeled by a gain. For a torque control with bandwidth of 15Hz, the integral control gain is 240, which is used in the two simulations carried out in this section.
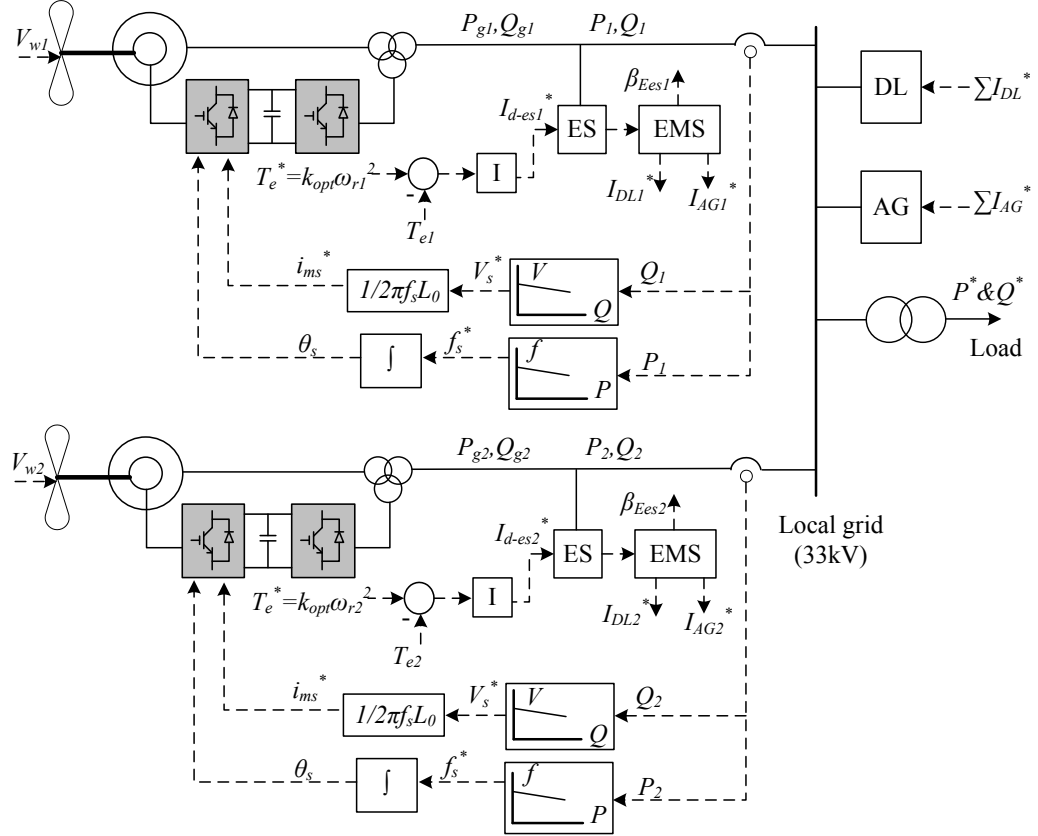
Figure 7.8. Droop-controlled wind farm while distributed ES within individual DFIGs controls the electrical torque of the associated DFIG

Simulation results1: Normal slew rate for pitch controllers

The simulated model is shown in Figure 7.8. The pitch angle maximum slew rate R_β=5°/sec. It is mentioned in [45] that "the pitch speed can exceed 10°/sec during emergencies". Therefore, 5°/sec seems to be a normal slew rate. The simulation results are shown in Figure 7.9. The wind speed and the simulation scenario are identical to those of Figure 7.5 (i.e. ES actuated by the shaft speeds). During the first 200sec, P^*=0.5pu which is less than $\hat{P}_{ext}$. As a result, E_{es} (Figure 7.9d) increases. For E_{es}>3.3pu$_{gen}$, the pitch angles (Figure 7.9i) rise to prevent E_{es} from further increase and hence introducing the DL. It is noted that the shaft speeds (Figure 7.9c), unlike Figure 7.5c, do not increase to their maximum limit. This is because in this structure the shaft speeds are controlled (indirectly) in order to extract the maximum wind power. Consequently, a slightly faster pitch control (5°/sec) than the one used in Figure 7.5i (i.e. 3°/sec) is required in order to

eliminate the need for a DL. Similar to Figure 7.5, over the second 200sec during which P^*=0.75pu, no AG and DL is needed. During the last 200sec, demand power is increased to 1pu. As in Figure 7.5, the energy levels of the ES reduce to less than 0.7pu$_{gen}$ which turns on the AG (Figure 7.9f). However, unlike Figure 7.5c, the shaft speeds (Figure 7.9c) do not decrease. This is because in Figure 7.5 the rotor inertia is exploited as an ES mechanism and its kinetic energy (ω_r) reduces when there is lack of energy (i.e. $P^*>\hat{P}_{ext}$). However in Figure 7.9, the shaft speeds stay at relatively high values in order to track the maximum wind power. As a result only 25pu energy is demanded from the AG (Figure 7.9g) which is half that in the case of the shaft speed-actuated ES system (Figure 7.5g).

Figure 7.10 shows the DFIGs output powers vs their shaft speeds on the P_t-ω_r characteristics for different wind speeds. Figure 7.10 demonstrates the effectiveness of the proposed torque control scheme in a multi-DFIG system including an AG and a DL.

It can be concluded that the advantage of this scheme is that it significantly reduces the required energy from the AG for $P^*>\hat{P}_{ext}$. This advantage comes with a slightly faster pitch angle requirements in order to eliminate the need for a DL for $P^*<\hat{P}_{ext}$. However, considering the DL as a long-term ES (such as hydrogen generation station, compressed air, etc), generating maximum wind power can be considered as an advantage rather than a disadvantage. An alternative approach is to operate in a non-MPT mode (e.g. CTM or the shaft speed-actuated ES control method explained above) for $E_{es}>\overline{E_{es}}$ (when $P^*<\hat{P}_{ext}$) in order to reduce the DL power, and also to switch over to the MPT mode for $E_{es}<\overline{E_{es}}$ (when $P^*>\hat{P}_{ext}$) in order to reduce the AG power. This approach, however, is not considered in this work.
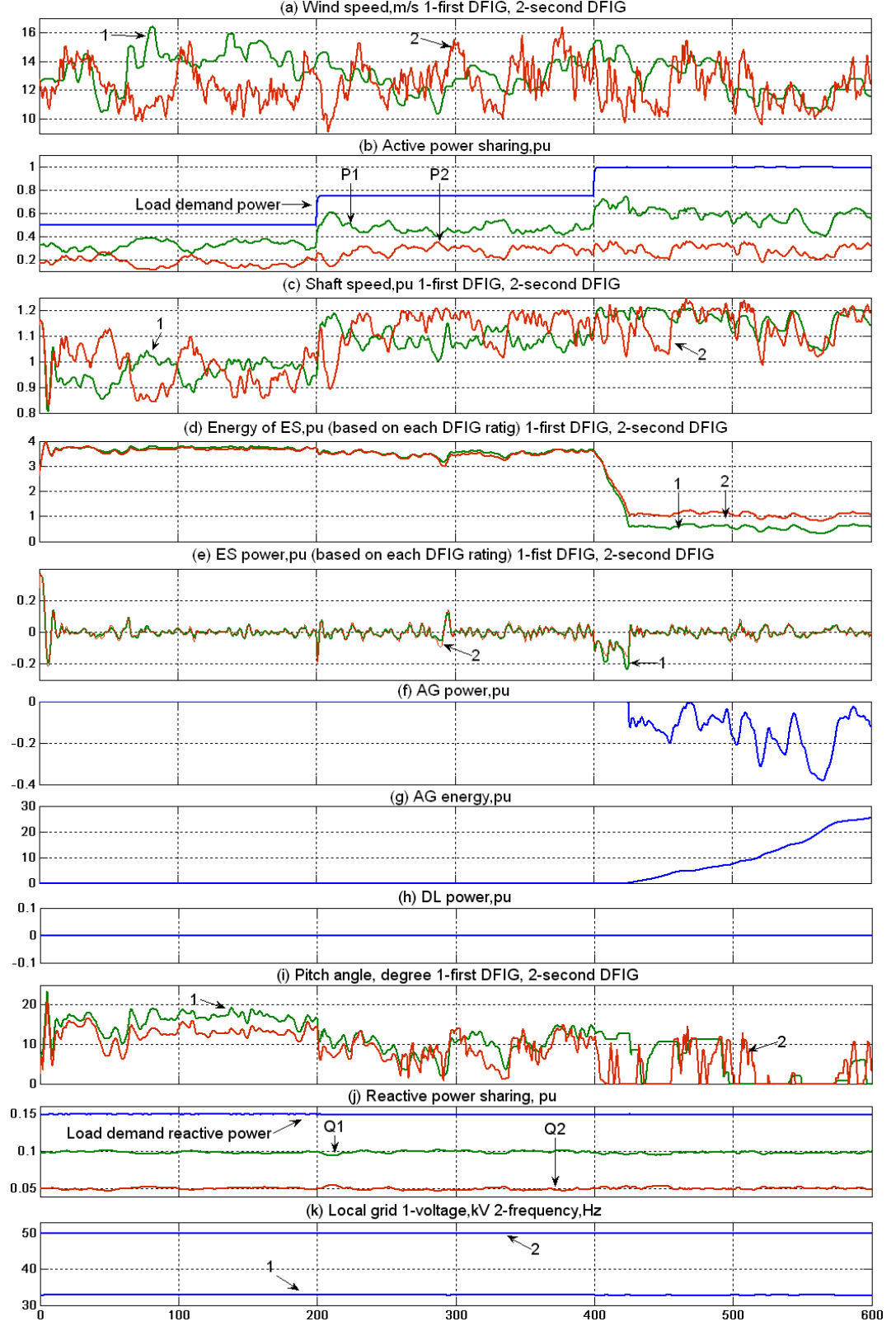
Figure 7.9. Simulation results of model shown in Figure 7.8 with pitch angle slew rate of 5º/sec
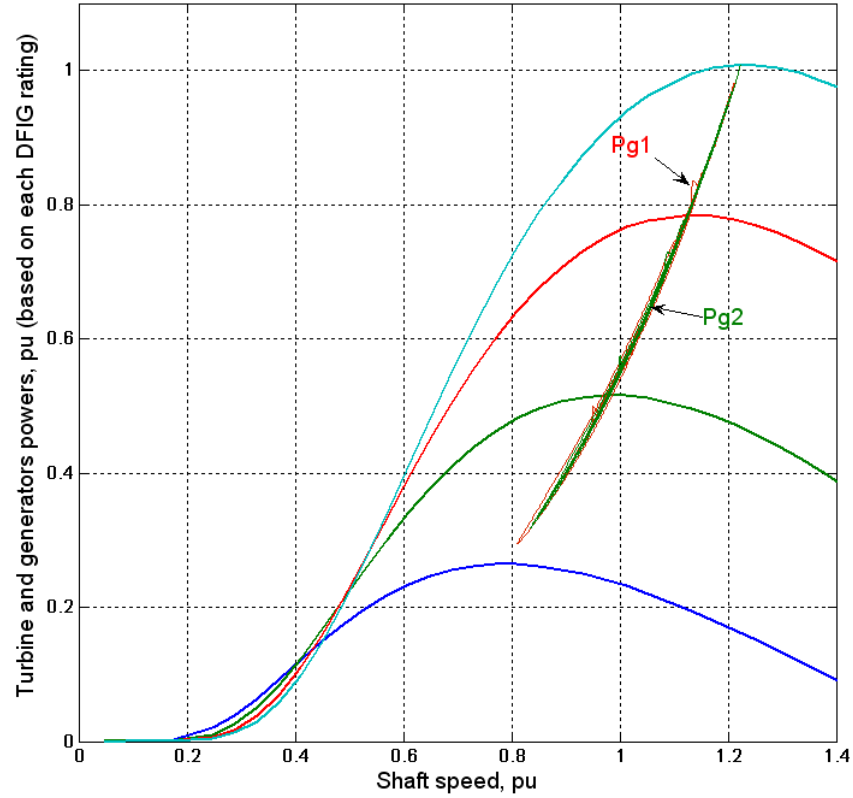
Figure 7.10. DFIGs output powers vs their shaft speeds on P_t-ω_r characteristics for different wind speeds

Simulation results2: Slow slew rate for pitch controllers

This section also simulates the model shown in Figure 7.8. But this time the maximum pitch angle slew rate is 1°/sec. The simulation results are shown in Figure 7.11. The wind speed profiles, simulation scenario, DFIGs' ratings, EMS thresholds and the torque controls are the same as the previous simulation (i.e. with 5°/sec pitch angle slew rate). The slow pitch angle (Figure 7.11e) slew rate results in the introduction of the DL (Figure 7.11g) during the first 200sec in which P^*=0.5pu. This is not the case for the normal pitch angle slew rate (Figure 7.9h). The slow pitch angle also causes the AG (Figure 7.11f) to inject energy for P^*=0.5 and P^*=0.75pu. Note that no energy from the AG is needed for P^*=0.5 and P^*=0.75pu in the case of a normal pitch angle slew rate (Figure 7.9f). This is simply because the pitch angle can return to smaller values fast enough in order to increase the output DFIG power and to prevent the introduction of the AG.

Figure 7.11. Simulation results of model shown in Figure 7.8 with pitch angle slew rate of 1°/sec

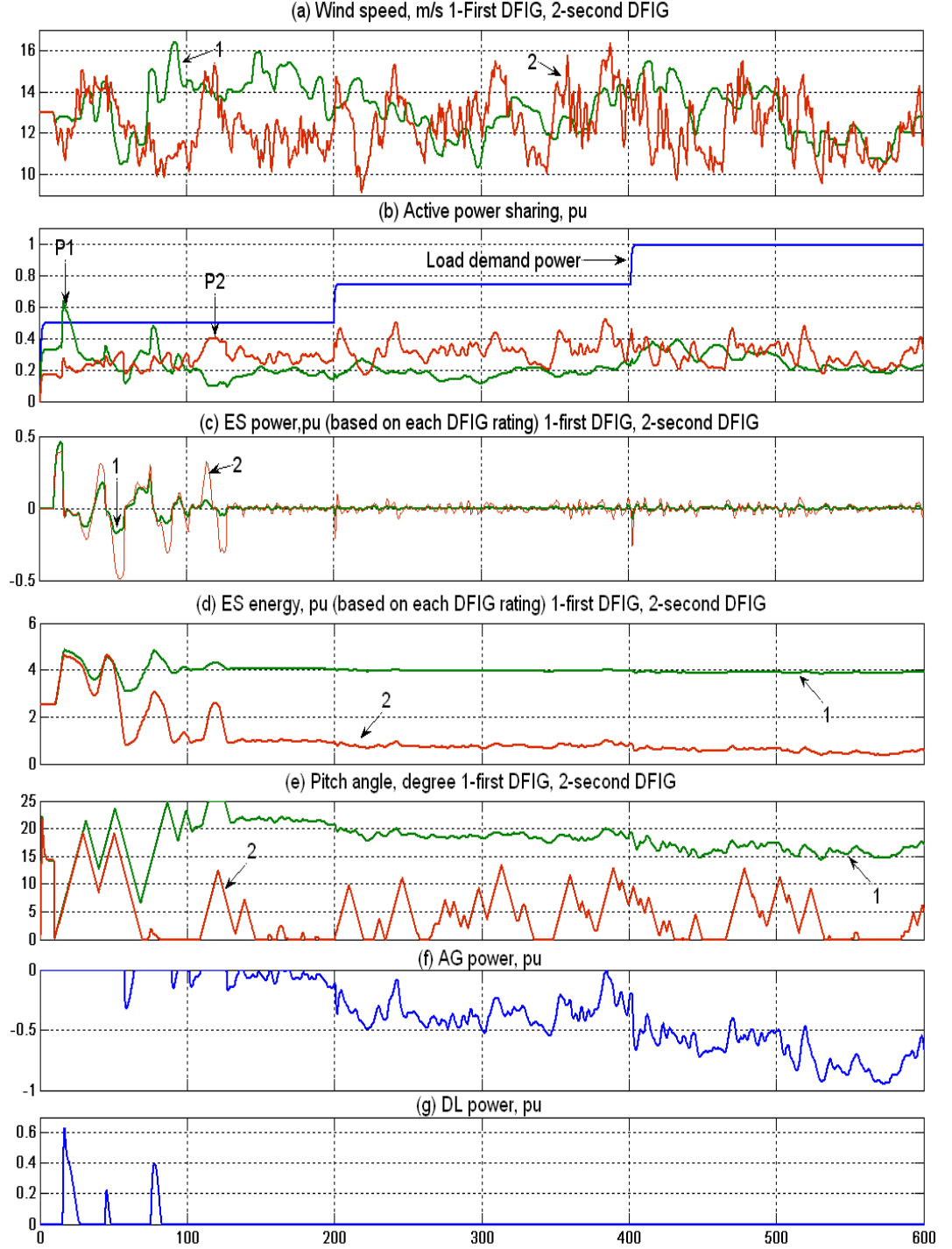It is noted that the increase in the AG power is an inevitable consequence of the slow pitch angle control which is also the case for the standard DSFO-controlled DFIG. Figure 7.11c shows that despite the slow pitch control, the ES powers are

still less than $\pm 0.6\text{pu}_{grn}$ which suggest that the ES can be connected to the DFIGs' DC-link. The reactive power sharing, local grid voltage and frequency are identical to the previous simulation and not shown here. The results given in Figure 7.9 and Figure 7.11 demonstrate the trade-off between the pitch angle slew rate and the size of the DL. The faster the pitch angle, the smaller the DL is required. Obviously, it is possible to have DL with normal slew pitch control by reducing (or even eliminating) β_{Ees} (Figure 7.7), if required.

7.5 Torque controlling-ES system using simplified DFIG model

PSCAD simulation of a multi-DFIG system including wind turbine, pitch controllers, real wind speed profiles and ES; connected to the AG and DL for the 600s simulation takes several hours. A simplified ISFO-controlled DFIG was introduced in section 5.4 in order to increase the number of the simulated DFIGs. The same concept is also used in Figure 7.12 in order to simplify a droop-controlled DFIG equipped with T_e-controlling ES scheme. In the simplified model the DFIG is represented by a droop-controlled voltage source while its electrical torque is derived by $T_e = P_g/\omega_r$, where P_g is the DFIG output power. The full wind turbine model is, however, included. The next section used the simplified model to simulate an array of droop-controlled DFIGs using the variable droop method introduced in Chapter 5.
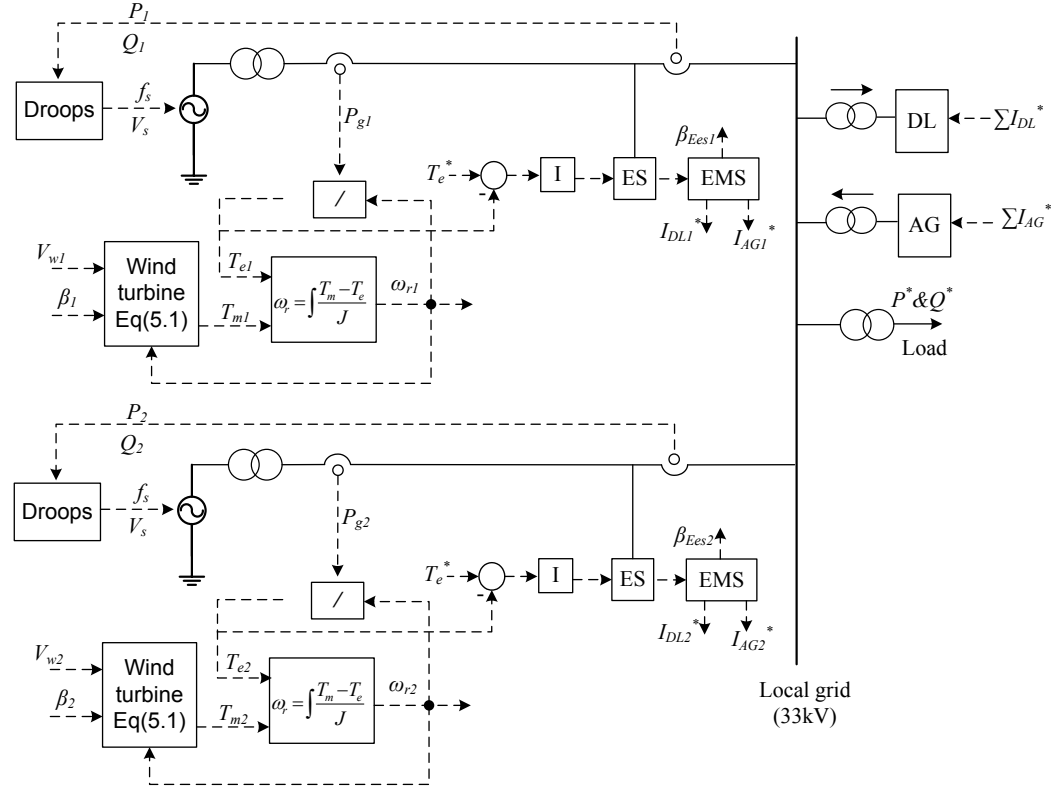
Figure 7.12. Simplified droop-controlled DFIGs equipped with torque controlling-ES systems

7.5.1 Simulation results of four simplified droop-controlled DFIGs equipped with distributed T_e-controlling ES systems

The model simulated in this section consists of four simplified droop-controlled DFIGs with distributed ES systems controlling the associated DFIG's electrical torque, as is shown in Figure 7.12. In Figure 7.12, for the sake of simplicity, only two DFIGs are depicted. However in the model simulated, four DFIGs are used. The droop characteristics, torque control loop, EMS and pitch controls (not shown in the figure) are the same as before. The objective of this simulation is to validate the EMS and the torque control scheme in a system consisting of more than two DFIGs. The rating of the first and the third DFIGs are 0.33pu while those of the second and the forth DFIGs are 0.17pu. There are two real wind speed profiles (Figure 7.13a) with the average of approximately 12.5m/s ($\hat{P}_{ave} \approx 1\text{pu}_{gen}$) and the

standard deviations of 1.28 and 1.39. The first wind speed profile is applied to the first and the fourth DFIGs while the second wind speed profile is applied to the second and the third DFIGs. Therefore, the DFIGs with the same rating are applied with different wind speed profiles. The simulation results are show in Figure 7.13. For the first 200sec, P^*=1pu (Figure 7.13b). Therefore the energy levels of the ESs (Figure 7.13c&d) drop below 0.7pu$_{gen}$ which turns on the AG (Figure 7.13k). Over the second 200sec, P^*=0.75pu. Since the maximum pitch angle (Figure 7.13i&j) slew rates are 3°/sec, the AG and DL (Figure 7.13l) powers are zero. And finally during the last 200sec, P^*=0.75pu which is less than $\hat{P}_{ext}$. Since the pitch angle is not fast enough, some DL power is required. The 3°/sec slew rate is chosen intentionally in order to test both AG and DL. It can be shown that using a slew rate of 5°/sec will make the presence of a DL unnecessary. It can be seen that the ES powers (Figure 7.13e&f) are much less than ±0.6pu$_{gen}$ which implies that the ES systems can be connected to the DFIGs' DC-link. Figure 7.13m shows the reactive power sharing for Q^*=0.15pu. Figure 7.13n illustrates that the local grid voltage and frequency are well-controlled by the droop-controlled DFIGs.
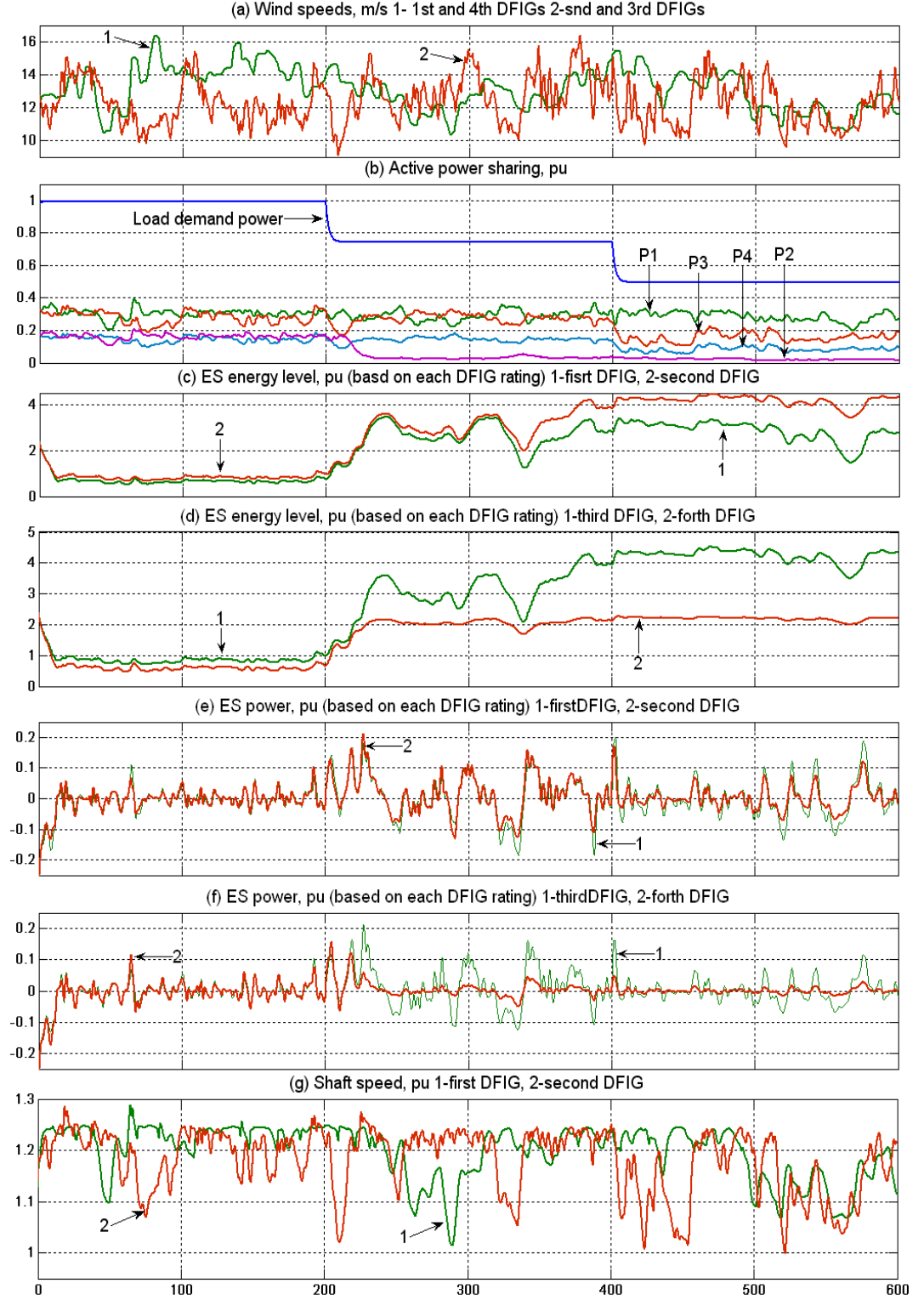
Figure 7.13 (Part 1): A microgrid including four droop-controlled DFIGs with distributed T_e-controlling ES systems, AG and DL
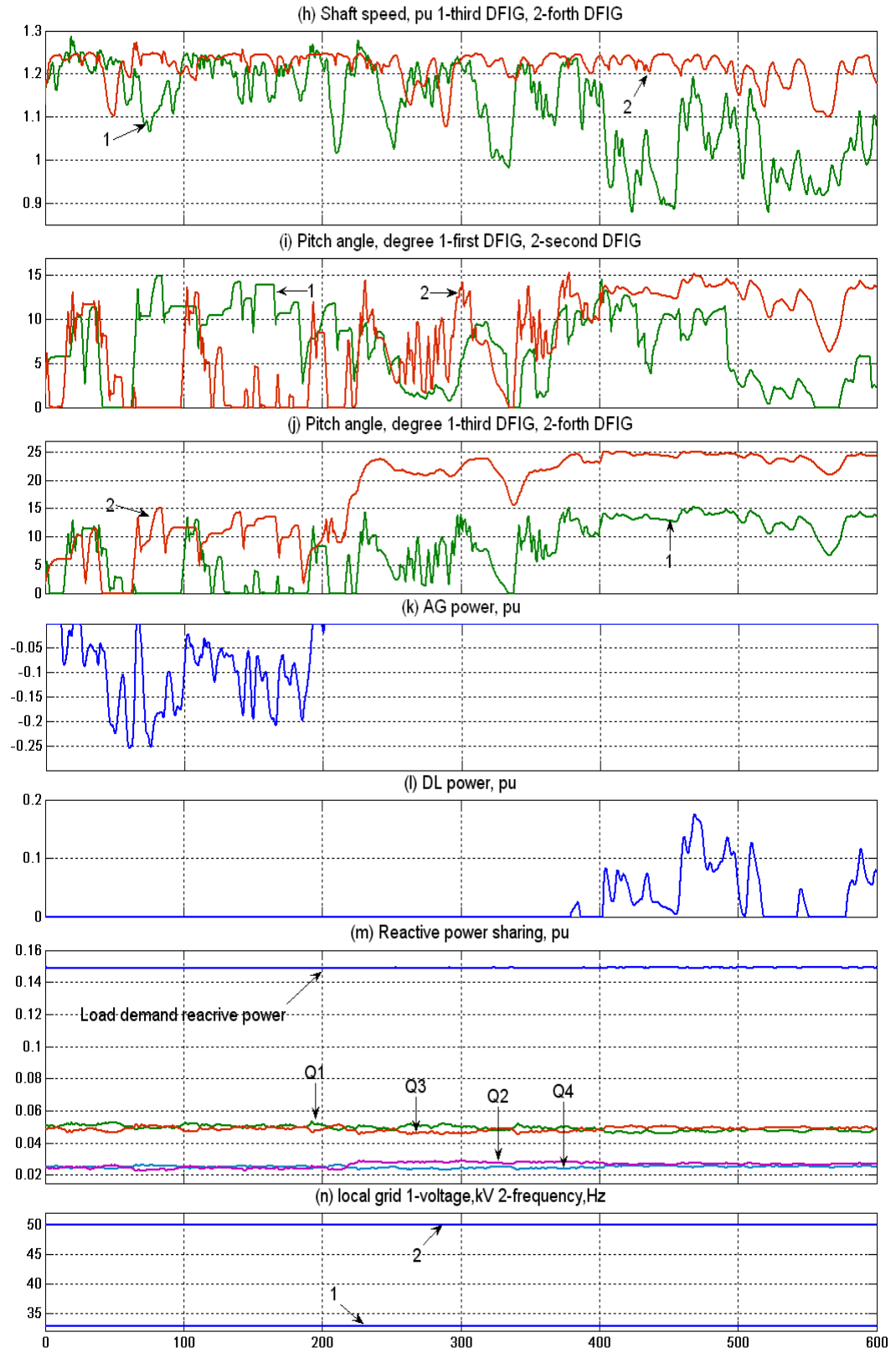
Figure 7.13. (part 2) A microgrid including four droop-controlled DFIGs with distributed T_e-controlling ES systems, AG and DL

7.6 Discussions and conclusions

This chapter considers a microgrid consisting of droop-controlled DFIGs, ES, AG and DL while the local grid voltage and frequency are fully controlled by the DFIGs. Two methods for controlling the ES system have been investigated. The first method exploits the turbine inertia as an ES mechanism. Hence, the shaft speed indicates the lack or excess of energy. In this scheme when ω_r is less/more than a certain threshold, the ES injects/absorbs the energy shortfall/excess. However in the second approach the ES power is regulated in order to control the electrical torque of the DFIG under MPT mode.

For both approaches a pitch angle control consisting of three components has been proposed. The first component is activated for $E_{es}>E_{es-high1}$ in order to reduce the wind energy captured. The second component is the standard pitch control which is used in order to maintain the output power at 1pu for wind speeds above rated. The third component, the presence of which is not critical for the system, is included to reduce the power rating of the ES through controlling the average of P_{es} towards zero using a slow PI controller. It is noted that the pitch angle controller proposed in Chapter 5 cannot be used here as it prevents the ES from charging up for $P^*<\hat{P}_{ext}$. However, the proposed pitch controller in this chapter allows the ES to charge up for $P^*<\hat{P}_{ext}$ which later can be used to compensate for the energy shortage in case of $P^*>\hat{P}_{ext}$. An EMS has been also suggested for the ES in which an AG/DL is used to inject/absorb the energy shortage/excess if E_{es} drops/raises below/above $E_{es-low}/E_{es-high2}$ ($E_{es-high2}>E_{es-high1}$). The EMS is needed in order to prevent the ES from saturation.

The proposed EMS and pitch controller are validated for the both ES control approaches using PSCAD simulations. It was shown that there is a trade-off between the pitch angle slew rate and the power rating of the DL in which a normal slew rate (3-5°/sec) can lead to the DL being unnecessary. It was also illustrated that regulating the ES power in order to control the DFIG under MPT mode can significantly reduce the required energy from the AG. However, this

comes at the expense of a slightly faster pitch control (5°/sec) required than that of the ω_r-actuated ES control (3°/sec) to eliminate the need for a DL. This is simply because the DFIG is tracking the maximum wind power which implies that either a faster pitch control or a larger DL is required for $P^* < \hat{P}_{ext}$. A larger DL, however, is not necessarily a disadvantage, when the DL is a long-term ES (e.g. a hydrogen generation station).

Finally, a simplified DFIG-ES system has been proposed in order to illustrate the EMS, torque control structure and pitch control in a multi-DFIG system with more than two DFIGs.

The next chapter studies the different scenarios and possible structures for the proposed control scheme.

8. Studying different system structures and operational scenarios

8.1 Introduction

In the previous chapter a microgrid consists of an array of droop-controlled DFIGs, ES systems, AG, and DL was considered, as shown in Figure 8.1.
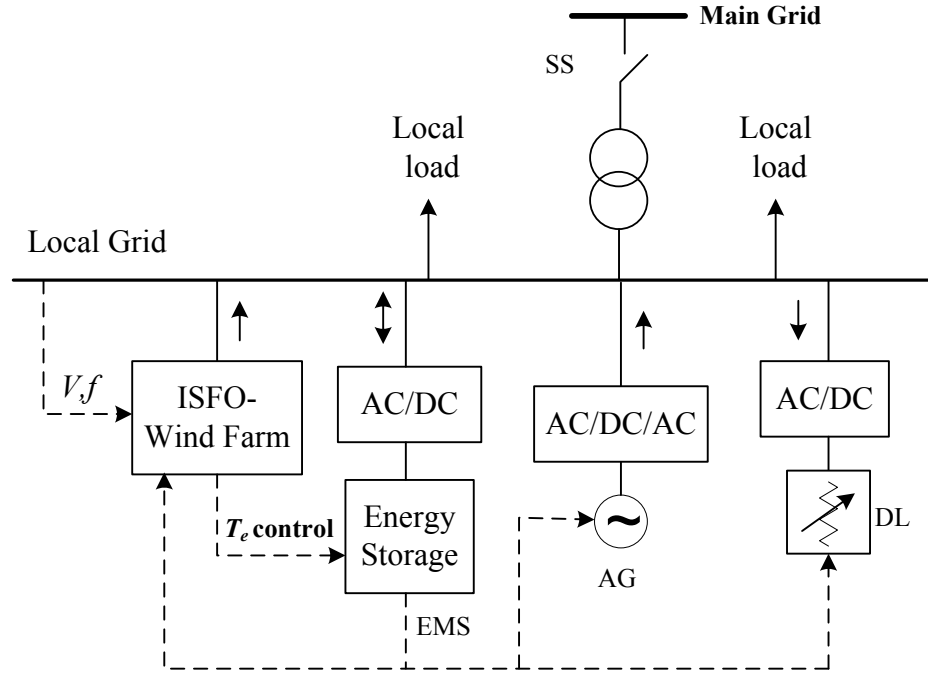
Figure 8.1. A microgrid consists of an array of droop-controlled DFIGs, ES, AG, and DL

In Chapter 7 the ES systems were distributed within individual DFIGs (unlike Figure 8.1) while the DL and the AG were aggregated on to the local grid. Unlike the AG, the DL can also be distributed within each DIFG which may to be a better place for a DL acting as a resistive dump load. Likewise, the ES system can be either distributed within individual DFIGs or aggregated on to the local grid. The current chapter considers the microgrid with the same components as that of the Chapter 7 and is intended to investigate the possible system structures regarding

the ES and DL placement. This is the subject of the sections 8.3 and 8.4. Before this the fault ride-through and no wind power scenarios are investigated for the microgrid structure used in the previous chapter.

8.2 Zero wind speed and fault ride-through scenarios

In this section two scenarios are studied. The first considers the ride-through strategy in case of zero wind speed and the second studies the ride-through in case of a 3-phase fault on the local grid.
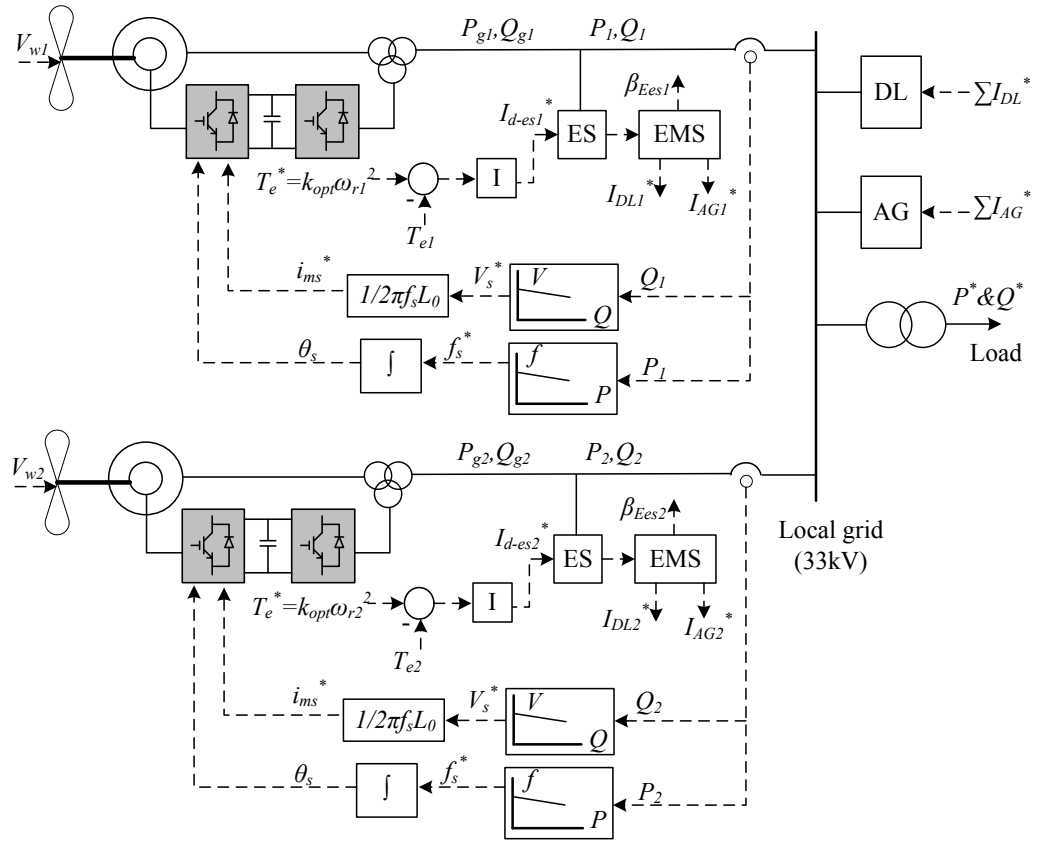
Figure 8.2. An array of droop-controlled DFIGs with distributed ES within each DFIG and aggregated DL on to the local grid

In both scenarios the system will have a DL aggregated on to the local grid while the ES systems are distributed within individual DFIGs. This structure, which is shown in Figure 8.2, is actually the one studied in the previous chapter.

8.2.1 Zero wind speed ride-through

In a standard DSFO-controlled wind farm, for wind speeds less than cut-in, the wind turbines simply stop generation. However, the challenge in a droop-controlled wind farm is that the wind generators also control the local grid voltage and frequency. The reactive power-voltage control is not the main challenge here since, for example, the DFIGs' grid side converters can also be used to support the local grid voltage, apart from the machines' stators. The active power-frequency control can, however, be quite a challenge. One possible solution is to make the AG take over the local grid frequency control as the DFIGs' out put powers die out. It may, however, restrict the choice for the AG. Another alternative solution is to control the DFIGs' grid side converters like STATCOM units in order to control the local grid frequency, as well as its voltage. However, this may require a sophisticated control because the control scheme must switch from controlling the real power from the machine rotor to a STATCOM control such as the one explained in Appendix C. This method is not studied in this thesis. Therefore, the main question here is whether the droop-controlled DFIGs can still control the local grid frequency with no wind power. The PSCAD simulations show that one DFIG (i.e. without droop) can control the local grid voltage and frequency even when the wind speed becomes zero. However, it becomes complicated in the case of a multi-DFIG system equipped with the variable droop control due to the fact that the variable droop gains varies according to the wind power.

It was discussed in Chapter 5 that in a multi-DFIG system controlled under the standard droop, if the wind speed of one DFIG drops, the output powers of the other DFIGs will also reduce to comply with the new operating frequency imposed by the first DFIG. This problem was addressed by the variable droop method explained in Chapter 5. The variable droop control method varies the *f-P* droop gains according to the available wind power, not just the DFIGs' ratings. It was shown that the variable droop method significantly reduces the energy required from the AG. Although the variable droop method was used in Chapters 6 and 7, it can be shown that the proposed control schemes can work with the standard droop at the expense of more energy demanded from the AG. Having said that, the worst

case scenario for the standard droop is when the wind speed of one of the DFIGs drops just above the cut-in wind seed and stays there for a long time. As a result, all DFIGs will generate according to the lowest wind power which will significantly increase the energy demanded from the AG. To avoid such a situation the variable droop control is used. The problem with the variable droop gain method is that the system may become unstable for large droop gains (i.e. small shaft speed). However, it will be illustrated in this section that a system controlled under the variable droop gain method only becomes unstable for shaft speed considerably less than 0.7pu which is the minimum DFIG operating shaft speed. Following zero wind speed in a DFIG, its shaft speed drops. In order to avoid instability, for $\omega_r < (0.7 - \Delta\omega)$pu, the DFGI's control is switched from the droop control to the standard DSFO control i.e.:

- The stator flux angle is derived by voltage and current measurements using, for example, a PLL (instead of the integration of the reference frequency).

- The q-component of the rotor current controls the active power with $P^* = 0$ (instead of $i_{rq}^* = \dfrac{-L_s}{L_0} i_{sq}$).

- The integral control of the T_e control scheme is reset i.e. $I_{d-es}^* = 0$.

Obviously, in order to control the local grid voltage and frequency, the final DFIG must stay under ISFO control. However this DFIG (i.e. the ISFO-controlled one) must operate either without the droop control or with the standard droop (not the variable droop so as to avoid the instability when its shaft speed becomes very small). This will require a communication between DFIGs through a central control unit. However, this central control unit is much simpler than those required in a DSFO-controlled wind farm generating a demand power.

8.2.1.1 Simulation results of zero wind speed ride-through

This section is intended to illustrate the zero wind speed ride-through procedure explained above. The model simulated is shown in Figure 8.2. The rating of the first DFIG is 0.66pu while that of the second one is 0.34pu. The torque control, EMS and pitch control (not shown in the figure) are identical to those explained in the previous chapter. The local grid voltage and frequency are regulated by the DFIGs through the variable droop control introduced in Chapter 5. The simulation results are shown in Figure 8.3. At 3sec, the wind speed (Figure 8.3a) of the first DFIG (larger one) drops to zero which causes its output power (Figure 8.3b1) and shaft speed (Figure 8.3c1) to reduce. It is noted that if the system was controlled under the standard droop, the second DFIG output power (Figure 8.3b2) and shaft speed (Figure 8.3c3) would also reduce. Since the demand power (Figure 8.3b) is

1pu (which is more than the extractable wind power $\hat{P}_{ext}$), the energy level of the ES (Figure 8.4d) becomes less than 1pu which turns on the AG (Figure 8.3f) to compensate for the energy shortfall. It can be seen from Figure 8.3c1 that the first DFIG shaft speed becomes less than 0.7pu while the variable droop-controlled DFIGs are still stable. When the shaft speed of the first DFIG becomes 0.3pu, the DIG control is switched over to the standard DSFO control with P^*=0. The 0.3pu shaft speed threshold is chosen in order to show that the system controlled under variable droop method is still stable for a shaft speed much less than 0.7pu. In practice the threshold can be just below 0.7pu. In the simulation, in order to make the shaft speed zero, the PSCAD induction machine model is switched from "torque mode" to "shaft speed mode" with ω_r=0. Therefore, the shaft speed and the output power of the first DFIG becomes zero while the local grid voltage and frequency are controlled by the second DFIG (smaller one). At 28sec, the wind speed of the second DFIG also becomes zero which causes reductions in its output power and shaft speed. Consequently, the AG power increases to maintain the demand power. Since DFIG 2 is the final DFIG, when its shaft speed drops to 0.3pu, the DFIG will still be controlled under ISFO mode but the droop controls are removed.
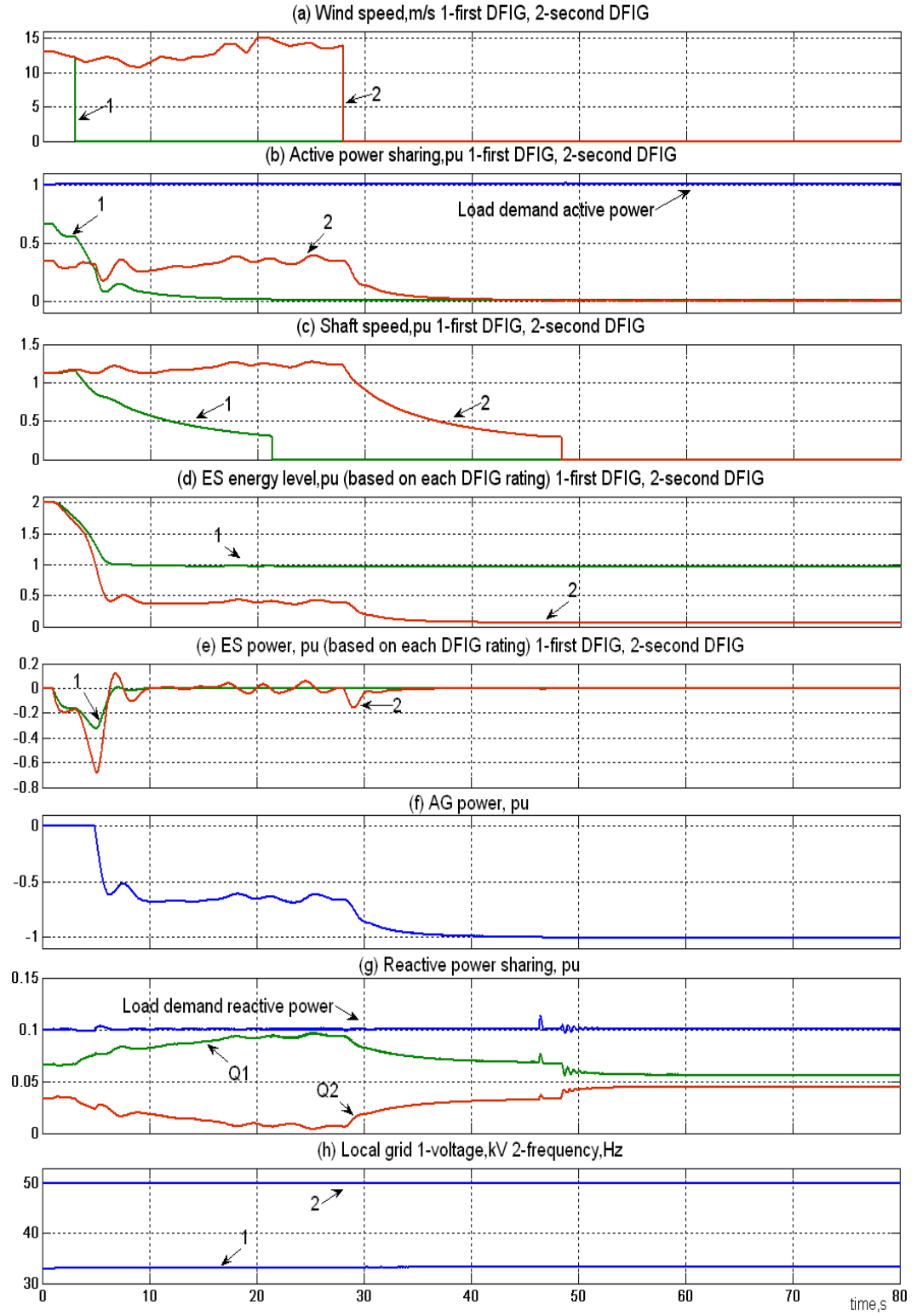
Figure 8.3. Zero wind speed operation of an array of droop-controlled DFIGs

As a result, the local grid frequency (Figure 8.3h) is provided by the second DFIG (which is 0.34pu) even though its wind speed is zero. It is noted that the reactive power-voltage droop is still active in both DFIGs. The total active power demand is supplied by the AG. Similar to the first DFIG, when the shaft speed of the second (final) DFIG drops to 0.3pu, the integral control of its T_e control scheme is reset which causes the small transient fluctuation in reactive power sharing (Figure 8.3g).

Therefore, the zero wind power ride-through can be summarized as follows:

- For all DFIGs before the final, if $\omega_r < 0.3$pu (or a value less than 0.7pu), the DFIG control scheme is switched from ISFO to DSFO method with $P^* = 0$ and $I_{d\text{-}es}^* = 0$.

- For the final DFIG, if $\omega_r < 0.3$pu (or a value less than 0.7pu), the droop controls are removed and $I_{d\text{-}es}^* = 0$.

This simulation results illustrate the zero wind speed ride-through procedure explained above and also demonstrate the ability of the ISFO-controlled DFIGs to control the local grid voltage and frequency even when the wind speed drops to zero. It also shows that a variable droop-controlled wind farm is stable for shaft speed considerably less than 0.7pu (i.e. down to 0.3pu). In other words, it seems that a multi-DFIG system controlled under the variable droop method is stable within the operating region of the DFIG. However, the author admits that a full system stability studies for the variable droop control method is still required which is out of the scope of this thesis.

8.2.2 Fault ride-through to a balanced grid fault

A major challenge for wind energy generation, especially for those with DFIGs, is their operation during grid faults [85]. New grid code requires the wind turbines to ride-through voltage sags which means that normal power production should be re-initiated once the nominal grid voltage has been recovered [50]. Another challenge, which is more crucial for large wind farms, is to promptly reduce the

wind power generation toward zero after a fault on the grid since there is no place for the wind power to flow. In [48] an offshore wind farm connected to a LCC-HVDC link is considered and the author, as a member of the research team, utilized the droop method in order to ride-through a balance fault on the AC grid. In [48], upon fault detection, the DFIGs are switched from the DSFO-controlled to droop-controlled and hence the wind power generation automatically drops to zero. It was shown in [48] that using the droop method a very good fault ride-through performance is achieved. Moreover, the droop method eliminates the "interacting current" flowing between the DFIGs following the fault. However, the drawback is the communication required from the AC grid to the DFIGs in order to switch to fault mode. It was found in [48] that a communication delay more than 20ms would make the wind farm grid voltage and frequency go outside the acceptable range.

This research proposes a control structure which uses the droop characteristics during normal operation. Therefore it is expected that the proposed system control to ride through a balanced fault on the local grid without the need for communication as both the normal and fault operations are based on droop method. This is the subject of this section. This study is restricted to a balanced 3-phase fault since it is the worst case fault for a DFIG based wind farm [48, 50].

8.2.2.1 Simulation results of fault ride-through on local grid

This section investigates a 3-phase fault ride-through scenario on the local grid as is shown in Figure 8.4. The fault is simulated by the PSCAD standard "3-phase fault" component and lasts 150ms. It is assumed that after 150ms, the protection relays remove the fault and the load is supplied by another parallel connection line. The line inductance between the fault location (Figure 8.4) and the wind farm grid is 0.05mH. The fault location is chosen to be close to the wind farm grid in order to make the wind farm grid voltage drops to zero following the fault which is the worst case scenario.
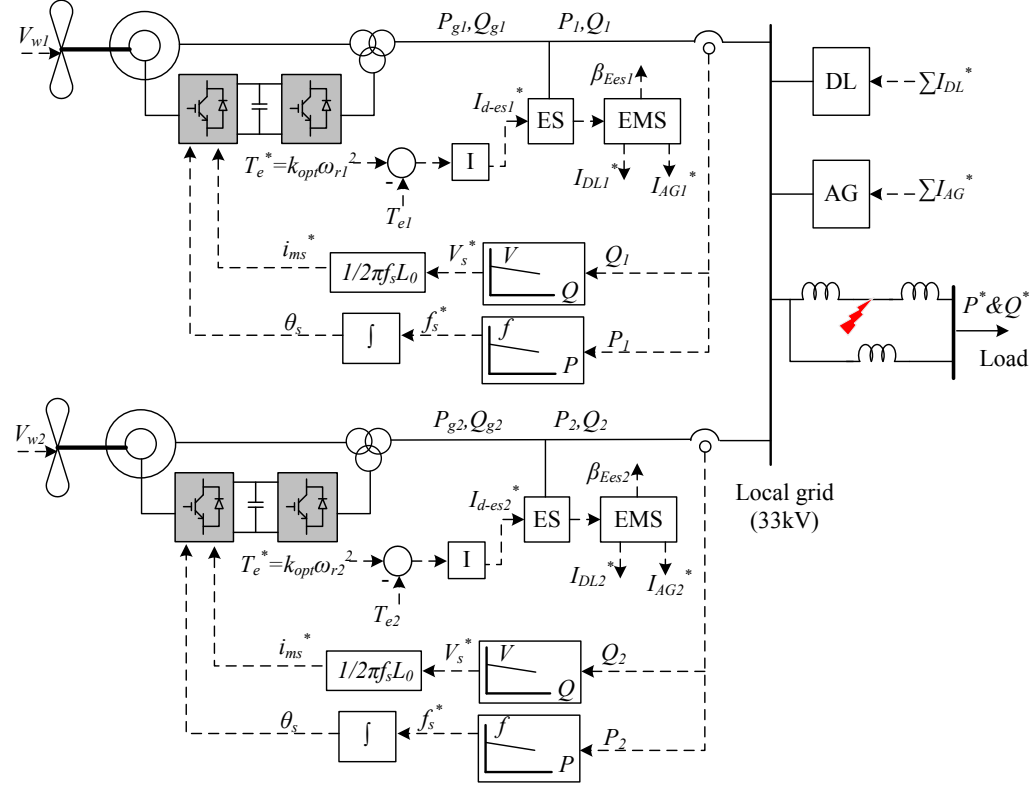
Figure 8.4. A 3-phase fault on the local grid of a droop-controlled wind farm

The ratings of the DFIGs are 0.66pu and 0.34pu with parameters given in Appendix B. The torque controllers, EMSs and pitch controllers (not shown in the figure) are identical to those explained in the previous chapter. The simulation results are shown in Figure 8.5. The balanced fault occurs at 3sec. The constant wind speed (Figure 8.5a) is 12.55m/sec (corresponding to almost 1pu$_{gen}$ extractable wind power). It is noted that since the fault lasts only 150ms, the wind speed variations do not matter. The active (Figure 8.5b) and reactive (Figure 8.5c) power demands before fault are 1pu and 0.1pu, respectively. It can be seen that the local grid voltage (Figure 8.5f) and frequency (Figure 8.5g) drop to almost 0kV and 42Hz, respectively. As a result, the measured active and reactive demand power become zero and so do the active and reactive power from each DFIG. However within 0.5sec after fault clearance, the local grid voltage and frequency are restored to their pre-fault values and so are the active and reactive powers.
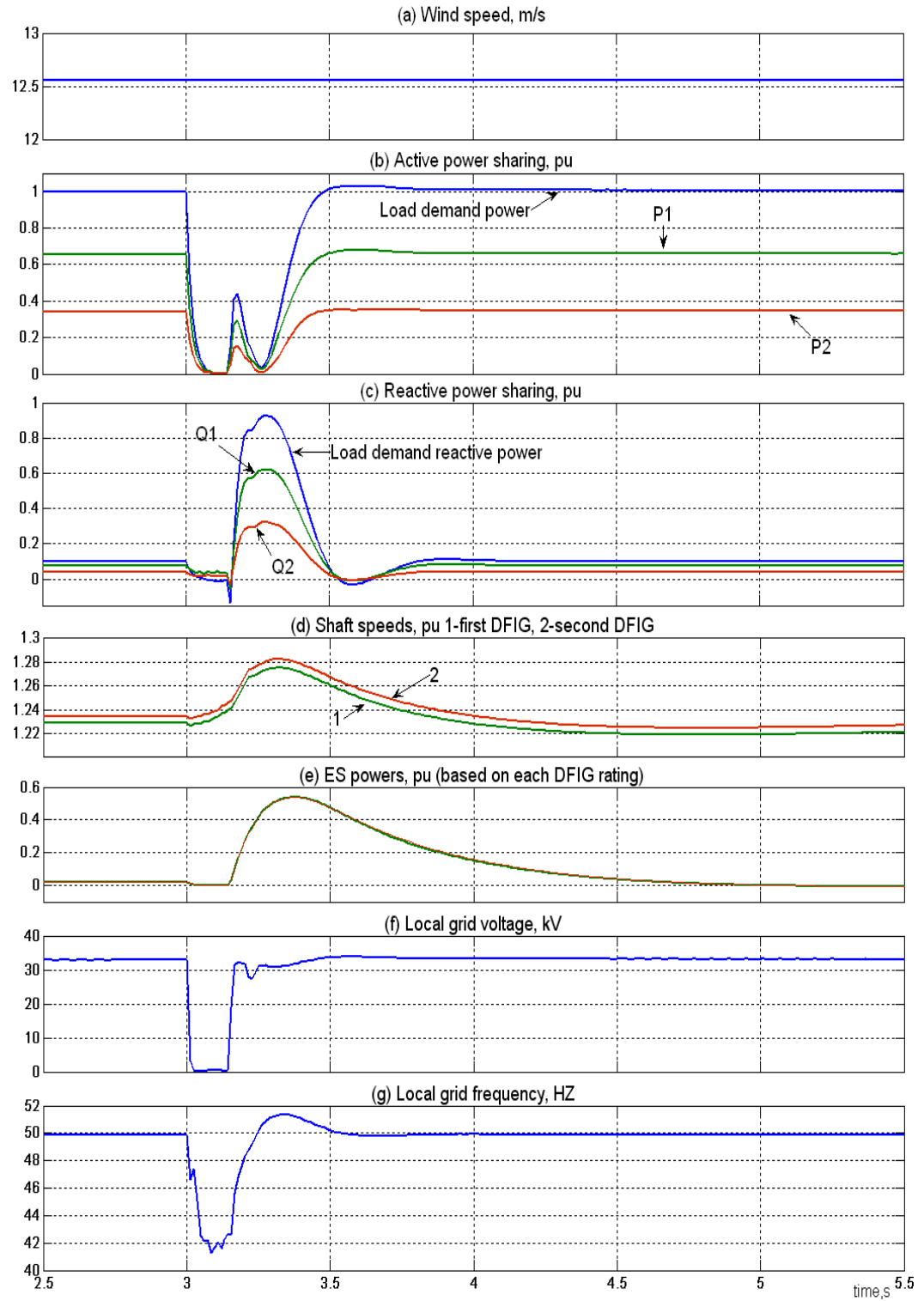
Figure 8.5. Results of the fault ride-through of the model shown in Figure 8.4

Figure 8.5d shows that the shaft speed variations of both DFIGs are within the operational region (note that it is the worst case scenario as the demand power is 1pu). Figure 8.5e shows that the ES power variations are less than $\pm 0.6\text{pu}_{\text{gen}}$. These results demonstrate the ability of the proposed control scheme to ride-through a fault on the local grid with no need for communications. It is noted that the standard DFIG protection schemes are still applicable.

8.3 System studies when ES and DL are distributed

The DL can be resistor banks, a hydrogen generation station or an irrigation system. For bulky DL, such as hydrogen generation, distributing the DL within individual DFIGs is probably not possible. However, for DL like resistor sets, distributing the DL within each DFIG seems not only possible but also reasonable since it only requires local communication between the DFIG and its associated DL. This section considers an array of droop controlled DFIGs while the ES and DL are distributed within individual DFIGs, as shown in Figure 8.6. The control paradigms of the EMS, torque control and pitch control are identical to Chapter 7. Although both the standard and variable droop methods are possible, only variable droop is simulated here.
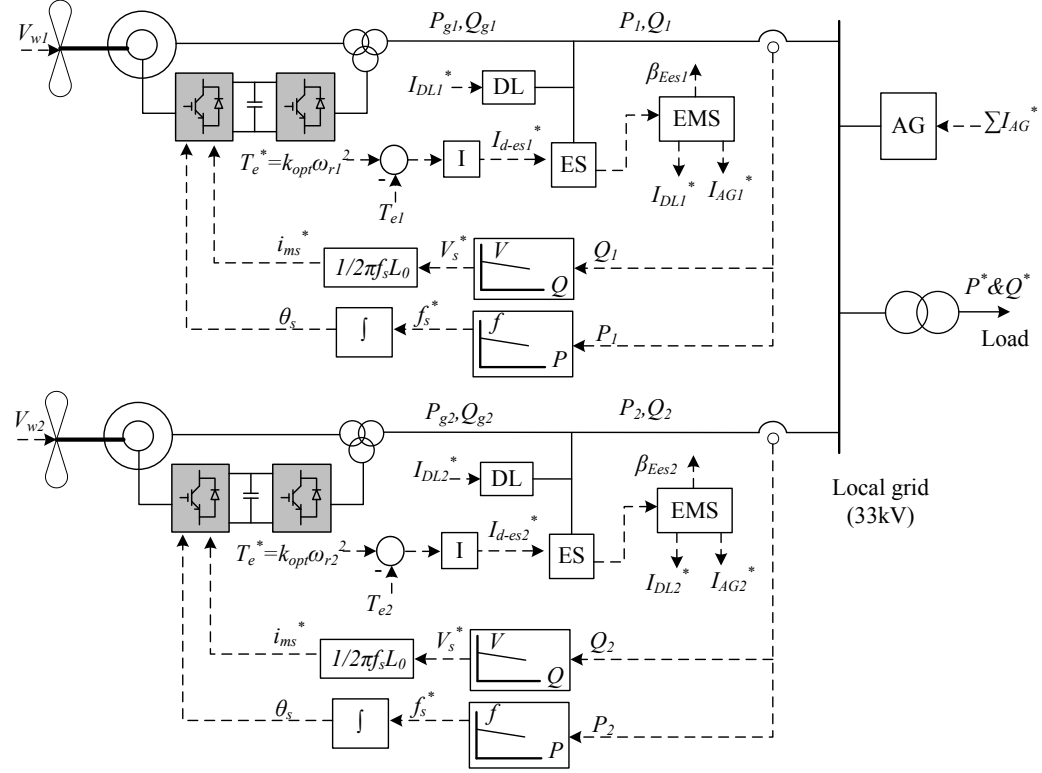
Figure 8.6. An array of droop controlled DFIGs with distributed ES and DL within each DFIG

8.3.1.1 Simulation results of distributed ES and DL

The model simulated here is shown in Figure 8.6. The objective of this simulation is to illustrate the functionality of the droop-controlled wind farm, EMS, torque control and pitch control for the distributed DL and ES. The capacity of the ES systems is 5pu$_{gen}$. The thresholds of the EMSs and the pitch control (not shown in the figure) are the same as those used in Chapter 7. The pitch angle slew rate is 3°/sec. Since the DL is distributed, the communication is local. However, the communication from the DFIGs to the AG is still needed. The ratings of the first and the second DFIGs are 0.66pu and 0.34pu respectively. The simulation results are shown in Figure 8.7. The average of the two real wind speed profiles (Figure 8.7a) is 12.5m/sec ($\hat{P}_{ave} \approx 1pu_{gen}$) while their standard deviations are 1.28 and 1.39, respectively.
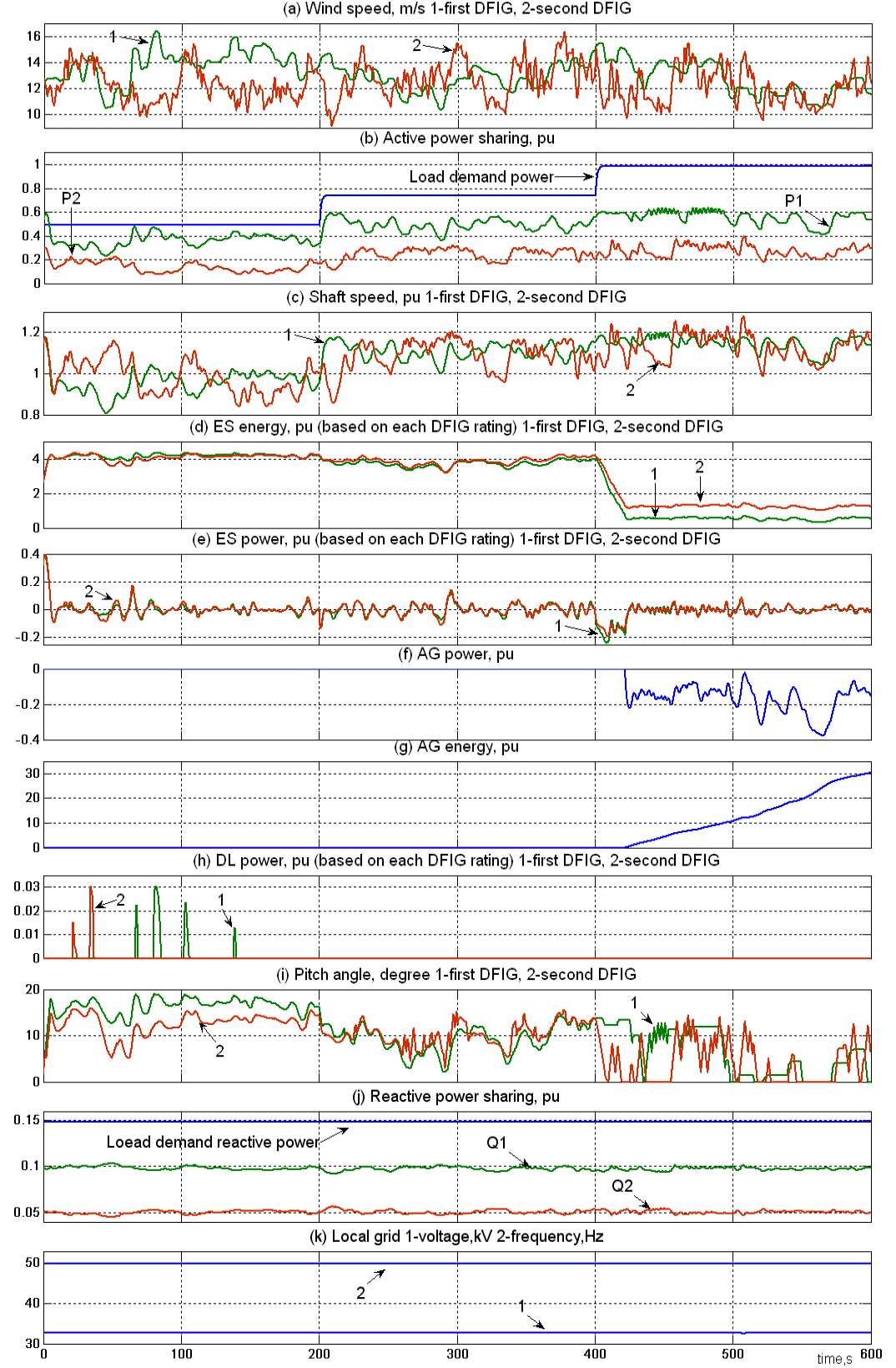
Figure 8.7. Simulation results of distributed ES and DL

For the first 200sec, the demand power (Figure 8.7b) is 0.5pu which is less than the extractable wind power (i.e. with β=0) $\hat{P}_{ext}$. Therefore, the ES are charged up (Figure 8.7d). For E_{es}>3.3pu$_{gen}$, the pitch angles (Figure 8.7i) are increased to reduce the wind energy captured. Since the pitch controls are not fast enough, the energy level of the ES becomes more than 4.3pu$_{gen}$ which causes its associated DL to turn on. Figure 8.7h shows that the power shed by the DL is only about 0.03pu$_{gen}$. It can be shown that a pitch control with slew rate of 5°/sec eliminates the need for a DL. Over the second 200sec, P^*=0.75pu which is occasionally more than $\hat{P}_{ext}$. Therefore, the shaft speeds (Figure 8.7c) increase and the pitch angles decrease to extract more energy from wind. Since the variable droop controlled is used here, the DFIGs compensate for one another and hence no power from the AG (Figure 8.7f) is demanded. It can be shown that in the case of the standard droop some power would be required from AG. Finally during the last 200sec, P^*=1pu which is more than $\hat{P}_{ext}$ for almost the entire period. Consequently, the energy level of the ES drops to 0.7pu$_{gen}$ which turns on the AG. The total energy demanded from the AG (Figure 8.7g) is 30pu which is almost 5pu more than that shown in Figure 7.9. The reason is that in Figure 7.9 the pitch angle speed was slightly faster (5 °/sec) which allows the pitch angles reduce faster, hence more wind power is generated which in turn reduces the energy demanded from the AG. Figure 8.7j shows the reactive power sharing for Q^*=0.15pu and Figure 8.7k shows that the local grid voltage and frequency are controlled.

8.4 System studies when ES and DL are both aggregated

The system structure studied in this section is shown in Figure 8.8 in which both ES and DL are aggregated on to the local grid. The ES system is still responsible for controlling the electrical torque of the DFIGs. Therefore, as Figure 8.8 shows, the summation of the DFIGs' electrical torque error $\sum T_{error}$ is formed and communicated to the ES through a communication link.
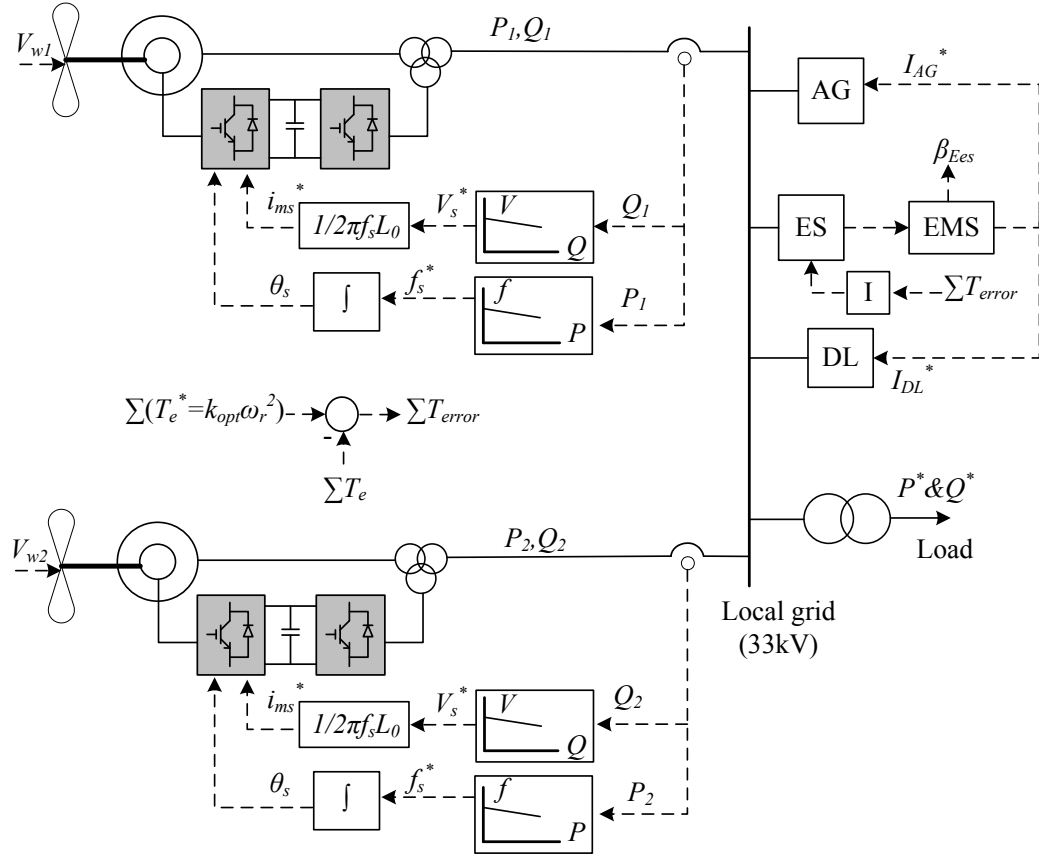
Figure 8.8. An array of droop controlled DFIGs with aggregated ES and DL within each DFIG

In cases where the ES is aggregated on to the local grid, only the variable droop is applicable. For cases with distributed ES, the droop control imposes the power on the combination of the DFIG and its ES system that controls its torque directly. Therefore, both the standard and the variable droop methods are applicable. However, if the standard droops are applied for cases with an aggregated ES system, the output powers of the DFIGs tend to be smooth as the standard droop shares the load according to the ratings of the DFIGs. This works against the ES system which tries to vary the output powers of the DFIGs according to the maximum wind power. Therefore, there would be a large error in the torque control which may even lead to instability. However, using the variable droop method, the droop gains also vary according to the maximum wind power (i.e. $k_{opt}\omega_r^3$) which makes the droops operate consistently with the torque control.

As explained in Chapter 7, the pitch control scheme consists of three components: $\beta^* = \beta_{Pes} + \beta_{Ees} + \beta_{max}$. The β_{max} component is the standard DFIG pitch control which is activated for wind speeds above rated to control the output power at 1pu. The β_{Pes} and β_{Ees} components are respectively used to reduce the power rating of the ES and to prevent the energy level of the ES from exceeding its maximum limit. Therefore, in the case of an aggregated ES, the β_{Pes} and β_{Ees} components are common between the pitch controllers of all wind turbines. The question here is whether it is correct to have the same pitch angle for wind turbines with different wind speeds. The β_{Pes} is very slow and has a negligible effect on the DFIG's output power. The β_{Ees} is activated if $E_{es}>$ a certain threshold, which only happens if $P^*<$ the total aggregated extractable wind power. This is because the variable droop makes the DFIGs compensate for each other. Therefore, the pitch control scheme is applicable in aggregated ES structure as well.

The advantage of the aggregated ES structure is more evident in large wind farms in which the total output power of the wind farm tends to be smoother than that of the individual DFIGs due to the possible phase difference in their wind speeds. The disadvantage of this structure, however, is the need for the communication between the ES and the wind farm.

8.4.1.1 Simulation results of aggregated ES and DL

This model simulated in this section, which is shown in Figure 8.8, consists of two droop-controlled DFIGs with aggregated ED and DL. The objective of the simulation is to illustrate the EMS and pitch control, and to validate the electrical torque control scheme for the case of the aggregated ES structure. The simulation results are shown in Figure 8.9. The real wind speed profiles and the simulation scenario are identical to the previous simulation. The pitch angle slew rate is 3°/sec. During the first 200sec, P^*=0.5pu (Figure 8.9b) which is less than $\hat{P}_{ext}$. Therefore, E_{es} (Figure 8.9d) increases more than 3.3pu which in turn makes the pitch angles (Figure 8.9i) rise to reduce the wind energy captured. It can be seen that the two pitch angles are equal.

Figure 8.9. Simulation results of aggregated ES and DL

189
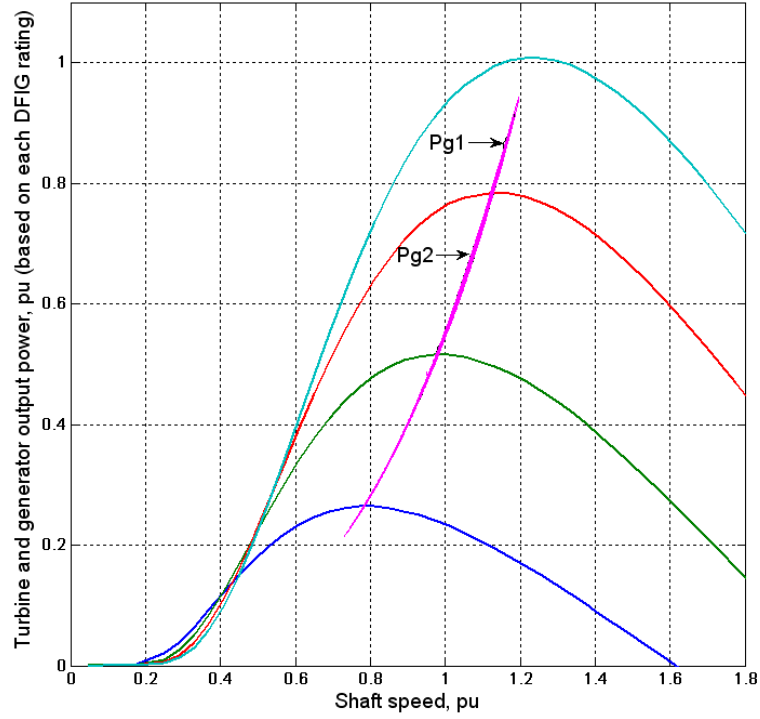
Figure 8.10. DFIGs output powers vs their shaft speeds on P_t-ω_r characteristics for different wind speeds while ES (torque control mechanism) is aggregated

Since the pitch angle slew rate is not fast enough, E_{es} becomes more than 4.3pu which turns the DL (Figure 8.9h) on in order to absorb the extra energy. The pitch angle slew rate is chosen in order to illustrate the system operation with DL and it can be shown that with a 5°/sec pitch angle control no DL is required. Over the second 200sec, P^*=0.75pu which is occasionally more than $\hat{P}_{ext}$. However since the DFIGs compensate for one another, no AG power (Figure 8.9f) is needed. The reason for the different pitch angle values is that the output power of the second DFIG occasionally approaches 1pu$_{gen}$ which causes its pitch angle (β_{max}) to increase. Finally for the last 200sec, P^*=1pu which is more than $\hat{P}_{ext}$. Therefore, E_{es} drops to 0.7pu which turns on the AG in order to balance the demand. Figure 8.9j shows the reactive power sharing for Q^*=0.15pu and Figure 8.9k illustrates that the local grid voltage and frequency are well-controlled by the DFIGs.

Figure 8.10 shows the output powers of the two DFIGs versus their associated shaft speeds on the P_t-ω_r characteristics for different wind speeds. The figure

illustrates that the output powers of the DFIGs track the maximum wind power. This illustrates the proposed torque control scheme which uses the aggregated ES power to control the electrical torque of the DFIGs.

Another possible structure is to distribute the DL within individual DFIGs (like Figure 8.6) while the ES is aggregated on to the local grid (like Figure 8.8). Since such a structure is a combination of the two previous cases, it is not simulated in this thesis. The grid fault ride-through and no wind ride-through scenarios for these structures are the same as those of the first structure and are not simulated here.

8.5 Discussions and conclusions

This chapter investigates zero wind speed and a balance fault ride-through scenarios and also studies different possible system configurations.

The zero wind power ride-through scenario was explained and it has been illustrated that an ISFO-controlled DFIG can control the local grid voltage and frequency even if the wind speed drops to zero. Through simulating the zero wind power ride-through, it has been also shown that a multi-DFIG system controlled under the variable droop method is stable for shaft speeds down to 0.3pu (which is much less than minimum operating shaft speed i.e. 0.7pu). Therefore, it seems that the system controlled under the variable droop method is stable within the operating region of DFIGs. Having said that, the variable droop method still requires further stability studies which is beyond the scope of this work.

A 3-phas balanced fault on the local grid has also been simulated and it was illustrated that once the fault is cleared, normal local grid voltage and frequency control is automatically (without any communication) restored and so is the active and reactive power sharing of the DFIGs.

It has been also shown that both ES and DL can be either distributed amongst the turbines sets or be aggregated on to the local grid. The advantage of the distributed elements is that the communications will be local. It was discussed that the aggregated ES system can only operate with variable droop control as the standard

droop works against the torque control that regulates the ES. The aggregated ES seems to be suitable for large wind farms since the total output power of the wind farm is likely to be smoother than that of the individual ones due to the phase shifts in the wind speeds. The distributed DL seems to be appropriate for small DL like sets of resistors while the aggregated DL is appropriate for bulky ones such as hydrogen generation units or an irrigation system.

9. Conclusions

9.1 Summary of the thesis

The vector control design of a DFIG has been reviewed and two control approaches were discussed. The first control approach in which the DFIG is field orientated off an external voltage source (e.g. the grid) is called Direct Stator Flux Orientation (DSFO). In the second approach, which is called Indirect Stator Flux Orientation (ISFO), the DFIG itself appears as a voltage source in the power system. The thesis is mainly concentrated on the ISFO control.

The thesis, then, identified two control strategies for wind generator(s)-ES systems: Power Smoothing Control (PSC) and Power Demand Control (PDC). In PSC the ES absorbs wind frequencies above a given frequency; hence, the output power is a smoother version of the wind power. Therefore, the PSC may not be quite appropriate for cases where wind energy supplies a significant part of the load as the capacity of the other generating units will be limited. However, since in the PDC the output power of the DFIG(s)-ES system is equal to the power demanded by the load, the PDC seems to be a good strategy for power systems with a high wind energy penetration.

The application of the above two strategies in a DSFO-controlled wind farm connected to both AC grid and HVDC link has been discussed. It has been shown that in order to apply the PDC in a DSFO-controlled wind farm, communications from a central control unit to individual DFIGs are needed to determine the DFIGs' reference powers and pitch angles. Moreover, it was explained that the capacity of a DSFO-controlled DFIG to participate in wind farm grid frequency control is limited to the active power reserved. However, the ISFO-controlled DFIGs have the ability to be augmented with the frequency and voltage droop characteristics so as to control the local grid voltage and frequency. This ability can make the droop-controlled DFIGs a better choice for microgrid application or for power systems with high wind energy penetrations. This is because a droop

controlled wind farm can control the wind farm grid voltage and frequency, and can change the operating points without communication or the need for a central control. This thesis concentrates mainly on the microgrid application of a droop-controlled wind farm, however, it is explained that the droop-controlled wind farm can also be also be connected to the main grid through a HVDC link or an AC/DC/AC converter. The classical voltage and frequency droops were applied on ISFO-controlled DFIGs and it has been shown that such a control has the ability to ride-through grid loss without communication.

Two scenarios for a droop-controlled wind farm have been studied. The first scenario considers the integration of a droop-controlled wind farm into a microgrid when no external ES is available. In such a case the DFIGs' shaft speed varies according to the demand power P^* and the available wind power. The shaft speeds are an indicator of the shortage or excess of the wind energy. A pitch angle control has been designed which keeps the shaft speed within its limits for P^* less than the extractable wind power $\hat{P}_{ext}$. However, if the pitch control is not sufficiently fast and/or the P^* becomes grater than $\hat{P}_{ext}$ the shaft speed may go beyond its limits. Therefore, an Energy Management System (EMS) has been proposed to keep the shaft speed within limits and maintain the demand power. The EMS utilizes an Auxiliary Generator (AG)/Dispachable Load (DL) to inject/absorb the energy shortfall/excess if the shaft speed drops/rises below/above a certain low/high threshold value.

It was shown that the standard droop control is not the best option for the wind energy generation since if the wind speed of one turbine drops, the output powers of the other turbines will also drop in order to comply with the new operating frequency imposed by the first DFIG. Therefore a "variable droop" control method was proposed which adjusts the frequency-active power droops' gains according to the available wind power and it has been shown that the variable droop method can save noticeable amount of energy demanded from the AG.

The second scenario considers a droop-controlled wind farm with an external ES system. Two approaches for controlling the ES have been investigated and for

both an EMS has been proposed to keep the energy level of the ES within its limits using an AG and a DL. In the first approach the ES is actuated by shaft speed ("shaft speed actuated-ES"). This control approach is similar to the previous scenario, but this time the ES appears as a buffer between the turbine inertia (inertial ES) and the AG and the DL. In the second approach the ES power is used in order to control the electrical torque of the DFIG ("torque controlling-ES"). The torque control loop has been designed and validated for both Maximum Power Tracking (MPT) and Constant Torque Mode (CTM) methods; however, it can be used for other torque control methods as well. It was argued that the CTM (and in fact any non-MPT method) is not suitable for cases where AG is available. This is because for $P^* > \hat{P}_{ext}$, the DFIG should be controlled under MPT method to minimize the energy demanded from the AG. The advantage of a non-MPT mode such as CTM (or shaft speed actuated-ES approach) is that the energy stored in the turbine inertia is more that that of the MPT mode and hence a smaller external ES is needed. It has also been illustrated that the shaft speed actuated-ES approach (or any other non-MPT method such as CTM) requires a slower pitch control than the MPT to eliminate the need for a DL. However, this comes at the price of higher energy demand from the AG for $P^* > \hat{P}_{ext}$. Therefore, it may be possible to control the DFIGs under a non-MPT mode such as CTM (or shaft speed actuated-ES approach) for $P^* < \hat{P}_{ext}$ and switch to MPT mode for $P^* > \hat{P}_{ext}$. However for cases where DL is a long-term ES system (e.g. hydrogen generation station), controlling under MPT mode is an advantage rather than a disadvantage, even for $P^* < \hat{P}_{ext}$.

An array of the variable droop-controlled DFIGs controlled under MPT mode was considered and it has been shown that the ES and the DL can be either distributed amongst individual DFIGs or aggregated on to the local grid. Apart from the cases where ES is aggregated; both classical droop and the variable droop methods are applicable in principle.

The zero wind speed ride-through scenario was illustrated and it has been shown that the ISFO-controlled DFIG can control the local grid voltage and frequency

even if its wind speed drops to zero. Through a zero wind-power ride-through simulation it was shown that the system with variable droop control is stable for shaft speeds considerably less than 0.7pu. Therefore, it can be concluded that the variable droop controlled-DFIGs can be stable within the DFIGs' operating region. However, the stability issue requires further studies to be validated.

A balanced 3-phase fault on the local grid was simulated. The fault lasts for 150ms and it was illustrated that upon fault being cleared the system can restore the frequency and voltage control, and hence the active and reactive power sharing, without the need for communication.

9.2 Future work

The future works are listed below:

- Considering the dynamics of the AG and the DL in order to design the EMS. The slower the dynamics of the AG and DL the larger gains in the EMS are needed.

- Full stability studies for a multi-DFIG system controlled under the variable droop control method. To do so, a detailed mathematical model of the wind turbine, DFIG, ES, AG, DL, line inductances, etc is needed. Then the effect of the variable droop gains on the system eigenvalues must be investigated in order to determine the stable region.

- In this thesis a simplified model was introduced in order to simulate a system with more than two DFIGs. Although the results of the simplified model in case of two DFIGs are almost identical to those with the full DFIG model, it might be still required to simulate a multi-DFIG system consisting of more than two complete DFIG models.

- Making an experimental system in order to validate the proposed droop control. Obviously, at least two DFIGs are needed. The wind turbines can be emulated in the experimental system by DC motors.

10. References

[1]   *The United Nation Framework Convention on Climate Change*, November, 2005.

[2]   *Climate Action Network Euroup: Ratification Calandar.*, October, 2006.

[3]   K. Kook, K. McKenzie, Y. Liu *et al.*, "A study on application of energy stroage for the wind power operation in power system," in Power Engineering Society General Meeting, 2006.

[4]   S. Bozhko, R. G. Blasko, J. C. Clare *et al.*, "Control of Offshore DFIG-based Windfarm Grid with Line-Commutated HVDC Connection," *IEEE Trans on Energy Conversion,* vol. 22, no. 1, March, 2007.

[5]   T. Kinjo, T. Senjyn, N. Urasaki *et al.*, "Output levelling of renewable energy by electric double-layer capacitor applied for energy storage system," *IEEE Trans on Energy Conversion,* vol. 21, no. 1, pp. 221-227, March, 2006.

[6]   E. Bossanyi, Z. Saad-saud, and N. Jenkins, "Prediction of flicker produced by wind turbines," *Wind Energy,* vol. 1, no. 1, pp. 35-51, 1998.

[7]   J. Niiranen, "Voltage ride-through of doubly-fed generator eqqupped with an active crowbar," in Nordic Wind Power Conf., 2004.

[8]   C. Abbey, and G. Joos, "A doubly-fed induction machine and energy storage for wind power applications," in IEEE PESC, Aachen, Germany, 2004.

[9]   S. M. Bolik, "Grid requirements challenges for wind turbines," in Fourth international workshop on large scale integration of wind power and transmission networks for offshore wind farms, 2003.

[10]   S. Nomura, Y. Ohata, T. Hagita *et al.*, "Wind Farms linked by SMES systems," *IEEE Transaction on Applied Superconductivity,* vol. 15, no. 2, pp. 1951-1954, June, 2005.

[11]   K. Agbossou, R. Chahine, J. Hamelin *et al.*, "Renewable energy system based on hydrogen for remote applications," *Journal of Power Sources* vol. 96, pp. 168-172, 2001.

[12]   A. B. Arsoy, Y. Liu, P. F. Ribeiro *et al.*, "STATCOM-SMES systems in controlling power system dynamics," *IEEE Industry Application Magazine,* vol. 9, no. 2, pp. 21-28, 2003.

[13]   J. P. Barton, and D. G. Infield, "Energy storage and its use with intermittent renewable energy," *IEEE Transaction on Eenergy Conversion,* vol. 19, pp. 441-448, 2004.

[14]   C. Abbey, J. Chahwan, and G. Joos, "Energy storage and managment in wind turbine generator system," *EPE,* vol. 17, no. 4, pp. 6-12, Jan., 2008.

[15]   C. Abbey, and G. Joos, "Energy managment strategies for optimization of energy storage in wind power hybrid system " in PESC, 2005, pp. 2066-2072.

[16]   X. Li, C. Hu, C. Liu *et al.*, "Modeling and control of aggregated super-capacitor energy storage system for wind power generation," in IECON, 2008, pp. 3370-3375.

[17]   T. Kinjo, T. Senjyu, K. Uezato *et al.*, "Output leveling of wind power generation system by EDLC energy storage system," *Electrical Engineering in Japan,* vol. 124-B, no. 8, pp. 1059-1066, Aug., 2004.

[18]   E. Loukarakis, and I. Margaris, "Frequency control support and participation methods provided by wind generation," in Electrical Power &energy Conference, 2009.

[19]   R. Takahashi, and J. Tamura, "Frequency control of isolated power system with wind farm by using flywheel energy storage system," in International Conference on Electrical Machines, 2008.

[20]   A. Abedini, and A. Nasiri, "Output Power Smoothing for Wind Turbine Permanent Magnet Synchronous Generators Using Rotor Inertia," *Electric Power components and Systems,* vol. 37, no. 1, pp. 1-19, 2009.

[21]   L. Ran, J. R. Bumby, and P. J. Tavner, "Use of turbine inertia for power smoothing of wind turbines with a DFIG," in International Conference on Harmonics and Quality of Power, 2004, pp. 106-111.

[22]   A. Teninge, C. Jecu, D. Roye *et al.*, "Contribution to frequency control through wind turbine inertial energy storage," *IET Renew. Power Gener.,* vol. 3, no. 3, pp. 358-370, 2009.

[23]   A. Kusko, and J. DeDad, "Short-term, long-term energy storage methods for standby electric power systems," in IEEE IAS 40th Annual Meeting, Hong Kong, October, 2005.

[24]   J. M. Guerrero, L. G. De Vicuna, and J. Uceda, "Uninterruptible power supply systems provide protection," *IEEE Industrial Electronics Magazine*, pp. 28-38, Spring 2007.

[25]   M. Hasan Ali, J. Tamura, and B. Wu, "SMES strategy to minimize frequency fluctuations of wind generation system," in IECON, 2008, pp. 3382-3387.

[26]   R. Cardenas, R. Pena, G. M. Asher *et al.*, "Control strategies for enhanced power smoothing in wind energy systems using a flywheel driven by a vectored-controlled induction machine," *IEEE Trans Industrial Electronics,* vol. 48, no. 3, pp. 625-635, June, 2001.

[27]   R. Cardenas, R. Pena, G. M. Asher *et al.*, "Power smoothing in wind generation systems using sensorless vector controlled induction machine driving a flywheel," *IEEE Trans on Energy Conversion,* vol. 19, no. 1, pp. 206-216, March, 2004.

[28]   K. Agbossou, M. Kolhe, J. Hamelin *et al.*, "Performance of a stand-aloe renewable energy system based on energy storage as hydrogen," *IEEE TRANSACTION ON ENERGY CONVERSION,* vol. 19, no. 3, pp. 633-640, 2004.

[29]   D. Hayashi, T. Senjyu, R. Sakamoto *et al.*, "Generating power leveling of renewable energy for small power system in isolated island," in 13th International Coneference on Intelligent system Application to Power Systems 2005.

[30] A. Price, S. Bartley, S. Male *et al.*, "A novel approach to utility scale energy storage," *Power Engineering Journal,* vol. 13, no. 3, pp. 122-129, 1999.

[31] S. Lemofouet, and A. Rufer, "A hybrid energy storage system based on compressed air and supercapacitors with maximum efficieny point tracking," *IEEE Trans Industrial Electronics,* vol. 53, pp. 1105-1115, August 2006.

[32] J. M. Guerrero, J. Matas, L. G. de Vicuna *et al.*, "Decentralized control for parallel operation of distributed generation inverters using resistive output impedance," *IEEE Transaction on Industrial Electronics,* vol. 54, no. 2, pp. 994-1004, 2007.

[33] R. H. Lasseter, and P. Piagi, "Extended microgrid using distributed energy resources," in Power Engineering Society General Meeting, 2007, pp. 1-5.

[34] Z. Jiang, and R. A. Dougal, "Hierarchical microgrid paradigm for integration of distributed energy resources," in Power and Energy Society General Meeting, 2008, pp. 1-8.

[35] R. H. Lasseter, and P. Piagi, "Microgrid: a conceptual solution," in PESC 04, Aachen, Germany, 2004, pp. 4285 - 4290.

[36] Z. Jiang, and X. Yu, "Power electronics interfaces for hybrid DC and AC-linked microgrids," in IPEMC, 2009, pp. 730-736.

[37] A. Siddiqui, C. Marnay, K. Hamachi *et al.*, "Customer adoption of amall-scale on-site power generation," in Proceeding of European Council for an Energy Efficient Economy Summer Study, Mandelieu, France, 2001.

[38] J. Eto, V. Budhhraja, C. Martinez *et al.*, "Research, development and demostration needs for large-scale, reliability-enehancing, integration of distributed energy resources," in Proceeding of the 33rd Annual Hawaii International Conference on System Sciences, 2000, pp. 1-7.

[39] C. Wang, and M. H. Nehrir, "Analytical approaches for optimal placement of distributed generation sources in power systems," *IEEE Trans on Power System,* vol. 19, no. 4, pp. 2068-2076, Nov., 2004.

[40] M. I. Marie, E. F. El-Saadany, and M. M. A. Salama, "An inteligent control for the DG interface to mitigate voltage flicker," in Proceeding of the Eighteenth Annual IEEE Power Electronics Coneference, 2003, pp. 179-183.

[41] F. Blaabjerg, Z. Chen, and S. B. Kjaer, "Power electronics as efficient interface in dispersed power engineering systems," *IEEE Trans on Power Elecrotronics,* vol. 19, no. 5, pp. 1184-1194, Sep.2004, 2004.

[42] E. Barklund, N. Pogaku, M. Prodanovic *et al.*, "Energy managment in autonomous microgrid using stability-constraned droop control of inverters," *IEEE Transaction on Power Electronics,* vol. 23, no. 5, pp. 2346-2352, 2008.

[43] R. Pena, J. C. Clare, and G. M. Asher, "Doubly fed induction generator using back-to-back PWM converters and its application to variable speed wind energy generation," *IEEE Proc.-Electr. Power Appl.,* vol. 143, no. 3, pp. 231-241, May, 1996.

[44] R. Pena, J. C. Clare, and G. M. Asher, "A doubly fed induction generator using back to back PWM converters supplying an isolated load from a

varialble speed wind turbine," *IEEE Proc.-Electr. Power Appl.,* vol. 143, no. 5, pp. 380-387, Sep., 1996.

[45] T. Ackermann, *Wind Power in Power Systems*, Sweden: John Wiley & Sons, Ltd, 2005.

[46] S. Muller, M. Deicke, and R. W. De Doncker, "Doubly fed induction generator for wind turbines," *IEEE Industry Application Magazine,* vol. 8, no. 3, pp. 26-33, 2002.

[47] N. Horiuchi, and T. Kawahito, "Torque and power limitations of variable speed wind turbines using pitch control and generator power control," in Power engineering society summer meeting, 2001, pp. 638-643.

[48] L. Risheng, "Control of offshore wind farm with line commutated HVDC link connection," Electrical and Electronic engineering, The University of Nottingham, 2008.

[49] T. Sun, "Power quality of grid connected wind turbines with DFIG and their interaction with the grid," Faculty of Engineering & Science, Institute of Energy Technology, Alborg University, 2004.

[50] P. Andreas, "Analysis, modeling and control of Doubly Fed Induction Generators for wind turbines," Department of Energy and Environment, KTH, Goteborg, Sweden, 2005.

[51] L. Xu, and P. Cartwritght, "Direct active and reactive power control of DFIG for wind energy generation," *IEEE Trans on Energy Conversion,* vol. 21, no. 3, pp. 750-758, September, 2006.

[52] Y. Lai, J. H. Chen, and C. H. Liu, "A universal vector controller for induction motor drives fed by voltage-controlled voltage source converter," in Power Engineering Society Summer Meeting 2000, pp. 2493-2498.

[53] P. M. Anderson, and A. Bose, "Stability simulation of wind turbine systems," *IEEE Transaction on Apparatus and Syatems,* vol. PAS-102, no. 12, pp. 3791-3795, December, 1983.

[54] C. Luo, B. Banakar, B. Shen *et al.*, "Strategies to smooth wind power fluctuations of wind turbine generator," *IEEE Transaction on Eenergy Conversion,* vol. 22, no. 2, June, 2007.

[55] T. Luu, A. Abedini, and A. Nasiri, "Power smoothing of doubly fed induction generator wind turbines," in Industerial Electronic, 2008.

[56] M. Fazeli, G. M. Asher, C. Klumpner *et al.*, "Wind turbine-energy storage control system for delivering constant demand power shared by DFIGs through droop characteristics," in EPE, Barcelona, Spain, 2009, pp. 1-10.

[57] R. G. de Almeida, E. D. Castronuovo, and J. A. Pecas Lopes, "Optimum generation control in wind park when carrying out system operator request," *IEEE Trans on Power System,* vol. 21, no. 2, pp. 718-725, May, 2006.

[58] A. D. Hansen, P. Sorensen, F. Lov *et al.*, "Power control of a wind farm with active stall wind turbines and AC grid connection," in European wind Energy Conference, Athens (GR), 2006, pp. 6.

[59] Z. Lubosny, and J. W. Bialek, "Supervisory control of a wind farm," *IEEE Transaction on Power Systems,* vol. 22, no. 3, pp. 985-994, 2007.

[60] T. Senjyu, R. Sakamoto, N. Urasaki *et al.*, "Output power leveling of wind turbine generator foe all operating regions by pitch angle control," *IEEE Trans on Energy Conversion,* vol. 21, no. 2, pp. 467-475, June, 2006.

[61] J. Arrillaga, *High voltage direct current transmission*, London, 1998.

[62] L. Xu, and B. R. Anderson, "Grid connection of large offshore wind farms using HVDC," *Wind Energy,* vol. 9, no. 4, pp. 371-382, 2005.

[63] N. M. Kirby, L. Xu, M. Luckett *et al.*, "HVDC transmission for large offsore wind farms," *IEE Power Engineering Journal*, June, 2002.

[64] C. Feltes, and I. Erlich, "Variable frequency operation of DFIG based wind farm connected to the grid through VSC-HVDC limk," in Power Engineering Society General Meeting, 2007, pp. 1-7.

[65] http://www.abb.com/industries/us/9AAF400197.aspx, "HVDC-light, on 8/3/2010."

[66] L. Xu, B. R. Anderson, and P. Cartwritght, "VSC transmission operating under unbalanced AC conditions-analysis and control design," *IEEE TRANS on Power Delivery,* vol. 20, no. 1, pp. 427-434, 2005.

[67] Y. Ming, L. Gengyin, L. Guangkai *et al.*, "Modeling of VSC-HVDC and its active power control scheme," in International Conference on Power System Technology, Singapore, 2004.

[68] A. Arulampalam, J. B. Ekanayake, and N. Jenkins, "Application study of a STATCOM with energy storage," *IEE Proceeding-Generation, Transmission and Distribution,* vol. 150, no. 3, pp. 373 - 384, May, 2003.

[69] P. Cartwritght, and L. Xu, "The integration of large scale wind power generation into transmission network using power electronics," in CIGRE General Session, Paris, 2004.

[70] B. R. Anderson, and L. Xu, "Hybrid HVDC for Power transmission to island network " *IEEE TRANS on Power Delivery,* vol. 19, no. 4, pp. 1884-1890, 2004.

[71] M. Fazeli, S. Bozhko, G. M. Asher *et al.*, "Voltage and frequency control of offshore DFIG-based wind farms with line commutated HVDC connection," in PEMD, York, 2008, pp. 335-339.

[72] R. Li, S. Bozhko, G. M. Asher *et al.*, "Offshore grid frequency control desine for line commutated converters high voltage direct current link connected wind farm," *IET Renew. Power Gener.,* vol. 1, no. 4, pp. 211-219, 2007.

[73] M. Shahabi, M. R. Haghifam, M. Mohamadian *et al.*, "Microgrid dynamic performance improvement using a doubly fed Induction wind generator," *IEEE Transaction on Energy Conversion,* vol. 24, no. 1, pp. 137-145, March, 2009.

[74] L. Fan, Z. Miao, and D. Osborn, "Wind farm HVDC delivery in load frequency control," *IEEE Transaction on Power Systems,* vol. 24, no. 4, pp. 1894-1895, 2009.

[75] N. Pogaku, M. Prodanovic, and T. Green, C, "Modeling, analysis and testing of autonomous operation of an inverter-based microgrid," *IEEE Transaction on Power Electronics,* vol. 22, no. 2, pp. 613-625, 2007.

[76] M. C. Chandorkar, D. M. Divan, and R. Adapa, "Control of parallel connected inverters in standalone ac supply systems," *IEEE TRansaction on Industry Applications,* vol. 29, no. 1, pp. 136-143, 1993.

[77] U. Borup, F. Blaabjerg, and P. N. Enjeti, "Sharing of nonlinear load in parallel-connected three-phase converters," *IEEE Transaction on Industry Applications,* vol. 37, no. 6, pp. 1817-1823, 2001.

[78] K. S. Parlak, M. T. Aydemir, and M. Ozdemir, "Active and reactive power sharing in parallel operated inverters," in IEEE MELECON, Benalmadena, Spain, 2006.

[79] J. M. Guerrero, L. G. de Vicuna, J. Matas *et al.*, "A wireless contoller to enhance the dynamic performance of parallel inverters in distributed generation systems," *IEEE Transaction on Power Electronics,* vol. 19, no. 5, pp. 1205-1213, 2004.

[80] J. M. Guerrero, L. G. de Vicuna, J. Matas *et al.*, "Output impedance design of parallel-connected UPS inverters with wireless load sharing control," *IEEE Transaction on Industrial Electronics,* vol. 52, no. 4, pp. 1126-1135, 2005.

[81] K. De Brabandere, B. Bolsens, V. den Keybus *et al.*, "A voltage and frequency droop control for parallel inverters," in 53th annual IEEE Power Electronics Specialists conference, Aachen, Germany, 2004.

[82] T. Senjyn, R. Sakamoto, N. Urasaki *et al.*, "Output power leveling of wind turbine generator foe all operating regions by pitch angle control," *IEEE Trans on Energy Conversion,* vol. 21, no. 2, pp. 467-475, June, 2006.

[83] T. Senjyn, R. Sakamoto, N. Urasaki *et al.*, "Output power control of wind turbine generator by pitch angle control using minimum variance control," *Electrical Engineering in Japan,* vol. 154, no. 2, 2006.

[84] K. Ogata, *Modern control engineering, the Fourth Edition*: Prentice Hall, New Jersy, 2001.

[85] J. Morren, S. W. H. De Haan, and H. Polinder, "Ride-through of wind turbines with doubly-fed induction generator during vpltage dip," *IEEE Transaction on Eenergy Conversion,* vol. 20, no. 2, 2005.

11. Publication

- "Novel control scheme for wind generation with energy storage supplying given demand power" EPE-PEMC 2010, Macedonia
- *Poster presentation*: "Novel integration of energy storage with wind turbines" EWEC 2010, Warsaw, Poland
- "Wind turbine-energy storage control system for delivering constant demand power shared by DFIGs through droop characteristics" EPE 2009, Barcelona, pp. 1-10
- "Voltage and frequency control of offshore DFIG-based wind farms with line commutated HVDC connection" PEMD 2008,York, UK, pp. 335-339

Submitted papers

- IEEE Transaction on Energy Conversion, 2011
- IEEE Transaction on Industrial Electronics, Special Section: Distributed Generation and Microgrid, 2011
- Following the acceptance of these two papers, more paper can be published

Appendix A: Design of DFIGs' PI controllers

This appendix offers the computer codes in order to the design of a DFIG's PI controllers. The codes are written in MATHCAD since the software uses very similar mathematical expressions to the standard mathematic ones which make the codes very easy to follow. The codes are given for a 1000MVA DFIG; however, they are used to design the PI controllers of DFIG with different ratings such as: 660, 340 and 3MVA. In order to obtain the PI controllers for other ratings, it is needed to change the rating of the DFIG and choose appropriate parameters.

The codes are as follows:

$Sb := 1000$　　　　MVA　　　　**DFIG rating**

$Wb := 314.159$　　rad/s　　　**Electrical frequency**

$Nsr := 1$　　　　**Stator/rotor turns ratio**

$E := 2$　　kV　　　**DFIG DC-link voltage**

$m1 := 0.85$

$m2 := 0.76$　　　**modulation index**

Stator (Y connected):

$Vsb := 1$　　　kV　　**(Line to line rms)**

$Isb := \dfrac{Sb}{\sqrt{3} \cdot Vsb}$　　kA

$\dfrac{1}{Isb} = 0.0017$

$Xsb := \dfrac{Vsb}{\sqrt{3} \cdot Isb}$　　Ohms

$Lsb := \dfrac{Xsb}{Wb}$　　H

$Sm := \dfrac{Nsr \cdot m2}{\sqrt{3} \cdot m1}$

Rotor (Y connected):

$Vrb := \dfrac{Vsb}{Nsr}$　　kV

$Vrb = 1$　　　**(line to line rms)**

$Irb := \dfrac{Sb}{\sqrt{3} \cdot Vrb}$　　kA

$\dfrac{1}{Irb} = 0.0017$

$$Xrb := \frac{Vrb}{\sqrt{3} \cdot Irb} \qquad \text{Ohms}$$

$$Lrb := \frac{Xrb}{Wb} \qquad \text{H}$$

PU values:

$Rspu := 0.0066$

$Rrpu := 0.0044$ **stator and rotor resistance**

$L0pu := 3.07$

$lspu := 0.07$ **stator leakage inductance**

$Lspu := L0pu + lspu$

$Lspu = 3.14$

$lrpu := 0.15$ **rotor leakage inductance**

$Lrpu := L0pu + lrpu$

real values (Ohms & H):

$Rs := Rspu \cdot Xsb$

$Rr := Rrpu \cdot Xrb$

$Ls := Lspu \cdot Lsb$

$Lr := Lrpu \cdot Lrb$

$L0 := L0pu \cdot Lsb$

$$\sigma := 1 - \frac{L0pu^2}{Lspu \cdot Lrpu}$$

$$\frac{L0pu}{Lspu} = 0.9777$$

$$\sigma s := \frac{Lspu}{L0pu} - 1$$

$$1 + \sigma s = 1.0228$$

referred to rotor (Ohms & H):

$$Rsr := \frac{Rs}{Nsr^2}$$

206

$$\frac{1 + \sigma s}{Rsr} = 1.549699 \times 10^5$$

$Rrr := R\iota$

$$Lsr := \frac{Ls}{Nsr^2}$$

$Lrr := L\iota$

$$L0r := \frac{L0}{Nsr^2}$$ **assuming that theL0 is on the stator side**

referred to stator(Ohms & H):

$Rss := Rs$

$Rrs := Nsr^2 \cdot R\iota$

$Lss := Ls$

$Lrs := Nsr^2 \cdot L\iota$

Rotor side converter:

current loop:

$\zeta := 0.85$

$\omega := 250$ Hz

$\omega n := \omega \cdot 2\pi$ rad/s

$$Tr := \frac{3 \cdot \zeta}{\omega n}$$

$Tr = 0.0016$

$$-\zeta \cdot \omega n + \omega n \cdot i \cdot \sqrt{\left(1 - \zeta^2\right)} = -1335.1769 + 827.4683i$$

Plant:

$$G(s) := \frac{1}{Rr + s \cdot \sigma \cdot Lr}$$

$$Kc := \frac{1}{\sigma \cdot Lr}$$

$$bc := \frac{Rr}{\sigma \cdot Lr}$$

Pole-placement:

$$a := bc$$

$$kpc := \frac{\ln(9)}{Kc \cdot Tr}$$

$$kpc = 9.411 \times 10^{-4}$$

$$kic := a \cdot kpc$$

$$tc := \frac{1}{kic}$$

$$tc = 167.9164$$

Grid side converter:

$Vgb := 33$ kV   **Line to line rms**

$Vcb := 1$ kV   **Line to line rms**

$$Ngc := \frac{Vgb}{Vcb}$$

$$Igb := \frac{Sb}{\sqrt{3}\,Vgb}$$

$$Xgb := \frac{Vgb}{\sqrt{3}\cdot Igb}$$

$$Lgb := \frac{Xgb}{Wb}$$

$$Icb := \frac{Sb}{\sqrt{3}\cdot Vcb}$$

$$Xcb := \frac{Vcb}{\sqrt{3}\,Icb}$$

$$Lcb := \frac{Xcb}{Wb}$$

$Sct := 400$ MVA   *Converter Transformer*

208

$$\text{Xtpu} := 0.12 \qquad \textbf{Based on Transformer rating}$$

$$\text{Xlpu} := \text{Xtpu} \cdot \frac{\text{Sb}}{\text{Sct}}$$

$$\text{Xl} := \text{Xlpu} \cdot \text{Xcb}$$

$$\text{Xl} = 3 \times 10^{-4} \qquad \boldsymbol{Ohms}$$

$$\text{Lc} := \frac{\text{Xl}}{\text{Wb}}$$

$$\text{Rtpu} := 0.005$$

$$\text{Rcpu} := \text{Rtpu} \cdot \frac{\text{Sb}}{\text{Sct}}$$

$$\text{Rc} := \text{Rcpu} \cdot \text{Xcb}$$

current loop:

$$\zeta g := 0.85$$

$$\omega g := 250 \qquad \text{Hz}$$

$$\omega ng := \omega g \cdot 2\pi \qquad \text{rad/s}$$

$$\text{Trg} := \frac{3 \cdot \zeta g}{\omega ng}$$

$$-\zeta g \cdot \omega ng + \omega ng \cdot i \cdot \sqrt{\left(1 - \zeta g^2\right)} = -1335.1769 + 827.4683i$$

Plant:

$$\text{Gg}(s) := \frac{1}{\text{Rc} + s \cdot \text{Lc}}$$

$$\text{Kg} := \frac{1}{\text{Lc}}$$

$$\text{Bg} := \frac{\text{Rc}}{\text{Lc}}$$

Pole-placement:

$$\text{ag} := \text{Bg}$$

$$kpg := \frac{\omega ng}{Kg}$$

$$kpg = 0.0015$$

$$kig := ag \cdot kpg$$

$$tg := \frac{1}{kig}$$

$$tg = 50.9296$$

Voltage loop:

$$m1 = 0.85$$

$$C := 1 \qquad \textit{Farad}$$

$$\zeta v := 0.75$$

$$\omega v := 20 \qquad \text{Hz}$$

$$\omega nv := \omega v \cdot 2\pi \qquad \text{rad/s}$$

$$Trv := \frac{3 \cdot \zeta v}{\omega nv}$$

$$-\zeta v \cdot \omega nv + \omega nv \cdot i \cdot \sqrt{\left(1 - \zeta g^2\right)} = -94.2478 + 66.1975i$$

Plant:

$$Gv(s) := \frac{3 \cdot m1}{4 \cdot C \cdot s}$$

$$Kv := \frac{3 \cdot m1}{4 \cdot C}$$

characteristic eq:

$$Kpv := \frac{2 \cdot \zeta v \cdot \omega nv}{Kv}$$

$$Kpv = 295.6793$$

$$Av := \frac{\omega nv^2}{Kpv \cdot Kv}$$

$Av = 83.7758$

$\dfrac{1}{Av} = 0.0119$

$Kiv := Av \cdot Kpv$

$Tv := \dfrac{1}{Kiv}$

$Tv = 4.037 \times 10^{-5}$

ISFO-controlled DFIG-Stator magnetizing current:

$\zeta m := 0.85$

$\omega m := 20 \qquad Hz$

$\omega nm := \omega m \cdot 2\pi \qquad rad/s$

$Trm := \dfrac{3 \cdot \zeta m}{\omega nm}$

$-\zeta m \cdot \omega nm + \omega nm \cdot i \cdot \sqrt{\left(1 - \zeta m^2\right)} = -106.8142 + 66.1975i$

Plant:

$Km := \dfrac{Rsr}{Lsr}$

$Gn(s) := \dfrac{Km}{s + Km}$

$\dfrac{1}{Wb \cdot L0r} = 325.7329 \qquad$ **is used in voltage droop**

$Imspu := \dfrac{Vsb}{Wb \cdot L0r \cdot \sqrt{1.5}}$

Pole-placement:

$am := Km$

$kpm := \dfrac{\ln(9)}{Km \cdot Trm}$

$kpm = 163.9759$

kim := am·kpm

kim = 108.279

$$tm := \frac{1}{kim}$$

tm = 0.0092

Appendix B: System parameters

DFIGs:

Rated wind speed = 12.5m/s, Cut-in wind speed = 4.5m/s

Rated voltage = 1kV, Base angular frequency = 314.16rad/s

Shaft inertia = 3.5pu$_{gen}$

Stator resistance = 0.0066pu$_{gen}$, Rotor resistance = 0.0044pu$_{gen}$

Stator leakage inductance = 0.07pu$_{gen}$, Rotor leakage inductance = 0.15pu$_{gen}$, Magnetizing inductance = 3.07pu$_{gen}$

1000MVA

The capacitance of the 1000MVA DFIG's DC-link = 1F

Control loop	PI controller	Closed loop bandwidth, Hz
Rotor side current loop	$0.001 + \dfrac{1}{168s}$	250
Grid side current loop	$0.0015 + \dfrac{1}{51s}$	250
DC link voltage control	$295 + \dfrac{1}{4.04e^{-5}s}$	20

DFIG1-660MVA (0.66pu)

The capacitance of the 660MVA DFIG's DC-link = 0.7F

Control loop	PI controller	Closed loop bandwidth, Hz
Rotor side current loop	$0.0014 + \dfrac{1}{110.8s}$	250
Grid side current loop	$0.0023 + \dfrac{1}{33.61s}$	250
DC link voltage control	$207 + \dfrac{1}{5.8e^{-5}s}$	20

DFIG2-340MVA (0.34pu)

The capacitance of the 340MVA DFIG's DC-link = 0.45F

Control loop	PI controller	Closed loop bandwidth, Hz
Rotor side current loop	$0.0028 + \dfrac{1}{57.1s}$	250
Grid side current loop	$0.0044 + \dfrac{1}{17.3s}$	250
DC link voltage control	$133 + 8.9\dfrac{1}{5.8e^{-5}s}$	20

LCC-HVDC:

Rated current = 2kA, Rated voltage = 500kV

DC-link resistance = 5ohm, DC-link inductance = 1.2H

4-step switchable AC-filter:

The capacitance of each step = 25.4µF

The inductance of each step = 0.0028H

The resistance of each step = 1ohm

Appendix C: Control of STATCOM connected to LCC-HVDC link

There are a number of methods for controlling a STATCOM. In this appendix the control method introduced in [4], is briefly explained.

Figure 11 shows a DSFO-controlled wind farm connected to the grid through a LCC-HVDC link and STATCOM. The STATCOM controls the wind farm grid voltage and frequency. Constant voltage and frequency indicate that all wind power fluctuations are reflected on the STATCOM DC-link voltage E_s. Therefore the STATCOM DC-link voltage is used to control the HVDC current I_0 (active power) through regulating rectifier firing angle α.
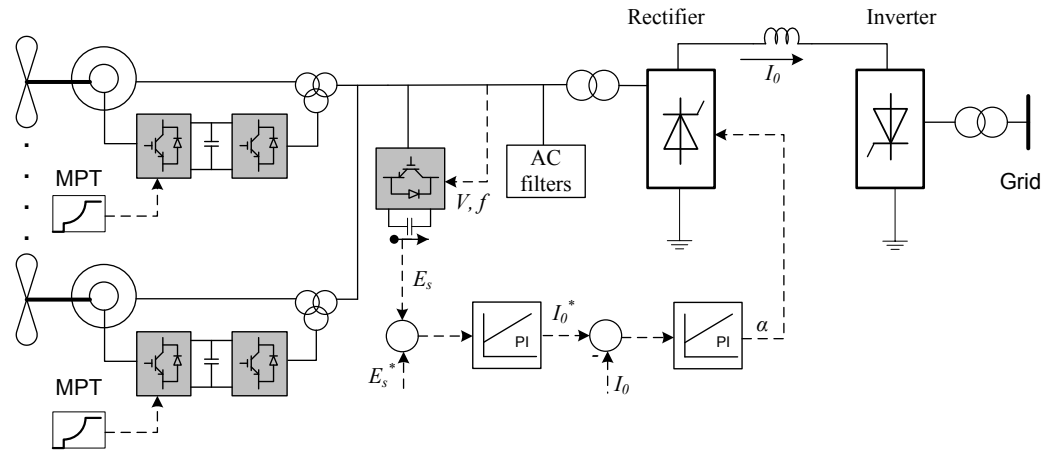

Figure 11. DSFO-controlled wind farm connected to LCC-HVDC link and STATCOM

In order to obtain a mathematical model of the power system for control design, the following assumptions are maid:

- Since wind turbines are under DSFO control, they can be represented by controlled current source.
- The AC harmonic filters are designed to suppress 11th and 13th harmonics and have natural frequency above the designed control system bandwidths. For control purpose, the filters are represented by their dominant capacitive properties.

215

- The HVDC inverter controls the HVDC DC-link voltage and has almost no effect on the wind farm grid control regime. Therefore it is replaced by an equivalent DC voltage source.

Figure 12 shows the simplified diagram of the system shown in Figure 11 based on the assumptions above. The DFIGs deliver current I_G and the HVDC absorbs current I_C. Capacitor C_f is the total capacitance of the filters, and R-L elements represents the transformers and cables parameters. Depending on operational demand, the STATCOM current I_S can be injected into/absorbed from the local AC grid. The parameters R_0 and L_0 represent the HVDC DC-link connection (the cable capacitance is neglected). The DC voltage source E_0 represents the HVDC inverter.
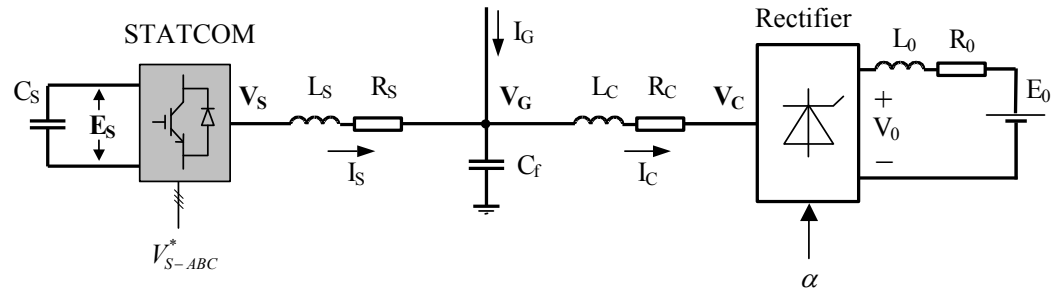

Figure 12. Simplified diagram of system shown in Figure 11

Seen from the wind farm grid, the HVDC rectifier is a current source dependent on the collector grid voltage. Seen from the HVDC DC side, the rectifier can be considered as a voltage source with magnitude of $V_0 \approx k_r V_C \cos\alpha$ where k_r is a constant defined by rectifier scheme [4]. The STATCOM is a voltage source converter and can be represented as a 3-phase voltage source V_S while the STATCOM DC-link can be represented by a DC-current source I_{S0} derived from I_S. The equivalent circuit of system is shown in Figure 13.
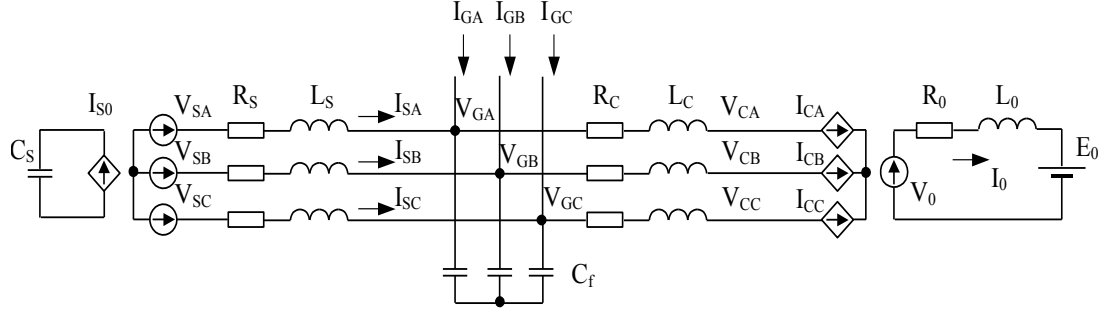
216

Figure 13. Equivalent circuit for mathematical modeling

In [4], a set of 3-phase non-linear equations is derived based on the equivalent circuit shown in Figure 3. Then those equations were transformed into a rotating *dq* frame with d-axis aligned on the rectifier AC terminal voltage. This gives a linear control plant:

$$C_f \frac{dV_{Gd}}{dt} = I_{Sd}^* - I_{Cdm} + I_{Gd}$$

$$C_f \frac{dV_{Gq}}{dt} = I_{Sq}^* - I_{Cqm} + I_{Gq} - \omega C_f V_{Gd} \tag{1}$$

$$C_S \frac{dE_{S0}^2}{dt} = -(2k_r V_{Gd0} \cos\alpha_0) I_0^* + 3V_{Gd0} I_{Gd}$$

Based on (1), control outputs are: V_{Gd}, V_{Gq} and E_{S0}^2; control inputs are: I_{Sd}^*, I_{Sq}^* and I_0^* while I_{Gd}, I_{Gq}, I_{Cdm} and I_{Cqm} are disturbances. Note that all the disturbances are available for direct measurement which allows feed-forward compensation to improve control loop performance. Figure 14 illustrates a simplified block diagram of control structure base on (1). More detailed control structure is given in [4]. The power transferred from wind farm into the HVDC is controlled by STATCOM DC-link voltage E_S through regulating HVDC DC-link current I_0. The HVDC DC current control loop design is out of the scope of this thesis and is discussed in [4]. The d-component of the grid voltage V_{Gd} is controlled by the STATCOM d-axis current I_{Sd} while V_{Gq} (or frequency) is controlled by I_{Sq}.
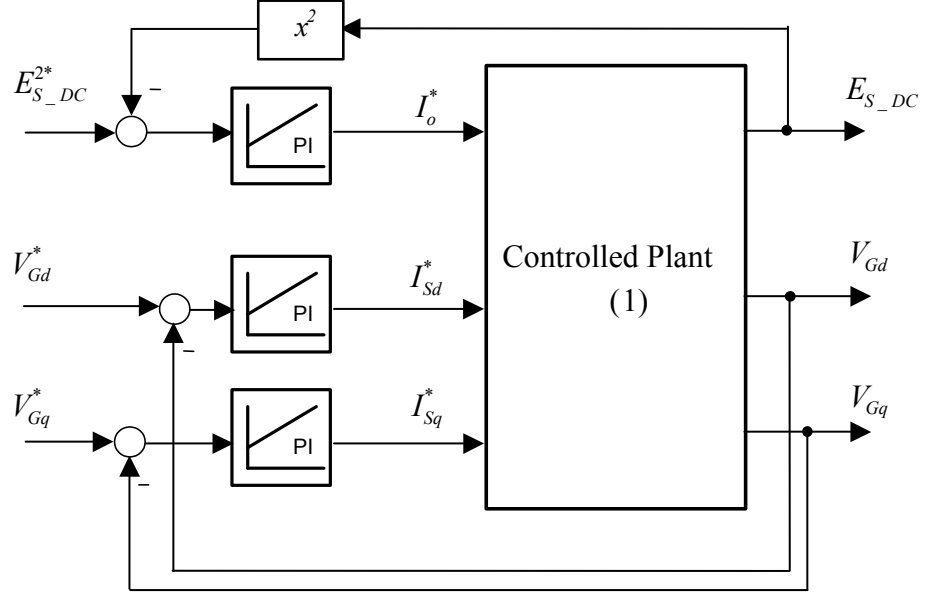
Figure 14. Simplified block diagram of control structure

A STATCOM can also be used as ES interface (ESI) [12, 68]. In this case the STATCOM DC-link voltage is controlled by the ES current, thus the active power balance is achieved. The HVDC current loop control design is out of the focus of this thesis and is explained in [4].

The PI controllers used in this thesis are given in the table below:

Control loop	PI controller	Closed loop bandwidth, Hz
ESI-STATCOM current loops	$2.7 + \dfrac{1}{9.3s}$	250
Voltage control	$1.03 + \dfrac{1}{0.0034s}$	90

Appendix D: Size of the ES

This appendix gives a perspective of the size of the ES, assuming that the ES is a flywheel. Letting the mass, radius and the thickness of the flywheel be *m*, *r* and *h* respectively, one can write:

$$\rho = \frac{m}{\pi h r^2}$$
$$J_{es} = 0.5mr^2$$
$$E_{es} = 0.5J_{es}\omega_{es}^2$$

$$(1)$$

where ρ, J_{es}, E_{es} and ω_{es} are, respectively, the flywheel density, inertia, energy capacity and shaft speed. Assuming that the flywheel is made of iron (ρ=7870kg/m^2) and rotating at ω_{es}=3000rpm, the energy capacity in Mjoules is:

$$E_{es} = 610hr^4 \tag{2}$$

Letting *r*=0.5m, Table 2gives the thickness of the flywheel for 1 and 3MVA DFIGs when the required energy capacity is 1, 5 and 20pu$_{gen}$.

Rating of DFIG	1MVA			3MVA		
E_{es}, pu$_{gen}$	1	5	20	1	5	20
h, meter	0.026	0.13	0.52	0.079	0.39	1.57

Table 2. Thickness of flywheel for different required energy capacities

For example, 5pu$_{gen}$ energy capacity for a 1MVA DFIG is 5Mjoules while that of a 3MVA DFIG is 15Mjoules. It can be seen that the 5pu$_{gen}$ energy capacity represents a very modest rotating mass. This is why the capacity of the ES simulated in this thesis is chosen to be 5pu$_{gen}$.

Appendix E: Changing the standard deviation of a given wind speed profile

The both wind speed profiles used in this thesis are real wind speed sampled at every second. The average of the wind speed profiles can be changed by adding a number to the all samples. The perturbation of a wind speed profile can be expressed by its standard variation:

$$\sigma = \sqrt{\frac{\sum_{i=1}^{N}\left(V_{wi} - \overline{V_w}\right)^2}{N}} \tag{1}$$

where V_{wi} is the ith sample of the wind speed profile, N is the number of the samples and $\overline{V_w}$ is the average wind speed. The standard deviations of wind profiles used in this thesis are 1.28 and 1.39 which seem to be above the normal wind variation. It can be helpful to be able to change the standard deviation of a wind profile while its average is kept the same. If the new standard deviation σ' is to be k times of the previous one, the ith sample of the new wind profile is defined by:

$$V_{wi}{}' = k\left(V_{wi} - \overline{V_w}\right) + \overline{V_w} \tag{2}$$

This can be easily demonstrated:

$$\sigma = \sqrt{\frac{\sum_{i=1}^{N}\left(V_{wi}{}' - \overline{V_w}\right)^2}{N}} \tag{3}$$

Substitution of (2) into (3) and simplifying it, gives:

$$\sigma' = \sqrt{\dfrac{\sum\limits_{i=1}^{N}\left(kV_{wi} - k\overline{V_w}\right)^2}{N}}$$

$$= \sqrt{\dfrac{k^2\sum\limits_{i=1}^{N}\left(V_{wi} - \overline{V_w}\right)^2}{N}} \tag{4}$$

$$= k\sigma$$

Now it is needed to be shown that the average of the new wind profile is the same as the original one. The average of the original wind profile is:

$$\overline{V_w} = \dfrac{\sum\limits_{i=1}^{N}V_{wi}}{N} \tag{5}$$

The average of the new wind profile is:

$$\overline{V_w}' = \dfrac{\sum\limits_{i=1}^{N}V_{wi}'}{N} \tag{6}$$

Substitution of (2) into (6) and simplifying it, gives:

$$\overline{V_w}' = \dfrac{1}{N}\left(k\sum\limits_{i=1}^{N}V_{wi} - (k-1)\sum\limits_{i=1}^{N}\overline{V_w}\right)$$

$$= \dfrac{1}{N}\left(k\sum\limits_{i=1}^{N}V_{wi} - (k-1)N\overline{V_w}\right) \tag{7}$$

Substitution of (5) into (7) yields:

$$\overline{V_w}' = \frac{1}{N}\left(k\sum_{i=1}^{N}V_{wi} - (k-1)\sum_{i=1}^{N}V_{wi}\right)$$

$$\frac{\sum_{i=1}^{N}V_{wi}}{N}$$

$$= \overline{V_w} \tag{8}$$

Equations (4) and (8) show that changing the wind speed samples according to (2) keeps the average the same and makes the standard deviations k-fold.

Appendix F: Calculation of optimum shaft speed

As Figure 15 illustrates, the optimum shaft speed ω_{opt} is the shaft speed at which the turbine power is maximum for a given wind speed and pitch angel. If pitch angle is zero, the turbine power is equal to the maximum extractable wind power $\hat{P}_{ave}$.
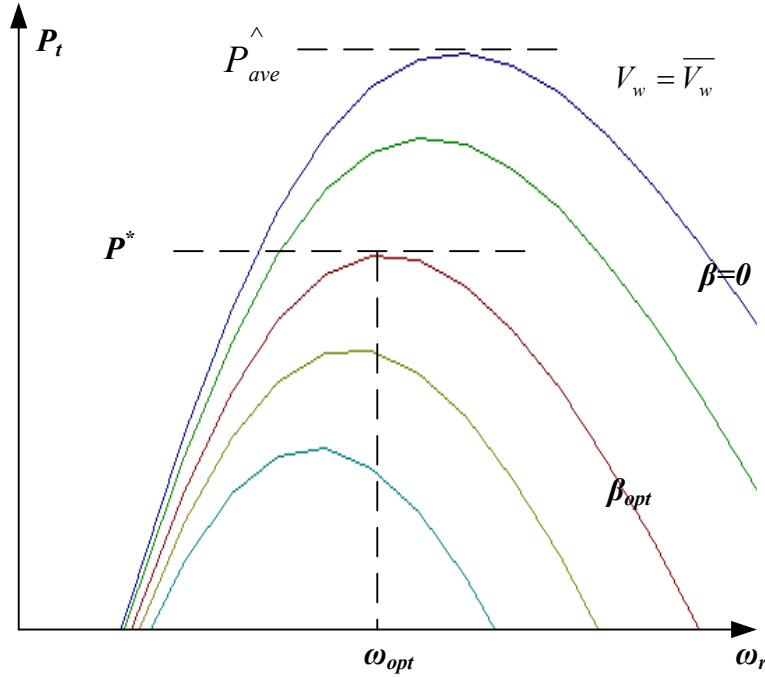

Figure 15. Turbine power-shaft speed characteristic

This appendix calculates ω_{opt} for a given P^* (hence β_{opt}) and wind speed V_w. The PSCAD wind turbine model, which is used in this thesis, is described by (1):

$$C_p = 0.5\left(\lambda - 0.022\beta^2 - 5.6\right)e^{-0.17\lambda}$$
$$\lambda = \frac{2.237\,NV_w}{\omega_r} \tag{1}$$

where C_p, λ and N are power coefficient, Tip Speed Ratio (TSR) and gear ratio respectively. For $P_t = P^*$, C_p^* is:

$$P^* = P_t = 0.5\rho A V_w^3 C_p^* \rightarrow C_p^* = \frac{P^*}{0.5\rho A V_w^3} \tag{2}$$

One can define optimum TSR as:

$$\lambda_{opt} = \frac{2.237\, N V_w}{\omega_{opt}} \tag{3}$$

For $P_t = P^*$, also one can write:

$$C_p = C_p^* \rightarrow 2C_p^* = \left(\lambda_{opt} - 0.022\beta_{opt}^2 - 5.6\right)e^{-0.17\lambda_{opt}} \tag{4}$$

As Figure 15 shows, the P^* line is asymptote for $\omega_r = \omega_{opt}$ and $\beta = \beta_{opt}$. Therefore the shaft speed derivation of the turbine power for $\omega_r = \omega_{opt}$ and $\beta = \beta_{opt}$ must be zero. Thus, the shaft speed derivation of C_p must be also zero for $\omega_r = \omega_{opt}$ and $\beta = \beta_{opt}$:

$$\frac{dC_p}{d\omega_r} = \frac{dC_p}{d\lambda}\frac{d\lambda}{d\omega_r} = 0 \tag{5}$$

And sine $\dfrac{d\lambda}{d\omega_r} = \dfrac{-2.237\, N V_w}{\omega_r^2} \neq 0$, $\dfrac{dC_p}{d\lambda}$ for $\omega_r = \omega_{opt}$ and $\beta = \beta_{opt}$ must be zero:

$$\frac{dC_p}{d\lambda} = 0.5\left[-0.17 e^{-0.17\lambda_{opt}}\left(\lambda_{opt} - 0.022\beta_{opt}^2 - 5.6\right) + e^{-0.17\lambda_{opt}}\right] = 0 \tag{6}$$

Substituting (4) into (6) and solving it for λ_{opt}, gives:

$$\lambda_{opt} = \frac{Ln\left(0.34 C_p^*\right)}{-0.17} \tag{7}$$

Equating (7) with (3) and solving it for ω_{opt}, yields:

$$\omega_{opt} = \frac{-0.38 N V_w}{Ln\left(0.34 C_p^*\right)}$$
(8)

where C_p^* is given in (2).